

NUREG/CR-2238 (2 of 4)
SAND81-1529 (2 of 4)
R7
Printed August 1982

Advanced Reactor Safety Research Quarterly Report April - June 1981

Volume 18

Advanced Reactor Research Program

Prepared by
Sandia National Laboratories
Albuquerque, New Mexico 87185 and Livermore, California 94550
for the United States Department of Energy
under Contract DE-AC04-76DP00789

8209270471 820930
PDR NUREG
CR-2238 R PDR

Prepared for
U. S. NUCLEAR REGULATORY COMMISSION

NOTICE

This report was prepared as an account of work sponsored by an agency of the United States Government. Neither the United States Government nor any agency thereof, or any of their employees, makes any warranty, expressed or implied, or assumes any legal liability or responsibility for any third party's use, or the results of such use, of any information, apparatus product or process disclosed in this report, or represents that its use by such third party would not infringe privately owned rights.

Available from
GPO Sales Program
Division of Technical Information and Document Control
U.S. Nuclear Regulatory Commission
Washington, D.C. 20555

and

National Technical Information Service
Springfield, Virginia 22161

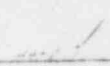
NUREG/CR-2238 (2 of 4)
SAND81-1529 (2 of 4)
Vol. 18
R-7

ADVANCED REACTOR RESEARCH PROGRAM
QUARTERLY REPORT
April-March 1981

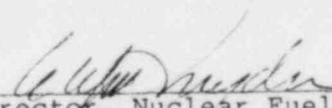
Advanced Reactor Research Program
Sandia National Laboratories
Albuquerque, NM 87185

Printed: August 1982

APPROVED:



Manager, Advanced Reactor Research



Director, Nuclear Fuel Cycle Programs

Sandia National Laboratories
Albuquerque, New Mexico 87185
Albuquerque, New Mexico 87185
operated by
Sandia Corporation
for the
U. S. Department of Energy

Prepared for
Division of Accident Evaluation
Office of Nuclear Regulatory Research
U. S. Nuclear Regulatory Commission
Washington, DC 20555
Under Memorandum of Understanding DOE 40-550-75
NRC FIN Nos.
A-1016, A-1021, A-1054, A-1172, A-1179,
A-1181, A-1182, A-1183, A-1197, A-1198,
A-1218, A-1219, A-1227, A-1247, A-1250

FOREWORD

Sandia Laboratories' Advanced Reactor Safety Research Program, initiated in FY 1975, is a comprehensive research activity conducted on behalf of the U.S. Nuclear Regulatory Commission (NRC) and is part of NRC's confirmatory research effort to assure that the necessary safety data and theoretical understanding exist to license and regulate the Liquid Metal Fast Breeder Reactor (LMFBR) or other advanced converters, breeders or advanced light water reactors which may be commercialized in the United States. The program includes a broad range of experiments to simulate accidental transient conditions to provide the required data base to understand the controlling accident sequences and to serve as a basis for verification of the complex computer simulation models and codes used in accident analysis and licensing reviews. Such a program must include the development of analytical models, verified by experiment, which can be used to predict reactor performance under a broad variety of abnormal conditions. Major program elements include studies of the coolability and containment of rubblelized cores to assure containment integrity. The program encompasses other energetics and inherent retention concerns such as large-scale sodium containment and structural integrity; aerosol source studies; transition phase energetics; fuel failure and motion; probabilistic accident delineation; and studies to quantify elevated temperature failure modes of critical component materials. A portion of the early effort in the program was directed toward obtaining data to support the licensing review of the Clinch River Breeder Reactor (CRBR) and the Fast Flux Test Facility (FFTF). Recently the emphasis has shifted toward applying advanced reactor safety technology to LWR Class 9 accident concerns which have been of considerable interest following the accident at TMI-2. For FY 1981, the program is organized in the following subtasks, progress on which is reported herein.

Task 1 Core Debris Behavior-Inherent Retention

- Subtask 1.1 Molten Core Containment
- 1.2 Core Retention Concept Assessment
- 1.3 PAHR Debris Bed
- 1.4 PAHR Molten Pool
- 1.5 Fragmentation
- 1.6 Sodium Containment and Structural Integrity
- 1.7 High Temperature Fission Product Chemistry and Transport

- Task 2 Containment Analysis
 - Subtask 2.1 CONTAIN Code Development
 - 2.2 MARCH Assessment Project
- Task 3 Elevated Temperature Design Assessment
- Task 4 LMFBR Accident Delineation
 - Subtask 4.1 Accident Delineation Study -- General
 - 4.2 Engineered Safety Systems (ESS)
 - 4.3 Accident Phenomenology
 - 4.4 Postaccident Phenomenology
- Task 5 Advanced Reactor Core Phenomenology
 - Subtask 5.1 Initiation Phase -- Fuel Dynamics
 - 5.2 Disassembly Phase -- Energetics
 - 5.3 Transition Phase
- Task 6 Light Water Reactor (LWR) Damaged Fuel Phenomenology
- Task 7 Test and Facility Technology
 - Subtask 7.1 ACRR Fuel-Motion Detection System
 - 7.2 ACRR Status

CONTENTS

	<u>Page</u>
FOREWARD.....	i
EXECUTIVE SUMMARY.....	E-1
1. Core Debris Behavior -- Inherent Retention.....	1-1
1.1 Molten Core Containment.....	1-1
1.2 Core Retention Concept Assessment.....	1-37
1.3 PAHR Debris Bed.....	1-52
1.4 PAHR Molten Pool.....	1-79
1.5 Fragmentation.....	1-83
1.6 Sodium Containment and Structural Integrity.....	1-85
1.7 High Temperature Fission Product Chemistry and Transport.....	1-99
2. Containment Analysis	2-1
2.1 CONTAIN Code Development.....	2-1
2.2 MARCH Assessment Project.....	2-2
3. Elevated Temperature Design Assessment.....	3-1
4. LMFBR Accident Delineation.....	4-1
4.1 Accident Delineation Study -- General.....	4-1
4.2 Engineered Safety Systems (ESS).....	4-3
4.3 Accident Phenomenology.....	4-24
4.4 Postaccident Phenomenology.....	4-28
4.5 CRBRP Risk Assessment Proposal.....	4-30
5. Advanced Reactor Core Phenomenology.....	5-1
5.1 Initiation Phase -- Fuel Dynamics.....	5-1
5.2 Disassembly Phase -- Energetics.....	5-11
5.3 Transition Phase.....	5-32
6. Light Water Reactor (LWR) Damaged Fuel Phenomenology.....	6-1
6.1 Introduction.....	6-1
6.2 Steam Loop Design.....	6-3

CONTENTS (Continued)

	<u>Page</u>
7. Test and Facility Technology.....	7-1
7.1 ACRR Fuel-Motion Detection System.....	7-1
7.2 ACRR Status.....	7-12

ILLUSTRATIONS

<u>Figure</u>		<u>Page</u>
1.1-1	Hypothetical Temperature -- Time History of Melt-Concrete Interaction.....	1-2
1.1-2	Limestone/Common Sand Crucible, Horizontal Rt. Cyl.....	1-5
1.1-3	Limestone/Common Sand Crucible, Spherical Cavity.....	1-6
1.1-4	Transient Test Apparatus.....	1-7
1.1-5	Crucible Configuration for X-Ray Imaging Test.....	1-9
1.1-6	Thermocouple Configuration.....	1-10
1.1-7	Base Configuration, Thermocouple Support Structure.....	1-13
1.1-8	Concrete Crucible.....	1-16
1.1-9	Temperature and Power vs. Time Hot Solid Scoping Test.....	1-20
1.1-10	Posttest Configuration Sustained Hot Solid Experiment (Scoping Test).....	1-21
1.1-11	SEM Photo of $MgU_2O_6-ZrO_2$ Oxide Precipitate From Basalt Melt at 1823 K (1550°C) for 1 Hour.....	1-24
1.1-12	UO_2 Content of Basalt at 1473 K (1200°C) for 1 Hour.....	1-25
1.1-13	UO_2 Content of Basalt at 1673 K (1400°C) for 1 Hour.....	1-26
1.1-14	UO_2 Content of Basalt at 1823 K (1550°C) for 1 Hour.....	1-27
1.1-15	Schematic of the Aerosol Source Term Model.....	1-33

ILLUSTRATIONS (Continued)

<u>Figure</u>		<u>Page</u>
1.2-1	Furnace Susceptor Support, Old Design.....	1-38
1.2-2	Furnace Susceptor Support, New Design.....	1-39
1.2-3	Steady-State Power vs. Temperature.....	1-41
1.2-4	Typical Titanium Dioxide Heating Curve.....	1-43
1.2-5	Melt Seepage Through an Initially Dry Gravel Bed.....	1-45
1.3-1	D7/D8 Crucible.....	1-54
1.3-2	Illustration of Design Simplicity in the D7 and D8 Experiment.....	1-56
1.3-3	Temperature in the D6 Bed Before Boiling...	1-60
1.3-4	D6 Boiling Data Compared With Series and Parallel Conduction Models.....	1-62
1.3-5	Bed Temperatures During the First Flashing Disturbance.....	1-63
1.3-6	Heat Flux From Boiling Zone vs. Boiling Zone Thickness at Dryout as Subcooling is Varied.....	1-67
1.3-7	Predicted and Measured Boiling Zone Heat Fluxes at Dryout.....	1-70
1.3-8	Bed Temperature, Power, and Pressure During the Final Dryout.....	1-71
1.3-9	WD-Series Experiment Package Design.....	1-78
1.4-1	Preliminary Design of New Molten Pool In-Pile Experiment Capsule.....	1-80
1.5-1	Test FRAG9, Scanning Electron Micrograph 1 Inch in From Bottom of the Vessel.....	1-84
1.5-2	Test FRAG9, Scanning Electron Micrograph 2 Inches in From Bottom of the Vessel.....	1-84

ILLUSTRATIONS (Continued)

<u>Figure</u>		<u>Page</u>
1.6-1	Transparent View Showing Instrumentation Layout for New Concrete Crucibles.....	1-87
1.6-2	SCAM Predictions for Penetration Rate.....	1-90
1.6-3	Cross-Section View of the Extinction Photometer for Large-Scale Test 19.....	1-97
3.1-1	Crack Growth Rates for 316 Stainless Subjected to Low Cycle Fatigue (No Hold Periods) at 866 K (593°C).....	3-3
3.1-2	Crack Growth Rates for 316 Stainless Subjected to 10 Minute Tensile Hold Periods at 866 K (593°C).....	3-4
4.2-1	Initiating Accident Event Tree for a Loss of Offsite Power.....	4-7
4.2-2	Initiating Accident Event Tree for Scenario 1 Earthquakes.....	4-10
4.2-3	Initiating Accident Event Tree for Scenario 2 Earthquakes.....	4-11
4.2-4	Initiating Accident Event Tree for Scenario 3 Earthquakes.....	4-12
4.2-5	Initiating Accident Event Tree for Scenario 4 Earthquakes.....	4-13
4.2-6	Initiating Accident Event Tree for Scenario 5 Earthquakes.....	4-14
5.1-1	Pin Power Profiles for the SAS-IIID LOF and the Proposed ACRR Power Transient.....	5-4
5.1-2	Temperature Calculated by SANDPIN at Different Radii.....	5-6
5.1-3	Radial Temperature Distributions for SNR-300 Calculated by SAS-3D (1980) and SANDPIN.....	5-7

ILLUSTRATIONS (Continued)

<u>Figure</u>		<u>Page</u>
5.1-4	Radial Distribution of Xenon for the Sibling Fuel Pellet PNL10-12.....	5-9
5.1-5	Radial Distribution of Cesium for the Sibling Fuel Pellet PNL10-12.....	5-10
5.2-1	Calculated Saturation Vapor Pressure of Liquid UO ₂ as a function of Reciprocal Temperature.....	5-16
5.2.2	Measured Vapor Pressures of Liquid UO ₂ as a Function of Reciprocal Temperature....	5-20
5.2-3	Measured and Calculated Saturation Vapor Pressures of Liquid UO ₂ as a Function of Internal Energy.....	5-25
5.2-4	Measured and Calculated Saturation Vapor Pressures of Liquid (U,Pu) Mixed Oxide as a Function of Reciprocal Temperature....	5-29
6.2-1	In-Pile Steam System Conceptual Design.....	6-4
6.2-2	Schematic of DFR Experiment.....	6-5
7.1-1	Comparison of Modulations Provided by the Current Fresnel Code Plate and the URA.....	7-3
7.1-2	Crossed Slit Aperture Geometry.....	7-5
7.1-3	Crossed Slit Aperture Collimator Design for the Core Slot.....	7-6
7.1-4	Geometry for Response Function Measurement of Forward Slit Aperture.....	7-7
7.1-5	Slit Image of ²⁵² Cf Source Exposures Separated by 3 mm.....	7-9
7.1-6	Canister Geometry With Bismuth Cup Background.....	7-10

TABLES

<u>Number</u>		<u>Page</u>
1-I	Transient Test Matrix.....	1-4
1-II	Crucible Thermocouple Locations for Sustained Hot Solid Experiments.....	1-17
1-III	Nomenclature.....	1-34
1-IV	Furnace Efficiency Study.....	1-40
1-V	Proposed Test Conditions Stainless Steel Melt Over ThO ₂ Gravel.....	1-51
1-VI	Bed Penetration Times for Proposed Test Conditions.....	1-51
1-VII	Specific Powers and Boiling Zone Heat Fluxes at Dryout.....	1-66
1-VIII	Tentative LWR Regraded Core Coolability Experiment Matrix.....	1-77
3-I	Fatigue Frowth Testing of 316 Stainless Steel at 593°C ($\epsilon = 4 \times 10^{-3} \text{ sec}^{-1}$).....	3-2
4-I	ESS Common Cause Relationships for Loss of Offsite Power.....	4-6
4-II	SHRS Response as a Function of Common Cause Relationships.....	4-8
4-III	Accident Types and Frequencies for the Loss of Offsite Power Initiators.....	4-9
4-IV	Earthquake Initiator Frequencies, Per Year.....	4-15
4-V	Consolidated Conditional ESS Probabilities (and Uncertainty Factors) for Earthquake Initiators.....	4-17
4-VI	Accident Category Frequencies Associated With Earthquake Scenario 1.....	4-19

TABLES (Continued)

<u>Number</u>		<u>Page</u>
4-VII	Accident Category Frequencies Associated With Earthquake Scenario 2.....	4-20
4-VIII	Accident Category Frequencies Associated With Earthquake Scenario 3.....	4-21
4-IX	Accident Category Frequencies Associated With Earthquake Scenario 4.....	4-22
4-X	Accident Category Frequencies Associated With Earthquake Scenario 5.....	4-23
5-I	Preliminary Test Matrix for the FD2/4 Experiments.....	5-3
5-II	Time Schedule for the FD2/4 Experiment Series.....	5-3
5-III	Research Goals.....	5-15

EXECUTIVE SUMMARY

Introduction

Sandia National Laboratories, Albuquerque, New Mexico is conducting the Advanced Reactor Safety Research Program on behalf of the U.S. Nuclear Regulatory Commission (NRC). The overall objective of the program is to provide NRC a comprehensive data base essential to (1) defining key safety issues, (2) understanding the controlling accident sequences, (3) verifying the complex computer models used in accident analysis and licensing reviews, and (4) assuring the public that advanced power reactor systems will not be licensed and placed in commercial service in the United States without appropriate consideration being given to their effects on health and safety.

The NRC program is carefully planned to complement the larger DOE program, but at the same time to satisfy the NRC obligation for independent confirmatory research.

Together with other programs, the Sandia effort is directed at assuring the soundness of the technology base upon which licensing decisions are made, and includes experiments and model and code development.

Sandia has been given the task to investigate seven major areas of interest which are intimately related to overall NRC needs. These are:

1. Core Debris Behavior -- Inherent Retention
2. Containment Analysis
3. Elevated Temperature Design Assessment
4. LMFBR Accident Delineation
5. Advanced Reactor Core Phenomenology
6. Light Water Reactor (LWR) Damaged Fuel Phenomenology
7. Test and Facility Technology

These major tasks are subdivided as necessary into subtasks to facilitate the organization of work and the interaction of subtask results into a body of coherent information which supports the requirements of the NRC.

EXECUTIVE SUMMARY

1. Core Debris Behavior -- Inherent Retention

1.1 Molten Core Containment

If core debris formed during a severe reactor accident is not coolable, the debris will penetrate the reactor vessel and interact with structural material in the reactor cavity. This interaction could lead to gas generation, production of flammable species and intense emission of radioactive aerosols in addition to erosion of the reactor basemat.

Study of the phenomena associated with ex-vessel interaction of core debris with structural material found in the reactor cavity is the purpose of the Molten Core Containment Program. In the recent past, the major part of this program was the study of core debris interaction with concrete. Penetration of core debris through steel liners has also been examined. Lately, greater attention is being given to core debris interactions with materials that would be superior to concrete for retaining core debris.

A preliminary test was run to look at the way in which hot solid debris attacks concrete. The purpose of the test was to evaluate experimental techniques but it also yielded some interesting data. The test involved a 50 kg stainless steel slug inductively heated in a basaltic concrete crucible. The power induced in the steel was about 0.15 W/g. This power level was sufficient not only to produce concrete erosion but also to melt some of the steel. Erosion rates in the horizontal and vertical directions were about 7 cm/hr. These were about twice the rate observed in a previous test with limestone/common sand concrete.

At the conclusion of the test, water was injected into the crucible. No energetic interactions were observed. Neither the steel nor the molten concrete fragmented.

In basaltic melts, the solubilities of UO_2 and ZrO_2 at temperatures likely to be encountered in hot, solid core debris attack on concrete are reported. Sufficient data have been collected, apparently, to assure that the solubility is relatively low and can be estimated for most temperatures of interest.

EXECUTIVE SUMMARY

A serious effort to characterize the aerosol source term associated with melt/concrete interactions is underway. A critical question in any such investigation is how well must the aerosol source term be known. Clearly, uncertainties must be resolved well enough so that they no longer affect calculations of aerosol behavior in reactor containments or the consequences of aerosol release. An effort to define how well the aerosol source term must be known is now being pursued by examining the effects of source term description on the predicted behavior of aerosols. Early indications are that the aerosol will have to be characterized in terms of mass-weighted size distribution, number-weighted size distribution, shape factor and concentration in addition to chemical composition.

1.2 Core Retention Concept Assessment

The Core Retention Concept Assessment is a program to assess the engineering of core retention devices to replace concrete as the primary basemat material in reactor cavities. The program is currently focused on the engineering of magnesia retention devices.

Availability of a facility to prepare large (~ 200 kg) melts of UO_2 is essential for the execution of this research program. Consequently, development of the Large-Scale Melt Facility is a major task in the early phases of this effort.

Development of the Large-Scale Melt Facility was advanced by the work in this program during this quarter. A redesigned support for the furnace susceptor at the facility was tested. The new support greatly limits the loss of heat from the bottom of the furnace. Heat loss data obtained during the test agreed well with that calculated with the CINDA-3G model of the furnace. Thermal efficiencies of the furnace were found to vary with temperature over the range of 53 to 63%; these efficiencies are outstanding.

A report on the CINDA-3G model of the furnace, K. H. Barhydt, Thermal Analysis of the Large Melt Furnace - Performance Evaluation of the Susceptor/Crucible Design, SAND81-1262, is now available.

EXECUTIVE SUMMARY

Densified charges of TiO_2 for the so-called "simulant" test of the furnace were being prepared during the quarter. The charge is prepared by hot-pressing and sintering. Sintering was found to be significant at temperatures above 1873 K (1600°C). Charge densities of 75 to 85 percent of theoretical density can be achieved by this method.

The understanding of the furnace performance and the charge sintering has enabled program personnel to define heating schedules for the simulant test. These schedules involve a rapid heat up to 2073 K (1800°C).

Temperatures are arrested at this level to permit complete sintering of the charge. The temperature is then raised to 2273 K (2000°C) to complete melting and super-heating the charge. The heating requirements are all well within the capability of the Large-Scale Melt Facility.

Investigators have abandoned the $UO_2-Y_2O_3$ mixture as a charge for the Large-Scale Melt Facility. Instead, they will use a mixture of UO_2 and ZrO_2 partially stabilized by Y_2O_3 . This charge is more useful for reactor safety studies and will be easier to handle at the facility.

Analytic studies of the gravel bed core retention concept are reported this quarter. The gravel bed concept could be used to retrofit existing reactors to prevent core debris interactions with basemat concrete. The possibility that liquid steel would penetrate the interstices of gravel was examined. Results of the analysis indicate that gravel smaller than 790 μ m would have to be used to prevent metal flow into the gravel if no coolant were present. This analysis was conducted to define a range of parameters for testing the gravel bed core retention concept.

1.3 PAHR Debris Bed

Requirements for the safe shutdown of an LMFBR have led to many studies of Post Accident Heat Removal (PAHR) from disrupted core geometries. Studies of in-vessel and

EXECUTIVE SUMMARY

ex-vessel PAHR have been motivated largely by the significant reduction in radiological hazard potential which results from retention of fuel and coolant within the primary or secondary containments.

Following a core disruptive accident, molten core materials may exit the core region and contact sodium where solid fuel debris will be formed and collected on horizontal surfaces within the vessel. This debris is still capable of generating significant power through the decay of fission products. Should insufficient cooling be afforded by natural processes, the debris could remelt and threaten the vessel. The purpose of this task is to determine the natural cooling of such debris.

Debris bed experiment D5 is the first experiment in which bed behavior at extended postdryout conditions will be investigated. The principle objectives are to observe bed behavior at elevated temperatures, to evaluate crucible design for future high temperature experiments, and to evaluate double containment concepts for D-series experiments.

During this quarter, the D5 hardware fabrication was completed and assembly began. A charge of 4.89 kg of UO_2 was loaded into the crucible. Final procedure checks were made, followed by final assembly of the primary containment vessel. After closure of the primary containment vessel, the cover plate was welded to the vessel. Toward the end of June, investigators loaded the D5 primary containment vessel with 4.09 kg of liquid sodium. Various inspections were performed to assure the integrity of the apparatus and its proper performance. Some minor problems are being addressed.

Debris bed experiment D7 will investigate the coolability of a shallow stratified bed. Specifically, the experiment will attempt to determine the ability of such a bed to make the transition to channeled bed behavior. Such a transition would be expected to increase greatly the potential coolability of stratified beds. The D8 experiment will determine the coolability of a stratified bed with an extended particle size distribution to determine the effects of such a distribution.

EXECUTIVE SUMMARY

Design work on the D7 and D8 experiments continued. A preliminary design was prepared in April by the experiment team. This design incorporates numerous improvements over previous debris bed experiments; these improvements address safety issues as well as simplicity and ease of assembly. The debris bed is held in an insulated crucible fabricated of Inconel 617 and stainless steel, with a Min-K thermal insulation. This crucible, and other design features, should reduce heat losses in the downward and radial directions. The radiological containment for the D7 and D8 experiments features 2 independent barriers, a minimum number of mechanical seals, and a simplicity of design which should reduce assembly difficulties. The operational aspects of the safety instrumentation for D7 and D8 are yet to be fully resolved. This process of resolution is proceeding as is the fabrication of experiment hardware.

D9 is the first debris bed experiment to be cooled from both top and bottom. The objective is to develop data for use in comparing the coolability of debris beds cooled simultaneously from top and bottom to that of top cooling alone.

The out-of-pile systems test (OPST) for demonstrating bottom cooling for in-pile experiments was completed in April. Analysis of the experiment data showed an effective heat transfer coefficient varying from 300-700 W/m²-K for a helium mass flow of 7-90 kg/hr.

The above data applied to a practical and conservative D9 design indicate that the bottom finned plate will provide adequate heat removal for investigating typical engineering designs of SNR300 and Super Phenix.

The analysis of debris bed experiment D6 continued. The D6 experiment was the first in the D-series to investigate the coolability of a debris bed of UO₂ particles in sodium; these particles are stratified by size, monotonically increasing with elevation. All aspects of the experiment except stratification were retained as identical to the previously accomplished D2 experiment to allow a clear comparison of the effects of particle stratification.

EXECUTIVE SUMMARY

Single-phase convection before boiling did not occur in the D6 test even though it did occur in the D2 test. This suppression of convection may be due to the top layer of small particles restricting flow from the bed into the overlying pool. Prior to boiling, heat removal was by conduction with the bed conductivity agreeing well with the Kampf-Karsten formula. With boiling present, heat removal was found to be modeled well by the series conduction model in which the vapor from the boiling zone is assumed to be condensed at the base of an overlying subcooled zone in the bed.

Two flashing disturbances occurred which were similar to those observed in D2 and D4. The amount of superheat observed before flashing was in fair agreement with Schwarz's flashing model but the cavities on the UO₂ particles must also be assumed to become non-wetted during the boiling or dryout process. After the disturbance, the bed height was permanently increased by 6 mm.

Before the flashing disturbance, the dryout power in the D6 test ranged from 285 W/kg to 375 W/kg as the subcooling ranged from 325°C to 486°C. After the disturbance, the dryout power ranged from 315 W/kg to 445 W/kg as the subcooling ranged from 335°C to 493°C. The 11 to 19% increase in dryout power is the result of loosening and expanding of the bed by the liquid superheat disturbance.

In all cases the dryout power was less than the dryout power of 760 W/kg observed in the D2 experiment. This reduction results from a combination of suppressed single-phase convection and reduced heat transfer efficiency in the boiling zone, both caused by stratification. Modification of the Lipinski one-dimensional dryout model for packed beds yields fair agreement with the dryout data.

Because of the low dryout powers and agreement with a packed-bed model, program personnel infer that channeling did not occur in the D6 bed. This is in contrast to the D2 test in which channeling did occur (by inference), even though D6 spanned the same subcooling range and underwent a larger flashing disturbance than did D2. The reason for the failure to channel before dryout is believed to be the low dryout power, which resulted in very thick (54-74 mm) subcooled zones at dryout.

EXECUTIVE SUMMARY

Sandia National Laboratories has initiated a program to determine the coolability of LWR degraded cores. This program is an extension of the Sandia PAHR experiments that are currently addressing the coolability of postulated LMFBR degraded cores. In a manner similar to the PAHR program, the LWR degraded core coolability studies are emphasizing in-pile experiments in the ACRR using fission heating of uranium to simulate the decay heat expected following a core disruptive accident. The scope of the LWR degraded core coolability studies during the remainder of FY81 encompasses the following:

- a. Identify the governing phenomenological uncertainties and evaluate their impact on present analytical models.
- b. Formulate an experiment matrix to resolve these uncertainties.
- c. Determine the feasibility of performing in-pile experiments in the central irradiation cavity of the ACRR.
- d. Design the experiment package and accessories necessary to perform the experiment.

During this quarter, a survey of current coolability programs, experimental results and existing analytical models was performed. This survey revealed the existence of the following phenomenological uncertainties that govern the determination of coolability for a postulated LWR degraded core:

- | | |
|---------------------|------------------------------|
| a. Particle Size | e. Core Structural Materials |
| b. Bed Depth | f. Bottom Fed |
| c. Pressure Effects | g. Distorted Pin Bundle |
| d. Stratification | |

A preliminary experiment matrix for Sandia's LWR Degraded Core Coolability Experiment Program lists 8 experiments. Each experiment is intended to identify and investigate separately one of the governing phenomenological uncertainties. The fuel in all experiments is expected to be 3%-enriched UO₂. The design of the

EXECUTIVE SUMMARY

experiment package is basically generic for all of the planned experiments with minor modifications for particular phenomena being investigated. The experiment packages are preassembled and placed in the ACRR cavity for operation. This enables 2 to 3 experiments to be performed annually.

1.4 PAHR Molten Pool

The PAHR Molten Pool Program interfaces closely with both the Molten Core Containment and the PAHR Debris Bed Programs. After a major reactor accident, if the core-material debris is uncoolable it will progress to a molten state. The progression of the debris to a molten state and the interaction of the melt with structural and core retention material is being investigated experimentally in the molten core studies. High-temperature, laboratory-furnace tests and first-of-a-kind neutronically-heated experiments are providing significant data on many PAHR related issues including the thermal response of dried UO_2 and steel particulate beds to internal decay heating, the formation of crust and voids in pools of internally heated molten fuel material, and the interaction of hot fuel debris with core structure and retention material. As with other safety research programs, investigators are using the experimental results to develop and verify analytical models that will be used to study reactor behavior under a wide variety of accident conditions.

The elevated temperatures associated with molten core materials have required unique technological developments in the field of high temperature material compatibility and diagnostic instrumentation. Sandia program personnel have shown that ultrasonic thermometry, developed as part of the molten pool studies, is a valuable diagnostic of temperature and temperature gradients up to the UO_2 melting point (3150 K).

To date, Sandia has performed five in-pile fission-heated experiments in the Annular Core Pulse Reactor and the Annular Core Research Reactor (ACPR and ACRR). In these experiments, investigations were made into UO_2 melt behavior, UO_2 interaction with steel and MgO barriers and

EXECUTIVE SUMMARY

migration of molten steel in initially uniformly mixed beds of steel and UO_2 . Ultrasonic thermometry has been used successfully in these experiments to measure temperatures up to 3150 K in environments where the high radiation fields, lack of visual access, and very high temperatures precluded the use of thermocouples and optical pyrometry.

Concurrent with the in-pile experiments, furnace tests were conducted to study sintering and wetting properties of UO_2 /steel systems, and the interaction of these systems with retention and crucible materials including W, Ta, ThO_2 , ZrO_2 , Al_2O_3 , and MgO. The data obtained from these tests have contributed significantly toward a data base on interactions among molten reactor materials. In addition, furnace experiments have provided the capability for extensive development on ultrasonic thermometry for use in molten pool and debris bed experiments, and in future research programs.

In this quarter, the design of an advanced experimental package was continued. This design emphasizes the addressing of problem areas encountered in previous molten pool experiments. Specific changes in the new capsule include compatibility with the helium trailer used in the D-series debris bed experiments to increase cooling, the use of argon as a cover gas to simulate better the thermal behavior of sodium vapor, and the use of a B_4C neutron-spectrum modifier to flatten the bed power profile. A dosimetry experiment has also been defined that will reduce the uncertainty in the power normalization from about 25% to 5%. Ultrasonic-thermometersystem development has concentrated on improving the electronics. A new multiplex system avoids the old system's synchronization problems.

1.5 Fragmentation

Most severe accident scenarios for advanced sodium-cooled reactor systems involve the production of significant amounts of molten fuel and steel. The ultimate dispersal of this molten material often depends on either bulk freezing of the melt or the establishment of coolable, particulate beds. Scenarios which differentiate between the dispersal modes involve questions of the fragmentation of substantial quantities of melt when contacted

EXECUTIVE SUMMARY

with coolant. Previous investigations yielding quantitative information involve very small quantities of fuel melt, leaving unanswered the question as to whether or not large quantities would yield different particulate size distribution due to vapor blanketing of the bulk stream. A knowledge of particle size distributions is crucial to the resolution of postaccident coolability of cores which have been reduced to rubble.

Following whole-core accidents in which all, or most, of the sodium remains in the reactor vessel, molten/vaporized core materials and sodium will come in contact, resulting in sudden freezing and fragmentation of the core debris, which may then settle on various surfaces within the vessel. If recriticalities do not occur, this fragmentation and onset of settling roughly denotes the beginning of the postaccident sequence.

In this program, melts of core material about a factor of 10 larger than previously used are contacted with sodium. Characterization of the fragmented debris size and the settling of this debris within the residual sodium pool are the most important results expected from this program.

The effort during this quarter was to finalize posttest analyses of debris produced in the previous tests. Scanning electron micrographs of the debris are being taken to determine surface morphology of the debris and to define the differences between oxide and metallic phase particle sizes.

1.6 Sodium Containment and Structural Integrity

The Sodium Containment and Structural Integrity Program is an investigation of safety phenomena that will develop should molten sodium contact structural or shielding concrete during a reactor accident. Quantitative evaluation of these phenomena, leading to development of models for use in predicting the ways in which these phenomena might threaten the reactor containment is a major goal of this program. Quantitative evaluation of structural flaws in reactor cell liners is also sought in this program because these flaws can provide pathways for sodium to contact concrete.

EXECUTIVE SUMMARY

This program has shown that sodium/concrete interactions proceed in two phases. The first phase is relatively mild and is characterized by the reaction of water from the concrete with sodium to yield hydrogen and NaOH. The second phase of the interaction is more energetic and involves erosion of the concrete as well as hydrogen generation.

When sodium first contacts the concrete, the interaction is relatively mild and consists mostly of the reaction of water from the concrete with sodium. At the temperatures and hydrogen partial pressures encountered in the experiments, the condensed product of reaction is NaOH which is partially soluble in sodium. After this mild phase of interaction has progressed for a while it abruptly evolves into a very energetic interaction in which concrete is actually eroded. During this energetic phase, sodium pool temperatures rise to near boiling.

A large-scale test article that will allow approximately one-dimensional sodium/concrete interactions has been designed. Tests with this configuration will be particularly suited for verifying the CONTAIN code with the SCAM module for sodium concrete interactions. Data acquisition and instrumentation at the test site have been upgraded in anticipation of the need for code verification. Development of the SCAM model has progressed with particular attention being given to the effect of pressure on sodium/concrete interactions. Both pressure and concrete porosity have been found to affect the rate of sodium attack on basaltic concrete. The rate increases with pressure to a maximum and thereafter decreases. The precise location of the maximum rate and the rates of attack at higher pressures are not well known and require further experimentation.

Small-scale tests are well-suited for the experimentation necessary to develop SCAM. The small-scale or "physical separate effects" tests can be done rapidly, can cover a broader parameter range, and can be more precisely controlled. Test articles for small-scale limestone concrete interactions tests were prepared. These test articles will be used to investigate (a) effect

EXECUTIVE SUMMARY

of Na_2CO_3 on the interaction, (b) effect of concrete constraint and consequently porosity on the interaction, (c) the effect of pressure on the interaction, and (d) the effect of pool stirring on the interaction.

During this quarter, crucibles were poured for large, one-dimensional tests with limestone and basalt concretes. These test configurations will be especially useful for CONTAIN development and verification. Preparations were started for the next large-scale test (No. 19). This test will use a conventional limestone-aggregate crucible with an initially shallow sodium pool and provision for adding fresh sodium during the test. Two physical, separate-effects tests with limestone concrete were completed. These tests were part of a series designed to determine the conditions necessary to obtain results similar to those of the large-scale tests. Modeling of the sodium interaction with basalt concrete has been advanced to include the effects of concrete porosity on the interaction rate.

1.7 High Temperature Fission Product Chemistry and Transport

The purpose of the High Temperature Fission Product Chemistry and Transport program is to establish the data base necessary to predict properly fission product behavior during severe accidents. This experimental task is being pursued by three interrelated activities:

- (1) Definition of thermodynamic data and chemical reaction characteristics of particular fission products of interest.
- (2) Examination of the transport properties of fission products in prototypic environments of steam and hydrogen.
- (3) Comparison of the observed behavior of the fission products with predictions made by purely thermodynamic considerations.

Transport properties of the fission products will be studied in the Fission Product Reaction Facility being developed as part of this program. The facility will

EXECUTIVE SUMMARY

allow moderately volatile fission products to be generated in flowing steam and hydrogen mixtures at temperatures up to 1273°K (1000°C). The fission product stream passes over steels representative of structural materials in reactor cores. A Raman spectroscopy unit is being developed that may allow determination of the chemical form of fission products in the vapor state.

The Fission Product Reaction Facility was operated for about 50 hours during this quarter to verify that it would perform as predicted. Several minor modifications were made to the system to improve its performance and ease of handling. A mass spectrometer was interfaced with the system to monitor the production of noncondensable gas. A bleed stream of argon is included in the flow as an internal standard for monitoring changes in the concentrations of noncondensable gases.

During checkout tests the rate of steam oxidation of stainless steel to yield hydrogen becomes significant at temperatures between 1073°K and 1273°K (800 and 1000°C). This is consistent with the known behavior of stainless steels in steam.

The vapor pressure of CsOH over the temperature range of 704-1133°K was completed. Data on the enthalpy of vaporization, derived from the vapor pressure measurements, agree well with data in the literature. Entropy values for vaporization are 2 e.u. lower than in the literature. This disagreement is sufficient to produce about a factor-of-3 difference in vapor pressures.

EXECUTIVE SUMMARY

2. Containment Analysis

The goal of this task is the development of CONTAIN, a general and comprehensive systems code that will analyze a variety of accident sequences following the breach of the primary containment vessel through the breach of the secondary containment. It will provide detailed treatments of phenomena such as material interactions, heat-transfer, aerosol behavior and fission product transport. The models will be sufficiently general to apply to all advanced reactor and light-water reactor containment systems. In addition, the MARCH code, which describes core-melt accidents in an LWR is being assessed to determine improvements needed for current and anticipated applications.

2.1 CONTAIN Code Development

During this quarter, work has concentrated on completion of the models and coding for version 1A of CONTAIN. These models and coding include the phenomenological models for containment analysis that are common to both LWR and LMFBR applications. This work devoted a substantial effort to testing the resulting code. A draft of the documentation for CONTAIN 1A has been completed and made available for limited distribution.

A quasi-steady flow option has been added to the intercell flow calculation, which omits the inertia term from the calculation of flow velocities. This allows high frequency oscillations to be eliminated from the intercell flow when these oscillations are irrelevant to the problem at hand and thereby allows the use of larger time steps.

A debris-concrete model is operational and provides a simple calculation of the erosion of concrete by molten core debris and the consequent generation of gases. The Sodium-Concrete Ablation Model (SCAM) has been implemented as a set of subroutines which can be run in CONTAIN. This provides a mechanistic physical model of the interaction of sodium with basalt concrete.

EXECUTIVE SUMMARY

2.2 MARCH Assessment Project

At NRC's request, Sandia is undertaking an assessment of the MARCH code, used to analyze severe LWR accidents. This is being done under the auspices of the Containment Analysis Program.

The focus of LWR safety concerns has recently expanded beyond the large LOCA design-basis accident to consideration of system response to severe core damage accidents (including meltdown) of several hours duration. The MARCH computer code was conceived as a tool for use in risk assessments; however, because MARCH models severe core-damage sequences, it has been used to satisfy previously unanticipated, but pressing analysis needs. The expanded usage of MARCH has generated many questions regarding the extent, appropriateness, and accuracy of the modeling in the code. Considerable discussion has ensued regarding the application and interpretation of MARCH results. An assessment of MARCH was initiated in response to a request by NRC to clarify the capabilities and limitations of MARCH within the context of current applications, to evaluate the major modeling and phenomenological uncertainties associated with the calculation of severe accident progression, and to recommend how MARCH should be used and/or improved.

During this quarter, all of the anticipated contributions for the assessment were received and the accumulated list of identified code limitations has exceeded 100. A small computer code was written and is in use to sort these limitations, by attributes, into a number of useful categories including basic classification by accident phase and degree of importance.

An overview of the assessment was prepared and presented to the Class 9 Subcommittee of the ACRS. This provided useful feedback on the conclusions that have been reached. The body of the draft report on the MARCH assessment has been finished, and copies have been produced for internal and external review.

The MARCH code, developed primarily for risk analysis, is difficult to use in analyzing the results of severe core-damage sequences. The difficulties arise from the

EXECUTIVE SUMMARY

structure of MARCH, the assumptions used in modeling and the simplistic character of some of the models.

Significant improvement in the level of modeling in MARCH is possible, but would in some cases be limited by inadequate knowledge concerning specific phenomena. Also, the structure and programming of MARCH, together with limited code documentation, hinder the assessment. The design of MARCH did not anticipate assessment and verification requirements. Finally, limitations, errors and deficiencies identified in MARCH may seriously compromise the validity of some code predictions.

In terms of current computing costs, MARCH is very inexpensive to run. A large (i.e., an order of magnitude) increase in execution time, if coupled with a corresponding increase in model complexity, detail, and algorithmic rigor, would not seriously hinder the bulk of current applications of MARCH.

Some modifications of MARCH to improve its capabilities would be difficult. One significant deterrent to modification is the sequential processing structure of the code which prevents the treatment of some parallel (and coupled) phenomena. However, the clear need of NRC for severe accident sequence calculations appears to the assessment team to require the early implementation of a robust NRC program for the improvement of MARCH or the development of alternatives.

EXECUTIVE SUMMARY

3. Elevated Temperature Design Assessment

The primary objectives of the elevated temperature design assessment studies are: (a) to determine how microstructures evolve due to thermomechanical history resulting in mechanical property changes, (b) to evaluate the validity of material damage rules used in design, and (c) to develop and evaluate nondestructive evaluation techniques.

Crack growth behavior was compared for samples subjected to three types of creep-fatigue tests: non-hold periods, 5-min tensile hold, and 10-min tensile hold. Data for the three tests with creep components show that growth rates from all tensile hold creep fatigue tests conducted to date are roughly equivalent and average about five times higher growth rate per cycle than the continuous cycle tests.

The microstructural analyses are continuing in cooperation with Oak Ridge National Laboratory to understand why Modified 9Cr-1Mo exhibits damaging compressive-hold-time effects even though it does not oxidize. Surface oxidation has been identified as the cause of compressive-hold-time effects in ferritic alloys of lower chromium content. Microstructural studies have revealed, further, that cycling with hold times (creep-fatigue) results in growth of the carbide precipitates.

EXECUTIVE SUMMARY

4. LMFBR Accident Delineation

The purpose of the LMFBR Accident Delineation Study (ADS) is to investigate the applicability of the methodology developed by the Reactor Safety Study (WASH-1400) to advanced systems such as an LMFBR, and to apply this methodology insofar as is possible to systematize the existing body of LMFBR safety information. Goals include: (a) provide a demonstrated methodology for delineating LMFBR accident sequences, (b) determine dominant accident sequences with corresponding radioisotope-release categories, and (c) identify and systematize the key phenomena governing the accident sequences. Illustrative facilities used in the study include the CRBRP and, more recently, alternative designs such as the DOE's Conceptual Design Study (CDS). The delineation study is organized into three major areas designated engineered safety systems (ESS), accident phenomenology, and post-accident phenomenology.

Phase I of the ADS was completed at the end of FY80 and results were described in detail in the Phase I Final Report. This work included comprehensive qualitative delineation of LMFBR accident sequences from the initiating subsystem failures to definition of radiological release categories. Event tree methodology was used throughout and simplified fault tree models were developed (but not quantified) for three ESS functions (detection, SCRAM, and shutdown heat removal system (SHRS) availability).

In Phase II of the ADS, now underway, ADS personnel will undertake a more detailed, more quantitative evaluation for certain selected topics identified in Phase I as being of great interest. In the ESS area, the work involves an approximate quantification of the simplified Phase I fault trees in order to estimate relative recurrence frequencies of the various accident categories and, thus, permit analyses in the Accident Phenomenology area to concentrate on the categories found to be most important. Consistent with this goal and with the level of effort involved, results obtained in the ESS analysis are to be treated as relative probability estimates, not predictions of actual recurrence frequencies or absolute probabilities.

EXECUTIVE SUMMARY

During this quarter, work in the ESS area concentrated on analyzing the contributions to the various accident categories that arise from loss of offsite power and from earthquake initiators. Results indicate that these are potentially significant contributors to major accident categories but that these initiators may not be dominant, i.e., the estimated contributions to the various recurrence frequencies from these causes did not exceed corresponding contributions estimated for other major accident scenarios.

Application of the SAS3D code continued in order to analyze UTOP accidents resulting from uncontrolled rod withdrawal without SCRAM in the CRBRP heterogeneous core (BOC4 configuration). Withdrawal of a single rod inserts 65¢, which was found to be insufficient to lead to probable pin failure. Withdrawal of a bank of six rods at maximum possible speeds (72 in/min) can insert up to \$2.86 at rates of 20¢/s; for this scenario, pin failures are predicted to occur after sodium boiling has started in some coolant channels. Difficulties with the SAS3D code and its User's Manual have slowed this work significantly.

Work was initiated to define better the protected accident scenarios that could threaten core integrity, and also to define the time of onset of core disruption for various postulated SHRS failures. Toward this end, negotiations were initiated with the University of Arizona for obtaining assistance with installation of its BRENDA code on a VAX computer system available to the investigators. Also, five SHRS-failure scenarios were defined and sent to Brookhaven National Laboratory (BNL) for analysis with its SSC code.

In the postaccident phenomenology area, the current effort to clarify containment-research priorities has been largely completed. A draft report describing this effort and its results has been completed and is now in the Sandia review process. Though significant revisions of the draft are likely, investigators do not expect that the major results of the study will differ greatly from those cited in previous quarterly reports.

EXECUTIVE SUMMARY

An effort was initiated to assess the response of the CRBRP containment systems to large accidents. Work during this period included planning, data collection, and familiarization with the CONTAIN code which will be the principal analysis tool. Important phenomena that CONTAIN cannot yet treat were identified. In addition, prior analyses of containment response were subjected to a brief review. This work included gathering information on the primary boundary's ability to withstand CDA energetics, and also obtaining information on the capabilities and limitations of existing analysis tools for treating this problem.

At the NRC's request, the possibility of scaling up the ADS into a risk assessment for CRBRP was addressed in some detail. This proposal, named the Clinch River Risk Assessment Study (CRRAS), would draw upon the expertise and methodologies developed in both the Interim Reliability Evaluation Program (IREP) and the ADS program. The proposed CRRAS was found to be a desirable program provided its purpose is accepted as being largely exploratory rather than concentrating principally on the development of firm numerical risk estimates for CRBRP. A formal proposal for the CRRAS was prepared and sent to NRC.

EXECUTIVE SUMMARY

5. ADVANCED REACTOR CORE PHENOMENOLOGY

The Advanced Reactor Core Phenomenology program is directed toward developing a data base for the understanding of the key in-core events in a core disruptive accident which determine the progression and severity of a reactor accident. For the advanced reactor, understanding in-core events is particularly important since significant energy release from the core is possible. The magnitude of this energy release, and therefore the ultimate threat to the containment, is determined by the competing positive and negative reactivity effects caused by the motion and temperature of fuel, cladding and coolant.

This program involves experimental and analytical efforts to determine the magnitude and characteristics of these reactivity effects in the three phases of an advanced reactor core disruptive accident. These phases are:

- a. Initiation Phase -- Fuel Dynamics
- b. Disassembly Phase -- Energetics
- c. Transition Phase -- Fuel Freezing and Streaming.

5.1 Initiation Phase -- Fuel Dynamics

The major efforts this quarter focused on defining the FD2/4 test matrix, reviewing the PIE work for the FD1 series of fuel disruption experiments, and drafting a topical report for the HRR series of experiments. The goal of the FD2/4 test series is to investigate the initial fuel disruption process for LOF accident transients in LMFBRs. This series of experiments, sponsored jointly by KfK and NRC, will use high-speed photography to study the disruption phenomena. Posttest analysis will determine the timing of the disruption, the state of the fuel at disruption, the general mode of the disruption, and the roles played by the molten fuel expansion, fission products and vapor pressure.

A range of LOF transients and fuel types will be used in the FD2/4 tests. Two types of heating transients are proposed. The first simulates LOF heating conditions

EXECUTIVE SUMMARY

for homogeneous-core reactors such as SNR-300 or CRBR. The second simulates LOF heating conditions for heterogeneous-core reactors such as the new CRBR. A total of 10 experiments are planned.

KfK examination of the FDI fuel has revealed significant fuel swelling. For the FDI.7 experiment, the swelling occurred mainly in the unrestructured and equiaxed zones. Furthermore, the swelling in the unrestructured zone appeared to be caused by extensive intragranular fractures. Some swelling of smaller magnitude also occurred near the pin center. These results conflict with earlier interpretation of the swelling and cracking.

Completion of the HRR experiments in 1980 has led to the following conclusions:

- a. Fuel disruption occurs well before fuel vapor pressure generation for both fresh and irradiated fuel.
- b. Irradiated fuel disrupts earlier than fresh fuel and is more energetic. The melt fractions at the time of disruption are near 60% for irradiated fuel and 100% for fresh fuel.
- c. The disruption appears as a rapid expansion of very small particles (<1 mm) which are near the fuel melt temperature. The particle velocities are approximately 5 m/s, consequently under prompt burst time scales (a few ms) not enough fuel motion can occur to cause significant reactivity feedback. Thus, the fuel-particle interactions with sodium vapor must be examined to study extended fuel motion and its reactivity effects.

5.2 Disassembly Phase -- Energetics

Studies are being performed to examine the energetic response of reactor fuel-clad-coolant systems to superprompt critical conditions. In particular, the

EXECUTIVE SUMMARY

objective is to identify and characterize the phenomena resulting in pressure generation and in the conversion of thermal energy to work.

On prompt burst timescales the pressure source from fuel vapor, inherent impurity gases, and fission gases as well as the accelerations produced by these pressure sources are of central importance. Thus the program in this area centers on determination of the effective equation-of-state (EEOS) of fresh and irradiated fuels, the dynamics of pressurization (rate effects) and the ability of this pressure to disperse fuel.

Efficient heat transfer from fuel to coolant can give rise to significant work energy driven by expansion of coolant vapor. The fundamental question here is whether the oxide-fuel-sodium-coolant system is capable of supporting large-scale efficient thermal interactions. The program in this area is directed at determining if significant fuel coolant interactions (FCI) can occur in the oxide-sodium system and to determine the dominant controlling parameters and corresponding sensitivities.

Disassembly Phase activities in FY81 will focus on performing the KfK-NRC collaborative EEOS experiments and performing preliminary planning and analysis for future sodium-UO₂ FCI experiments.

During this quarter, a comprehensive, critical review of reactor fuel vapor pressure data and measurement methods was performed. This study, performed as part of the joint NRC-KfK effective-equation-of-state (EEOS) program, concluded that significant uncertainties still exist in the available data. Preparations for the high precision EEOS experiment series in the ACRR continued. Preliminary experiments are scheduled to begin in the fourth quarter of FY81. Planning for the fuel-coolant interaction tests aimed at the issue of propagation in the UO₂-Na system continued. A onedimensional FCI analysis code currently called thermal explosion analysis system (TEXAS) is being developed to provide a tool for experiment analysis and allow examination of modeling assumptions and sensitivities.

EXECUTIVE SUMMARY

5.3 Transition Phase

The key issues in the Transition Phase are the formation of fuel blockages leading to a confined or "bottled" core configuration, and the behavior and reactivity implications of this pool of fuel-steel in the core region if the fuel blockages do lead to this state. The Transition Phase program addresses the question of fuel penetration into the upper core structure. If deep penetrations occur, nonenergetic shutdown is probable while short penetration will lead to a transition phase and the possibility of further energetics.

The TRAN experiments address this question using prototypic reactor materials under carefully controlled conditions. The ACRR is used to create high temperature fuel-steel melts which are driven under controlled pressure into a heated channel to determine melt penetration behavior. The experiments provide a data base for the evaluation and further development of fuel freezing and streaming models for use in accident analysis.

The second TRAN-Series I experiment, TRAN-2, was performed at higher steel and fuel temperatures, but at a lower driving pressure. Fuel motion detectors were employed for the first time, and the driving pressure was applied earlier. Two very well-defined blockages, a long crust length, and indirect evidence of fuel slumping were observed in TRAN-2. In TRAN-2 the channel was completely blocked to gas flow until very late in the experiment, however.

Posttest examination (PIE) of the fuel debris in TRAN-1 continued in an effort to understand the dominant freezing and plugging processes. Most of the small amount of debris located at the very top of the apparatus appears to have frozen elsewhere and been transported to the top plate.

Analysis of the gas-flow behavior in TRAN-1 and TRAN-2 shows blockage formation, in agreement with radiographs. Calculations are also being performed to refine an experimental measurement of the fuel energy depositions in TRAN-1, -2 and -3. Finally, an analytical model of fuel freezing has been developed; this model agrees well with the results of ANL thermite tests and the TRAN experiments.

EXECUTIVE SUMMARY

6. LIGHT WATER REACTOR (LWR) DAMAGED FUEL PHENOMENOLOGY

This program is directed toward examining the key phenomena that determine the core-damage configuration during the progression of a core melt sequence in an LWR loss-of-coolant accident. This program uses the information and perspectives gained in current LWR safety programs such as SASA and the MARCH Code Assessment Project and focuses on the design of experiments which can contribute to the resolution of important severe-damage issues.

The two major areas of interest regarding in-vessel core retention are:

- a. The behavior of fuel and cladding during the stages of major core deformation from a pin-lattice geometry to a severely damaged state, and
- b. The response of the damaged core to reintroduction of (ECCS) coolant; especially the questions of redistribution of quenched material, increased steam generation, and oxidation reaction kinetics.

Resolution of the first item is required to predict the course and duration of core damage progression and associated effects in containment; resolution of the second provides the essential information to guide action that would terminate the accident and/or mitigate its consequences, and to preclude action that could exacerbate the accident.

Early work under this subtask focuses on the in-pile applications because neutronic heating allows prototypic heat generation under severely damaged conditions.

EXECUTIVE SUMMARY

A series of ACRR experiments is planned that addresses the above-described severe core damage issues:

- Debris Formation and Relocation Experiments (DFR) -- Visually observed fuel damage in flowing steam environment using neutronic heating in multi-rod-section configurations.
- Damaged Fuel Quench Experiments (DFQ) -- Postmortem observation of damage configuration after ECCS flooding of damaged fuel materials.

Feasibility studies have begun for the visual diagnostics, Debris Formation (DFR) experiments. Two basic concepts have been explored. In one concept the entire steam system is enclosed inside experiment containment. The alternate concept uses an out-of-pile boiler and condenser with only the test section in-pile. The latter concept results in a test package that is smaller than the first concept, but consideration must be given to handling contaminated out-of-pile components. Several shroud and thermal-barrier designs have been proposed for the experiment test section. Visual diagnostics similar to Sandia FD experiments are planned. Many of the issues can possibly be addressed with relatively small-pin-bundle (~ 9 pins) experiments in a flowing steam environment.

EXECUTIVE SUMMARY

7. Test and Facility Technology

7.1 ACRR Fuel Motion Detection System

The ACRR fuel motion detection system is designed to monitor the motion of nuclear fuel in simulated reactor accidents by imaging (through a slot in the core) gamma rays emitted by the test fuel. Currently the imaging is accomplished by modulating the collimated gamma-ray beam with a coded aperture and allowing the modulated beam to strike a thin scintillator. The visible-light image is then amplified and recorded with an optical image intensifier and framing camera respectively. Both of these are protected from background radiation by a massive shield.

During this quarter, the changes required to test two configurations (different from the Fresnel zone code) were drafted and procedures for fabrication of parts were initiated. Both configurations are designed to reduce the influence of spatial noise in the images of test fuel. The first aperture will be a uniformly redundant array (URA) and the second will be the crossed slit aperture (CSA).

Sandia Laboratories, Los Alamos and the University of Arizona are continuing to investigate the coded aperture responses in the presence of spatial noise. These studies use both idealized and experimentally generated data.

An experiment plan has been devised to test the new configurations during November of 1981.

7.2 ACRR Status

This section contains comments on the general status of overall ACRR operation and remarks concerning experimental activities involving the ACRR.

The ACRR is operating normally in support of weapons program research and advanced reactor safety experiments.

ADVANCED REACTOR SAFETY RESEARCH
QUARTERLY REPORT
APRIL - JUNE 1981

1. CORE DEBRIS BEHAVIOR -- INHERENT RETENTION

1.1 Molten Core Containment

(J. E. Brockmann, 4422; T. Y. Chu, 1537; W. C. Luth, 5541; D. A. Powers, 4422; W. W. Tarbell, 4422; H. R. Westrich, 5541; F. J. Zanner, 5836)

If core debris formed during a severe reactor accident is not coolable, the debris will penetrate the reactor vessel and interact with structural material in the reactor cavity. This interaction could lead to gas generation, production of flammable species and intense emission of radioactive aerosols in addition to erosion of the reactor basemat.

Study of the phenomena associated with ex-vessel interaction of core debris with structural material found in the reactor cavity is the purpose of the Molten Core Containment Program. In the recent past, the major part of this program was the study of core debris interaction with concrete. Penetration of core debris through steel liners has also been examined. Lately, greater attention is being given to core debris interactions with materials that would be superior to concrete for retaining core debris.

1.1.1 Melt-Concrete Interactions

Core-concrete interactions are postulated to occur throughout the decay-power time event. For convenience, a generalized temperature-time curve has been developed to describe the significant phases of the interaction. Figure 1.1-1 is a simplified representation of the relationship of the four phases that have been defined. The symbols are intended to illustrate the areas that required additional experimental effort to aid the understanding of a postulated reactor accident.

As Figure 1.1-1 depicts, qualitative and quantitative data are lacking in both the ultra-high and low-temperature phases. Work during this period has concentrated on addressing these two areas.

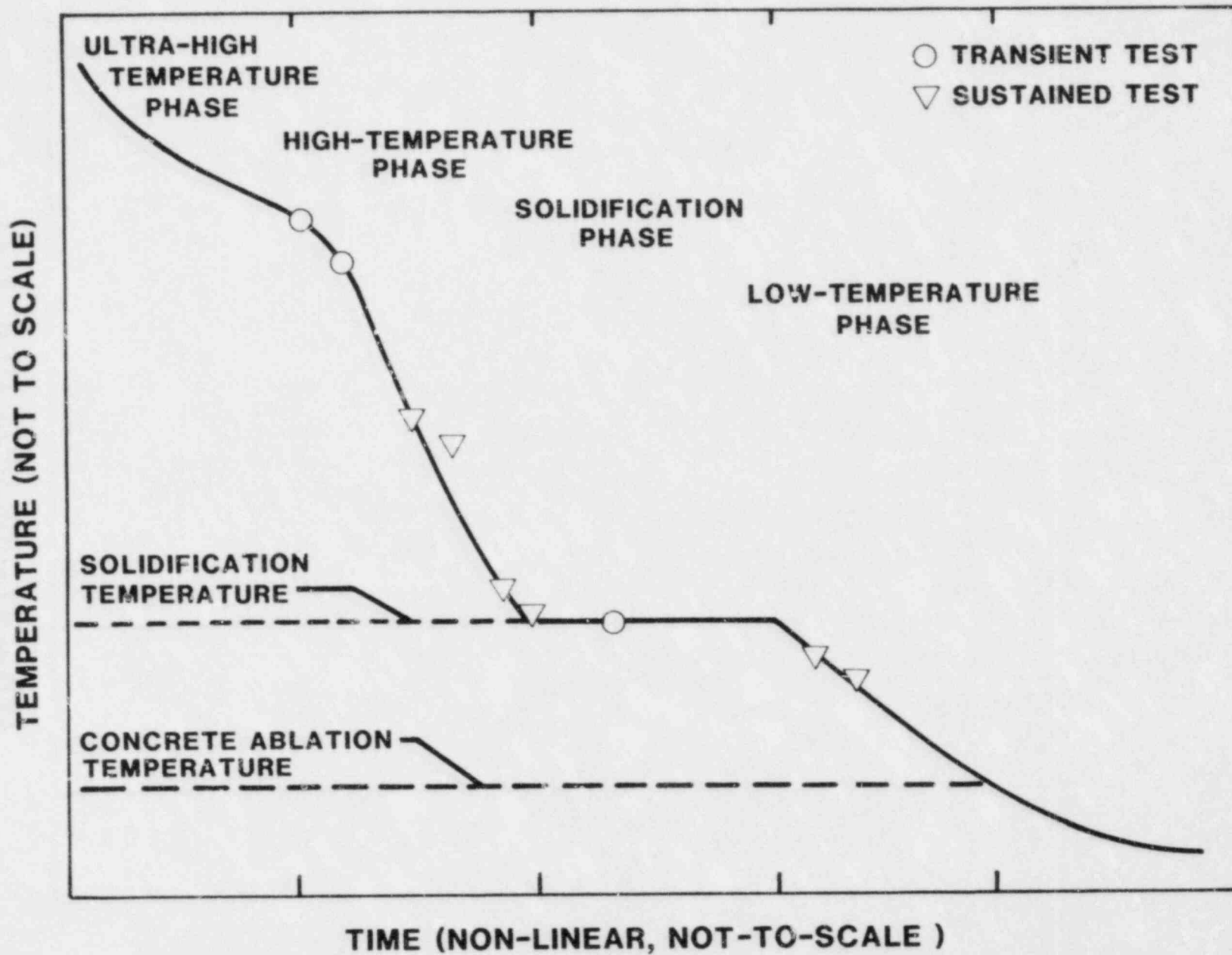


Figure 1.1-1. Hypothetical Temperature--Time History of Melt--Concrete Interaction

1.1.1.1 Transient Ultra-High Temperature Tests

Previous studies^{1-1,1-2,1-3} in the ultra-high and high temperature regions used thermitically-generated melts of iron and alumina in contact with calcereous or basaltic based concretes. These tests demonstrated that the interaction between the core simulant and concrete is extremely vigorous. The data have been used for code comparison studies that have pointed out the need for additional information. Principal among these requirements are:

- a. Effect of geometric features on heat transfer characteristics.
- b. Effect of melt depth on heat flux.
- c. Viability of heat transfer models.
- d. Gas and aerosol generation.

To satisfy the above needs, a matrix of 5 tests has been developed. Table 1-1 describes some principle features of each test.

To diagnose the effluents produced by the interaction, an instrumentation tower had to be attached to the concrete crucible. Previous work used very massive structures to permit survival in the extremely hostile environment. The disadvantage of this technique is that it provides many surfaces that protrude into the gas flow. The net effect of these surfaces is to cause coalescing of the airborne particles and to disturb the upward heat flux patterns.

A new instrumentation tower is being prepared in an attempt to overcome the difficulties described above. The device (Figure 1.1-4) consists of a large expansion volume placed on the crucible. The lower portion of the volume is protected by a sacrificial radiant heat shield and insulating blanket. By allowing the gas to expand, the net heat flux per unit of wall area will be reduced. The vertical stack is terminated by an instrumented section containing devices for measuring aerosol concentration, gas flow, and heat flux and equipment for sampling gas and aerosol composition. The assembled apparatus is designed to be used at Sandia's X-ray facility to permit real-time image intensification of the melt-concrete interface.

Table 1-I

Transient Test Matrix

Test No.	Cavity Geometry	Melt Mass	Comments
1.	Vert. Rt Cyl 12 cm dia x 45 cm deep	11 kg	Compare to data of Ref. 1-3
2.	Horz. Rt Cyl 22 cm dia x 10 cm long intersected by 10 cm dia. cyl (Figure 1.1-2)	8 kg	Geometric effect on heat transfer--no sharp transient bwt bottom and sidewall
3.	Spherical 21 cm dia intersected by 9.5 cm dia cyl 2 cm long (Figure 1.1-3)	10 kg	Effect of continuously varying interface geometry on heat transfer
4.	Horz. Rt Cyl 21 cm dia x 25 cm deep	11 kg	Compare melt depth effort to Test 1
5.	Horz. Rt Cyl 21 cm dia x 25 cm deep	5 kg	Compare melt depth effect to Test 4.

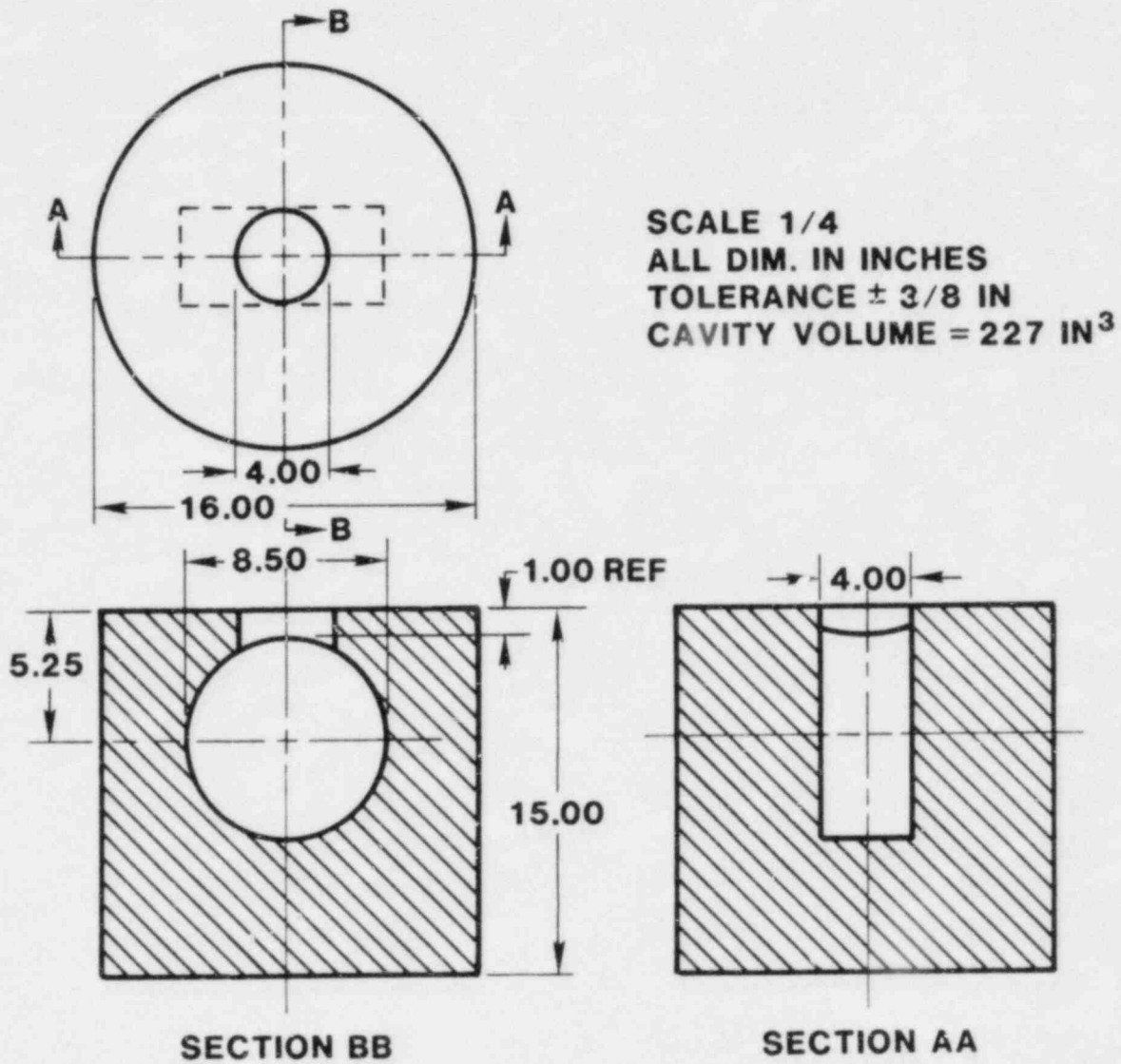


Figure 1.1-2. Limestone/Common Sand Crucible, Horizontal Rt. Cyl.

VOLUME OF SPHERICAL CAVITY $\approx 294 \text{ IN}^3$

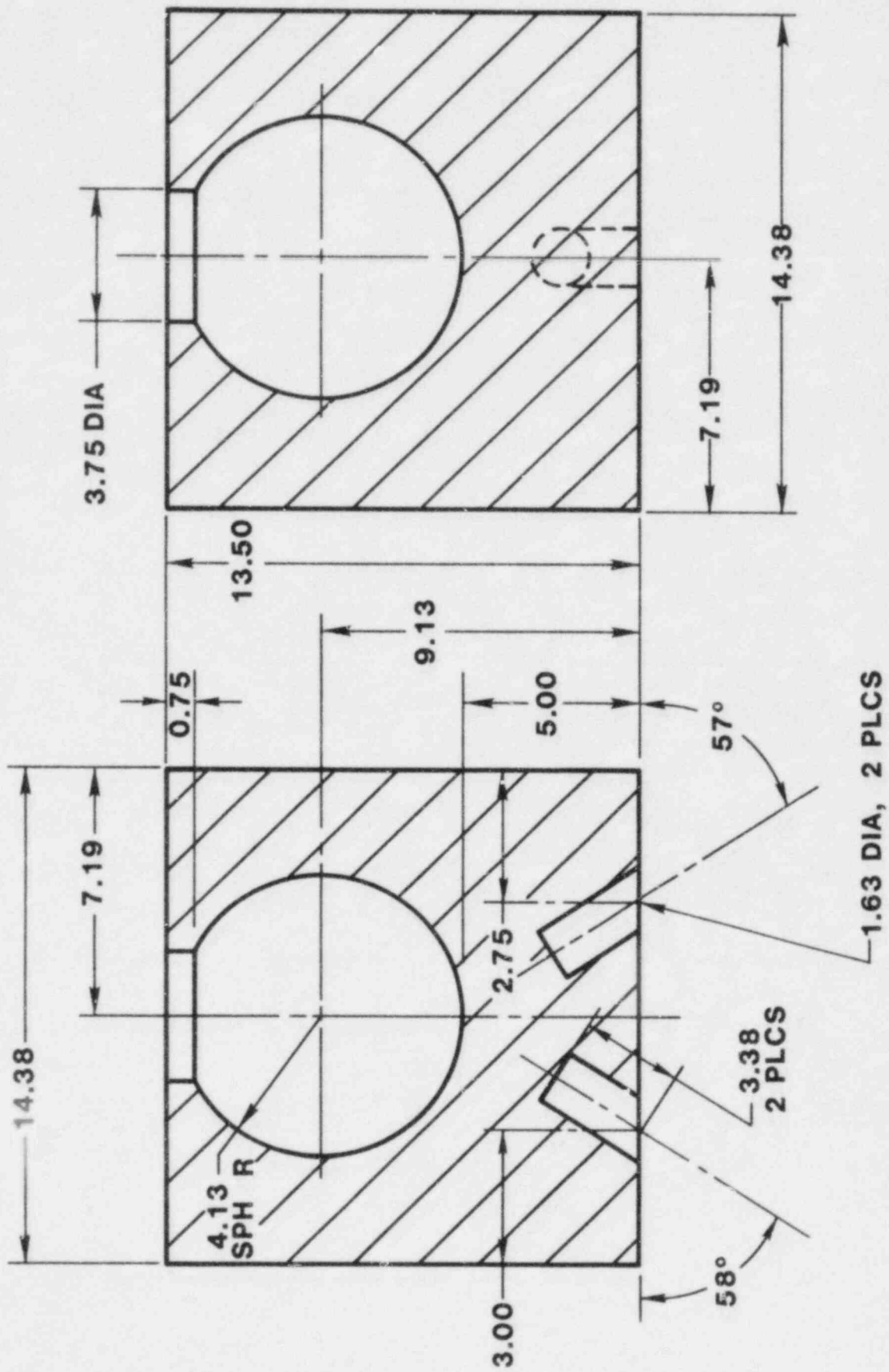


Figure 1.1-3. Limestone/Common Sand Crucible, Spherical Cavity

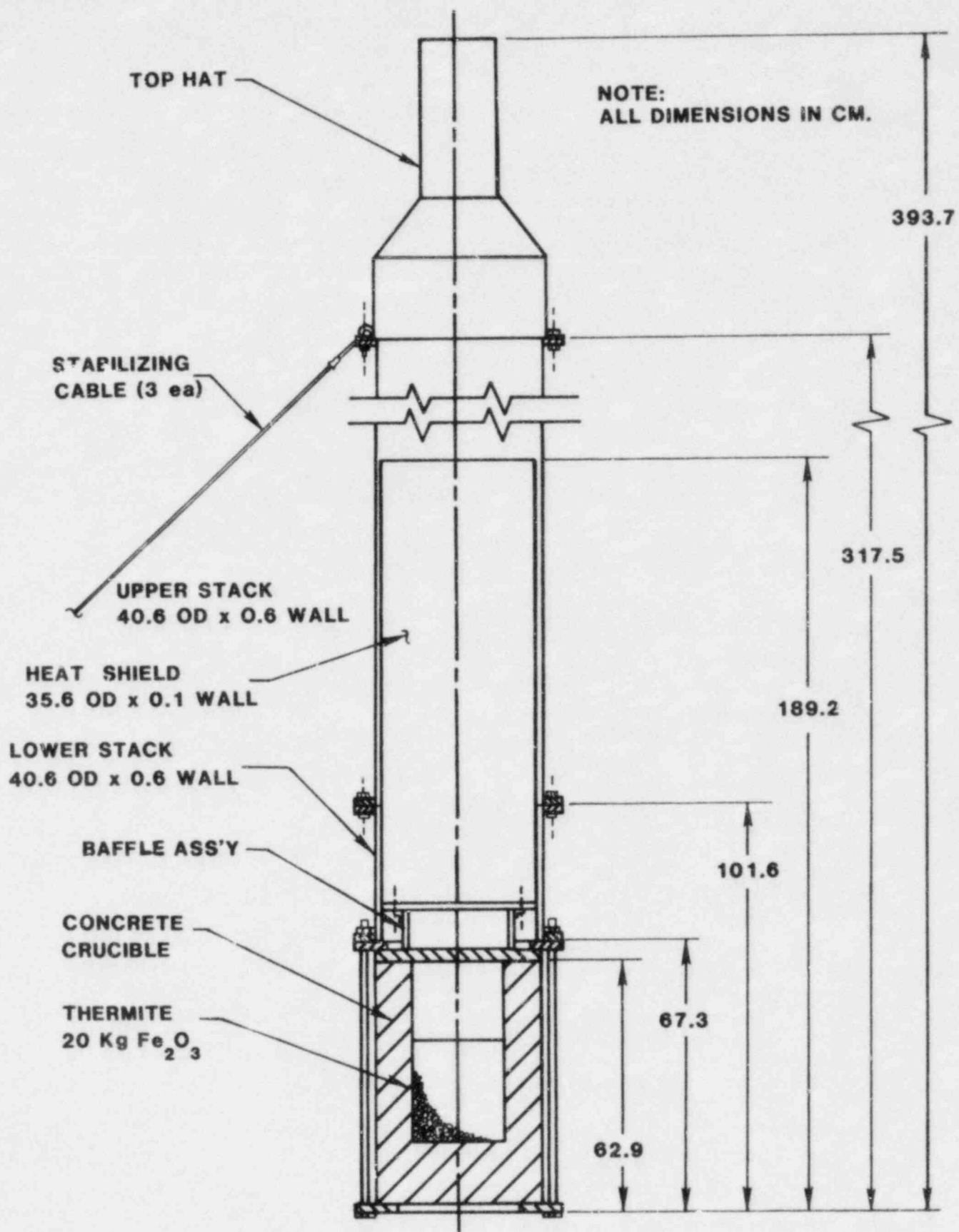


Figure 1.1-4. Transient Test Apparatus

The concrete crucibles will be instrumented with embedded thermocouples (TC) to evaluate concrete temperatures and heat flux data. Program personnel have directed efforts toward improving the methods for determining the position of the sensing junction after concrete casting. The relatively small dimensions of the TC sheath combined with the inherent unsharpness of X-ray techniques results in errors of several millimeters. A new technique has been developed that uses a relatively massive lead cylinder on the sheath, placed an accurate distance from the tip of the TC. This technique is described below.

A limestone/common sand concrete crucible was tested with the Linatron X-ray facility to determine if the sensing tip of a 1.59 mm diameter thermocouple could be accurately located with X-ray imaging. The results of these tests revealed that this technique can be used to locate thermocouples cast in concrete crucibles.

The crucible tested is shown schematically in Figure 1.1-5. The crucible had been previously used for a transient test. Four 9.5-mm diameter holes were drilled into the crucible in a plane 2.5 cm from the back edge. The holes were positioned 5.1 cm apart on a vertical line. The holes were drilled to a depth of 6.0 cm.

The TC configuration is shown in Figure 1.1-6. This configuration was placed in each of the four holes drilled in the crucible. A 2.0-mm-diameter copper wire was used to represent the stainless steel sheath for the TC. A tubular piece of vinyl insulation 2.0-mm ID x 4.0-mm OD x 13-mm long was used to separate the lead cylinder from the copper wire. In an actual assembly the vinyl would be replaced with a tube of alumina or mullite ceramic insulation to isolate the lead from the stainless steel sheath so as not to affect the heat transfer to the TC. For the same reason, the lead cylinder will be located between 10 to 20 TC-sheath-diameters away from the sensing tip. If the lead should melt and come in contact with the TC sheath their thermoconductivity coefficients are nearly the same. The thermoconductivity coefficients for lead and stainless at 373 K are 28 to 34 W/m·K and 23.9 to 27 W/m·K, respectively. The thermoconductivity of lead decreases with higher temperature and of stainless increases with higher temperature, allowing the values to approach each other.

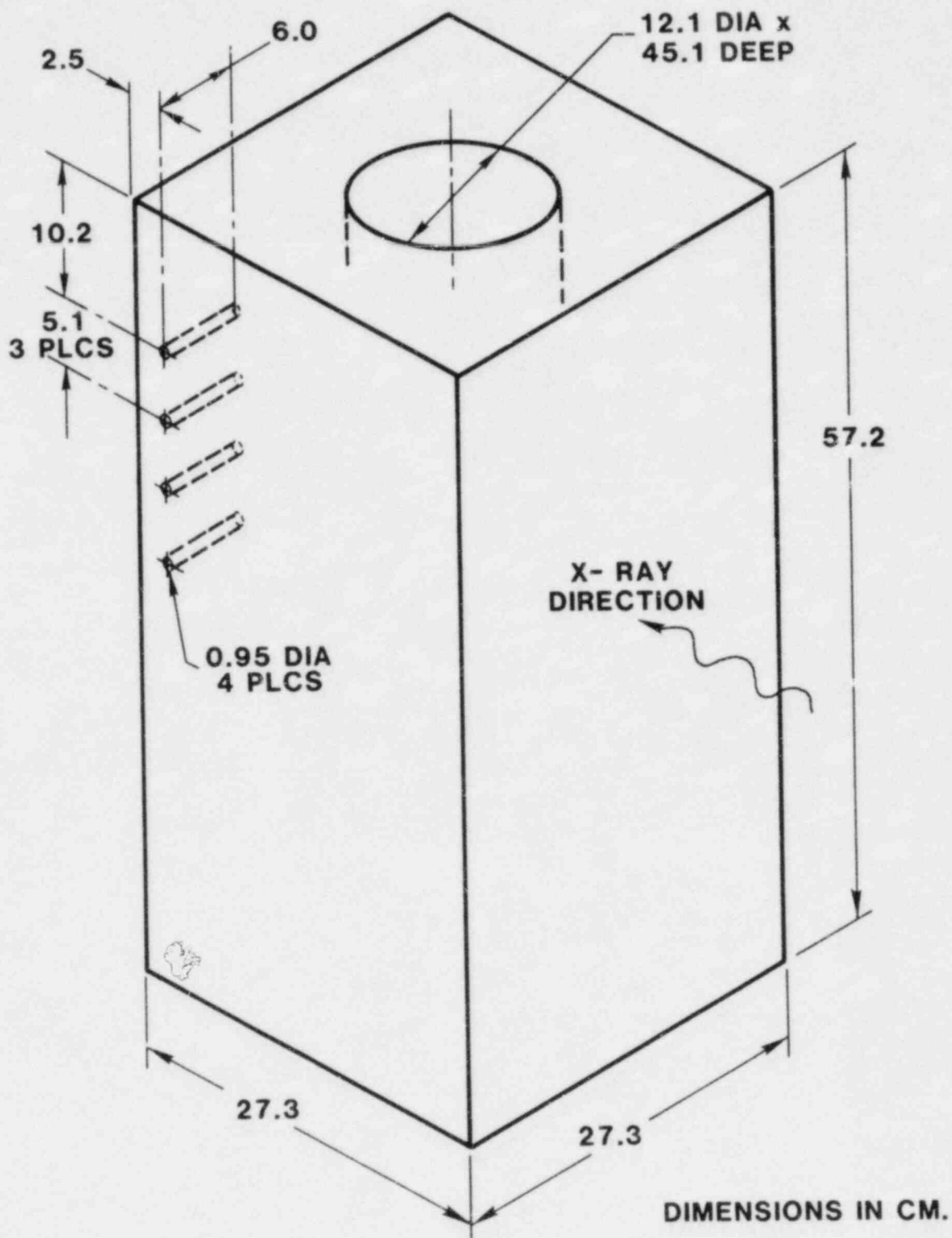


Figure 1.1-5. Crucible Configuration for X-ray Imaging Test

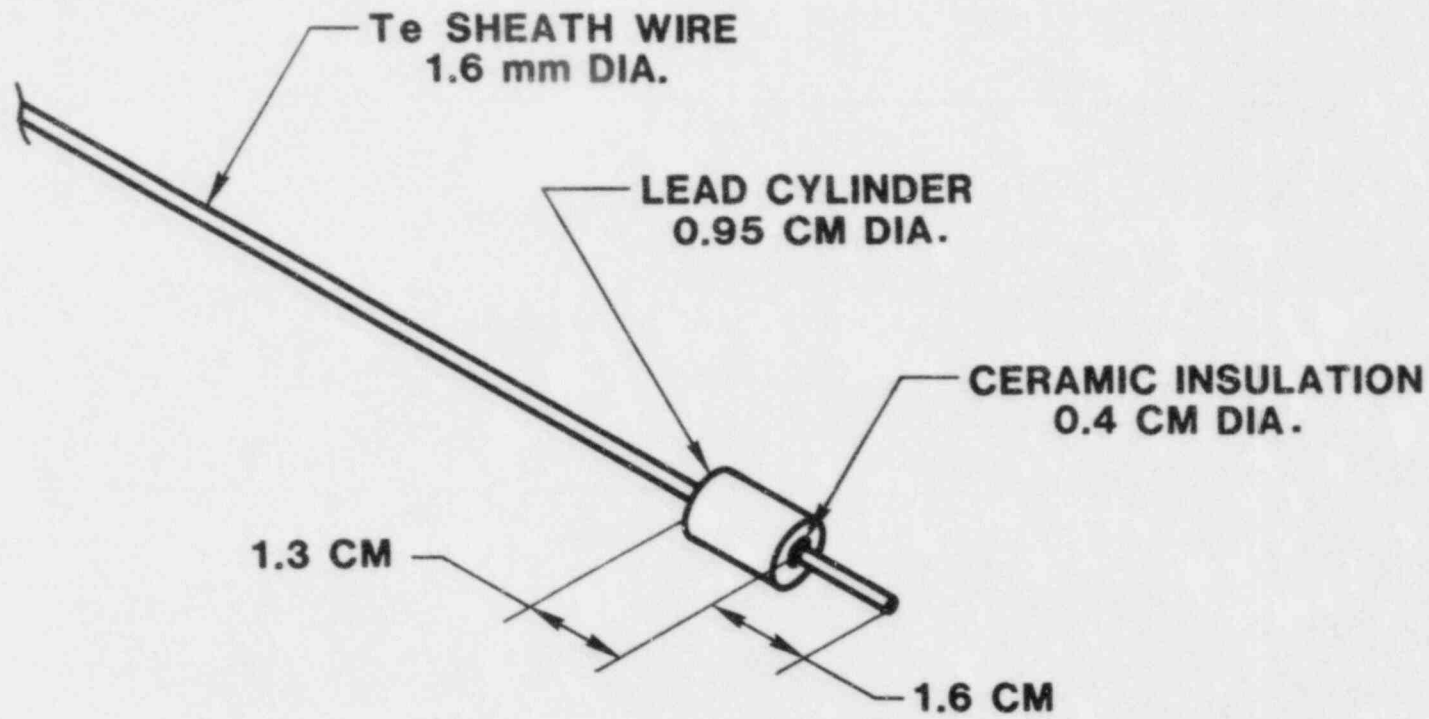


Figure 1.1-6. Thermocouple Configuration

The lead cylinder shown in Figure 1.1-6 was used so that this part of the configuration could be distinctly seen in the X-ray photograph. Lead was chosen over other high density materials because it is a good absorber of X-rays, easily machined, easily configured, inexpensive and readily available. The good X-ray imaging characteristics of the lead, plus careful placement of the cylinder onto the sheath of the TC, will provide for accurate location of the sensing tip.

Unsharpness in radiography is defined as the blurring of the edges of the images. Two primary causes using high energy X-rays (≥ 2 MeV) are geometric and film unsharpness. Geometric unsharpness (U_g) is defined by¹⁻⁴

$$U_g = F(t/D_0) \quad (1.1)$$

where

- U_g = geometric unsharpness
- F = X-ray focal spot size (< 2 mm)
- t = distance from front of specimen to film
- D_0 = distance from source to front of specimen.

The Linatron was placed 4.6 meters from the front of the concrete crucible. The video image was optimized at this distance and the geometric unsharpness was calculated from the above equation to be 0.12 mm.

A second cause of unsharpness using high energy X-rays (> 2 MeV) is film unsharpness (U_f).¹⁻⁵ Experimental values of film unsharpness are tabulated in Reference 1-5. A value of 0.58 mm was recorded for an X-ray machine operating at 7.5 MeV using fine grain film with lead screens.

The total unsharpness¹⁻⁵ (U_t) combining the effect of geometric and film unsharpness is calculated by

$$U_t = U_g + U_f^2/2U_g - U_f^2/2U_g \quad \text{Exp}(-2 U_g/U_f) \quad (1.2)$$

Substituting the values of geometric and film unsharpness given earlier into eqn (1.2) gives a total unsharpness of 0.6 mm.

The Linatron was operated at an energy of 7.5 MeV. The X-ray picture was taken with a total dose of 2 kilorads lasting 108 seconds. Lead shields 6.4 mm thick were placed in front of the crucible in areas not to be photographed. This helped minimize the scattered X-rays reaching the film. A lead penetrometer graduated into 25.4 mm increments was placed into the crucible cavity perpendicular to the X-ray beam. This provided for scaling the photograph.

The contrast in the developed X-ray film provided sharp definition of the lead cylinders, lead penetrometer, and crucible geometry. The copper wire could not be detected well. However, the lead cylinders positioned on the copper wire could be easily seen with a resolution equal to the value of total unsharpness calculated earlier (0.6 mm). The sensing tip of the thermocouple with this technique could be located well within 2 mm (0.08 in).

The support mechanism for the TCs has been redesigned to provide better resistance to the forces encountered during the casting and curing operations. Figure 1.1-7 illustrates a typical assembly.

A concept verification test is planned for early August to determine the viability of the new apparatus. If the design proves successful, the test matrix outlined in Table 1-1 will be initiated in late August.

1.1.1.2 Plans for Sustained Tests of Hot Solids

The low temperature phase is considered as the region between the melt solidus and concrete ablation temperatures. Only a few scoping tests have been performed providing very little qualitative information. An extensive experimental test matrix has been developed to study comprehensively the phenomena associated with this area.

Work to date has been directed towards developing the experimental test techniques. Included in these efforts is improvement of diagnostic capabilities, design of test hardware, and assessment of the heating method. Each of these areas is discussed in more detail below.

Data acquisition on core/concrete interactions has been difficult because of the large heat fluxes and copious amounts of reaction by-products. Investigators anticipate that the phenomena will not be as severe in the

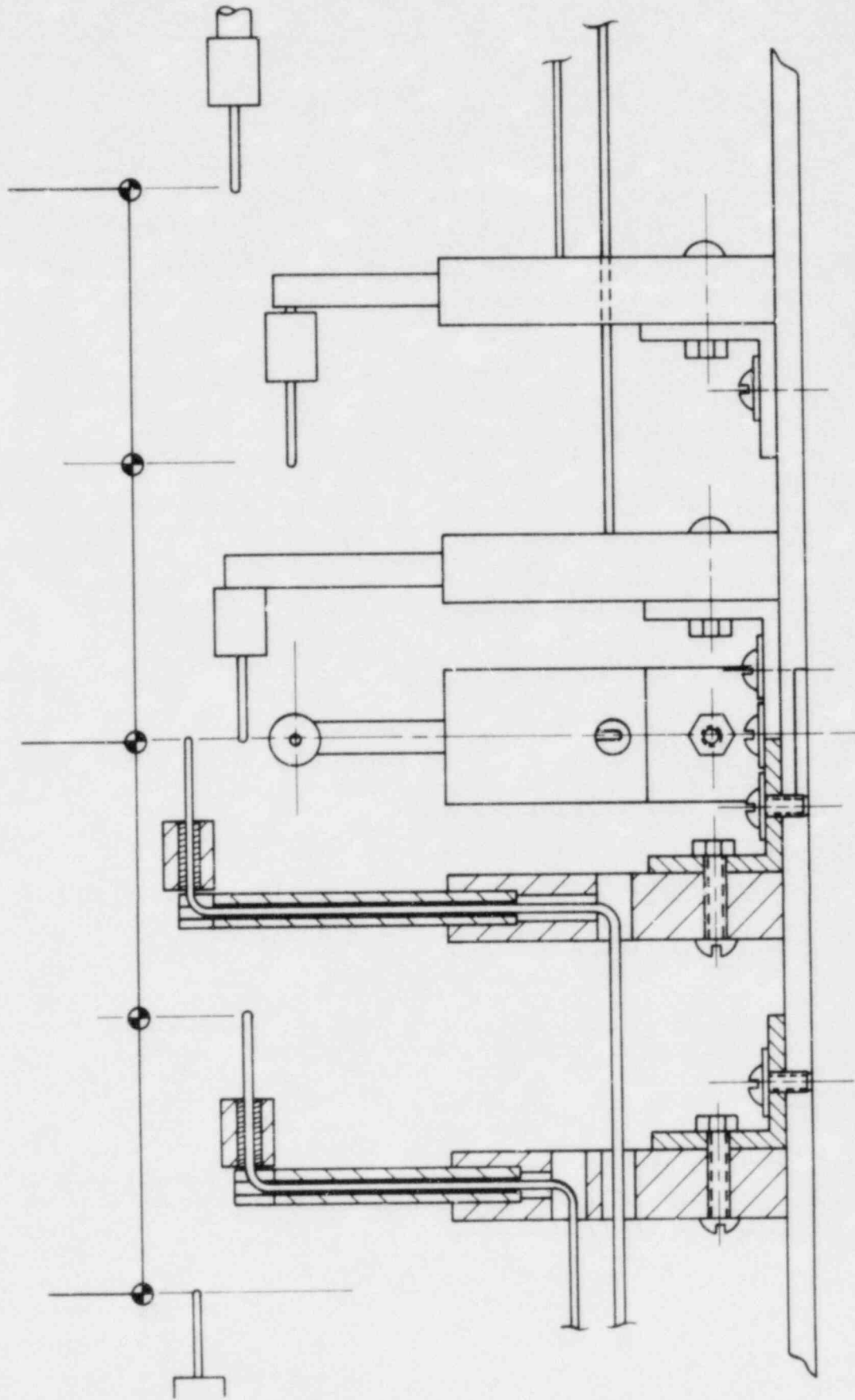


Figure 1.1-7. Base Configuration, Thermocouple Support Structure

low-temperature tests so that instrumentation improvements can be anticipated. Variables of principal concern are gas and aerosol generation and concrete erosion. A photometric aerosol detection device is being developed to obtain real-time aerosol generation data. In addition, filter sample units will be employed to obtain data at discreet intervals.

Gas generation is typified by relatively low outputs (compared to high temperature interactions) interrupted by large transient bursts. Instrumentation for gas flow must be sensitive to low levels, but must also respond to sudden variations. Most pressure probe devices are ill-suited owing to clogging of apertures by particulate matter or lack of good frequency response because of acoustic filtering. A mass flow device using a vibrating u-shaped tube shows good promise for this application. The device is capable of measuring fluids and gases independent of liquid properties. Several flow ranges are available so that some additional definition of the expected behavior will be required before an acquisition decision can be made.

In previous tests, concrete erosion has been detected using embedded thermocouples (TC) or ultrasonic sensors. Both techniques require considerable interpretation of data and produce results of questionable accuracy. X-ray imaging is a powerful diagnostic that has been valuable when used in transient events. However, the inductive heating equipment required for sustaining reactions is not available at the Sandia X-ray facility. Two alternatives to the problem exist; (1), an inductive power supply and associated equipment could be transferred for use at the X-ray site or (2), portable X-ray equipment could be used at the existing core/concrete test facilities. The advantage of the first approach is that the large 10 MeV Linatron source and Decalix image intensifier could be employed for continuous viewing of the event. The resulting video record would then provide a real-time view of the entire test with the capability for adjusting the view as characteristics change. The main obstacle to this approach appears to be the development of an adequate cooling water supply for the induction furnace. Design-concept studies are progressing at this time.

The second technique, using portable X-ray sources, appears to be limited by the penetrating power of the sources available. The largest device now on hand, a 2.3 MeV pulser, is not currently operational. When it becomes

available, tests will be conducted with a mock experiment apparatus to assess the penetration capabilities of the device. If this method is feasible, a cassette film holder must be developed to allow multiple exposures over the duration of the melt/concrete event. The device will permit the X-ray film packets to be interchanged remotely.

The experimental hardware design has concentrated on the development of a concrete crucible configuration. An initial scoping test (described later) has indicated that the downward penetration rate is slightly higher than the horizontal attack. In addition, a crust of melted concrete by-products formed over the melt and attached itself to the sides of the cavity. Figure 1.1-8 shows the crucible design selected based on the results of the scoping test and previous experience.

Thermocouple locations given in Table 1-II have been selected to obtain heat transfer data as the solid penetrates into the concrete. Additional sidewall TC's are included to aid in interpreting the heat radiated to the sidewall. The depth of the cavity is intentionally large for two reasons: first, it provides sufficient wall length for the attachment of crusts and second, it isolates the instrumentation tower's metallic components from the inductive field.

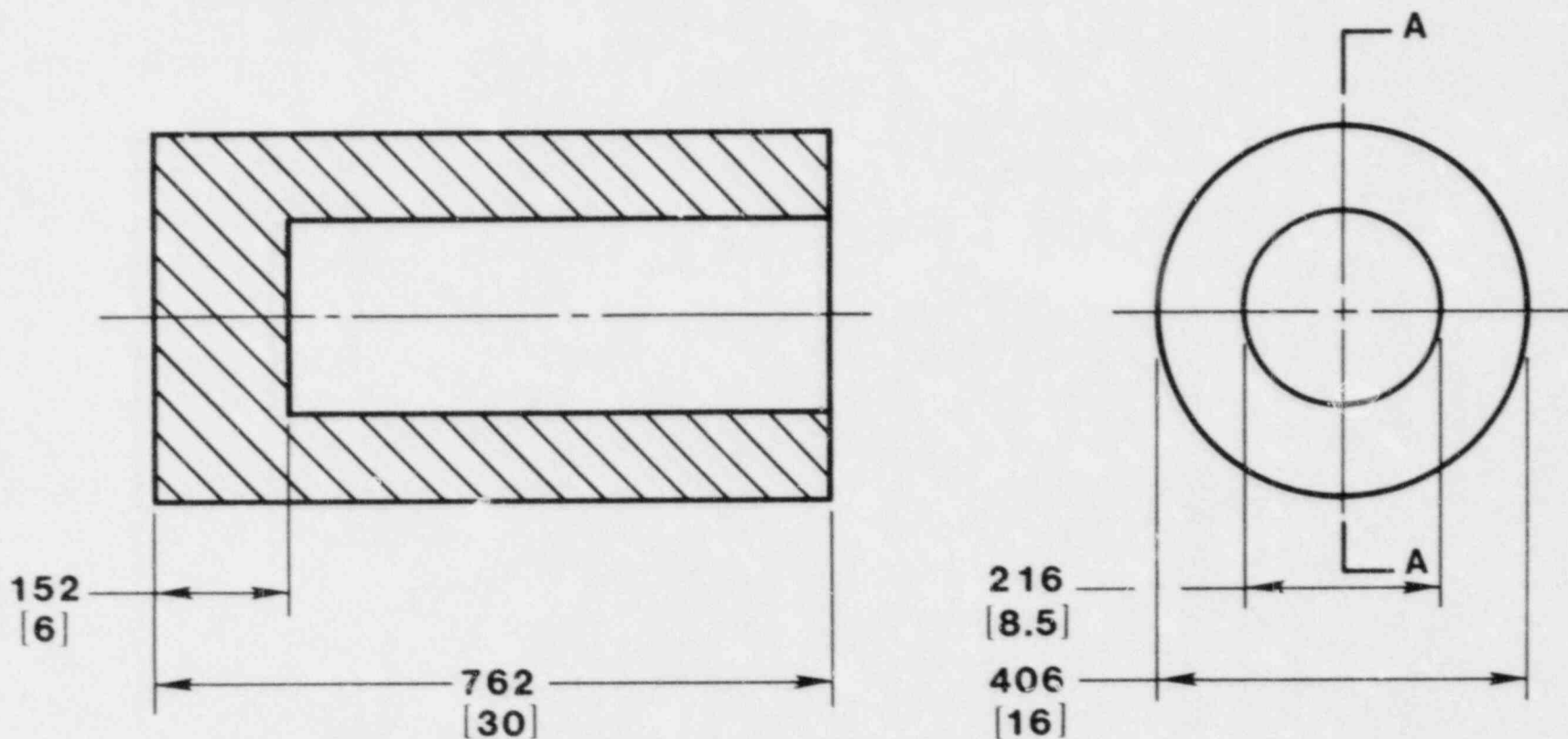
The remainder of the experimental apparatus will be designed to optimize the acquisition of gas, aerosol, and heat flux data. The less severe thermal characteristics of this type of experiment will permit more latitude in the design than that described in the transient high temperature experiments.

The efficiency of an inductively heated test is dependent on a close geometrical match between the inductive coil and the item to be heated. For melt/concrete experiments, a specified quantity of concrete must be present around the melt charge to insure the desired interaction. Thus, investigators must compromise between making the concrete wall thin to improve efficiency and yet provide sufficient material for attack by the melt. The dimensions of the experiment described here are based on this compromise.

One of the primary variables of interest in melt/concrete interactions is the power density in the melt. This term can be related to the decay-power curve to predict the point in the accident sequence that the

NOTES :

1. MAT,L: LIMESTONE/COMMON SAND.
2. DIMENSIONS mm [IN] .
3. TOLERANCES ± 10 mm EXCEPT AS NOTED.

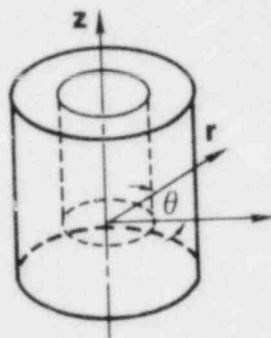


SECTION A-A

Figure 1.1-8. Concrete Crucible

Table 1-II

Crucible Thermocouple Locations for Sustained Hot Solid Experiments



COORDINATE DEFINED
AT CAVITY BOTTOM

TC No.	r (cm)	θ (deg)	z (cm)	TC No.	r (cm)	θ (deg)	z (cm)
1	0	0	-1	16	19	315	8
2	0	0	-2	17	12	0	0
3	0	0	-3	18	13	45	0
4	0	0	-4	19	14	90	0
5	0	0	-5	20	15	135	0
6	0	0	-6	21	16	180	0
7	0	0	-7	22	17	225	0
8	0	0	-8	23	18	270	0
9	12	0	-8	24	19	315	0
10	13	45	-8	25	12	0	10
11	14	90	-8	26	12	45	20
12	15	135	-8	27	12	90	25
13	16	180	-8	28	12	135	36
14	17	225	-8	29	12	225	46
15	18	270	-8	30	12	315	56

experiment simulates. Unfortunately, obtaining a power term during inductive heating is not easily done. A simplified power-balance equation for an induction heating sequence can be given by:

$$\text{Power input} = \text{Power to melt} + \text{Power losses}$$

Power losses are made up of: (1) electrical inefficiency of the coil/melt geometry, (2) dispersive losses from radiation and spurious coupling and (3) energy transferred to the crucible and surroundings. The terms of interest in the reactor-accident situation are the power to the melt combined with a third power loss factor. These quantities together represent the decay power state of the core simulant.

Experimentally, the input power can be obtained from the power supply instrumentation. The power lost to inefficiency can be determined by measuring the temperature rise in the cooling water supplied to the experimental apparatus. The power to the melt can be calculated by instrumenting the block to obtain the mean temperature profile change during a given period of time. The two factors that remain are the dispersive power loss and the energy loss to the surroundings.

Dispersive power losses can be inferred during the initial heating of the block by assuming that the heat transfer to the concrete is small. Whether this term remains constant during the heating cycle as the electrical and thermal properties change is not clear. A test is planned to heat a well-insulated block of typical geometry to determine the dispersive losses at elevated temperature.

If all the terms in the power-balance equation can be obtained, then the power lost to the concrete and surroundings can be determined. Assuming that the dispersive losses are known, then heating the block to an equilibrium state (no temperature change) would permit this determination. Thus, a heating sequence of a series of power increments would yield power loss verses temperature. An experiment of this type will be performed for a series of temperatures that approaches to near the melting point of concrete. Above this point, the reaction of the concrete causes the time-at-temperature dependency to be important.

1.1.1.3 Scoping Test of Hot Solid Debris Attack on Concrete

During this period a scoping test of hot solid debris attack on concrete was performed. The specific objective of the experiment was to determine if sufficient power was available in the experimental device to create the desired power density. Only minimal instrumentation was used. The apparatus consisted of a 50 kg billet of type 304 stainless steel placed in a basalt concrete crucible. The steel was in the form of a right circular cylinder 20 cm in diameter by 20 cm tall placed in a cavity 21 cm in diameter by 46 cm deep. Several thermocouples were placed in the block to assess temperature change. Input power for the test was held constant at nominally 50 kw for slightly over 3 hours total time.

Figure 1.1-9 presents the block temperature and power vs time for this experiment. The total power represents the combination of the input to the block and the power lost to the concrete. The scatter in results is due to imprecision in measuring the cooling water temperature. The net power was determined from the recorded temperature in the block. The steady decrease in term is indicative of the amount of energy being transferred to the concrete and environment above the melt.

Figure 1.1-10 is a schematic representation of the posttest configuration of the melt. Several solidified crust layers were formed above the melt. These layers were grayish-black in color and were highly porous except for the top surface of each layer. The depression in the top layer is a "blow-hole" of nominally 8-cm diameter that penetrated into the interior of several layers. The second feature of note is the shape of the metal slug, similar to an inverted "toadstool." The fact that the metal flowed indicated that the power density was sufficient to cause melting, thus achieving the objective of the experiment.

The significant change in the slope of the temperature profile coincided with the observation of crust formation. This behavior indicates that even a molten crust has a large effect on the upward heat flux. The crust was intentionally penetrated at the 145 minute point to assess structural integrity. Although no definitive information was obtained, the layer was easily pierced by a 1-in-diameter steel bar. At all times, both

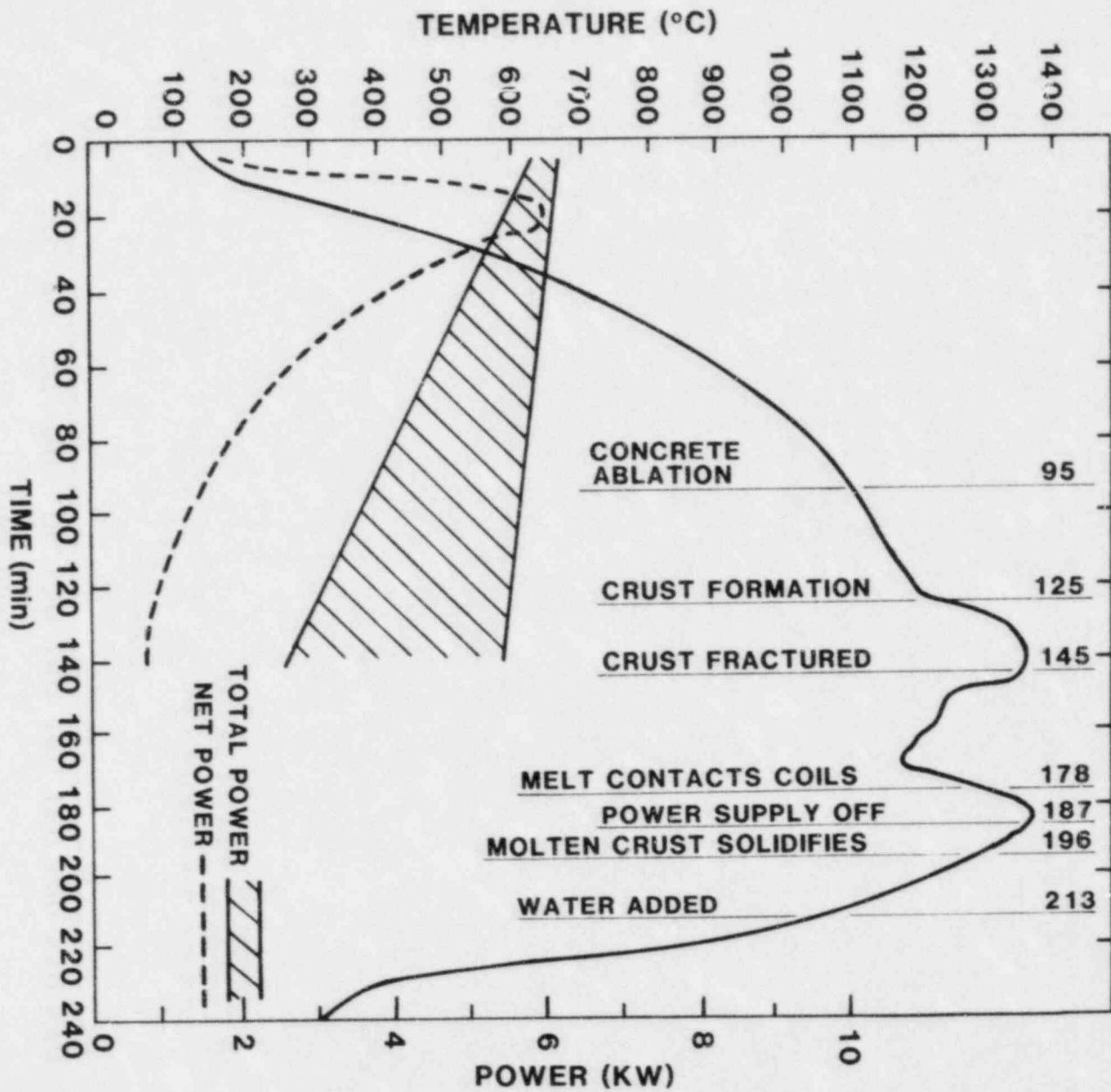
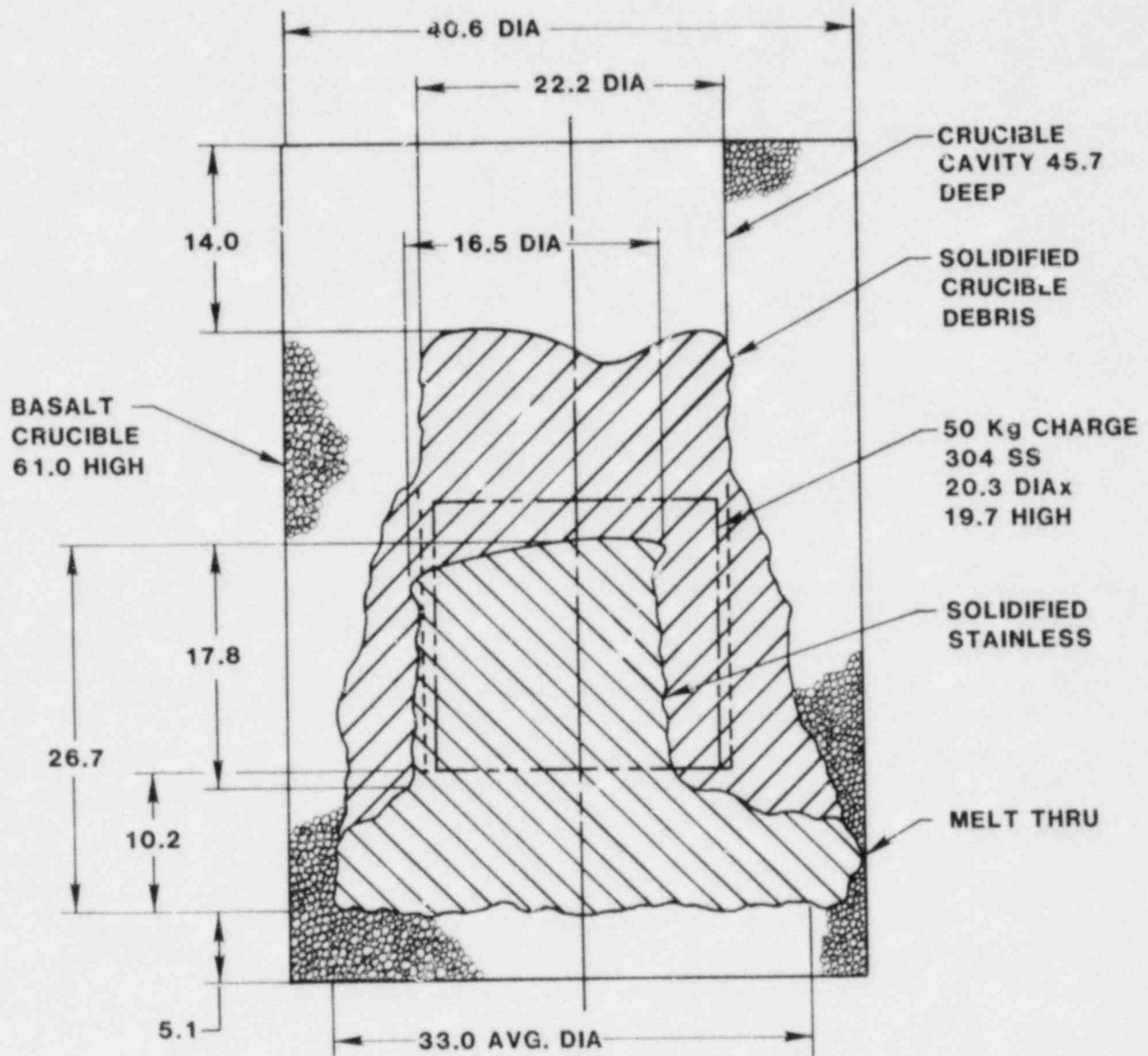


Figure 1.1-9. Temperature and Power vs Time Hot Solid Scoping Test



NOTE: ALL DIMENSIONS IN CENTIMETERS

Figure 1.1-10. Posttest Configuration, Sustained Hot Solid Experiment (Scoping Test)

before and after penetration, gas was visibly escaping through and around the crusted layer with spontaneous ignition predominant. The gas burned with a yellow-gold flame typical of sodium D excitation in a burning gas.

Approximately 20 minutes after the crust was broken, it reformed again into an intact layer. Only the large central hole and several small holes were apparent in the upper layer. At approximately 178 minutes after the start of the test, fluctuations in the power-supply instrumentation were noted, indicating a possible ground fault. Power was terminated at 187 minutes with a corresponding drop in temperature.

Observation of the cavity after termination of power showed the crust had changed color from a bright orange to a dark brown. Probing with a bar revealed the crust to be solid, although considerable gas was still escaping through and around the top layer. The concrete showed numerous cracks, with two large vertical fissures emanating from the embedded lifting bosses. All of the exposed surfaces appeared to be completely dehydrated and light grey in color.

At 213 minutes, the cavity above the crust was flooded with tap water. No immediate reaction was apparent, but steam was observed emanating from the cracks in the concrete with the water level dropping steadily. After several minutes, peripheral boiling was observed at the crust, followed by more vigorous boiling over the entire surface. The cavity dried out within 5 minutes after the addition of the water. Steam continued to escape through the cracks after the disappearance of the surface water. A significant temperature depression was noted after the water was added.

The above procedure was repeated two more times, each time with the same result. Following the last sequence, the temperature of the block was less than 573 K (300°C).

Posttest inspection of the experiment required removal of the debris by chipping away the crucible. The concrete appeared to be completely decomposed and offered virtually no resistance when struck. The solidified concrete debris was very dark in color with some embedded aggregate near the outer boundary. The material was almost glassy in appearance with large porosity near the upper layers. The penetration in the downward direction

was fairly constant over the entire interaction front while the lateral penetration was shifted slightly in the orientation indicated in Figure 1.1-10. The reason for the nonsymmetrical movement in the horizontal plane is not apparent. On the average, the downward penetration was slightly greater than the lateral. The fact that the lateral erosion may continue to progress with the duration of the event contradicts the initial assumption that sidewall penetration would be asymptotic. This behavior may be due to the flowing of the stainless steel and may not be present if the block retains its original shape.

The experiment was successful in determining if sufficient power is available to perform the test matrix. The results demonstrated that understanding the partitioning of power is vital in future experiments. The recovered remains indicate some interesting and unexpected behavior. However, the lack of precision in this experiment would dictate that the results be used with great caution.

1.1.2 UO₂/ZrO₂ Solubilities in Basaltic Melts

The solubilities of UO₂ and ZrO₂ in "quenched" basaltic glasses were reported previously¹⁻⁶ for several temperatures. The large uncertainties associated with these analyses were partially due to exsolution of UO₂ and ZrO₂ from the melt upon cooling. The feathery or dendritic texture of the exsolved phases (Figure 1.1-11) suggests crystal growth during cooling (cooling rate from 1823 K \approx 2 K/s). Some evidence of oxide precipitation was observed for those runs held at 1673 K while 1473 K runs did not exhibit "quench"-growth crystals.

The 1473, 1673, and 1823 K runs were subject to multiple microprobe analyses using a 4 μ m beam in 10 μ m steps and the data were plotted against the cation/oxygen ratio (in a wt. % oxide analysis) for comparison. These plots for UO₂ content are shown in Figure 1.1-12, -13, -14 for the one-hour-duration runs. A significant amount of UO₂ variability exists in these traverses, even at 1473 K. Some of this variation results from oxide or oxide-glass analyses while the rest is caused by local UO₂ heterogeneity in the glass. These differences cannot be readily resolved for the 1673 and the 1823 K runs. However, cooling the samples at a higher rate might metastably preserve the U/Zr-rich glass without precipitation of the oxide phases.

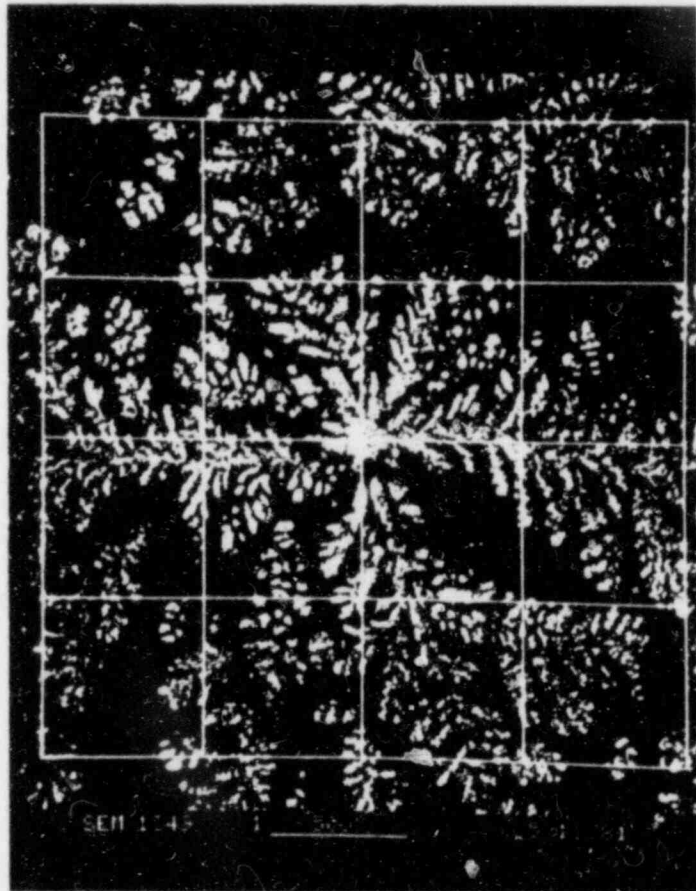


Figure 1.1-11. SEM Photo of $\text{MgU}_2\text{O}_6\text{-ZrO}_2$ Oxide
Precipitate from Basalt Melt at
1823K (1550°C) for 1 Hr.

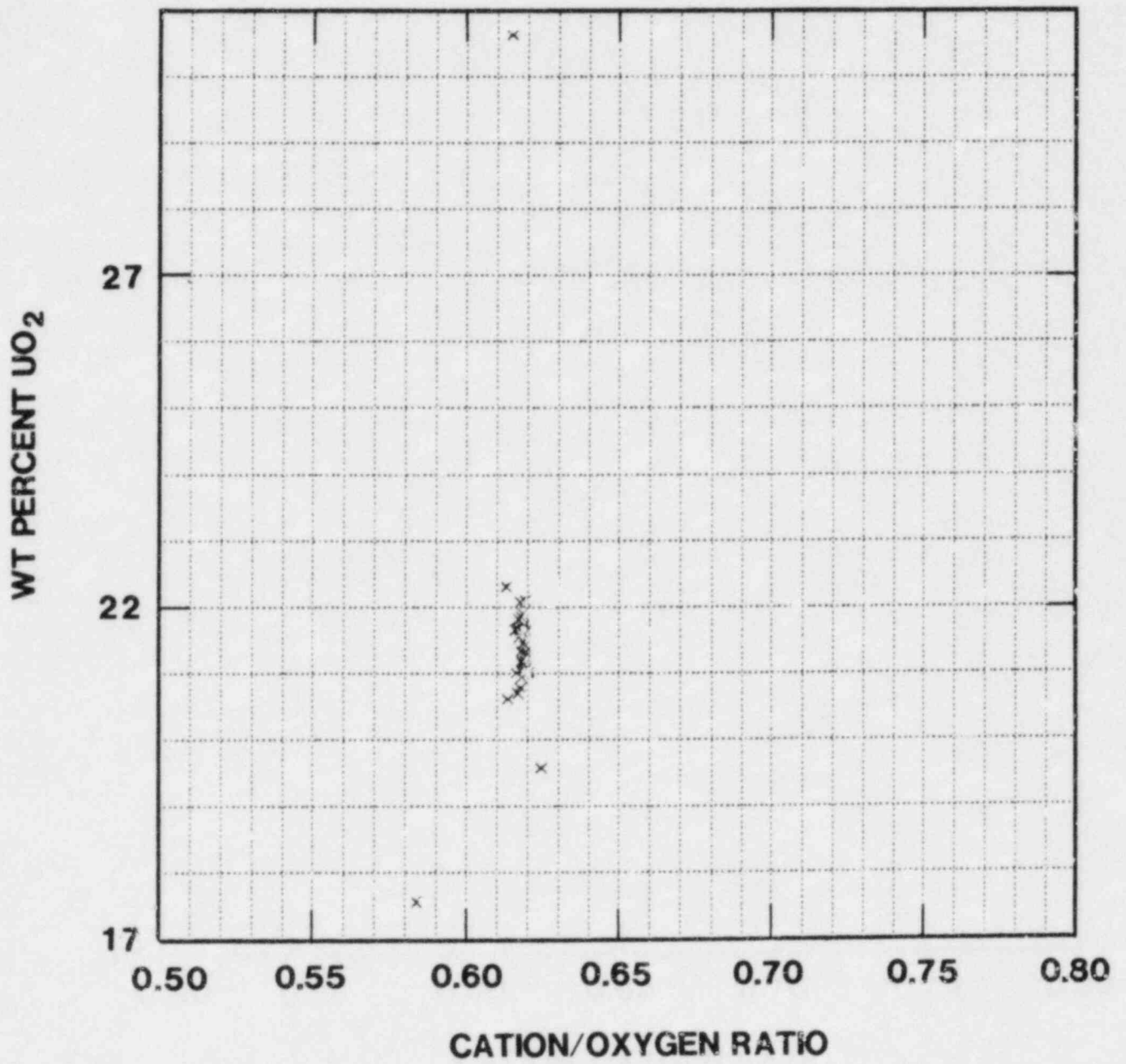


Figure 1.1-12. UO₂ Content of Basalt at 1473K (1200°C) for 1 Hr.

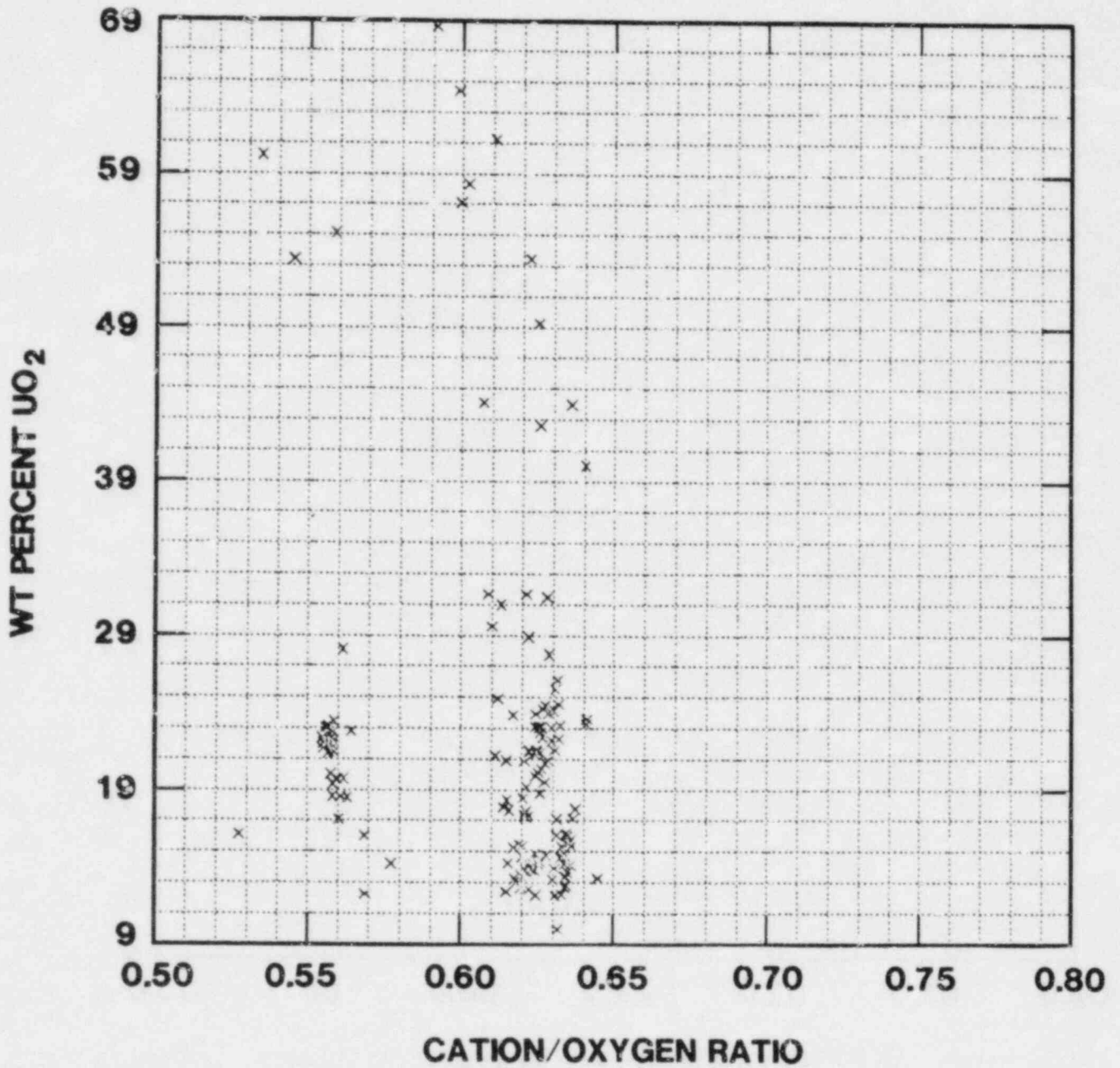


Figure 1.1-13. UO₂ Content of Basalt at 1673K (1400°C) for 1 Hr.

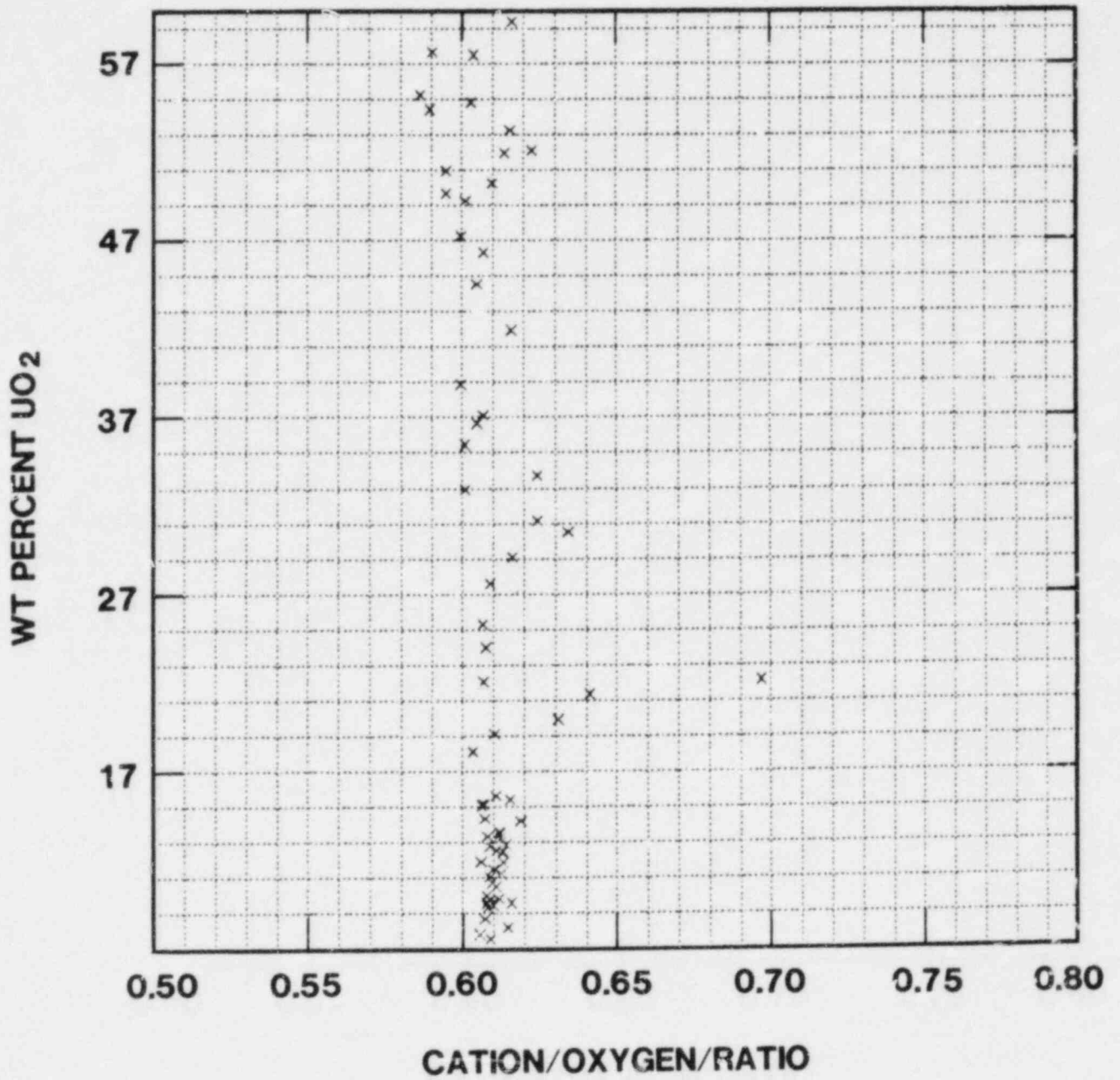


Figure 1.1-14. UO₂ Content of Basalt at 1823K (1550°C) for 1 Hr.

Using a vertical-tube MoSi₂ furnace and suspending the basalt/UO₂-ZrO₂ samples by a Pt wire, one-hour-duration runs were made at temperatures of 1473, 1573, 1673, 1773, and 1823 K. At the end of each run, the samples were pulled from the furnace, cooling them to below 1173 K within 5 s (a cooling rate of approximately 100 K/s). Initial microprobe analyses suggest that high-temperature-melt compositions (UO₂ and ZrO₂ solubilities) can be preserved or estimated at all temperatures. Additional microprobe analyses and computer data reduction shall continue during the next quarter.

1.1.3 Aerosol Source Term Characterization

This program involves several possible projects beyond experimental measurement of aerosols during melt-interaction tests. These projects include development of sampling and measuring techniques, design of specific phenomenological experiments, and development of a source-term model. They will be guided by sensitivity studies of predicted aerosol behavior in containment; the studies will be used to pinpoint the important aspects of the source term and identify the types of measurements to be made. The objective of the work is to provide an aerosol source term description satisfactory for reactor safety analyses and for aiding other research efforts sponsored by the NRC to study aerosol behavior.

Since every melt-interaction experiment evolves aerosols, Sandia program personnel are in a unique position to examine the effects of these aerosols on mitigation devices. Placement of a model heat exchanger in the reaction chamber will provide information on failure of the heat transfer surfaces under aerosol deposition. The aerosol may be ducted through such removal devices as filters, granular beds, and water suppression pools to study loading characteristics and aerosol penetration. The aerosol may be allowed to flow through calibrated cracks to study penetration and plugging. Data obtained with prototypic aerosols at prototypic concentrations will be of use in more detailed studies being conducted elsewhere with simulant aerosols.

The aerosol source term may be considered in two phases. The second phase, which will be called the source term, is an established aerosol some distance from the melt. This phase is the input from the aerosol behavior codes and is assumed to be homogeneous throughout

containment. The first phase involves the formation mechanisms that yield the source term. These generation mechanisms operate close to the surface of the melt. Characterization of these mechanisms provides the basis for definition of an aerosol source term that may be extrapolated to real reactor situations.

This established aerosol, the source term, is characterized by a size distribution function, a chemical composition distribution, and a time dependence. These characteristics may be correlated with such properties as temperature, evolved gas rates, and melt composition. A correlation with the experimental geometry may also exist which is undesirable unless it can be accounted for.

A model of the first phase, the formation process, provides a framework within which to make the experimental correlations. Such a model is being developed.

1.1.3.1 Aerosol Source Term Model

A model of the aerosol source term for melt interactions incorporates multiple generation modes, calculates their behavior, and yields the aerosol source term.

The generation modes considered are hydrodynamic, vapor condensation, and chemical reaction. The hydrodynamic mode, predominantly bubble bursting, depends upon gas evolution through the melt, velocity of the gas, settling velocity of the aerosol, and material properties such as melt viscosity and surface tension. It may be determined experimentally and a literature search may reveal helpful correlations.

The vapor condensation mode arises from condensation of supersaturated vapor into particles. Molecular collision with an accommodation factor of 1 is assumed to be the condensation mechanism. The vapor and the condensation aerosol may be scavenged by the large hydrodynamic mode aerosol by intermodal coagulation. The model indicates when this is the case. The vapor-condensation mode depends upon vapor pressure, temperature, dilution rates, and scavenging by the large mode. It may be determined experimentally or by theoretical analysis based on equilibrium vapor pressures and the model described in the next sections.

Chemical reaction as a generation mechanism is not included at this time but may be included later. More experimental evidence is required for consideration of chemical reactions.

1.1.3.1.1 Model Structure

Consider three regions: (1) the melt, (2) the region directly above the melt where condensation occurs, and (3) the containment volume. The model treats the second region and the adjacent interfaces, taking input from the melt and yielding output to containment.

The following is a qualitative description of the process. The hydrodynamic mode is generated at the surface and is carried up with condensable vapor by the evolved gas. Convection in containment, and radiation, cool the gas and increase the upward transport. The cooled vapor condenses to form particles and these coagulate with the hydrodynamic-mode aerosol. This resulting aerosol is the source term that is convected into and mixed in containment.

1.1.3.1.2 Model Description

As it is now written, the model incorporates only vapor input, hydrodynamic input, self-coagulation and scavenging. The hydrodynamic mode is assumed to be invariant in the source-term-model region. The vapor is assumed to act as a coagulating aerosol, colliding with itself and the hydrodynamic mode. The model describes the distribution of the condensation aerosol as it undergoes coagulation and scavenging by the hydrodynamic-mode aerosol. This case fits into the two-equation model for coagulation with a simultaneous sink term developed by Brockmann.¹⁻⁷

If the hydrodynamic mode is represented as a monodisperse aerosol and the free molecule collision frequency function is written as given by Friedlander:¹⁻⁸

$$\beta(D_p, D_p') = \left(\frac{GkT}{\rho_p} \right)^{1/2} (D_p + D_p')^2 \left(\frac{1}{D_p^3} + \frac{1}{D_p'^3} \right)^{1/2} \quad (1.1)$$

For the limiting case where $D_p \gg D_p'$,

$$\beta(D_p', D_p) = \left(\frac{GKT}{\rho_p}\right)^{1/2} D_p'^{-2} D_p^{-3/2} \quad (1.2)$$

$$\frac{dn(-D_p)}{dt} = -\left(\frac{GKT}{\rho_p}\right)^{1/2} \left(\frac{D_p'}{D_p}\right)^2 N' D_p^{-3/2} n(D_p). \quad (1.3)$$

This expression for the sink term, when substituted into the two-equation model gives

$$N = \frac{v^{1.664}}{[(1 + v^{1.221}) A(0.2425) + 1]^3}, \quad (1.4)$$

$$\frac{dV}{dB} = \frac{(0.6833)v^{2.328}}{A[(1 + v^{1.221}) A(0.2425) + 1]^{1.5}}. \quad (1.5)$$

The ratio of coagulation-number change to sink-number change is R . When R is large, the loss can be ignored and concentration is given as:

$$N = (0.506B + 1)^{-615} \quad (1.6)$$

$$DNG = N^{-1/3}. \quad (1.7)$$

For given A , $R > R'$ for

$$B < 1.977 \cdot \left(\left(\frac{0.534 A}{R'} \right)^{15/7} - 1 \right).$$

The dimensionless time B is

$$B = \left(\frac{192 kT \text{ DNG}}{\rho_p} \right)^{1/2} N_o t_{res}. \quad (1.8)$$

The parameter A is

$$A = 4 \sqrt{2} \cdot \frac{N_o}{N'_o} \cdot \frac{\text{DNG}_o^2}{D_p^2}. \quad (1.9)$$

In this simple form, the model will indicate the presence of a significant condensation mode if it exists.

Proposed experiments to support, improve and validate the model involve aerosol measurements in the model regime. This requires development of a sampler-diluter probe and will probably require both mass and number distribution measurements. Phenomenological tests can be designed to isolate a single formation mechanism.

This model indicates that the existence of a significant condensation mode is viable and should be a consideration in subsequent sensitivity studies.

Figure 1.1-15 is a schematic of the aerosol source term model. Table 1-III lists the nomenclature used to describe the model.

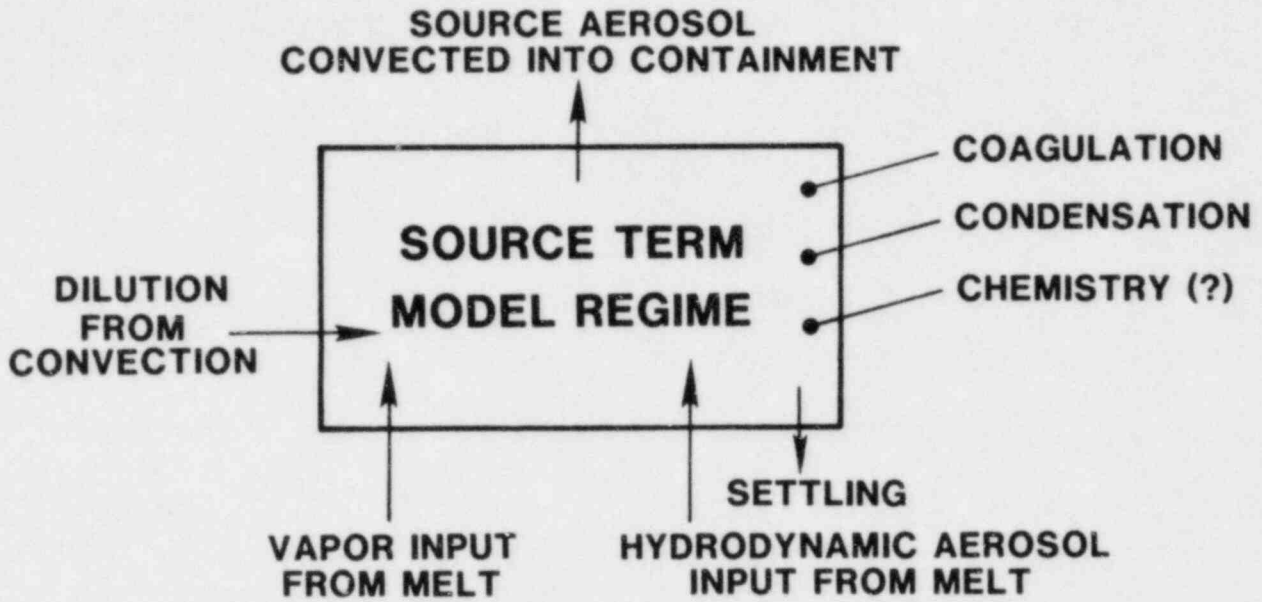
1.1.3.2 Containment Sensitivity Study

A sensitivity study of aerosol behavior in containment, using the aerosol code MAEROS¹⁻⁹ as incorporated in the CONTAIN code, is being undertaken. Two aspects are being considered. The first is the sensitivity to the source term given by the source term model. Sensitivity to the various shape factors is the second aspect.

1.1.3.2.1 Sensitivity to Source Term

The predicted distribution resulting from source terms with different condensation-mode components is underway. The source-term model indicates a significant

SCHEMATIC OF MODEL



WHAT IS NOW INCORPORATED

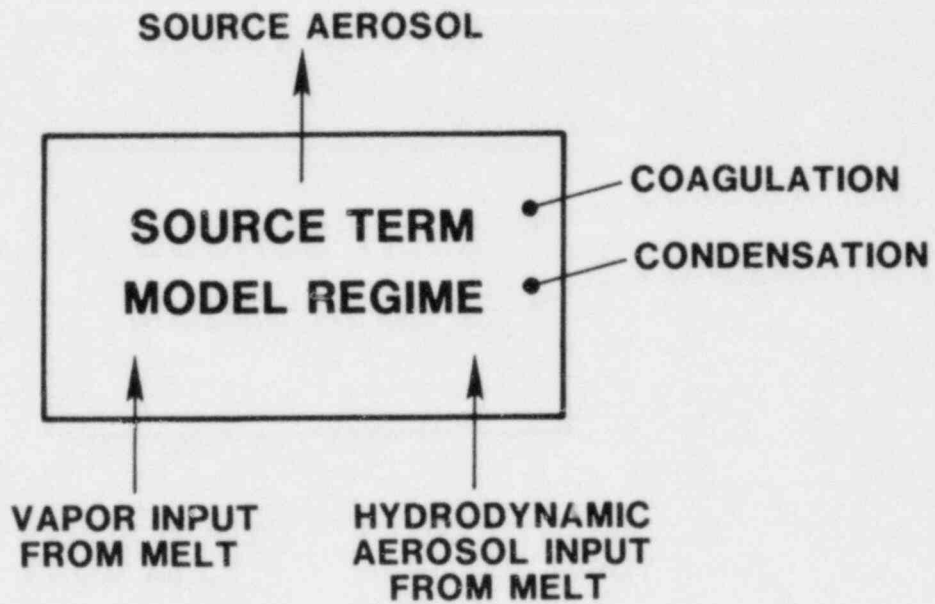


Figure 1 1-15. Schematic of the Aerosol Source Term Model

Table 1-III

Nomenclature

- A - Dimensionless parameter relating coagulation and loss in the condensation mode (-)
- B - Dimensionless time (-)
- D_p - Particle diameter (L)
- D_p' - Particle diameter of large mode
- DNG - Number geometric mean particle diameter divided by DNG_0 (-)
- DNG_0 - Initial value of DNG (L)
- k - Boltzmann's constant
- N - Fraction of initial total number concentration (-)
- N' - Number concentration of large mode
- N_0 - Initial total number concentration ($\#/L^3$)
- n - Number distribution function ($\#/L^6$)
- R - Ratio of coagulation number change to loss number change (-)
- T - Absolute temperature
- V - Fraction of initial total volume concentration (-)
- β - Collision frequency function
- ρ_p - Particle density

vapor condensation mode is present for realistic values of material vapor pressures and hydrodynamic mode generation rates.

Calculations will be made for bi-modal as well as unimodal source terms and the results compared. Preliminary results indicate that the presence of a condensation mode skews the particle-size distribution toward the small end for calculations covering 2 hr. and constant generation rates. These results are of interest in the analysis of consequences, especially in the event of early containment failure. The condensation mode material is concentrated in the smaller size range and, hence, shows different deposition characteristics than the hydrodynamic mode material. This is significant to assessing the transport of specific materials.

1.1.3.2.2 Sensitivity to Shape Factors

The sensitivity of predicted aerosol behavior to shape factors is in the formative stages. Realistic values for shape factors have been obtained from the literature. 1-10, 1-11, 1-12, 1-13, 1-14

Aerosol behavior, such as settling and inertial deposition, diffusion, and collision, is a function of size. Descriptive expressions are generally formulated with respect to spherical particles. A nonspherical particle of a given mass may be described by a number of equivalent spherical particle parameters based on a specific behavior. The mass equivalent diameter is the diameter of a particle of mass m having the material density ρ . It is useful in conserving mass in behavior calculations. The aerodynamic diameter is the diameter of a unit density sphere with the same settling velocity as the particle in question. Inertial classification devices such as impactors and centrifuges indicate an aerodynamic diameter. The collision diameter is the diameter of a sphere of material density which exhibits the same collision frequency as the particle in question. This diameter is necessary in agglomeration calculations.

Shape factors relate these various equivalent diameters and permit transformation from one to the other. They also allow number distributions to be calculated from mass distributions and vice-versa. Different measurement techniques yield mass or number distributions with respect

to one equivalent diameter. Hence, shape factors become important.

Just how important shape factors are to the predicted aerosol distribution will be indicated by the sensitivity study. Part of the source term identification may of necessity be values for shape factors.

The goal of these sensitivity studies is to determine how the form of the source term and the values of the shape factors affect the predicted aerosol distribution. These results will be used to indicate the information about the source term which needs to be obtained and to determine the measurements to be made.

1.2 Core Retention Concept Assessment

(T. Y. Chu, 1537; M. Pilch, 4425; D. A. Powers, 4422)

1.2.1 Introduction

The Core Retention Concept Assessment is a program to assess the engineering of core retention devices to replace concrete as the primary basemat material in reactor cavities. The program is currently focused on the engineering of magnesia retention devices.

Availability of a facility to prepare large (~200 kg) melts of UO_2 is essential for the execution of this research program. Consequently, development of the Large-Scale Melt Facility is a major task in the early phases of this effort.

The primary objectives of this program during the quarter were to prepare the Large-Scale Melt Facility for tests with molten TiO_2 and to begin analysis of a core retention concept that could be retrofitted into light water reactors.

Work on the Large-Scale Melt Facility consisted of redesigning the susceptor support in the furnace, testing the new design, preparing the TiO_2 charge, and defining a heating schedule for the test. The test with TiO_2 is intended to be a verification of all the previous modifications to the facility.

1.2.2 Large-Scale Melt Facility

1.2.2.1 Facility Design

The furnace susceptor support at the Large-Scale Melt Facility was totally redesigned during this quarter. In the old design (Figure 1.2-1), the susceptor was supported by the copper pedestal through a series of pyrolytic graphite rings and a porous carbon ring. In the new design (Figure 1.2-2), the susceptor is supported by eight 1-inch-diameter graphite rods screwed into the susceptor. Two sets of 2 pyrolytic graphite rings, one next to the susceptor and one next to the copper pedestal, are used to provide lateral support for the graphite rods. The space between the 2 sets of rings is filled with graphite felt. This new design reduces the heat loss from the bottom of the susceptor because the graphite felt limits the lateral conduction of the radiant heat flux impinging on the inside

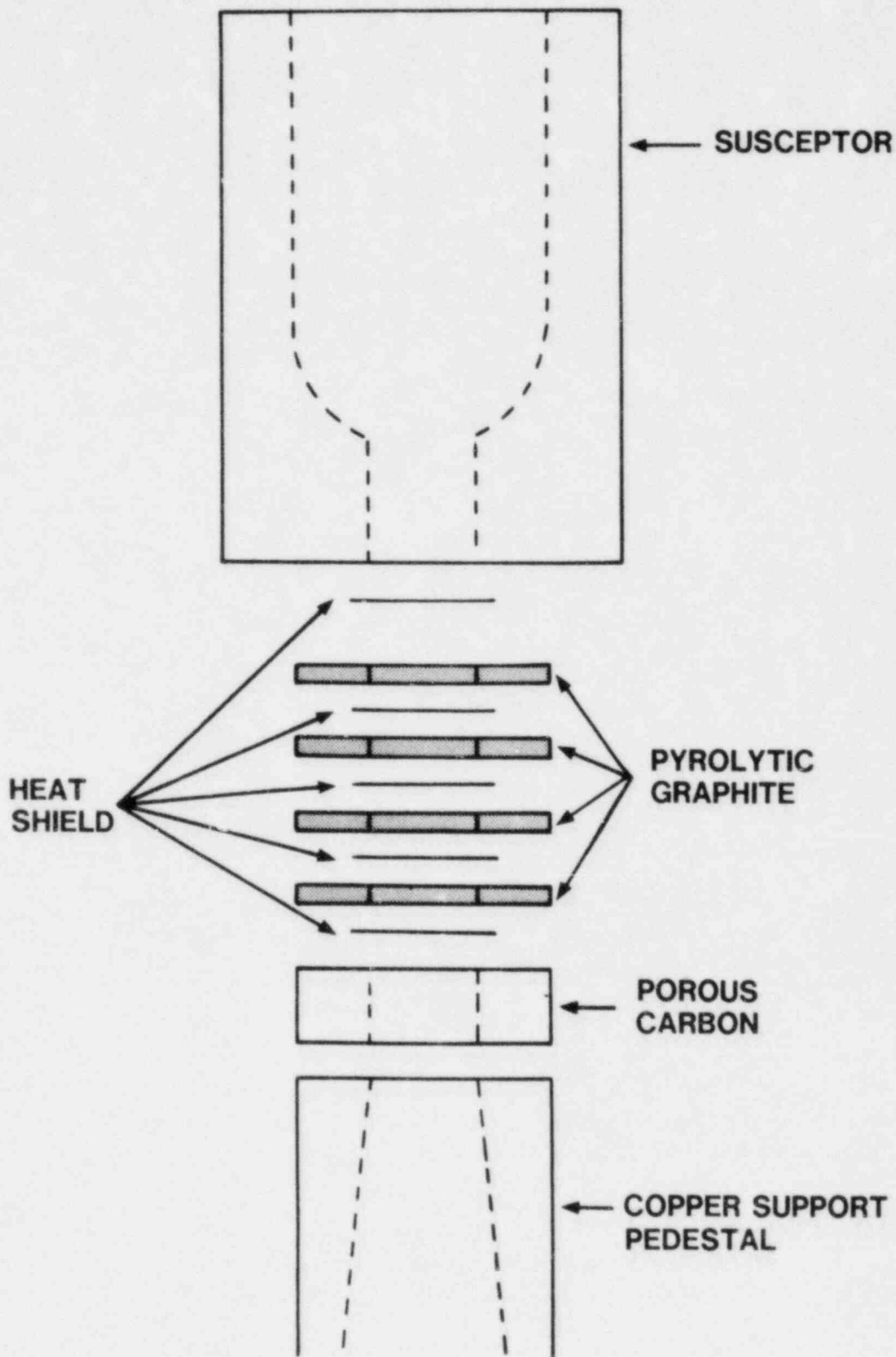


Figure 1.2-1. Furnace Susceptor Support, Old Design

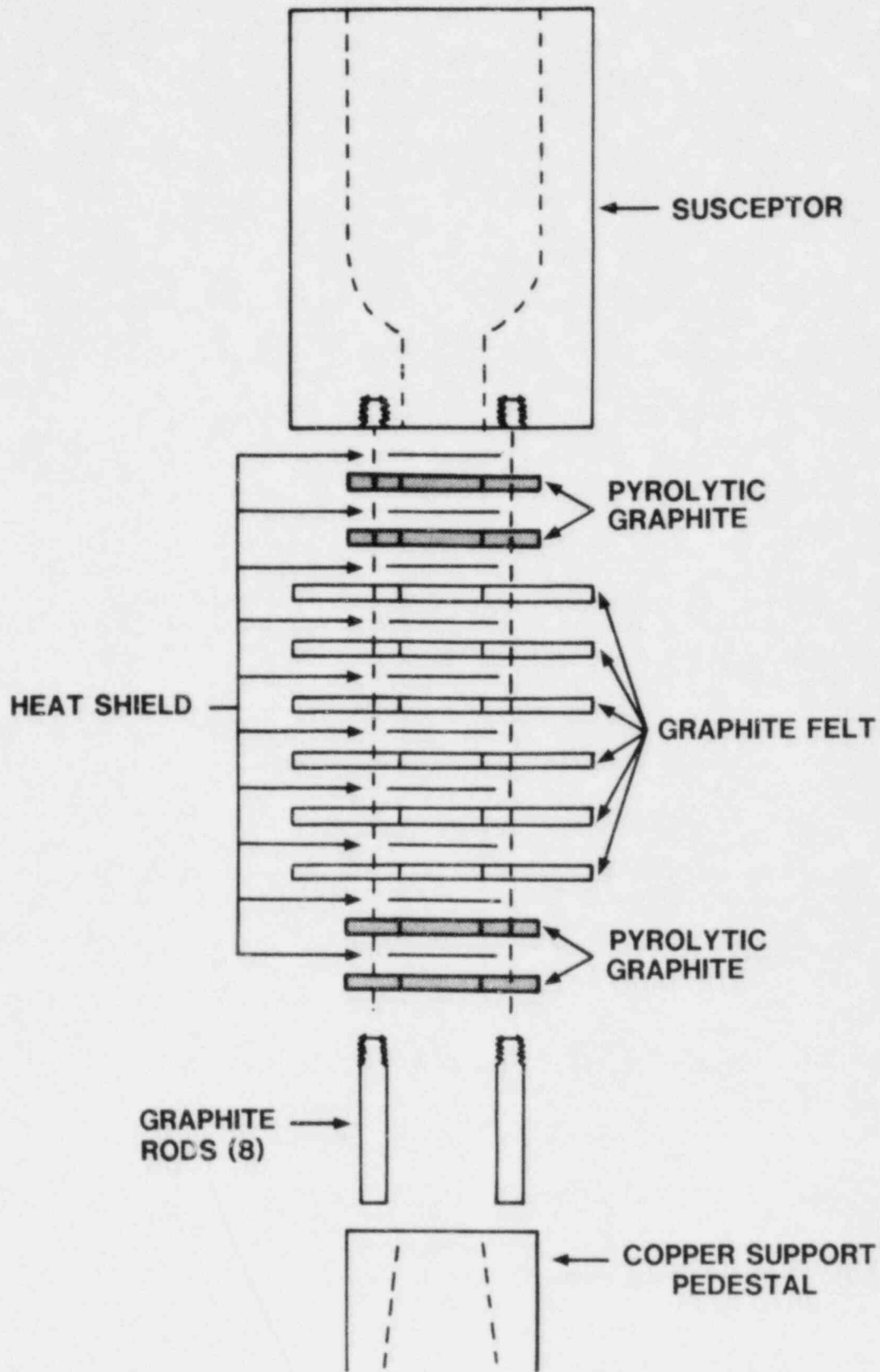


Figure 1.2-2. Furnace Susceptor Support, New Design

diameter of the susceptor support assembly. The removal of the porous carbon ring also eliminated the problem of sulfur emission from the porous carbon ring.

Investigators performed a dummy load experiment in mid-May to determine the operating characteristics of the furnace with the new support. This experiment used a solid graphite cylinder having the same outside dimension as the susceptor assembly. Investigators monitored the surface temperatures of the insulating felt and the water, the argon flow rates, and the inlet and outlet temperatures as the graphite load was brought through a series of constant temperature plateaus. From these, a steady-state temperature vs power operating curve was obtained (Figure 1.2-3). At the plateaus the net power input was balanced by the heat loss. The heat loss values were calculated; the ratio of heat loss and the power input is the coupling efficiency. This efficiency was found to be slightly temperature-dependent, varying, with temperature, between 53 percent and 60 percent. Table 1-IV summarizes the furnace information. The experimentally determined heat loss values were compared with computer-model calculations and the agreement appeared to be very good (Table 1-IV) considering the approximations involved in the computer calculations. With the above information, a heating schedule (see later sections) based on the predictions of the transient thermal model can be translated into a power setting-vs-time operating curve for the test.

Table 1-IV

Furnace Efficiency Study

*Graphite Dummy Load

*Steady State Heat Loss vs Applied Power

	Power kW	Heat Loss (Exp.) kW	Heat Loss (Model) kW	Efficiency (Exp.) %
1699°C	28	18.0	19.0	64
2215°C	64	33.8	31.6	53
2810°C	115	66.1	68.5	58

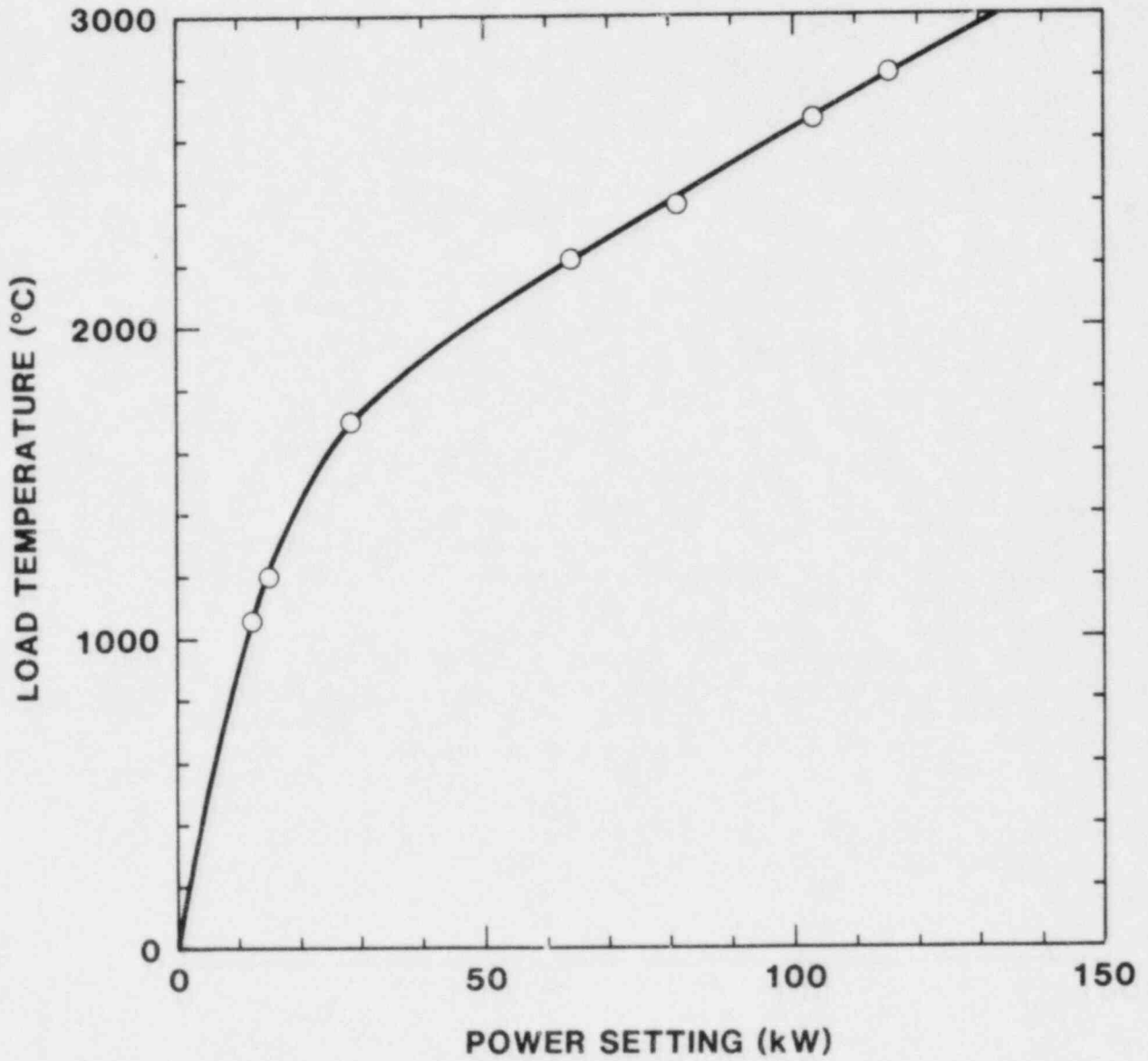


Figure 1.2-3. Steady-State Power vs Temperature

1.2.2.2 Test Charge

Production of the TiO_2 charge started at Los Alamos this quarter. The charges made thus far suffered cracks during cooldown. Initial investigation indicates that the cracks were caused by thermal stresses and the problem could be rectified by a powered cooldown to reduce the cooling rate. The last pressing was not severely cracked and was judged to be usable. It was banded together and machined for use in the experiment. One more cylinder and a hemisphere section have yet to be made. Los Alamos encountered some pressure fluctuations in the hydraulic ram of the sintering press. Work is underway to remedy the problem.

Sintering experiments were performed on pressed samples of TiO_2 charge with initial densities of 56.7 percent to 71.5 percent of theoretical density. The samples were heated and held at 1523 K (1250°C), 1673 K (1400°C) and 1873 K (1600°C) for 1 to 2 hours. The samples exposed to 1523 K and 1673 K showed no significant densification while samples exposed to 1873 K for 2 hr showed final densities varying from 84.2 percent to 87.6 percent. This variation is much smaller than the initial variations. In view of this information, the heating schedule (see following section) was designed to raise the temperature throughout the charge to at least 1873 K before the start of the melting plateau at 2273 K (2000°C).

Phase diagram work on the $\text{UO}_2/\text{Y}_2\text{O}_3$ charge was completed. The phase diagrams showed no minimum melting point, therefore the mixture will not be suitable for use. A new mixture of UO_2 and ZrO_2 (stabilized with Y_2O_3) will be used. Initial melting determinations have been made. Mixtures with a melting range of 2773 K to 2848 K (2500°C-2575°C) were found.

1.2.2.3 Thermal Analysis

The report on the CINDA thermal analysis of the crucible susceptor assembly was completed (K. H. Barhydt, Thermal Analysis of the Large Melt Furnace - Performance Evaluation of the Susceptor/Crucible Design, SAND81-1262). The transient program is used for formulating a heating schedule for the TiO_2 test. Figure 1.2-4 shows a typical result. The crucible is brought to 2073 K (1800°C) in 2 hr. and held there for 3 hr. to allow the interior of the charge to heat through. At the end of this 3-hr soaking period the crucible is ramped to 2273 K (2000°C) in

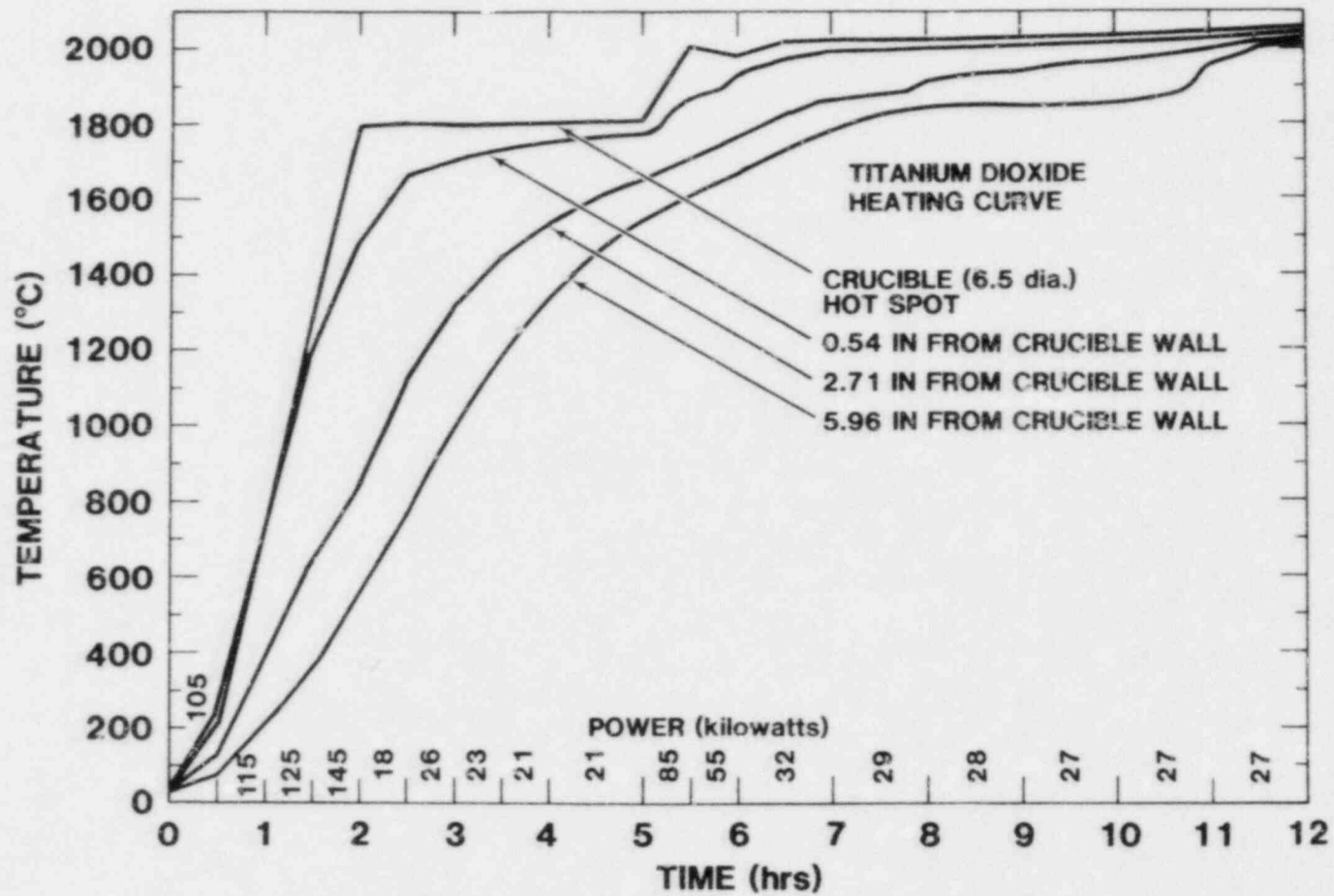


Figure 1.2-4. Typical Titanium Dioxide Heating Curve

0.5 hr. At this time the central region reached approximately 1873 K (1600°C). The crucible is then held at 2273 K (2000°C) until melting is completed. The melting temperature arrest at 2113 K (1840°C) is shown clearly in the figure. The particular heating schedule was conservative because convection enhancement was not induced in the calculation.

1.2.2.4 Instrumentation

Three ultrasonic thermometers (UT), each with 7 sensing segments, were designed and fabricated during this report period. One will be used to monitor the axial temperature profile in the susceptor. The other two will be used in the crucible. The sensors will be provided with tantalum sheaths and further protected by a tungsten-coated tantalum instrumentation well. The sensor is isolated (acoustically) from the sheath by a series of short thoria sleeves kept in place by pinches on the tantalum sheath. A thin coating of graphite is applied to the thoria sleeves. During heatup, the graphite and tantalum form a carbide diffusion barrier to prevent tantalum diffusion into the sensor. High-temperature conditioning and calibration of the sensors will be carried out in the next quarter.

1.2.3 Melt Seepage Through an Initially Dry Gravel Bed

1.2.3.1 Introduction

Thorium dioxide gravel has been proposed as a possible ex-vessel core-retention device. A ThO₂ gravel bed, saturated with primary-system coolant, could provide long term cooling of the fragmented core debris that falls upon the bed. A saturated gravel bed cannot be assured under all accident scenarios. As a result, melt seepage through an initially dry gravel bed is an issue which must be addressed in order to assess the acceptability of gravel beds as core retention devices.

The model developed below considers a time-dependent gravity head as the driving term for flow. The model also includes head losses resulting from laminar and turbulent flows. Capillary pressure can either augment or retard flow depending on whether the melt wets the gravel. Melt freezing within the gravel is not considered at this time. Geometry is presented in Figure 1.2-5 for the analysis which follows. Melt over the bed is always assumed.

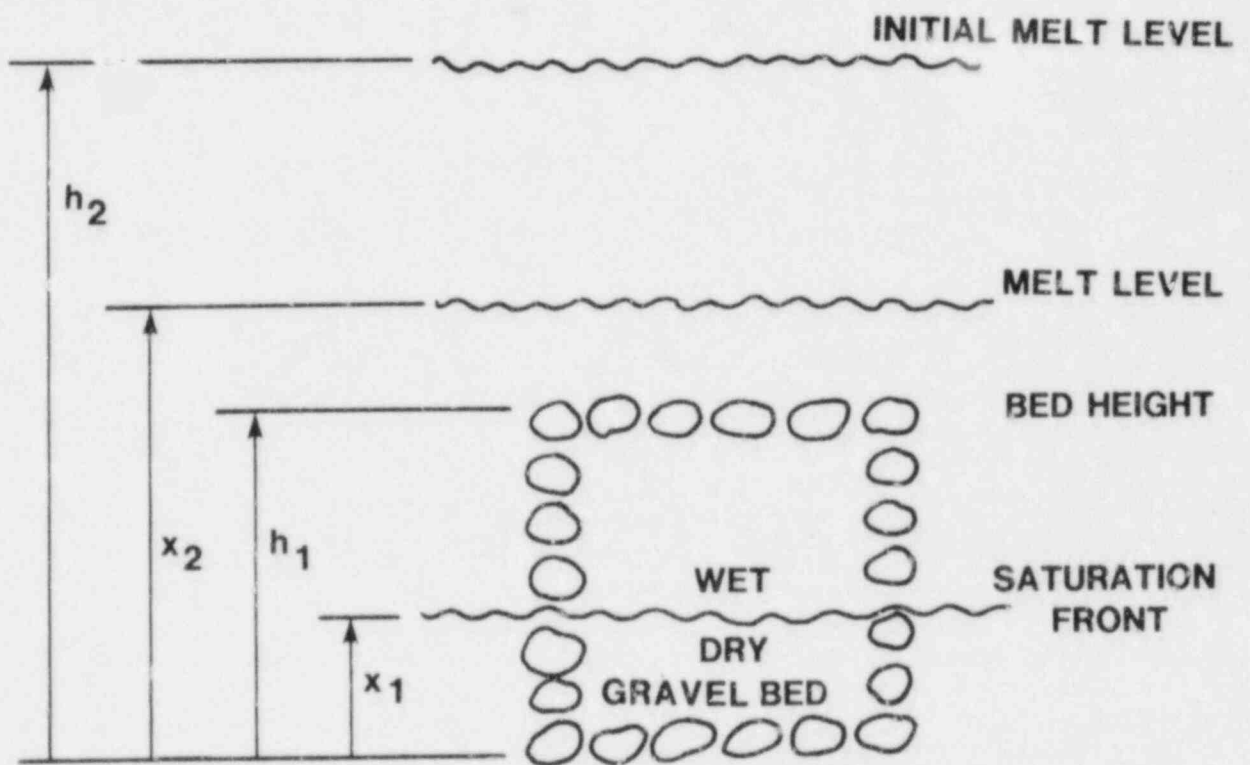


Figure 1.2-5. Melt Seepage Through an Initially Dry Gravel Bed

1.2.3.2 Model Development

The melt conservation equations for downward flow through a gravel bed are given below, assuming quasi-steady flow.

Momentum:

$$\frac{dp}{dx} = \frac{\mu v}{k} - \frac{\rho v^2}{\eta} + \rho g = 0 \quad (1.10)$$

Continuity:

$$\frac{d(\rho v)}{dx} = 0 \quad (1.11)$$

Here p is pressure; x is the elevation above the bed bottom; μ is dynamic viscosity; v is the melt velocity within the bed; k is the permeability; ρ is the melt density; η is the "passability"; and g is the gravitational acceleration.

Equation (1.10) is the Ergun¹⁻¹⁵ equation which varies smoothly from Darcy's Law (laminar flow) to the Burke-Plummer equation (turbulent flow) as k or η dominate. Continuity says that the instantaneous flow velocity is independent of position within the saturated zone of the bed.

The permeability and passability are given in Bird, Stewart, and Lightfoot.¹⁻¹⁵

$$k = \frac{D^2 \epsilon^2}{150(1 - \epsilon)^2} \quad (1.12)$$

$$\eta = \frac{D \epsilon}{1.75(1 - \epsilon)} \quad (1.13)$$

Here D is the particle diameter and ϵ is the bed porosity. Equation (1.12) is known as the Kozeny-Carmen relation.

The momentum equation can be integrated from a point just above the saturation front level (x_1) to just below the top of the gravel bed (h_1).

$$P(h_1^-) - P(x_1^+) + \frac{\mu v}{K}(h_1^- - x_1^+) - \frac{\rho v^2}{2}(h_1^- - x_1^+) + \rho g(h_1^- - x_1^+) = 0 \quad (1.14)$$

Bernoulli's equation can be applied to a unit cell above an average pore located on the upper gravel bed surface.

$$P(h_1^-) - P(x_2) + \rho \frac{v^2 - V^2}{2} + \rho g(h_1^- - x_2) = 0 \quad (1.15)$$

The flow velocity (V) above the bed is related to the flow velocity within the bed by continuity.

$$V = \epsilon v \quad (1.16)$$

The capillary pressure at the saturation front is given by Scheidegger.¹⁻¹⁶

$$P(x_1^+) - P(x_1^-) = \pm \frac{6\sigma(1 - \epsilon)}{\epsilon D} \quad (1.17)$$

Here σ is the surface tension; the upper sign is used if the melt does not wet the gravel while the lower sign is used if the melt does wet the gravel.

Combining equations (1.14-1.17) yields the following.

$$\frac{\rho v^2}{2} \left[1 + \frac{2}{1 - \epsilon^2} \frac{h_1 - x_1}{\eta} \right] - \frac{\mu(h_1 - x_1)}{k(1 - \epsilon^2)} v$$

$$= \frac{\rho g(h_2 - h_1)}{1 - \epsilon^2} + \frac{\rho g(1 - \epsilon)(h_1 - x_1)}{1 - \epsilon^2} + \frac{6\sigma(1 - \epsilon)}{D(1 - \epsilon^2)}$$

(1.18)

Here it is assumed that $P(x_1) = P(x_2)$. This implies that gas below the saturation front can easily escape.

The terms on the left hand side of Equation (1.18) represent head losses due to turbulent and laminar flow respectively. Gravity head is represented by the first two terms on the right hand side of Equation (1.18). Notice that the total gravity head increases as the melt seeps into the bed. Capillary pressure is represented by the third term on the right hand side of Equation (1.18).

As stated in the introduction, this analysis only applies when there is melt above the bed. Continuity yields the following condition for this analysis to apply:

$$x_1 \geq \frac{\epsilon h_1 - (h_2 - h_1)}{\epsilon} \quad (1.19)$$

It is useful to introduce the following dimensionless variables.

$$u = \frac{v}{v^*} = v \left(\frac{1 - \epsilon^2}{2g(h_2 - h_1)} \right)^{1/2} = \frac{dz}{dT} \quad (1.20)$$

$$z = \frac{h_1 - x_1}{h_2 - h_1} \quad (1.21)$$

$$T = t \frac{v^*}{h_2 - h_1} \quad (1.22)$$

Here v^* represents the initial drainage velocity into air from a reservoir open to the atmosphere; z represents the normalized penetration depth of the melt into the bed.

Normalizing Equation (1.18) yields the following.

$$\left(\frac{dz}{dT}\right)^2 \left[1 + R_2 z\right] + R_1 z \frac{dz}{dT} - (1 - \epsilon)z - 1 \pm R_3 = 0 \quad (1.23)$$

i.c. $z(0) = 0$

$$R_1 = \left\{ 4.5 \times 10^4 \frac{(1 - \epsilon)^4}{\epsilon^4 (1 - \epsilon^2)} \frac{\mu^2 (h_2 - h_1)}{\rho^2 g D^4} \right\}^{1/2} \quad (1.24)$$

$$R_2 = 3.5 \frac{1 - \epsilon}{\epsilon (1 - \epsilon^2)} \frac{h_2 - h_1}{D} \quad (1.25)$$

$$R_3 = \frac{6(1 - \epsilon)}{\epsilon} \frac{\sigma}{g(h_2 - h_1)D} \quad (1.26)$$

Here R_1 is the initial ratio of laminar head loss to gravity head; R_2 is the initial ratio of turbulent head loss to gravity head; and R_3 is the initial ratio of capillary pressure to gravity head. The upper sign is used in front of R_3 when the melt does not wet the gravel; the lower sign is used when the gravel is wet by the melt.

The grouping $1+R_3$ represents the initial normalized driving term for flow. Flow always occurs when the melt wets the gravel ($+R_3$). When the melt does not wet the gravel, flow will occur only if

$$1 - R_3 > 0 . \quad (1.27)$$

Substituting for R_3 , the minimum particle diameter for flow to occur can be written,

$$D_m > \frac{6(1 - \epsilon)}{\epsilon} \frac{\sigma}{\rho g(h_2 - h_1)} \quad (1.28)$$

This result can be obtained more directly by writing down the static force balance between gravity and surface tension forces at the bed surface.

1.2.3.3 Sample Calculation: Stainless Steel Melt Over a ThO₂ Gravel Bed

Equation (1.23) is a nonlinear ordinary differential equation describing melt seepage into a gravel bed in the absence of melt solidification. Equation (1.23) has been numerically integrated for the conditions of a proposed experiment in which an inductively heated stainless steel (nonwetting) melt will be poured onto ThO₂ gravel. Proposed test conditions are given in Table 1-V.

Table 1-VI lists the predicted bed-penetration times for several initial particle sizes. The minimum gravel size for flow to occur is 793 μm . Repeated integration of Equation (1.23) for various gravel sizes indicates that surface tension is a significant force retarding flow (non-wetting liquid) only when the gravel diameter is near the critical diameter for flow (Equation 1.28).

Table 1-V

Proposed Test Conditions
Stainless Steel Melt Over ThO₂ Gravel

$h_1 = .33$ m bed height
 $h_2 - h_1 = .176$ m initial melt height
 $\epsilon = .5$ bed porosity
 $\rho = 6785$ kg/m³ melt density
 $\mu = 4.6 \times 10^{-3}$ Pa-s melt viscosity
 $\sigma = 1.547$ N/m

Table 1-VI

Bed Penetration Times
for Proposed Test Conditions

<u>D(μm)</u>	<u>t(s)</u>
5000	1.6
1000	7.5
800	14.0
793	∞

1.3 PAHR Debris Bed

(J. E. Gronager, 4421; G. W. Mitchell, 4421;
C. A. Ottinger, 4421; K. R. Boldt, 4421;
R. J. Lipinski, 4425; M. Schwarz, 4425)

1.3.1 Introduction

The PAHR Debris Bed program addresses issues concerned with the formation of solid fuel debris and its collection on horizontal surfaces within the containment vessel. This debris remains capable of generating significant power through the decay of fission products. Should natural processes fail to provide sufficient cooling, the debris could remelt and threaten containment. The PAHR Debris Bed program seeks to determine the natural cooling of such debris. During this period, experiments and analysis of debris bed studies continued.

1.3.2 Debris Bed Experiment D5

Debris bed experiment D5 is the first experiment in which bed behavior at extended postdryout conditions will be investigated. The principal objectives are to observe bed behavior at elevated temperatures, to evaluate crucible design for future high temperature experiments, and to evaluate double containment concepts for D-series experiments.

During this quarter, the D5 hardware fabrication was completed and assembly began. Program personnel have completed the assembly of all internal components of the primary container (thermocouples, displacement tube and crucible).

A charge of 4.89 kg of UO_2 was loaded into the crucible. Final procedure checks were made, followed by final assembly of the primary containment vessel.

After closure of the primary containment vessel, the sealing structural weld between the cover plate and the vessel was made. When the weld was x-rayed, a small defect was found and repaired.

Toward the end of June, investigators loaded the D5 primary containment vessel with 4.09 kg of liquid sodium. X-ray inspection of the sodium level within the vessel assisted investigators in identifying a procedural error

which allowed liquid sodium to be injected into the internal displacement tube. Once the liquid sodium enters the displacement tube the possibility exists that the internal insulation (Zirconia) of the crucible would be exposed to liquid sodium. X-rays of the crucible proved to be of little use in confirming or denying this possibility. Sodium within the crucible insulation will result in loss of the insulation's thermal properties as well as constituting operational difficulties. Thus, the vessel must be opened to inspect and correct conditions within the displacement tube and crucible.

1.3.3 Debris Bed Experiments D7 and D8

Debris bed experiment D7 will investigate the coolability of a shallow stratified bed. Specifically, the experiment will attempt to determine the ability of such a bed to transition to channeled bed behavior. Such a transition would be expected to increase greatly the potential coolability of stratified beds. The D8 experiment will determine the coolability of a stratified bed with an extended particle size distribution to determine the effects of such a distribution.

1.3.3.1 Design Activities

The design of the D7 and D8 experiments continued during this quarter. Based on the braze testing, heat exchanger Out-of-Pile Systems Test (OPST), and prototype closure fabrication described in the previous quarterly, a preliminary design was prepared in April by the experiment team. This design incorporates numerous improvements over previous debris bed experiments; these improvements address safety issues as well as simplicity and ease of assembly.

The debris bed is held in an insulated crucible fabricated of Inconel 617 and stainless steel with a Min-K thermal insulation (Figure 1.3-1). This crucible and other design features, should reduce heat losses in the downward and radial directions to less than 50 W (0.3 percent of D7 maximum expected bed power of 16 kW). The temperature of the sodium surrounding the crucible will be measured during the experiment to help quantify the losses.

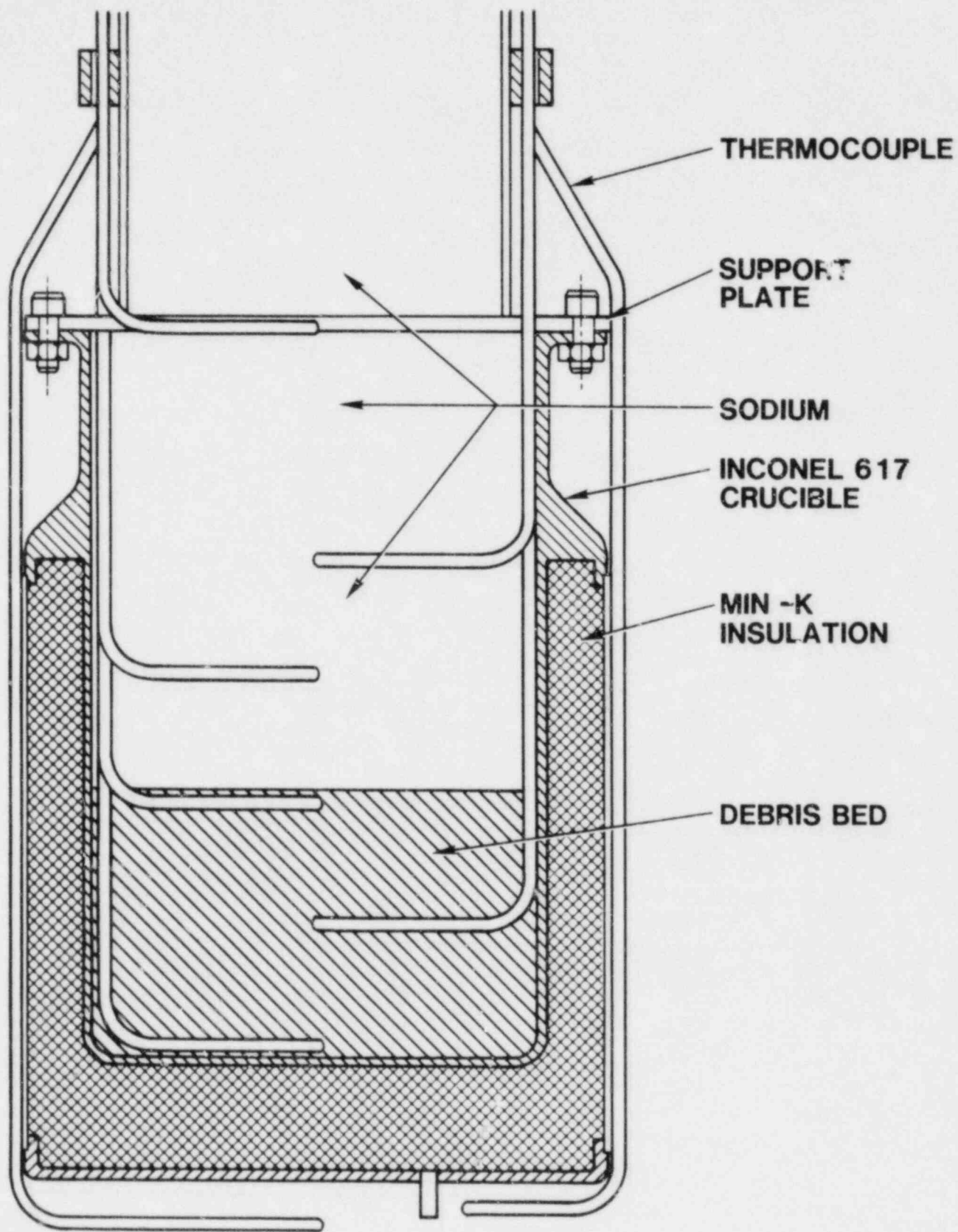


Figure 1.3-1. D7/D8 Crucible

The radiological containment for the D7 and D8 experiments features two independent barriers, a minimum number of mechanical seals, and a simplicity of design which should reduce assembly difficulties (Figure 1.3-2). The primary containment consists of a cover plate through which all instrumentation penetrates and from which the crucible containing the debris bed is suspended. This allows installation and positioning of all bed thermocouples which are then brazed in place, eliminating numerous Swageloks. The debris bed is then formed in the crucible and the cylindrical containment shell is threaded into position. A final seal weld is performed at the top of the containment.

The secondary containment is similar in concept to the primary containment. The cover plate contains all instrumentation penetrations in the form of Sandia-developed electrical feedthroughs. The cover plate is positioned and welded in place after all electrical connections have been made and the B_4C neutron filter has been loaded between the containment walls.

A vacuum tank attached to the primary containment vessel with a single operation valve is included in the D7 and D8 design. This tank is intended to allow the experimenter to reduce the pressure in the primary vessel during experiment operation, thereby extending the range of subcooling which can be investigated in a single experiment. This feature, together with a maximum expected bulk-sodium temperature capability of 973 K (700°C), should allow investigation of a 300 K range of subcooling.

The operational aspects of the safety instrumentation for the D7 and D8 experiments are yet to be fully resolved. However, since the transducers are long-lead-time items, they were ordered in April with an expected delivery in September. The design specifications of the pressure transducers ordered for the experiment would not support their use in a hard wired automatic scram if the transducers, as received, perform at the limit of the specifications. However, the performance of the transducers used in past experiments has varied considerably and may fall in a range which would allow their use in the "as-received" condition. If not, perhaps some form of temperature compensation can be performed which would meet the safety requirements.

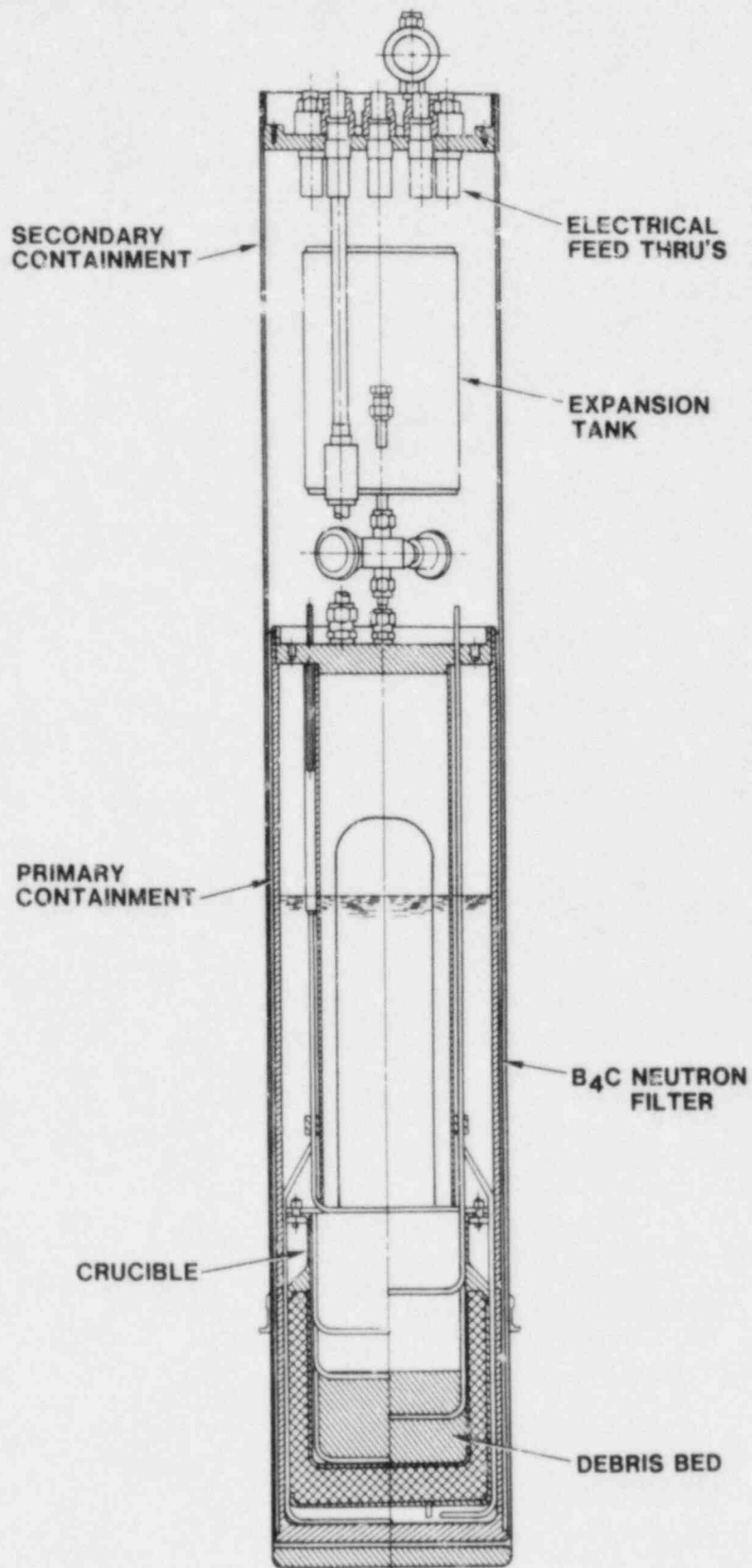


Figure 1.3-2. Illustration of Design Simplicity in the D7 and D8 Experiment

1.3.3.2 Fabrication Activities

Preparation of the D7 and D8 design for fabrication has been significantly affected by two events: implementation of Sandia's Advanced Reactor Research Department (Organization 4420) quality assurance program for reactor experiments and the appointment of a project fabrication coordinator in the shops. While these events have caused some delay in the initiation of experiment fabrication, they should improve both the quality and the timeliness of fabrication activities.

Although the 4420 quality assurance program is not yet formally implemented, the D7 and D8 experiments are attempting to follow the program as it currently exists. The program requires preparation of an experiment quality assurance plan, which includes identification of critical components and close control of fabrication and assembly processes.

The fabrication coordinator has served as the single point of contact between the shops and 4420 design personnel. In May and June, the D7/D8 design was reviewed with particular attention to fabrication processes. Numerous suggestions for design change and process control are being incorporated in a revised set of design drawings.

1.3.4 Debris Bed Experiment D9

D9 is the first debris bed experiment to be cooled from both top and bottom. The objective is to develop data for use in comparing the coolability of debris beds cooled simultaneously from top and bottom to that of top cooling alone.

The OPST for demonstrating bottom cooling for in-pile experiments was completed in April. Analysis of the experiment data showed an effective heat transfer coefficient (h_{eff}) varying from 300-700 W/m²-K for a helium mass flow of 7-90 kg/hr.

With the above data applied to a practical and conservative design for D9, the overall k_{eff} for the bottom plates may be somewhat less (~300-400 W/m-K). This indicates that the bottom finned plate will provide adequate heat removal for investigating typical engineering designs (as Sandia personnel understand them) of SNR300 and Super Phenix. In order to investigate the

full range of bottom-cooled debris-bed phenomena, the k_{eff} of the finned plate would need to be increased. This could be done by upgrading the helium loop to provide larger flow rates, and/or by using different materials; such as copper, for the finned plate.

By selecting other materials, calculations show that h_T can be improved greatly using

$$\psi_m = h_{T_m} h_{T_{SS304}}$$

where ψ_m for SS304, Cu, Ni and Fe are respectively 1, 1.54, 1.43 and 1.38. Hence, a copper plate of similar design will yield a h_T of 1078 W/m²-K.

Another factor being investigated for its potential to improve h_T is increasing the number and height of the fins. By increasing the number of fins from 24 to 48 and the height from 1.5 cm to 3.8 cm, a copper fin plate may yield a h_T of approximately 3700 W/m²-K.

Presently, a new fin plate is being fabricated to investigate the above calculations.

1.3.5 Debris Bed Analysis/Modeling

Analysis of the recent D6 debris bed experiment was completed. The analysis may be divided into preboiling, boiling, flashing disturbance and dryout.

1.3.5.1 Preboiling

The thermocouple data for the nonboiling control runs (CR1 and CR2) accomplished during the experiment were compared with a one-dimensional numerical conduction model, using temperature-dependent thermal conductivities calculated by means of the Kampf-Karsten relation.¹⁻¹⁷ The bed-to-bulk-sodium heat transfer was calculated using the usual MacDonald-Connolly correlation,¹⁻¹⁸ the bottom of the bed was assumed to be perfectly insulated, and radial heat losses were modeled by a one-dimensional sink:

$$S_r = -2h(T - T_0)/R \quad (1.29)$$

where h is the radial heat transfer coefficient through the insulation (about $2.2 \text{ W/m}^\circ\text{C}$), T is the bed temperature, T_o is the outer boundary temperature (the temperature of the B_4C filter measured by thermocouples I5 and I6) and R is the bed radius.

The analysis of control run 1 indicates that heat removal across most of the bed may be modeled by conduction (see Figure 1.3-3) and that agreement with the Kampf-Karsten model is within + 10 percent. The analysis of control run 2 has shown that following a prolonged period of boiling, the lower region of the bed (Region 1) was 22 percent more conductive. The enhancement could be related to the action of the boiling which may have redistributed UO_2 particles in the bed which remained after rewetting, thus making the sodium distribution anisotropic. Evidences of liquid channels were found in D4 at the end of the experiment.¹⁻¹⁹

The control-run analysis shows that preboiling heat transfer in D6 was by conduction alone. In contrast, single-phase convection occurred in the similar, but unstratified, D2 experiment. To compare stratified and mixed particle beds, the average permeability for multi-layer beds must be defined. One possible way is by adding the resistance of each layer in series and averaging the result over the total bed thickness. This results in an average permeability:

$$\bar{k} = \frac{H}{\sum_i \frac{e_i}{k_i}} \quad (1.30)$$

where H is the bed height, e_i and k_i the layer thickness and permeability, respectively. The permeability for a layer with angular shaped particles is¹⁻²⁰

$$k_i = \frac{1}{247} \frac{\epsilon_i^3}{(1 - \epsilon_i)^2} \bar{d}_i^2 \quad (1.31)$$

where \bar{d}_i is the average particle diameter in the layer.

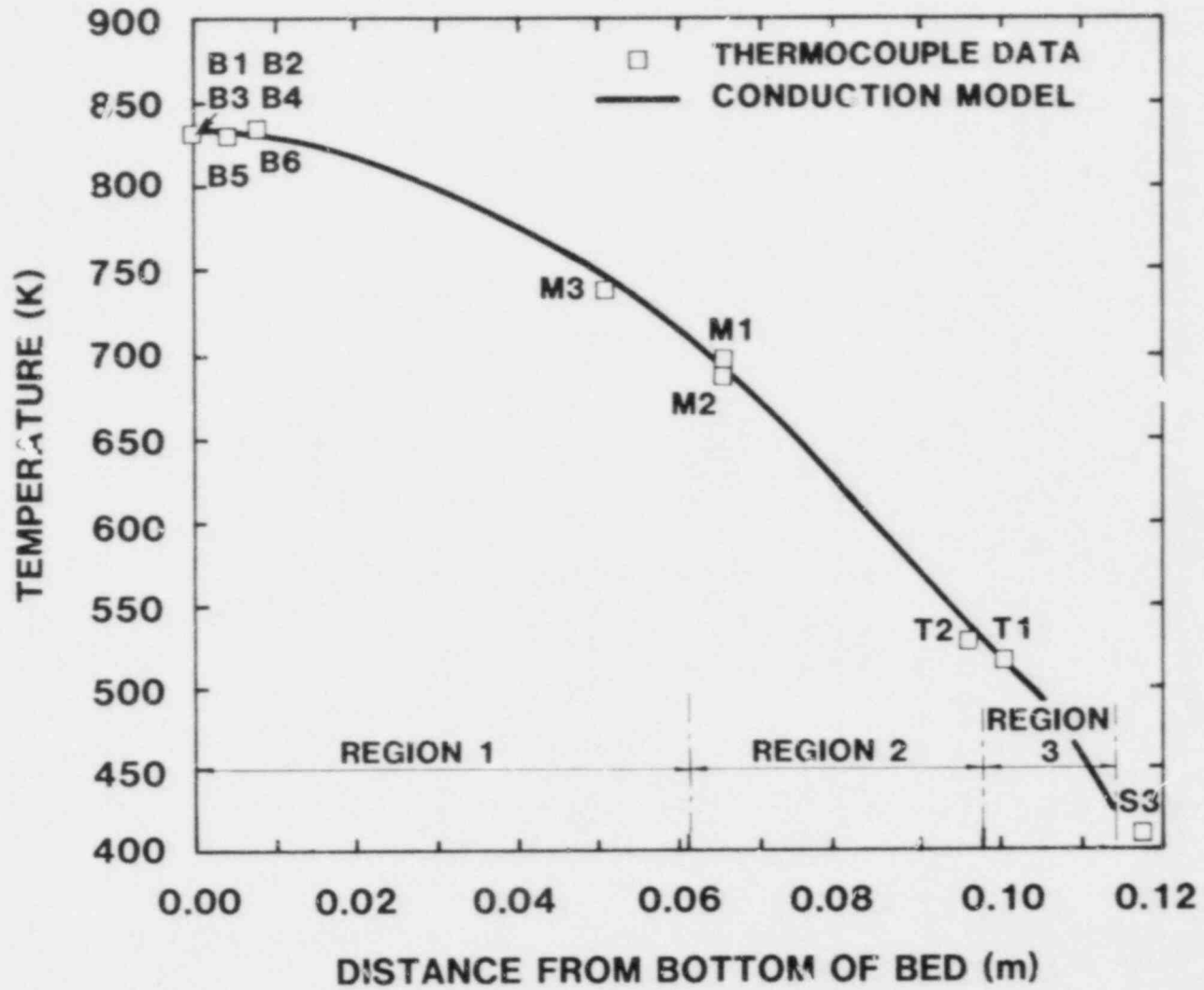


Figure 1.3-3. Temperature in the D6 Bed Before Boiling

Using Equation (1.31) and the D6 particle distribution, the average permeability is $9.94 \times 10^{-12} \text{ m}^2$. The internal Rayleigh numbers corresponding to control runs 1 and 2 are respectively 2.4 and 2.5. For such numbers, single phase convection enhances the heat removal by 50 percent in a uniformly mixed bed having the same overall particle distribution as D6. The lack of convection in D6 compared with D2 indicates that stratifying a uniform bed suppresses convection. The disagreement with previous correlations indicates that the suppression is even more than would be predicted by using a "stratified permeability" defined by Equation (1.30).

1.3.5.2 Boiling

When boiling begins, the heat removal across the overlying subcooled region of the bed becomes more complicated. Analysis of the previous D-series experiments has shown that in a boiling sodium particle bed with subcooled overlying sodium, heat removal can be approximated by the series conduction model.^{1-19,1-21} In this model, the vapor generated in the boiling zone is assumed to condense at the base of an overlying subcooled zone. An alternate model is the parallel conduction model in which the vapor is assumed to penetrate entirely the subcooled zone.

The differences between calculated and measured temperatures are compared in Figure 1.3-4 for five subcoolings (490°C, 445°C, 490°C, 360°C, and 320°C). The data agree well with the series conduction model in all cases, suggesting that sodium vapor does not penetrate deeply into the subcooled zone for the range of subcooling investigated (320°C-490°C).

1.3.5.3 Flash Disturbance

After the dryout investigation at 873 K (600°C) bulk temperature, the temperature at the bottom of the bed dropped 34°C below the saturation temperature. Upon reheating, a superheating of 45°C was observed. The flashing of the superheated liquid resulted in a gross bed disturbance, identical to those experienced by the D2 and D4 beds.^{1-19,1-21} The temperature traces recorded by the bed thermocouples at that time with a one-second time resolution are presented in Figure 1.3-5.

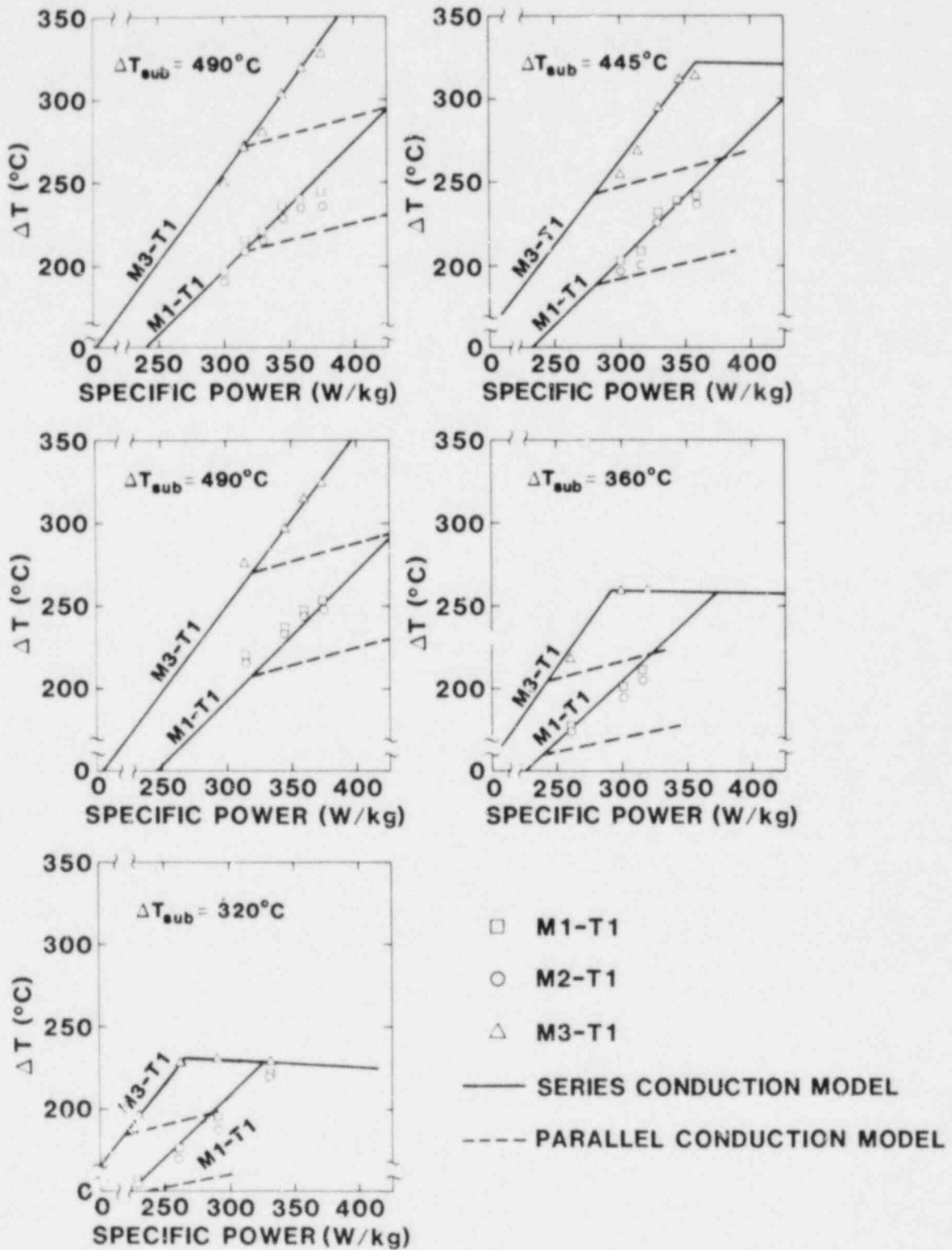


Figure 1.3-4. D6 Boiling Data Compared with Series and Parallel Conduction Models

1-63

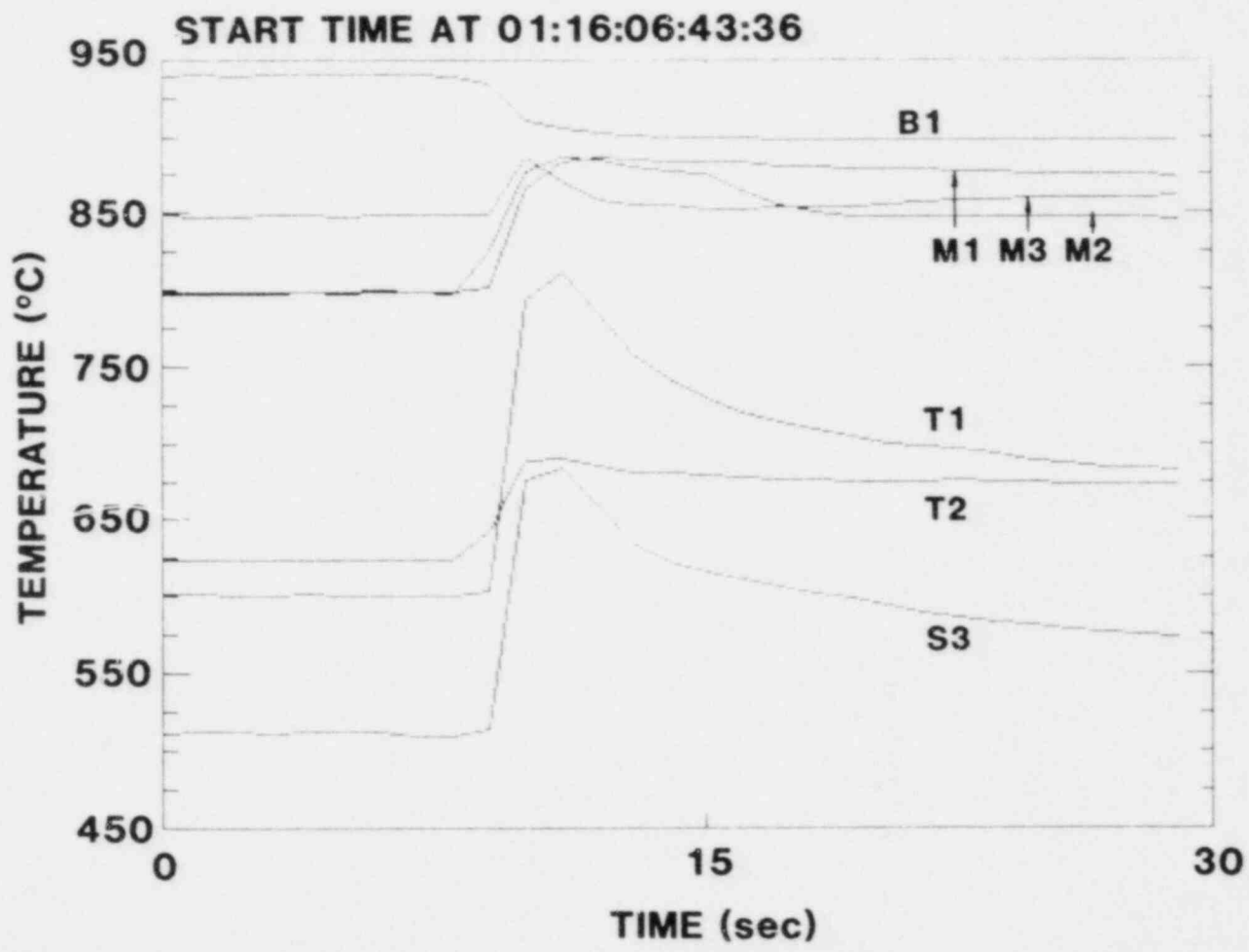


Figure 1.3-5. Bed Temperature During the First Flashing Experiment

The bed bottom temperature is observed to drop rapidly and all other temperatures to rise rapidly at the same time. This most likely results from the passage of large amounts of sodium vapor, but may also be caused partly by the expulsion of hot liquid sodium from the bed bottom or even some levitation of the entire bed. Most of the temperatures decreased to new steady-state values higher than before the disturbance. This suggests that the bed was permanently and fairly uniformly expanded by the event. Thermal analysis of the bed's state after disturbance indicates that the bed thickness was increased by 6 mm.

Another disturbance occurred just before the last dryout. The bed bottom temperatures fell 9°C below saturation, and upon reheating, 7°C of superheat was achieved. Thus, the event was very small.

The amount of liquid superheat expected after a first boiling cycle and a cooling phase may be estimated using the conical cavity model previously developed by Schwarz and presented in Reference 1-19. The amount of superheat depends on the pressure-temperature history of the particles:

$$\Delta T \approx \frac{R_g T_s^2 \sigma}{h_{fg} M \sigma_m} \frac{P_{lm} - P_{sm}}{P_1} \quad (1.32)$$

where R_g is the gas constant, T_s the saturation temperature in K, σ the surface tension at saturation temperature, h_{fg} the latent heat of vaporization, M the molar mass, P_1 the liquid pressure at the time of flashing, determined from the saturation temperature, P_{lm} the liquid pressure and P_{sm} the saturation pressure at the time of minimum liquid temperature at the bottom of the bed. Since experiment pressure is not greatly affected by small local changes in bed temperature, $P_{lm} \approx P_1$.

Equation (1.32) predicts a superheat of 33°C for the first disturbance with:

$$T_s = 1175^\circ\text{K}, P_{lm} \cong P_1 = 1.217 \times 10^5 \text{N/m}^2 \quad (1.33)$$

and

$$P_{sm} = .989 \times 10^5 \text{N/m}^2. \quad (1.34)$$

The measured superheat was 45°C.

Upon cooling of the bed after a new boiling and dryout cycle, the liquid will penetrate the cavities until the interface reaches a nonwetting condition. This should occur at the same radius at which the liquid had previously penetrated the cavity and therefore the same amount of superheat may be expected upon the next heating.

However, for the second disturbance the bottom temperature dropped by only 9°C below the saturation temperature and the observed amount of superheat was 7°C. This is in contradiction with the previous theory. If it was the first time the bed was rewetted, Equation (1.32) would have predicted a superheat of 10°C which is close to the value observed. This suggests the possibility that the wetting layer created during the first rewetting might have disappeared during the 6 hours the bottom of the bed was boiling and dried out.

1.3.5.4 Dryout

The dryout powers for D6 as a function of subcooling are given in Table 1-VII. The boiling zone thicknesses at dryout, determined by the series conduction model fit to the middle and top thermocouples are also shown in Table 1-VIII as well as the heat flux at the top of the boiling zone.

The boiling zone dryout fluxes are plotted vs. boiling zone thickness in Figure 1.3-6. The predisturbance points are fairly consistent and show no obvious zone-thickness dependence and an average dryout flux of 85 kW/m². The top of the boiling zone seems to be consistently limited to the third bed layer (between 41 and 61 mm above the bed bottom).

Figure 1.3-6 shows that the dryout fluxes after disturbance are also consistent, except for dryout 10. Excluding dryout 10, no zone-thickness dependence is apparent, and the average dryout flux is 108 kW/m². This is 27% higher than the average before disturbance. This increase may be attributable to an increase in bed porosity caused by the flashing disturbance.

Table VII. Specific Powers and Boiling Zone Heat Fluxes at Dryout

Dryout Number	T _{bulk}	T _{sat}	Subcooling	Dryout Power (+ 8%) (- 8%)	Boiling Zones Thickness	Heat Flux From Boiling Zone
	(°C)	(°C)	(C°)	(W/kg)	(mm)	(kW/m ²)

Pre-Disturbance:

2	402	888	486	360	41	82
3	440	893	453	345	44	85
4	402	888	486	375	43	90
5	491	901	410	330	46	83
6	547	909	362	300	51	84
7	590	915	325	285	57	89

Post-Disturbance:

9	392	885	493	445	44	109
10	494	902	408	375	40	83
11	547	911	364	360	57	112
12	583	918	335	315	61	104

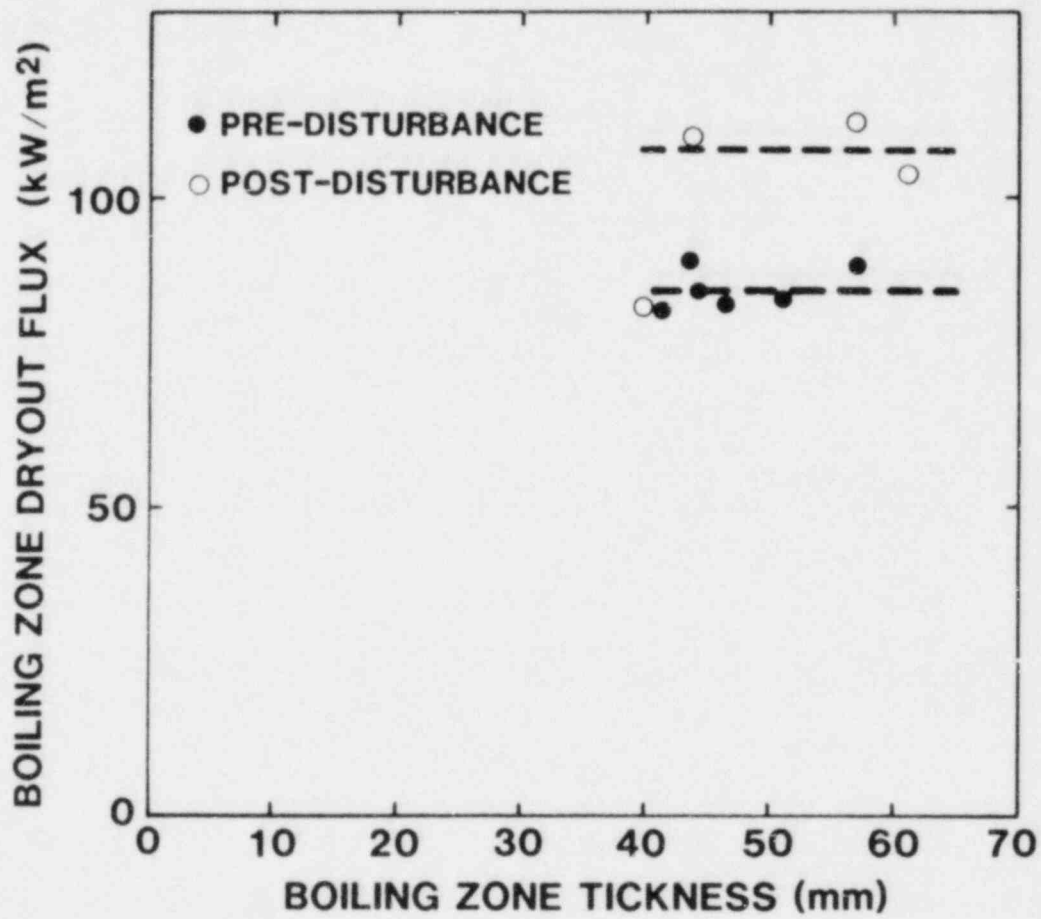


Figure 1.3-6. Heat Flux from Boiling Zone vs Boiling Zone Thickness at Dryout as Subcooling is Varied

The dryout fluxes both before and after the disturbance are fairly low and indicate that the bed is not channeled. An important finding of the D2 and D4 experiments^{1-19,1-21} was that the dryout flux in a bed can change considerably as conditions in the experiment change. In the D2 experiment, the dryout power ranged from 760 W/kg to more than 1270 W/kg; in D4 the dryout power ranged from 426 W/kg to 1970 W/kg. The D4 analysis¹⁻¹⁹ proposed that these large changes in dryout power were caused by a change in the bed state from packed to channeled.

The D6 subcooling range was chosen to be identical with the D2 range so that a clear test of channeling dependence on stratification could be made.

Under conditions very similar to those which allowed channeling in D2, channeling in D6 did not occur. Thus stratification seems to suppress channeling in subcooled beds. The most likely reason is the very low power at which dryout occurs in a stratified bed. This allows thick subcooled zones which prevent vapor channel formation.

The observed dryout powers may be compared with the predictions of the one-dimensional model of Reference 1-22. The model predicts that dryout in a stratified bed should be reduced because capillary forces would tend to keep the liquid near the small particles at the top of the boiling zone. The predicted dryout fluxes for the boiling zone are about 6-times the measured values using the model as published.

Reference 1-23 contains the suggestion that the relative permeability term in the model ($K_V = 1-1.11s$, where s is the saturation) be replaced by a more analytically based and experimentally verified one developed by Corey:¹⁻²⁴ $K_V = (1-s)$. Another important term in the one-dimensional model is the Leverett function, which relates the capillary force with saturation. Reference 1-22 uses a very crude linear function. A better fit to available data is

$$J = \frac{1}{\sqrt{5}} \left(\frac{1-s}{s} \right)^{0.175} \quad (1.35)$$

(This is a modification of a form suggested by Brooks and Corey.)¹⁻²⁴ Another consideration is that in the D6 test, the porosity in each layer was measured to increase slightly, on the average, with elevation. This increase

would tend to compensate for the smaller particles being at the top of the boiling zone. However, the measured porosities are subject to considerable error and the possibility exists that the porosity was reasonably constant throughout the bed. Even if the porosity were measured accurately, the boiling zone porosity may have been made uniform by the boiling agitation.

Modifying the one-dimensional model¹⁻²² with the suggestion described above, and assuming a constant porosity of 0.471 (bed average) in the boiling zone the resulting predicted dryout powers are in better agreement with the data, as Figure 1.3-7 shows. The drop near 41 mm is due to the change in particle diameter at that elevation.

The final dryout (no. 13) was initiated by a step increase in power from 375 W/kg to 690 W/kg. This procedure was in contrast to the small step increases in dryouts 1 through 12. Those dryouts were intended to investigate the steady-state incipient dryout behavior. Dryout 13 was conducted to simulate more closely the heatup of a debris bed under accident conditions in which the bed forms more rapidly than it heats up and the decay power is established at a high level. Investigators also speculated that a large power step might induce channeling by reducing the subcooled zone before dryout could occur. The power in dryout 13 was changed from 15 percent below the dryout power to about 60 percent above the dryout power.

The bed temperature history for dryout 13 is shown in Figure 1.3-8 along with the power and capsule pressure history. 103 seconds after the power increase the bottom of the bed indicated dryout as evidenced by a rapid increase of the bed bottom temperatures. When the reactor power was reduced (first from 690 W/kg to 390 W/kg and then to zero following the containment pressure increase) all temperatures declined.

The initial slope of the M1 temperature indicates that M1 was being heated by hot sodium being pushed past it from below by an expanding boiling zone at the bed bottom. When the bed bottom dried out, the midbed temperature at M2 fell slightly below saturation. This was caused by a reduction in heat being delivered to the base of the subcooled zone because the power in the dry zone was diverted into raising the dry zone temperature.

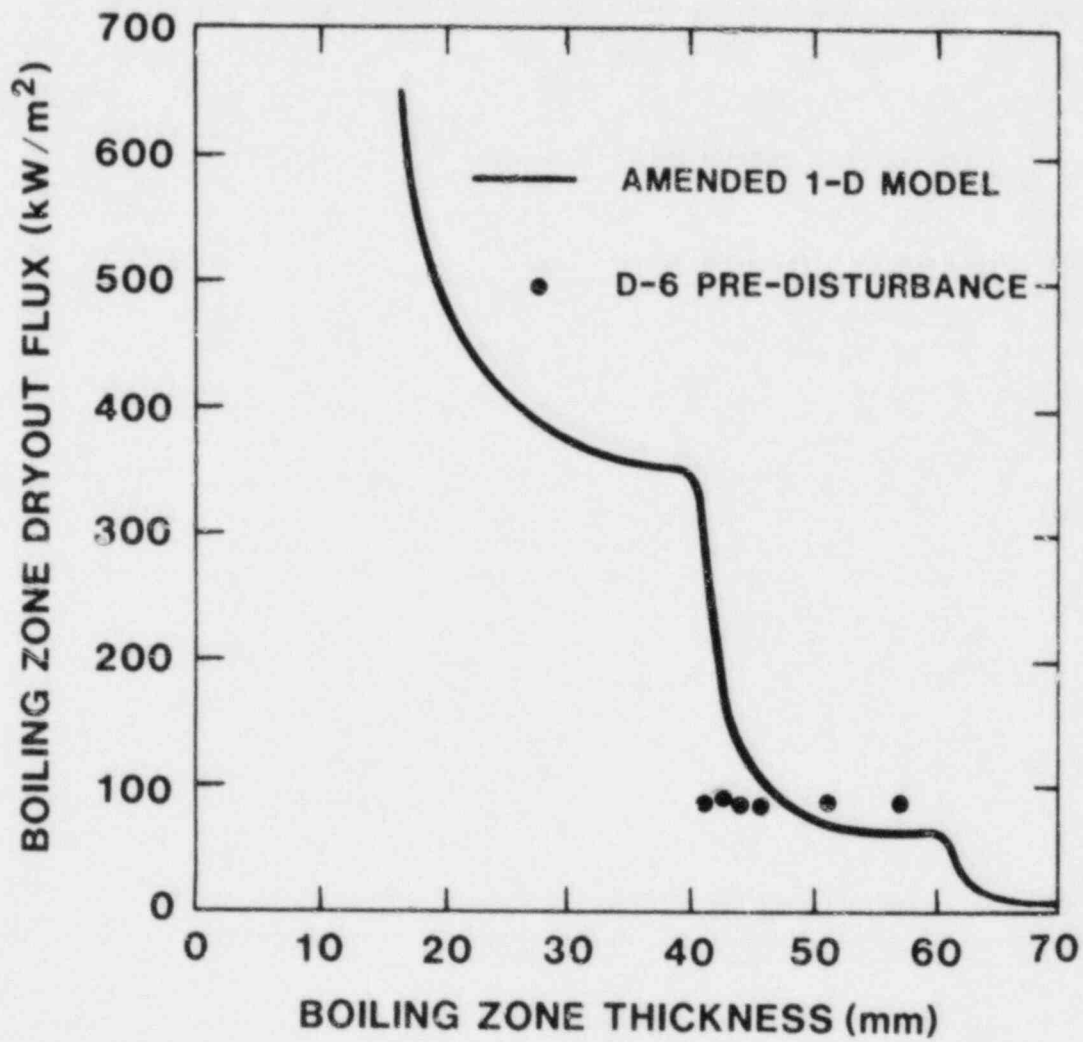


Figure 1.3-7. Predicted and Measured Boiling Zone Heat Fluxes at Dryout

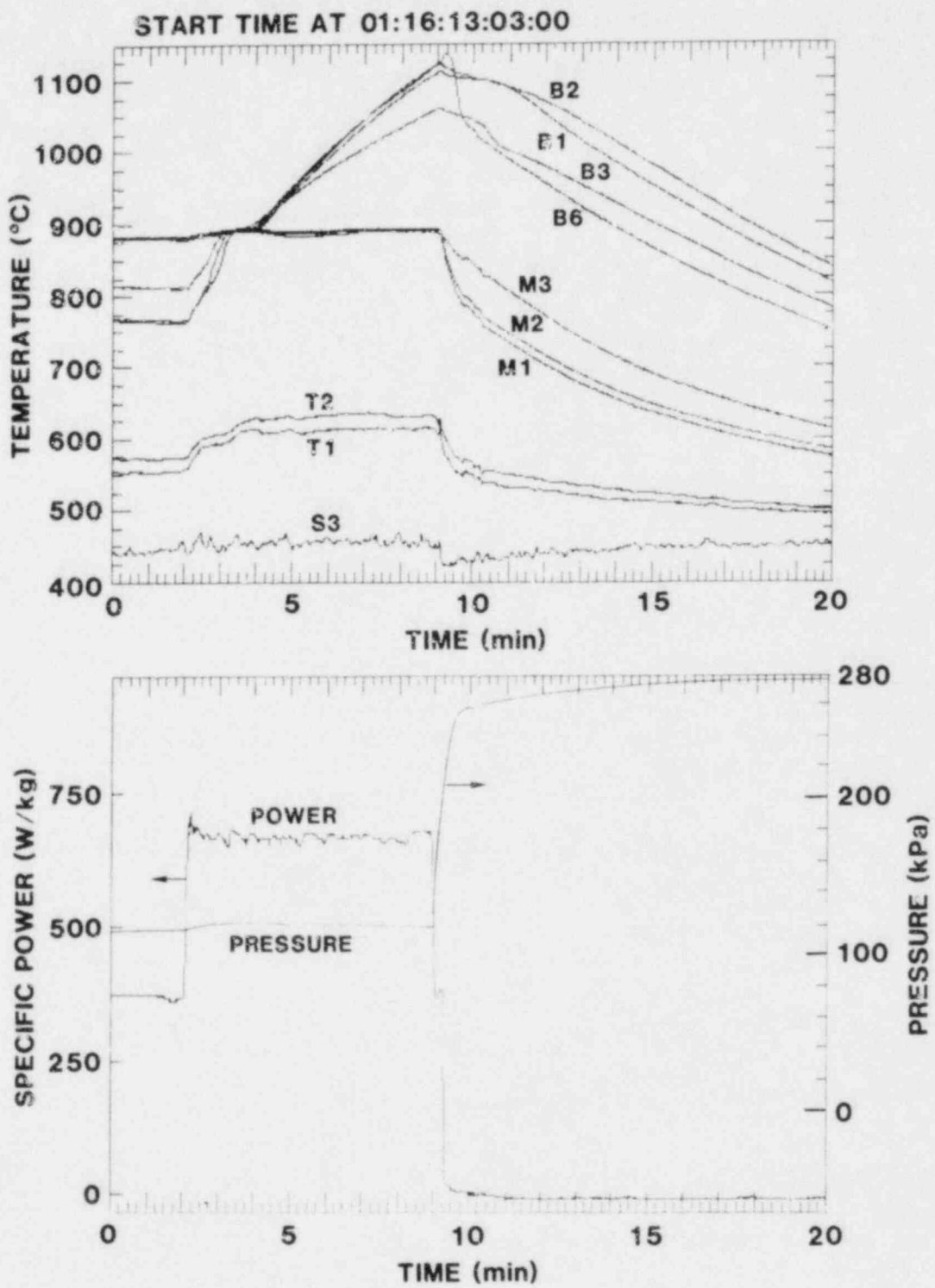


Figure 1.3-8. Bed Temperatures, Power, and Pressure During the Final Dryout

An important question concerning dryouts resulting from large power changes relates to the bed conditions at the start of dryout and the start of melt. In particular, a large power may be able to decrease the subcooled-zone thickness enough to allow channel penetration before a dry zone can be established or before a dry zone can heat to the melting point of UO_2 . Dryout 13 has shown that the subcooled-zone thickness at the start of dryout (or start of melt) is a very complicated function of initial conditions, coolant movement, the heating process, and the dryout criterion. Thus the subsequent prediction of whether channel penetration will occur before fuel melt is very difficult. Since a large-step power increase is similar to bed heatup conditions in an LMFBR, a suitable model for its bed behavior under these conditions may be important and needs development.

1.3.5 Summary

The D6 experiment was the first in the D-series to investigate the coolability of a debris bed of UO_2 particles in sodium; these particles are stratified by size, monotonically increasing with elevation. All aspects of the experiment except stratification were retained as identical to the previously accomplished D2 experiment to allow a clear comparison of the effects of particle stratification.

Single-phase convection before boiling did not occur in the D6 test even though it did occur in the D2 test. This suppression of convection may be due to the top layer of small particles restricting flow from the bed into the overlying pool. Prior to boiling, heat removal was by conduction with the bed conductivity agreeing well with the Kampf-Karsten formula. With boiling present, heat removal was found to be modeled well by the series conduction model in which the vapor from the boiling zone is assumed to be condensed at the base of an overlying subcooled zone in the bed.

Two flashing disturbances occurred which were similar to those observed in D2 and D4. The amount of superheat observed before flashing was in fair agreement with Schwarz's flashing model but the cavities on the UO_2 particles must also be assumed to become non-wetted during the boiling or dryout process. After the disturbance, the bed height was permanently increased by 6 mm.

Before the flashing disturbance, the dryout power in the D6 test ranged from 285 W/kg to 375 W/kg as the subcooling ranged from 325°C to 486°C. After the disturbance, the dryout power ranged from 315 W/kg to 445 W/kg as the subcooling ranged from 335°C to 493°C. The 11- to 19-% increase in dryout power is the result of loosening and expanding of the bed by the liquid superheat disturbance.

In all cases the dryout power was less than the dryout power of 760 W/kg observed in the D2 experiment. This reduction results from a combination of suppressed single-phase convection and reduced heat transfer efficiency in the boiling zone both caused by stratification. Modification of the Lipinski one-dimensional dryout model for packed beds yields fair agreement with the dryout data.

Because of the low dryout powers and agreement with a packed-bed model, program personnel infer that channeling did not occur in the D6 bed. This is in contrast to the D2 test in which channeling did occur (by inference), even though D6 spanned the same subcooling range and underwent a larger flashing disturbance than did D2. The reason for the failure to channel before dryout is believed to be the low dryout power, which resulted in very thick (54-74 mm) subcooled zones at dryout.

1.3.6 Light Water Reactor (LWR) Degraded-Core Coolability

1.3.6.1 Introduction

Sandia National Laboratories has initiated a program to determine the coolability of LWR degraded cores. This program is an extension of the Sandia PAHR experiments which are currently addressing the coolability of postulated LMFBR degraded cores. In a manner similar to the PAHR program, the LWR degraded core coolability studies are emphasizing in-pile experiments in the ACRR using fission heating of urania to simulate the decay heat expected following a core disruptive accident. The scope of the LWR degraded core coolability studies during the remainder of FY81 encompasses the following:

- a. Identify the governing phenomenological uncertainties and evaluate their impact on present analytical models.
- b. Formulate an experimental matrix to resolve these uncertainties.
- c. Determine the feasibility of performing in-pile experiments in the central irradiation cavity of the ACRR.
- d. Design the experiment package and accessories necessary to perform the experiment.

During this quarter, a survey of current coolability programs, experimental results and existing analytical models was performed. This survey revealed that the following phenomenological uncertainties exist that govern the determination of coolability for a postulated LWR degraded core:

- a. Particle Size -- Debris generated early in the accident sequence prior to melt of the fuel consists of rubblized, fractured and/or desintered fuel pellets with particle diameters on the order of millimeters. Debris generated following dispersal of molten fuel is much finer with average particle diameters on the order of tenths to hundredths of a millimeter. For water-starved steam explosions, there is the possibility of a bimodal particle size distribution consisting of coarse (~mm) rubble with finer particles (~0.01 mm) interspersed.
- b. Bed Depth -- Deep beds up to 2+ meters are possible in LWR's.
- c. Pressure Effects -- Depending on the reactor (BWR or PWR) and the type of accident (LOCA, LOHSA, SMBLA, etc.), the pressure in the primary containment can be between 1 and 170 atmospheres.
- d. Stratification -- Settling of debris following an energetic dispersal can result in a bed with larger particles on bottom and finer particles on top.

- e. Core Structural Materials -- Core structural materials (Zr, stainless steel, etc.) will be mixed in the bed either as eutectics or separate particles. This will affect particle diameters, bed power density and material interactions.
- f. Bottom Bed -- Debris beds formed on porous structures (reactor grid plate and support plate) have the potential of a natural or forced convection loop supplying water to the bottom of the bed.
- g. Distorted Pin Bundle -- Requenching an uncovered portion of the core prior to melt of the fuel can lead to a distorted pin bundle with debris interspersed in coolant channels. The resultant geometry may be analytically treated as a "debris bed" with some modification of bed parameters (e.g., particle diameter, permeability, porosity).

This list is not intended to be complete; additional phenomenological uncertainties may be identified in early scoping experiments.

Table 1-VIII gives a preliminary experiment matrix for Sandia's LWR Degraded Core Coolability Experiment Program. In total, 8 experiments are tentatively planned. The objective of each experiment will be to identify and investigate separately one of the governing phenomenological uncertainties. The fuel in all experiments is expected to be 3-%-enriched UO_2 with a bed diameter of 10 cm. The bed height is variable with most experiments having 50-cm depth (the effective irradiation height of the ACRR). In each experiment dryout and postdryout behavior will be investigated as a function of pressure, which is variable from 1 to 170 atmospheres. Bed power is adjustable up to 1.5 W/g UO_2 . This power density corresponds to the LWR decay power at approximately one minute after a shutdown during an accident condition. Some changes in the fuel parameters are expected as neutronics calculations are continued with emphasis on decoupling the local power density from the liquid fraction in the bed.

Figure 1.3-9 illustrates the WD-series (water/debris) package design. The design is basically generic for all of the planned experiments with minor modifications for a particular phenomenon being investigated. The debris is contained in a double-wall insulated crucible to prevent radial heat transfer. Heat generated in the bed transfers to the overlying water bath. The bath is cooled by conduction through two walls of the containment vessels to a helium heat exchanger. Hot helium is cooled to the atmosphere by a mobile cooling loop system similar to the current Sandia PAHR Program. Experiment diagnostics and helium cooling conditions are monitored and controlled at instrumentation consoles located adjacent to the reactor room. Experiment diagnostic instrumentation includes bed temperatures, bath temperatures, bed power and primary vessel pressure. Additional parameters are monitored for the secondary containment and helium system to satisfy safety requirements.

Table 1-VIII. Tentative LWR Degraded Core
Coolability Experiment Matrix

Experiment	Depth (CM)	Debris	Composition	Objective
WD-1	50	Large Particles	UO ₂	Early Debris Deep Bed Pressure Effects LMFBR Models
WD-2	50	Small Particles	UO ₂	Late Debris
WD-3	50	Small Particles	UO ₂	Stratified
WD-4	50	Large Particles	UO ₂ /ZrO ₂ /Zr/SS	Material Effects
WD-5	50	Large Particles	UO ₂	Bottom Fed
WD-6	50	Degraded Pin Burdle	UO ₂ /ZrO ₂ /Zr	Bottom Fed Distorted Pins
WD-7	50	Bi-Modal Distribution	UO ₂	Water-Starved Explosions
WD-8	25	Small Particles	UO ₂	Bed Depth

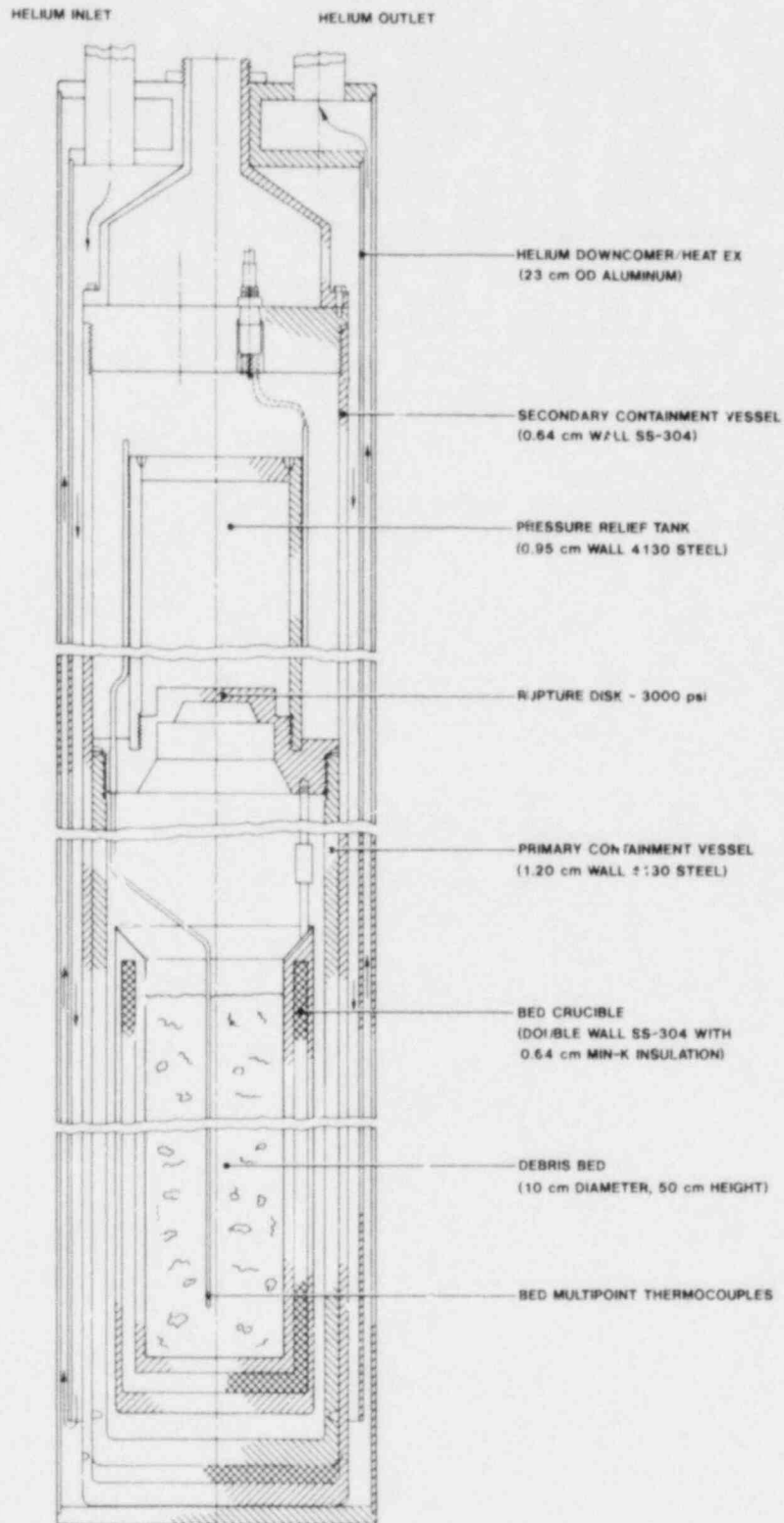


Figure 1.3-9. WD--Series Experiment Package Design

1.4 PAHR Molten Pool
(J. T. Hitchcock, 4421; T. M. Kerley, 4422)

1.4.1 Introduction

The molten pool studies are using prototypic reactor materials to investigate experimentally the progression of a debris bed from dryout to melt and the interaction of the melt with structure and core retention material.

In the current quarter, design work continued on an advanced experimental package. This design emphasizes the addressing of problem areas encountered in previous molten pool experiments. Specific changes in the new capsule include compatibility with the helium trailer used in the D-series debris bed experiments to increase cooling, the use of argon as a cover gas to simulate better the thermal behavior of sodium vapor, and the use of a B₄C neutron-spectrum modifier to flatten the bed power profile. A dosimetry experiment has also been defined that will reduce the uncertainty in the power normalization from about 25 to 5%.

Ultrasonic-thermometer-system development has concentrated on improving the electronics. A new multiplex system avoids the old system's synchronization problems.

1.4.2 In-Pile Experiment Package Design

The design of an advanced in-pile experiment package for use with the MP-6 and subsequent molten pool experiments has continued. Figure 1.4-1 shows the preliminary design. The design features increased cooling capability, argon cover gas, and a neutron spectrum modifier.

One objective of this design activity is to address the deficiencies and problems encountered in previous molten pool experiments. The new capsule will use the helium loop currently used in the D-series experiments. This increased cooling capability will allow larger fuel loadings, up to 2 kg of fully enriched UO₂. Previous fuel loadings were 0.8 kg for experiments MP-1 and -2 and 0.6 kg for experiments MP-3, -4, and -5. The enhanced cooling will also allow flexibility in establishing temperature gradients in the bed, longer experiment duration and quasi-steady-state operation. Cooling limitations required previous experiments to be fully

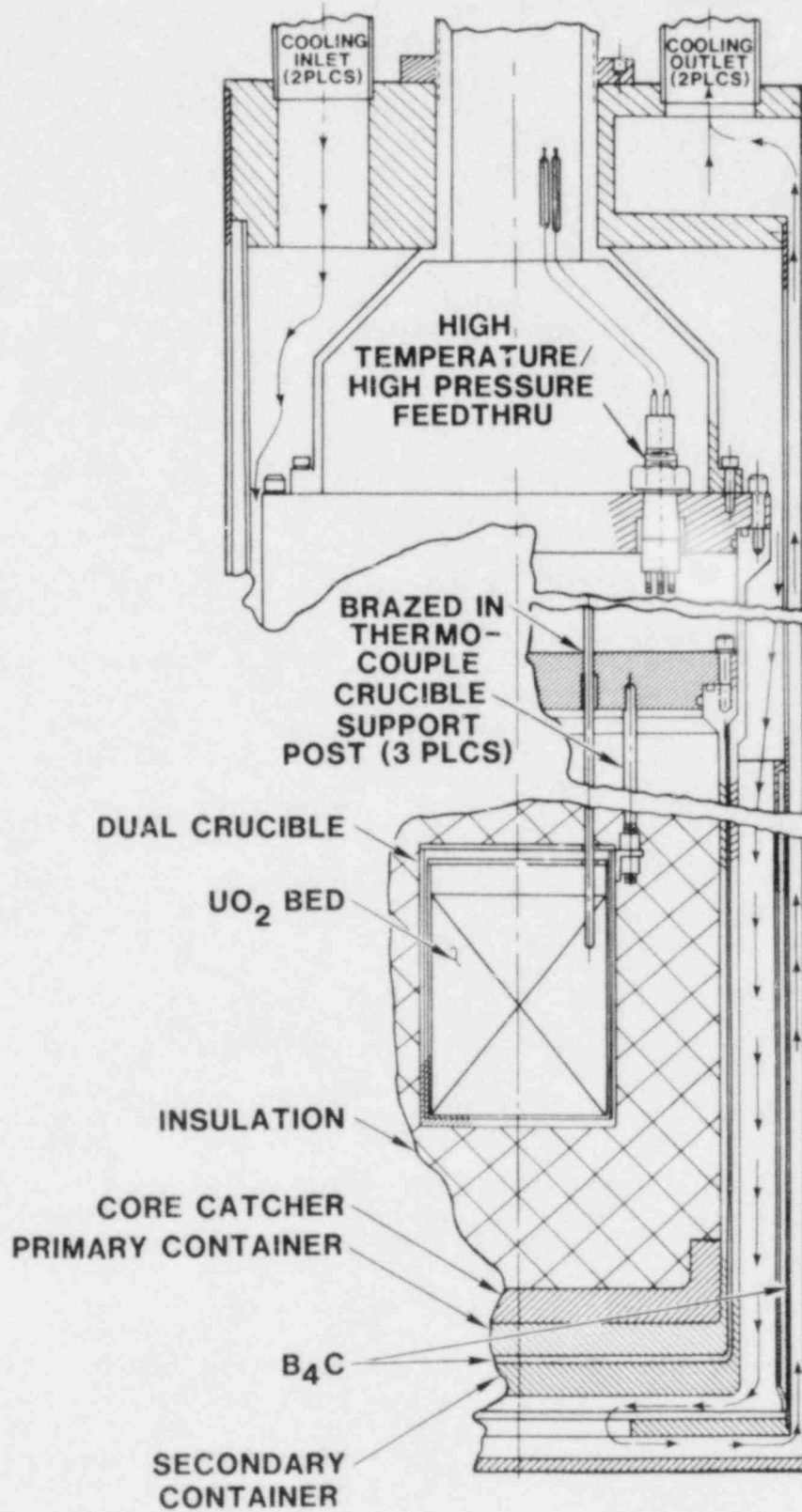


Figure 1.4-1. Preliminary Design of New Molten Pool In-Pile Experiment Capsule

insulated and essentially isothermal. Since one of the reasons for doing these experiments in-pile is to examine the effects of thermal gradients on the phenomenology of molten pool formation, materials migration and materials interaction, this parameter should be accentuated. Large thermal gradients also improve the accuracy of thermal conductivity measurements. Operation in a steady-state condition simplifies the thermal analysis of the experiments.

A second improvement in subsequent in-pile experiments using the new capsule will be the use of argon cover gas as a much better thermal simulant of sodium vapor. As reported in Reference 1-25, the use of helium cover gas in previous experiments limits their usefulness in validating porous-bed heat-transfer models because the experiments did not offer a severe test for radiation. With helium, conduction dominates and all reported correlations agree fairly well in predicting the effective conductivity of UO_2/He beds at high temperatures, whereas they disagree on the radiation component which dominates in actual dry debris. Also, argon decreases the conductivity of the ZrO_2 insulation by a factor of 3 adding flexibility to experiment design.

The new capsule will contain a B_4C neutron spectrum modifier to flatten the energy deposition profile within the bed. Previous experiments had a peak/minimum power ratio of up to 3. Neutronic calculations on the new design indicate that this can be reduced to about 1.4 with one-eighth inch of B_4C .

A further problem encountered in the thermal analysis of previous molten pool experiments concerns the large uncertainty in the bed power deposition. Uncalibrated neutronic calculations have been used to relate the bed power to the reactor power, which itself is known to only about 10%. By using data-fitting techniques, the best estimate of the analysts is that the power coefficients are in error by about 25%. To reduce this uncertainty a dosimetry experiment has been defined which will use an absolute fission counter to calibrate foils distributed throughout a dry particulate bed. This method should reduce the power deposition uncertainty to about 5%.

1.4.3 Ultrasonic Thermometer Development

Development activities on the ultrasonic thermometer (UT) have continued this quarter with an objective of improving the reliability and accuracy of this high temperature diagnostic. Improvements in the housing hardware have greatly increased the temperature capability while maintaining the high sealing capacity required for in-pile use. A smaller housing diameter allows closer radial spacing while a new means of sensor height adjustment facilitates experiment assembly.

Changes have also been made in the ultrasonic-thermometer electronics to facilitate and improve compatibility with the data acquisition system. A scanner has been incorporated to act as a control unit to bypass all of the multiplex system in the UT chassis. In the improved system all of the elements on each sensor are put on a single multiplex system. This arrangement avoids the synchronization problems encountered in the old system.

1.5 Fragmentation (T. Y. Chu, 1537)

1.5.1 Introduction

The ultimate dispersal of molten materials produced by most postulated severe accident scenarios for advanced sodium-cooled reactor systems often depends on either bulk freezing of the melt or the establishment of coolable, particulate beds. Scenarios which differentiate between the dispersal modes involve questions of the fragmentation of substantial quantities of melt when contacted with coolant. The fragmentation studies are attempting to find out whether the behavior of small quantities of melt, previously investigated, can be extrapolated to larger quantities of melt. Whole-core accidents may result in sudden freezing and fragmentation of the core debris, which may then settle on various surfaces within the vessel. Characterization of the fragmented debris size and the settling of this debris within the residual sodium pool are the most important results expected from this program.

1.5.2 Analysis

The debris from various experiments are being examined with a scanning electron microscope (SEM) to determine the distribution of metal and oxide phases as a function of depth. SEM is also used to determine the surface morphology of the debris. From this study, an investigator might be able to deduce the mode of fragmentation. Program personnel expect to finish this work in the next quarter.

Figures 1.5-1 and 1.5-2 illustrate typical results. SEM photographs in the figures show the variation of metal and oxide fragment ratios as a function of depth in the debris bed (for test FRAG 9). Obviously, more oxide is present in the upper portion (2 in.) of the bed. The separation is probably due to density differences between iron and alumina.

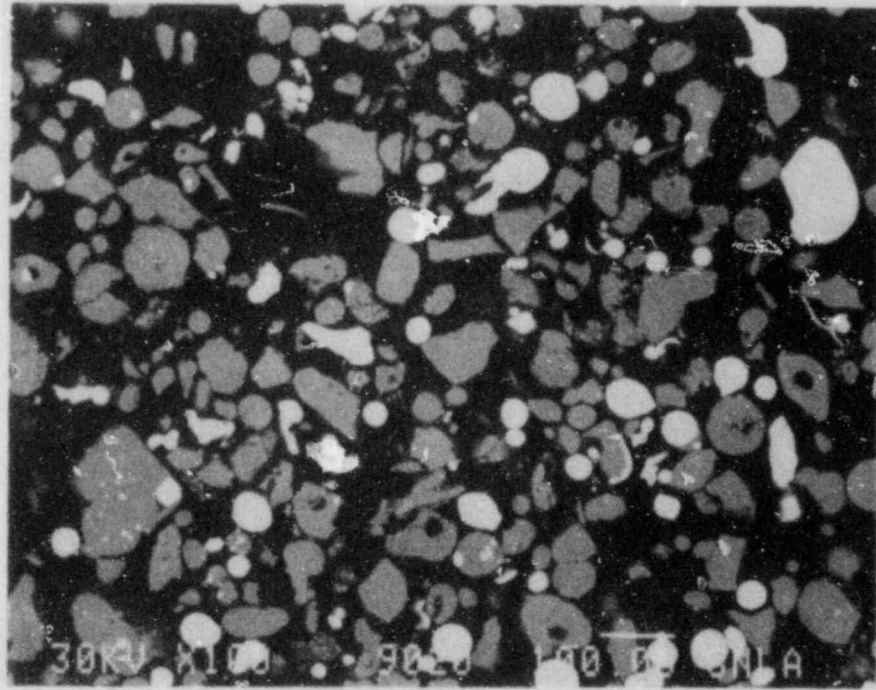


Figure 1.5-1. Test FRAG 9, Scanning Electron Micrograph
1 Inch in From Bottom of the Vessel

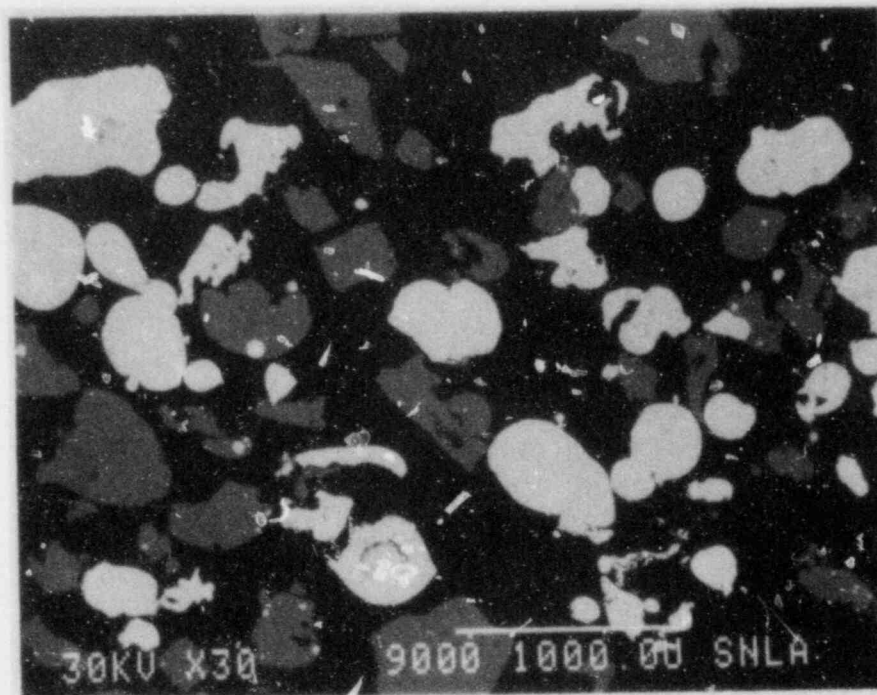


Figure 1.5-2. Test FRAG 9, Scanning Electron Micrograph
2 Inch in From Bottom of the Vessel

1.6 Sodium Containment and Structural Integrity
(J. E. Smaardyk, 4422; R. U. Acton, 1537;
W. A. Averill, 5846; A. Suo-Anttila, 4425;
J. Brockmann, 4422; R. A. Sallach, 5846)

1.6.1 Introduction

During this quarter, crucibles were poured for large one-dimensional tests with limestone and basalt concretes. These test configurations will be especially useful for CONTAIN development and verification. Preparations were started for the next large-scale test (No. 19). This test will use a conventional limestone-aggregate crucible with an initially shallow sodium pool and provision for adding fresh sodium during the test. Two physical, separate-effects tests with limestone concrete were completed. These tests were part of a series designed to determine the conditions necessary to obtain results similar to those of the large-scale tests. Modeling of the sodium interaction with basalt concrete has been advanced to include the effects of concrete porosity on the interaction rate.

1.6.2 Test Facility

Two modifications to the Large-Scale Test Facility have been completed during this quarter. The first allows experimenters to control the transfer of liquid sodium from the shipping containers to the dump tank from a remote location. This change was made to increase safety for facility personnel.

The second modification permits the addition of fresh sodium to the test article during a test. To date, the Phase II or erosion phenomena have been observed in limestone test articles only for shallow sodium pools. Investigators can now see whether the erosion phase can be sustained. This fresh sodium can be added in carefully controlled increments as small as 0.25 kg.

1.6.3 Large-Scale Testing

One limestone and one basalt crucible were cast from a design new to the Sandia program. This design is similar to a design used by the Hanford Engineering Development Laboratory (HEDL) in some of its large-scale sodium/concrete

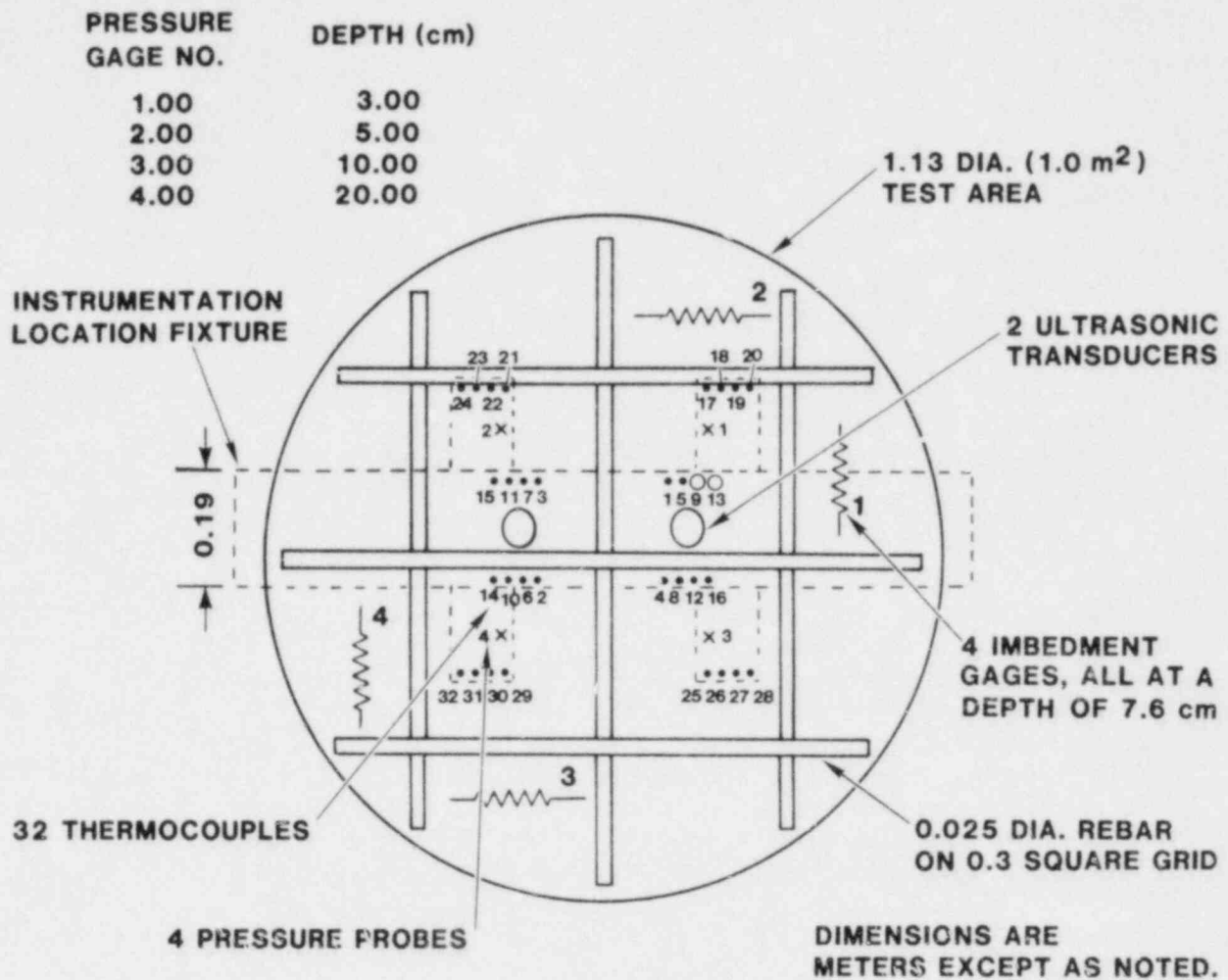
interaction tests. The crucible test section is heavily constrained. Beside the usual instrumentation, these new crucibles contain small-diameter stainless steel tubes for use in trying to measure pressure as a function of time and position within the concrete during the test.

The instrumentation layout has been developed for the new crucible design (Figure 1.6-1). The instrumentation package features 32 thermocouples, 4 pressure probes, 4 imbedment gages and 2 ultrasonic transducers. The thermocouples will measure temperature as a function of time and position during the test. The pressure probes will provide information to check the computer code USINT. This code predicts heat and mass transfer within heated concrete. Until now, no experimental pressure data have been available to check the code predictions. The ultrasonic transducers will monitor the erosion of the concrete by the sodium. The imbedment strain gages will be monitored to see if they will indicate crucible cracking. In addition to the strain gages, hydrogen-gas sensors will be mounted in the test cell outside the crucible for the same purpose. (The test cell should be free of hydrogen gas unless the crucible has cracked allowing hydrogen gas to escape from the crucible.)

Preparations were begun for the next large-scale test (No. 19) to be conducted during the next quarter. Test 19 will involve limestone concrete prepared to the mix specifications for the Clinch River Breeder Reactor. The limestone-concrete crucible cavity will be filled with sodium at 873 K (600°C) to a depth of 12.5 cm. This pool depth should saturate rapidly with sodium hydroxide and trigger the vigorous Phase II reactions seen in the first three tests of this program. If the Phase II reactions are generated, then fresh molten sodium will be added to the pool to see if that stops (or slows) the reaction... or near sodium depletion to see if the reaction will continue. The modifications to the facility will allow fresh molten sodium to be added to the crucible at a rate of about one-eighth kg per second.

1.6.4 Physical Separate Effects Testing

Two tests were completed during this period. They are part of a series of tests with limestone concrete to determine the conditions required to reproduce the phenomena observed in the initial large-scale test series at Sandia. These two tests were of the "standard"



THERMOCOUPLE NO.	DEPTH (cm)	THERMOCOUPLE NO.	DEPTH (cm)	THERMOCOUPLE NO.	DEPTH (cm)
1.00	1.00	12.00	15.00	23.00	3.00
2.00	1.00	13.00	25.00	24.00	5.00
3.00	2.00	14.00	35.00	25.00	1.00
4.00	2.00	15.00	50.00	26.00	2.00
5.00	3.00	16.00	60.00	27.00	3.00
6.00	3.00	17.00	1.00	28.00	10.00
7.00	4.00	18.00	2.00	29.00	1.00
8.00	4.00	19.00	3.00	30.00	2.00
9.00	5.00	20.00	4.00	31.00	3.00
10.00	7.00	21.00	1.00	32.00	20.00
11.00	10.00	22.00	2.00		

Figure 1.6-1. Transparent View Showing Instrumentation Layout for New Concrete Crucibles. (Depths Listed are into Concrete from Sodium-Concrete Interface.)

configuration with 4 kW heaters in the sodium pool. These heaters shorted, in the first test, at the start of the test. The pool cooled continuously and did not proceed beyond the (mild) Phase I interaction.

The standard test was repeated for the second test. A charge of 7.3 kg of sodium was heated to 1000 K (727°C) and dumped rapidly into the crucible. The pool heaters were energized immediately and began to heat the pool within 10 minutes. Minimum pool temperature was about 783 K (510°C). The setpoint of 873 K (600°C) was reached by 30 minutes. This temperature was maintained for 1 hour with no indication of the Phase II interactions. The test was terminated at that point.

Investigators have designed a third test to examine the effect of sodium carbonate (Na_2CO_3) on the interaction. One hypothesis has been advanced that Na_2CO_3 can form a protective barrier between sodium and concrete. Another hypothesis suggests that Na_2CO_3 reacts energetically with sodium and may even be responsible for the abrupt transition from Phase I to Phase II. The test configuration was the same as the first two tests but with the addition of 0.7 kg of Na_2CO_3 powder on top of the concrete.

A report has been written that describes the release of water from heated concretes.¹⁻²⁶ The three concretes, limestone, basalt, and magnetite, are discussed.

1.6.5 Sodium/Concrete Ablation Model

Several small-scale, basalt concrete tests were conducted at Sandia and the test results were reported in Section 3.6 of a previous quarterly.¹⁻²⁵ All of the small-scale tests, with the exception of the high pressure test, exhibited a penetration rate greater than that found in the large-scale tests. The major differences between the large-scale and small-scale tests are the surface-to-volume ratio and the level of concrete constraint. The SCAM code predicts a small effect due to changing surface-to-volume ratio, thus investigators expect that surface-to-volume ratio is not the main parameter underlying the differences in the observed penetration rate between large- and small-scale tests.

The level of concrete constraint varies considerably between the large- and small-scale tests. In the large-scale tests, the reaction zone is constrained radially by a large mass of reinforced concrete. In the small-scale tests the radial constraint consists of a steel jacket, or nothing at all. During the small-scale tests, the steel jacket is heated to temperatures that will allow for deformation, thus the constraint is considerably less rigid compared to large-scale tests.

The observed variation in penetration rate prompted the investigation of the effects of permeability and porosity. Permeability and porosity are related by Equation (1.29).

$$K = \frac{\alpha^3}{5S_0^2(1-\alpha)^2} \quad (1.29)$$

where

- K = permeability
- α = porosity (void fraction)
- S_0 = pore surface area/unit volume.

As Equation (1.29) shows, an increase in porosity leads to an increase in permeability. Likewise, a decrease in pore surface area/unit volume leads to an increase in permeability. Both of these effects are expected to occur in the reaction zone of sodium ablated concrete. The sodium hydroxide that is produced from the sodium-water reaction will react with and dissolve the microstructure of the cement paste. In doing so, much of the original surface area will be lost causing an increase in permeability. Experimental evidence indicates that a large amount of swelling takes place because of the secondary reaction and this effect will increase the porosity. Physically constraining the concrete can limit the amount of swelling, and thus the increase in porosity. Figure 1.6-2 shows the SCAM predictions for penetration rate as a function of pressure for three different levels of constraint. The tightest constraint is presumed to occur in the large-scale tests wherein a large concrete and steel rebar constraint is provided. This curve has the lowest penetration rate for a given ambient pressure. The middle curve corresponds to the penetration observed in an intermediate constraint like that provided by a

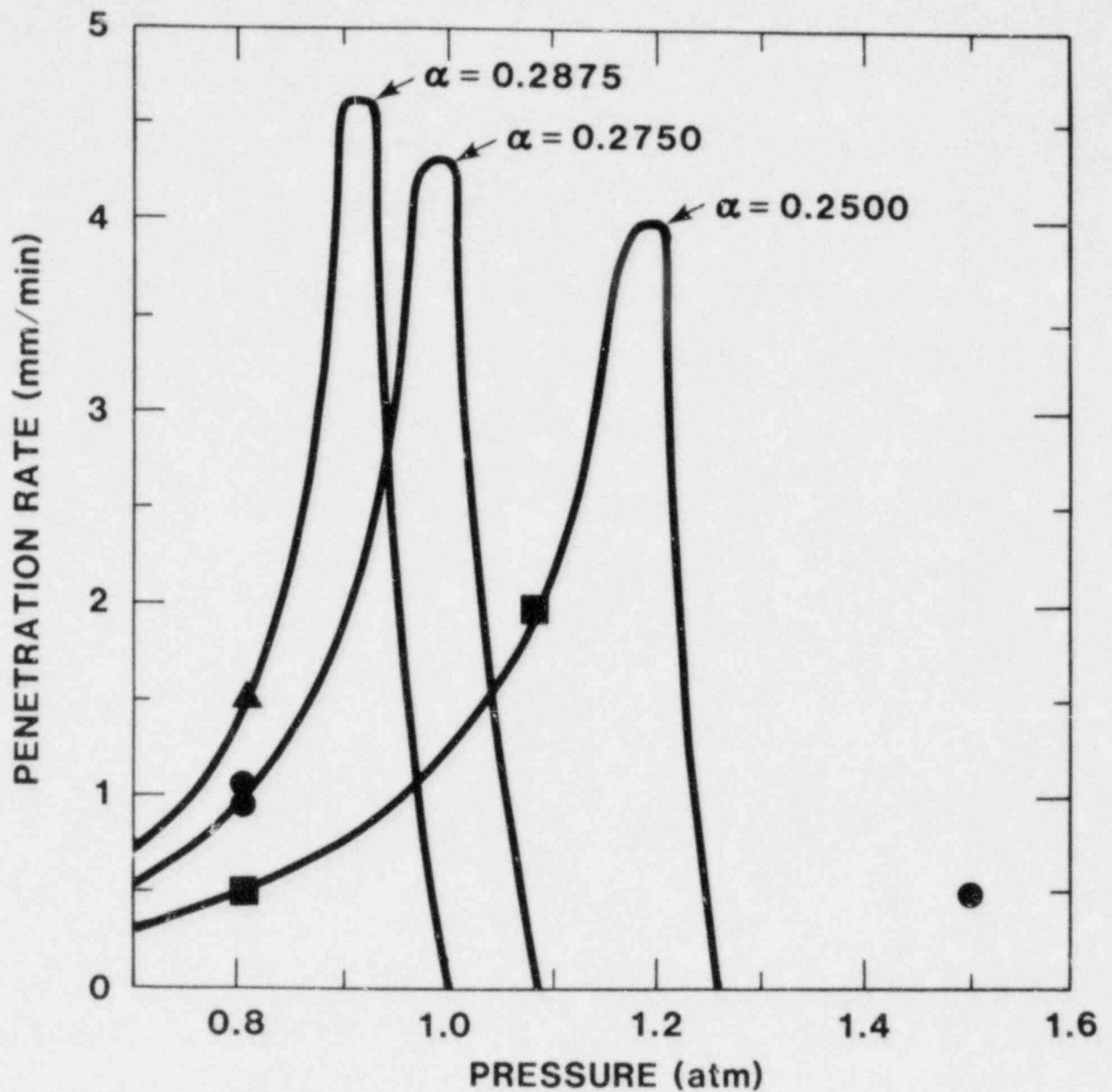


Figure 1.6-2. SCAM Predictions for Penetration Rate

steel jacket (which is heated by the interaction). The uppermost curve corresponds to a completely unconstrained concrete specimen. The effect of constraint is modeled in these calculations by increasing the value of the initial porosity. The curves shown are only intended to illustrate trends in behavior and are not intended to predict the exact penetration vs. pressure behavior of concrete subjected to different levels of constraint. With this in mind the SCAM code predicts the following trends:

1. At constant pressure, the rate of penetration increases for a decrease in the level of constraint.
2. The magnitude of the maximum penetration rate increases with decreasing levels of constraint.
3. The cutoff pressure increases with increasing levels of constraint.

Tightly constrained concrete will continue to react at higher pressures. Hence the addition of rebar should result in a slower penetration but one that can continue at slightly higher pressures.

Any cracking that occurs causes a local stress relief and thus an increase in local porosity, hence, enhanced penetration would be expected around cracked areas. This effect has been observed in Sandia's large-scale tests of the basalt concrete.

In conclusion, variations in penetration rate can be accounted for in the SCAM code by changes in the permeability and porosity of the concrete.

1.6.6 Chemistry Separate Effects Testing

1.6.6.1 NaOH-SiO₂ Interactions

Arrangements have been made for thermogravimetric analyses of sodium hydroxide vapor attack on silicon dioxide coupons. The initial test will involve suspending small SiO₂ coupons into an atmosphere in equilibrium with NaOH liquid. The nickel crucible needed to contain the liquid NaOH has been obtained. A high-purity alumina

tube, to contain the experiment, is being obtained. (Exceedingly high-purity alumina is needed; a preliminary literature search indicated that alumina or magnesia with as little as 2% silica contained within its structure would be vigorously attacked by NaOH.)

1.6.6.2 Na-Na₂CO₃ Interactions

In the last intermediate-sized separate effects test, molten Na at 973 K (700°C) was dropped into a crucible containing sodium carbonate and an explosion occurred. Consequently, studies of the interaction of Na and Na₂CO₃ have been undertaken. A small-scale dump-type experiment has been designed and will be conducted next quarter. A small crucible that can be emptied by siphoning has been designed. This crucible will allow the sodium to be heated to the required temperature and, by the application of a small argon overpressure to the crucible, the contents of the crucible can be poured in a matter of a few seconds onto the Na₂CO₃.

In other tests, small amounts of Na metal and Na₂CO₃ will be premixed at ambient temperatures in a crucible, then placed into a furnace where the temperature will be ramped slowly up to the point where the reaction occurs. Thus, the minimum reaction temperature will be defined for the Na-Na₂CO₃ interaction.

1.6.7 Studies of the (Na₂, Ca)((OH)₂CO₃) Reciprocal System

The interaction of molten Na metal with limestone-aggregate concrete does not occur in a direct reaction but rather via intermediate chemical species. Based on prior chemical evidence, investigators postulate that the controlling reaction is that between NaOH (formed by the Na + H₂O reaction) and limestone which is primarily CaCO₃.

A good understanding of the (Na₂, Ca)⁺((OH)₂, CO₃)⁺⁺ reciprocal system is necessary to elucidate the chemical phenomena occurring in these intermediate stages. In particular, the compositional and temperature limits of the liquid region are important. Three of the bounding binary phase diagrams are known at least partly. These binaries are NaOH + Na₂CO₃, Na₂CO₃ + CaCO₃, and Ca(OH)₂

+ CaCO₃.¹⁻²⁵ No data were found for the fourth binary, NaOH + Ca(OH)₂.

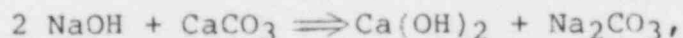
An investigation of the reciprocal system has been started. Differential thermal analysis (DTA) is being used to determine the liquidus temperatures (the temperature where a solid phase first appears). Concurrently, a gravimetric (microbalance) technique is used to determine the temperature at which dehydration of dissolved Ca(OH)₂ to form CaO takes place.

Preliminary results obtained thus far include:

- a. That portion of the NaOH + Ca(OH)₂ phase diagram for the compositions less than 12 mole % Ca(OH)₂, and,
- b. The decomposition temperatures of dissolved Ca(OH)₂ for the above compositions.

The NaOH + Ca(OH)₂ phase diagram for compositions containing < 12 mole % Ca(OH)₂ appears to be very similar to the NaOH + Ba(OH)₂ phase diagram.¹⁻²⁵ Solid solubility of Ca(OH)₂ in the high temperature form of NaOH is great with little solubility of Ca(OH)₂ in the low temperature form. The liquidus temperature rises gradually from 593 K (320°C) at pure NaOH to 603 K (330°C) at 8-10 mole % Ca(OH)₂. The solubility of Ca(OH)₂ in liquid NaOH, however, does not appear to exceed 10-12 mole % Ca(OH)₂. This contrasts with the NaOH + Ba(OH)₂ system where the solubility limit is > 80 mole % Ba(OH)₂.

The relatively small solubility of Ca(OH)₂ is important, however, because it affords a mechanism by which a potential barrier layer of product may be removed from the reacting interface (NaOH liquid + CaCO₃ solid). Writing the interface reaction as



both products are soluble in liquid NaOH and the interface can be kept clean of reaction products by diffusion away from the interface. Reactions have little effect on the chemical conditions at the interface.

The decomposition temperature of pure Ca(OH)₂ depends on the surrounding vapor pressure of H₂O. The partial pressure of water at equilibrium and 683 K (410°C) is

$P_{H_2O} = 2600 \text{ Pa (20 torr)}$. The decomposition temperatures for several $\text{NaOH} + \text{Ca(OH)}_2$ compositions (5-10% Ca(OH)_2) have been determined by continuously weighing the samples as the temperature was gradually increased. The decomposition temperature was taken to be that temperature at which a rapid loss of weight was observed. This temperature was $783 \pm 10 \text{ K (510} \pm 10^\circ\text{C)}$, showing an enhanced stability of Ca(OH)_2 in NaOH solutions.

Current and planned experiments will determine the liquidus and Ca(OH)_2 decomposition temperatures for solutions which also contain Na_2CO_3 (or CaCO_3). The experiments will concentrate on solutions which are such mixtures of NaOH and CaCO_3 as could result during the Na/limestone concrete interaction.

1.6.8 Studies of the Na + O + H System

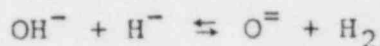
A knowledge of the phase relationships in the $\text{Na} + \text{O} + \text{H}$ system and the conditions for their stability is necessary for understanding the chemical processes resulting from Na/concrete interactions. The first step in any interaction is the reaction of Na with H_2O thermally driven from the concrete. The stability of the product NaOH with respect to excess Na is a major factor in determining the course of further chemical processes.

In previous quarters, data has been acquired about the equilibrium H_2 pressures of $\text{Na} + \text{NaOH}$ mixtures at $970 \pm 20 \text{ K}$ and $1070 \pm 20 \text{ K}$ (700 and 800°C). Additional data has now been taken for $1170 \pm 20 \text{ K}$ (900°C). These data are not as extensive as at the lower temperatures. At this temperature, materials interactions (as yet not understood) begin to occur between the container and its alumina support whenever the H_2 partial pressure is reduced below $\sim 40 \text{ kPa (300 torr)}$. As a result, reproducible data at lower pressures were not obtained.

Those data pertaining to the NaOH solution have been analyzed with the aim of demonstrating which chemical solution model (or models) would represent the data best. The model which best represents the data is one in which Na metal reacts with NaOH to form Na_2O and NaH . These compounds are not formed as separate phases but are dissolved in the remaining NaOH . The equilibrium reaction is simply stated as



or alternatively as



where only the dissolved species are represented.

The equilibrium constant for this reaction is

$$k = \frac{P_{\text{H}_2} A_{\text{Na}_2\text{O}}}{A_{\text{NaOH}} A_{\text{NaH}}}$$

The A's are the chemical activities of the O^{2-} , OH^- and H^- ions, respectively. The activities were taken as $A_i = X_i$ where the X_i s are the mole fraction of the corresponding species. This means that an ideal thermodynamic solution is assumed. This assumption yields calculated hydrogen pressures which are within ± 10 percent of the measured pressures.

Several attempts have been made to fit the experimental data to expressions containing second order chemical terms. These later expressions give slightly better calculated pressures, but are not as satisfying to chemical principles. Further work is needed.

The following conclusions can be drawn from the experimental results:

- a. Compositions which can be represented as mixtures of Na and NaOH have equilibrium hydrogen pressures much greater than 93 kPa (700 torr) in accordance with extrapolations of lower temperature data.
- b. The hydrogen pressure varies dramatically with composition so that compositions not too far from the Na + NaOH join (the line connecting the compositions for pure Na and pure NaOH) have hydrogen pressures less than 93 kPa (700 torr).
- c. As a result, NaOH-based solutions exist that are stable at temperatures as great as 1200 K (927°C).

- d. These solutions probably are the attacking phase wherein chemical dissolution of basalt and limestone concretes is accomplished.

As future work, the remaining experimental data will be critically examined in order to delimit the composition limits of these NaOH based solutions.

1.6.9 Aerosol Source Term

The aerosol instrumentation for Test 19 uses on-hand equipment. No new equipment is being fielded for this test since the aerosol program is still in a scoping phase.

The aerosol mass distribution between 1 and 15 μ m aerodynamic diameter will be obtained with two MRI (Meteorology Research, Inc., Altadena, CA) series 1500 cascade impactors. Provision has been made to heat the impactors to 523 K (250°C) during the sampling. One impactor sample will be taken during Phase I and the second during Phase II.

The two deposition samplers used in Tests 15 and 16 will operate in conjunction with the impactors. Each sampler consists of 2 rectangular channels through which the aerosol flows and deposits by diffusion and thermophoresis. Samples are collected on suitable surfaces for electron and optical microscopy.

While deposition as a function of particle size and distance down stream is not readily characterized in this instance, these samples should provide the best means for obtaining particle-shape factors and agglomeration characteristics.

Four filtration samples will be taken during the test. Two samples will use a fine wire mesh as a filter material and the other two will use a sintered steel screen. The use of these materials is necessary because of the action of Na on more conventional filter media such as teflon.

The above sampling devices will draw aerosol from the "top hat" through penetrations in the side of the top hat. The 4-inch exhaust pipe will contain an extinction photometer (Figure 1.6-3).

1-97

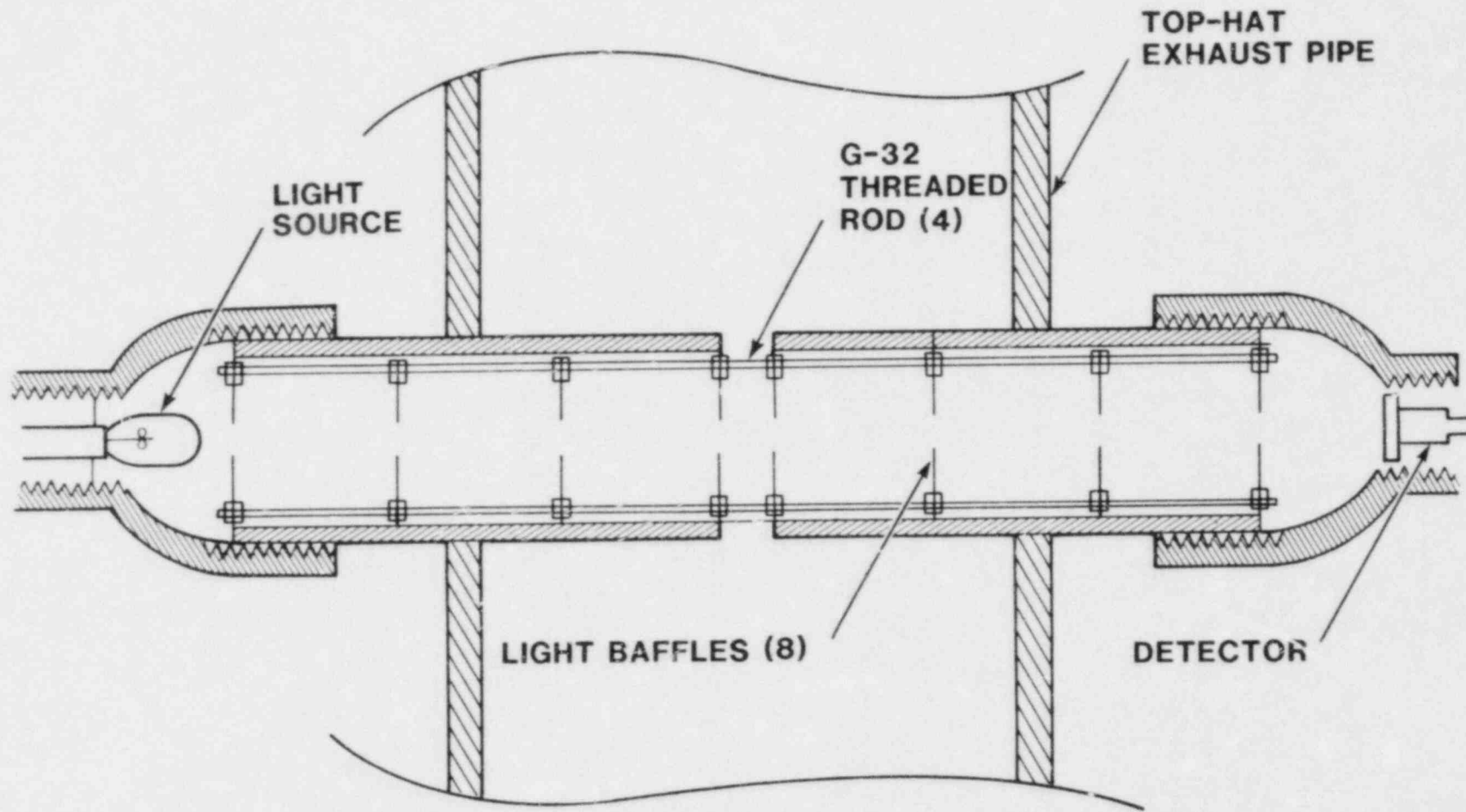


Figure 1.6-3. Cross-section View of the Extinction Photometer for Large-Scale Test 19

The photometer consists of a pin-to-photodetector and a light source contained in a 1 1/2"-OD tube separated by 8 baffles, each with a 1/4" hole in the center. Between the 4th and 5th baffles is a 1-cm space opened to the aerosol across which the light is attenuated by the aerosol. The photometric data will be correlated with the measurements of total mass given by the filters and impactors.

The use of electron microscopy and gravimetric analysis on the impactor samples should provide a quantitative description of the aerosol between 1 and 15 μ m. A microprobe and/or chemical analysis may be used to determine aerosol composition as a function of size. Coupled with the microscopic data on the sub-micron aerosol obtained with the deposition samplers, a fairly complete picture of the sodium/concrete aerosol may be obtained. This will provide valuable information on what to look for and the type of instrumentation to field in future tests.

1.7 High Temperature Fission Product Chemistry and Transport
(R. M. Elrick, 4422; R. A. Sallach, 5846)

1.7.1 Introduction

The purpose of the High Temperature Fission Product Chemistry and Transport program is to establish the data base necessary to predict properly fission product behavior during severe accidents. This experimental task is being pursued by three interrelated activities:

- (1) Definition of thermodynamic data and chemical reaction characteristics of particular fission products of interest.
- (2) Examination of the transport properties of fission products in prototypic environments of steam and hydrogen.
- (3) Comparison of the observed behavior of the fission products with predictions made by purely thermodynamic considerations.

Transport properties of the fission products will be studied in the Fission Product Reaction Facility being developed as part of this program. The facility will allow moderately volatile fission products to be generated in flowing steam and hydrogen mixtures at temperatures up to 1273 K (1000°C). The fission product stream passes over steels representative of structural materials in reactor cores. A Raman spectroscopy unit is being developed that may allow determination of the chemical form of fission products in the vapor state.

1.7.2 Documentation

The major effort during the first half of the quarter was completing the final draft of the vapor chemistry section for the report, Technical Bases for Estimating Fission Product Behavior During LWR Accidents. First, comments from the peer reviewers were incorporated into the draft and then written responses to these comments were prepared.

1.7.3 Fission Product Reaction Facility

During this quarter, the Fission Product Reaction Facility (water preheater, boiler, critical orifice, superheater, fission product vapor generator and condenser) was operated at a temperature of about 873 K (600°C) for a total of 50 hours to evaluate the general design and response of the steam facility.

Several additions were made and several changes considered for improved operation.

- a. A Granville-Phillips pressure controller is being modified to control system pressure downstream of the critical orifice, possibly to within 1%.
- b. A mass spectrometer has been installed to measure the type and amount of noncondensed gases present in the system.
- c. A drain has been designed and installed for continuously collecting and measuring the amount of condensed steam without affecting the system pressure.
- d. The critical orifice will be moved upstream of the superheater so the high temperature region of the facility, all downstream of the orifice, can be operated slightly above ambient pressure. Exerting a small positive pressure inside the system, ambient oxygen will be kept from leaking into a system that could contain free hydrogen. The small difference in pressure across the walls will also minimize wall stress. Downstream pressure relative to ambient will be measured with a mercury manometer. Steam pressure upstream of the critical orifice is held constant by overpressurizing a pressure-cooker valve on the boiler and is measured with a Bourdon pressure gauge.
- e. At full power, the steam system (excluding the superheater) has a maximum equilibrium temperature of a little more than 1273 K (1000°C) with 10 cm of insulation. Maximum system temperature could be increased most simply by adding insulation and, if necessary, additional calrods.

Before adding simulated fission products to the system, a study is planned to evaluate hydrogen production and oxidation in the 304 stainless steel system in the presence of steam at various temperatures. In the first of several tests, as the system temperature was increased from 1073 K (800°C) to about 1273 K (1000°C), the mass spectrometer detected increasing amounts of hydrogen in the system relative to a reference flow of argon used to control system pressure. Hydrogen production will be studied as a function of time at temperature in some detail to establish a base line for its generation in this simple steam system. To study oxidation in the system, preoxidized, cleaned and also cold worked coupons of 304 stainless steel will be exposed at temperature and examined after tests for oxidation reactions. These studies are deemed necessary to insure that fission-product studies are carried out under conditions that closely represent a range of reactor accident conditions.

Experimental investigations of CsOH, including its interaction with stainless steel in the system, can begin. The same general approach will be used: in-situ measurements of gas evolution plus posttest analysis of coupons and of the condensed steam. At this point, the Raman system will be used to measure spectra for some of the expected species in the cesium-iodine-steam system. The steam facility will then be interfaced with the spectrometer to begin the study of chemical reactions at temperature. The measurements will begin on the CsOH-steam system and in turn study the stability of CsOH with CsI and CsOH with I in combination with known amounts of hydrogen or oxygen. During this time some of these systems will be examined in the transpiration apparatus for anticipating results that might be expected in the steam facility.

A dialogue has begun with Battelle Columbus Labs on results of fission-product transport and chemistry work of mutual benefit and interest. Discussions include ongoing work as well as plans for future work, the direction of which could be beneficially influenced by these discussions.

A laboratory-scale experiment is being planned to investigate hydrogen burn and its effect on fission product chemistry, initially on that of CsI vapor. The design will be compatible with the steam system so the burn chemistry can be studied with Raman spectroscopy.

During July, additional power will be installed so the entire steam facility may be heated at both the Raman facility and in the adjoining room where the steam system is operated for all other tests.

Personnel from Oak Ridge National Laboratory will visit Sandia in August to discuss the possibility of developing a Raman spectrometer for hot cell experiments. The intent of the Oak Ridge experiments is to determine the chemical form and amount of fission products released by heating irradiated fuel pins in the presence of steam. The discussions will center on methods for introducing the laser beam into the hot cell and for capturing the maximum amount of scattered Raman light for analysis outside the cell. Sandia will help ORNL determine the conditions under which such a system could be practical and will aid in developing possible systems.

1.7.4 Vapor Pressure of Liquid CsOH

Additional transpiration experiments have been performed in which the measurements of vapor pressure of liquid CsOH were extended to both higher and lower temperatures. The temperature range is now 704-1133 K (431-860°C).

These additional experiments have permitted a better definition of the vapor pressure equation:

$$\log_{10} P = 9.76 \pm 0.46 - \frac{6611 \pm 397}{T}$$

where the vapor pressure, P, is measured in pascals (Pa) and temperature is measured in kelvin (K).

While no prior determinations of the CsOH vapor pressure are known, a vapor pressure can be calculated from the JANAF thermochemical data. The calculated vapor pressure equation is

$$\log_{10} P(\text{Pa}) = 10.2 - \frac{6514}{T(\text{K})} .$$

The calculated vapor pressure equation predicts the vapor pressure of CsOH to be about a factor of 3 larger than that measured experimentally. Note that the second terms of the calculated and experimental vapor pressure equations are very close,

$$-\frac{6611}{T} \text{ versus } -\frac{6514}{T} .$$

This term is proportional to the enthalpy of vaporization. Thus the differences between the calculated and experimental equations arise solely from the difference in the initial constant terms. This term relates primarily to the entropy of vaporization. A net relative change of only 2 cal-deg⁻¹-mole⁻¹ in the tabulated entropies of CsOH vapor or liquid would resolve this difference.

These data were presented at the Ninth Midwest High Temperature Chemistry Conference held at the Los Alamos National Laboratory on June 9-11, 1981.

References for Section 1

- 1-1. D. A. Powers and F. E. Arellano, Direct Observation of Melt Behavior During High Temperature Melt-Concrete Interactions, SAND81-1754, NUREG/CR-2283 (Albuquerque, NM: Sandia National Laboratories, to be published).
- 1-2. D. Perinic et al., "Concrete Crucible Tests With Thermite Melts," NRC Translation 669, December 1979.
- 1-3. D. A. Powers et al., Exploratory Study of Molten Core Material/Concrete Interaction, July 1975 - March 1977, SAND77-2042 (Albuquerque, NM: Sandia National Laboratories, February 1978).
- 1-4. Radiography in Modern Industry, 3rd ed., 1969 (Rochester, NY: Eastman Kodak Company, 1969).
- 1-5. R. Halmsow, Physics of Industrial Radiology (New York, NY: American Elsevier Publishing Co., Inc., 1966).
- 1-6. Advanced Reactor Safety Research Quarterly Report, January-March 1981, SAND81-1529(1of4), NUREG/CR-2238(1of4) (Albuquerque, NM: Sandia National Laboratories, to be published).
- 1-7. J. E. Brockmann, "Coagulation and Deposition of Ultrafine Aerosols in Turbulent Pipe Flow," Ph.D. Thesis, University of Minnesota, Department of Mechanical Engineering, June 1981.
- 1-8. S. K. Friedlander, Smoke, Dust and Haze (New York, NY: John Wiley and Sons, 1977).
- 1-9. F. Gelbard, Multi-AEROS User's Manual, SAND80-0822 (Albuquerque, NM: Sandia National Laboratories, 1980).
- 1-10. M. D. Allan et al., "Dynamic Shape Factors for LMFBR Mixed-Oxide Fuel Aggregates," J. Aerosol Sci., 10, pp. 43-48, 1978.

- 1-11. J. F. Van de Vate et al., "Dynamic Shape Factors: Measurement Techniques and Results on Aggregates of Solid Primaries," J. Aerosol Sci., 11, pp. 67-75, 1980.
- 1-12. J. F. Van de Vate et al., "Morphology and Aerodynamics of Sodium Oxide Aerosol at Low Relative Humidities," Proceedings of the CSNI Specialists Meeting on Nuclear Aerosols in Reactor Safety, NUREG/CR-1724, ORNL/NUREG/TM-404, CSNI-45 (Oak Ridge, TN: Oak Ridge National Laboratory, 1980).
- 1-13. K. Okuyama et al., "Evaluation of the Effect of Nonsphericity of Fine Aggregate Particles in Brownian Coagulation," J. Colloid and Interface Sci., 81, 1, pp. 21-31, 1981.
- 1-14. Nuclear Aerosols in Reactor Safety, M. Silberberg, ed. (Paris, France: Nuclear Energy Agency, OECD, June 1979).
- 1-15. R. B. Bird et al., Transport Phenomena (New York, NY: John Wiley and Sons, Inc., 1960) pp. 196-200.
- 1-16. A. E. Scheidegger, The Physics of Flow Through Porous Media, 3rd ed. (Toronto, Canada: University of Toronto Press, 1974).
- 1-17. H. Kampf and G. Karsten, "Effects of Different Types of Void Volumes on the Radial Temperature Distribution of Fuel Pins," Nuclear Application and Technology, 9, 1970.
- 1-18. J. S. McDonald and T. J. Connolly, "Investigation of Natural Convection Heat Transfer in Liquid Sodium," Nuclear Science and Engineering, 8, pp. 369-377, 1960.
- 1-19. J. E. Gronager, M. Schwarz, and R. J. Lipinski, PAHR Debris Bed Experiment D4, SAND80-2146, NUREG/CR-1809 (Albuquerque, NM: Sandia National Laboratories, 1981).
- 1-20. G. M. Fair and L. P. Hatch, "Fundamental Factors Governing Streamline Flow of Water Through Sand," J. Amer. Water Works, 25, pp. 1551-1565, 1933.

- 1-21. J. B. Rivard, Post-Accident Heat Removal: Debris-Bed Experiments D2 and D3, SAND78-1238, NUREG/CR-0421 (Albuquerque, NM: Sandia Laboratories, 1978).
- 1-22. R. J. Lipinski, "A One-Dimensional Particle Bed Dryout Model," Trans. Amer. Nucl. Soc., 38, pp. 386-387, 1981.
- 1-23. R. J. Lipinski, as reported in Advanced Reactor Safety Research Quarterly Report, October-December 1980, SAND80-1646(4of4), NUREG/CR-1594(4of4) (Albuquerque, NM: Sandia National Laboratories, February 1982).
- 1-24. J. Bear, Dynamics of Fluids in Porous Media (New York, NY: American Elsevier Publishing Company, 1968) p. 465.
- 1-25. Advanced Reactor Safety Research Quarterly Report, October-December 1980, SAND80-1646(4of4), NUREG/CR-1594(4of4) (Albuquerque, NM: Sandia National Laboratories, February 1982).
- 1-26. L. A. Kent, Water Release From Heated Concretes Used in Nuclear Reactor Construction, SAND81-1732, NUREG/CR-2279 (Albuquerque, NM: Sandia National Laboratories, 1981).

2. CONTAINMENT ANALYSIS

2.1 CONTAIN Code Development (M. J. Clauser, 4424; M. E. Senglaub, 4424; J. E. Kelly, 4425; P. J. Cooper, 4424; J. P. Odom, 4424)

The goal of this task is the development of CONTAIN, a general and comprehensive systems code that will analyze a variety of accident sequences following the breach of the primary containment vessel through the breach of the secondary containment. It will provide detailed treatments of phenomena such as material interactions, heat-transfer, aerosol behavior and fission product transport. The models will be sufficiently general to apply to all advanced reactor and light-water reactor containment systems. In addition, the MARCH code for describing the melt process in an LWR is being assessed to determine needed improvements so that it can be used to evaluate core melt mitigation devices.

During this quarter, work has been concentrated primarily on completion of the models and coding for version 1A of CONTAIN, and testing and debugging the resulting code. Version 1A contains models that are common to both LWR and LMFBR applications such as thermal debris coolant interactions, intercell flow of gases, aerosols and fission products, and the behavior of these within each cell of the containment system.

During the testing, several minor difficulties were encountered in setting up and running problems. Many of these difficulties result from such things as unclear or ambiguous documentation; the code and/or the documentation are being improved to avoid these difficulties. The existing equations-of-state for water vapor in the atmosphere have been found to be incorrect in some cases, and the errors have been corrected. The interface between the pool and the atmosphere in a cell has been restructured to correct some errors and to improve the treatment of sources of aerosols from the pool.

In several calculations, a high frequency oscillation has been observed in the flow between cells. This oscillation results from the inertia term in the intercell flow equation and is often irrelevant to the problem at hand. Because this limits the size of time steps, an option has been added which allows a quasi-steady flow calculation

to be used. This option allows the inertia term to be omitted, thereby eliminating the oscillations.

A debris-concrete model is now operational, providing a simple simulation of the erosion of concrete by molten core debris and the generation of gas (hydrogen and carbon dioxide). The water released from the concrete when it melts is assumed to react with the hot debris to form hydrogen. In this version, the CO₂ released from the concrete does not undergo further chemical reactions. The Sodium Concrete Ablation Model (SCAM) developed in the sodium-concrete interaction program has been implemented as a set of subroutines which can be run in CONTAIN. This provides the best available physical model for the interaction of sodium with basaltic concrete. No comparable model currently exists for limestone concrete (which will be used in Clinch River) as the governing mechanisms have not yet been established.

A draft of the documentation for CONTAIN 1A has been completed and is available for limited distribution. This provides details of the physical models, the code structure, and the input and output of the code.

As a test problem of some of CONTAIN's capabilities to handle LWR calculations, a portion of a TMLB¹ sequence at ZION I has been selected, in part because this sequence has been studied extensively in Sandia's SASA program using the MARCH code. For this problem, which calculates the containment response to predetermined steam sources, CONTAIN was set up to model the containment in the same fashion as MARCH to provide cross checks on the two codes. Generally good agreement was found.

Two papers were presented during the quarter. The first²⁻¹ was presented at the ANS/ENS conference in Munich in late April. It described the mathematical framework and models in SINTER, CONTAIN's pool model. The second²⁻² was presented at the ANS meeting in Miami, June 7-11, 1981 and described the general features of CONTAIN. It also gives an example of a CONTAIN calculation.

2.2 MARCH Assessment Project (J. B. Rivard, 4421; F. E. Haskin, 4424)

At NRC's request, Sandia is undertaking an assessment of the MARCH code, used to analyze severe LWR accidents.

This is being done under the auspices of the Containment Analysis Program.

The focus of LWR safety concerns has recently expanded beyond the large-LOCA design-basis accident to consideration of system response to severe core damage accidents (including meltdown) of several hours duration. The MARCH computer code²⁻³ was conceived as a tool for use in risk assessments; however, because MARCH models severe core-damage sequences, it has been used to satisfy previously unanticipated, but pressing analysis needs. The expanded usage of MARCH has generated many questions regarding the extent, appropriateness, and accuracy of the modeling in the code. Considerable discussion has ensued regarding the application and interpretation of MARCH results. An assessment of MARCH was prepared²⁻⁴ in response to a request by NRC to clarify the capabilities and limitations of MARCH within the context of current applications, to evaluate the major modeling and phenomenological uncertainties associated with the calculation of severe accident progression, and to recommend how MARCH should be used and/or improved.

To reduce the time required, the assessment was based primarily upon existing information (available from the NRC and its contractors). New evaluations were initiated only where the information needed was deemed essential and where the necessary resources and time were available. This paper summarizes the findings and recommendations of the assessment.

2.2.1 Findings

Although the MARCH code was developed primarily for risk assessment, it can provide broadly useful scoping examinations of coupled primary system and containment response to a spectrum of unterminated meltdown-accident sequences, including various loss-of-coolant accidents (LOCAs), and transients, with and without the action of various engineered safety systems. MARCH was not designed to treat the termination of severe core-damage accidents.

MARCH attempts a comprehensive treatment of meltdown accidents and reactor/containment types within a small code with rapid execution characteristics on present-day computers. This has required that phenomena and systems be modeled simplistically and with a minimum of detail. This approach was justified during code development on

the basis of the intended application, i.e., risk analysis. The approach may also have been partly due to limited resources for code development and/or the limited phenomenological knowledge base.

However, some of the models in MARCH are overly simplistic; they reduce phenomena and systems to a simplism that ignores complicating and often important factors. This modeling approach seriously restricts the usefulness of the code for many applications and can result in code predictions which are not physically realizable. Examples include a single-volume primary model, lumped-fuel/clad nodes, fixed pressure in the steam-generator secondary, and nonmechanistic heat-transfer modeling.

Many phenomena are not modeled in MARCH at all, and some of these phenomena are important for most applications. Examples include the oxidation of steel structures and other hydrogen sources (other than oxidation of zircaloy), the downward relocation of fuel as it melts and freezes, phenomena accompanying steam explosions (fragmentation, dispersal), and core barrel heatup/failure in PWRs.

Significant improvement in the level of modeling in MARCH is possible, but would in some cases be limited by inadequate knowledge concerning specific phenomena. For example, the changing geometry of the core as portions of it melt, flow downward, freeze and then remelt, cannot be described on a completely mechanistic basis because the geometry changes depend on poorly understood interactions between multicomponent phase change, chemical, heat transfer, and hydrodynamic effects. Other examples include the fragmentation and dispersal of quenched core materials, oxidation reactions during transient melt-water interactions, and certain aspects of the transport and burning of combustible gases.

The structure and programming of MARCH, together with limited code documentation, hindered the assessment. The design of MARCH did not anticipate assessment and verification requirements. In particular, the nonmodular structure (one subroutine exceeds 2400 statements), inadequate code comments, lack of systematic and global mass/energy balance information, and incomplete and misleading documentation, provide significant deterrents to understanding the detailed calculational procedures. Areas in which MARCH fails to comply with recommended practices for code

development (ANSI-ANS-10.5-1979), code documentation (ANSI N413-1974) and programming (ANS Std. 3-1971) are discussed in the assessment report.

The limited code documentation and the lack of several fully-documented sample problems provide an inadequate basis for applying MARCH.

In many applications, different users of a code like MARCH should expect to obtain similar results when calculating a given accident sequence for a certain plant. However, even with identical plant parameters for a given accident sequence, MARCH results could differ significantly between users because of the sensitivity of MARCH predictions to user-specified modeling parameters which are neither reactor-plant-determined nor accident-sequence-determined. In most cases, these parameters represent inputs which are made necessary by modeling simplisms within the code.

Taken together, limitations, errors and deficiencies identified in MARCH may seriously compromise the validity of some code predictions. Some examples are given in the assessment²⁻⁴ but a much more thorough study would be required to provide a comprehensive list of limitations, errors, and deficiencies. The evidence uncovered during the assessment does not support the sometimes-heard opinion that MARCH accident sequence predictions are "conservative" (more severe than realistically expected), although some features of MARCH, individually considered, do appear to be designed to give "conservative" results.

2.2.2 Recommendations

Although an NRC-sponsored program designed to assess more comprehensively the capabilities and limitations of MARCH would have some intrinsic merit and would provide a better basis for application of MARCH, the opinion of the assessment project group is that the resources which would be required would be better allocated to the improvement of MARCH or the development of alternatives. This conclusion results in part from the identification, in the assessment, of a number of changes and modifications which would substantially improve MARCH capabilities and which could be made immediately in spite of recognized phenomenological uncertainties.

In terms of current computing costs, MARCH is very inexpensive to run. A large (i.e., an order of magnitude) increase in execution time, if coupled with a corresponding increase in model complexity, detail, and algorithmic rigor, would not seriously hinder the bulk of current applications of MARCH.

Some modifications of MARCH to improve its capabilities would be difficult. One significant deterrent to modification is the sequential processing structure of the code which prevents the treatment of some parallel (and coupled) phenomena. However, the clear need of NRC for severe accident sequence calculations appears to the assessment team to require the early implementation of a robust NRC program for the improvement of MARCH or the development of alternatives.

Assuming that a program at some level will be instituted by the NRC to improve MARCH, an organizational structure to support this effort is recommended in the assessment report. Included would be a forum for MARCH users, both inside and outside the NRC, to provide comprehensive and balanced review, discussion, and recommendation of MARCH improvements.

The limitations identified in this assessment may seriously compromise the validity of some code predictions. The assessment also shows that code predictions are sensitive to the selection of input parameters and modeling options. Hence, it is recommended that application of this version of MARCH to formal safety evaluations be subject to two conditions:

- a. Code results be accompanied by explicit evaluation and discussion of code limitations with regard to their potential for invalidating the conclusions drawn from the code results.
- b. Calculations be made using a documented version of the code with data input appropriate to the plant and accident sequence, and with a fully accessible set of values for the modeling parameters and options used.

References for Section 2

- 2-1. M. E. Senglaub, "The Multi-Component Drift Flux Formulation for the SINTER Subsystem of CONTAIN," Proceedings of the International Topical Meeting on Advances in Mathematical Methods for the Solution of Nuclear Engineering Problems, Munich, April 27-29, 1981, pp 177-194.
- 2-2. J. P. Odom et al., "CONTAIN: A Computer Code for Simulation of Reactor Accident Containment," Transactions of the ANS Annual Meeting, Miami, Florida, June 7-11, 1981, pp 328-330.
- 2-3. R. O. Wooton and H. I. Avci, MARCH (Meltdown Accident Response Characteristics) Code Description and User's Manual, BMI-2064, NUREG/CR-1711 (Columbus, OH: Battelle Columbus Laboratories, October, 1980).
- 2-4. J. B. Rivard, Interim Technical Assessment of the MARCH Code, SAND81-1672, NUREG/CR-2285 (Albuquerque, NM: Sandia National Laboratories, November, 1981).

3. ELEVATED TEMPERATURE DESIGN ASSESSMENT
(C. H. Karnes, 5835; J. A. Van Den Avyle, 5835;
W. B. Jones, 5835; J. H. Gieske, 1552)

The primary objectives of the elevated temperature design assessment studies are (a) to determine how microstructures evolve due to thermomechanical history resulting in mechanical property changes, (b) to evaluate the validity of material damage rules used in design, and (c) to develop and evaluate nondestructive evaluation techniques.

3.1 Creep-Fatigue Studies

Additional creep-fatigue crack growth tests on 316 stainless steel were completed at 866 K (593°C) with two plastic strain ranges and different combinations of hold periods. Table 3-I lists all of the crack growth experiments conducted to date.

Figure 3.1-1 compares crack growth behavior at equivalent strain ranges for a sample (316-CG-2) subjected to pure fatigue and no hold periods, two samples (316-CG-14 and 19) subjected to 5 min. tensile hold, and one sample (316-CG-17) subjected to a 10 min. tensile hold. Data for the three tests with creep components show growth rates roughly equal and about five times greater than the non-hold test at the same levels of applied J , the change in the J integral parameter. All four curves contain a lower plateau of constant crack growth independent of J at short crack lengths. The general shapes from the combined creep-fatigue tests are similar to the pure fatigue tests.

Growth rates for 10 min. tensile holds at two strain ranges, 0.0012 (316-CG-17) and 0.0024 (316-CG-18), are compared in Figure 3.1-2 along with reference data from a non-hold test at a strain range of 0.0015 (316-CG-2). Again the two combined creep-fatigue experiment curves are equivalent and range about a factor of 5 higher in growth rate than the pure fatigue tests.

Generally, growth rates from all tensile hold creep-fatigue tests conducted to date are roughly equivalent, and average about 5 times higher growth rate per cycle than the continuous cycle tests. The one compressive hold test (316-CG-16) had growth rates midway between the non-hold and tensile hold curves.

Table 3-I. Fatigue Growth Testing of 316 Stainless Steel at 5/3°C ($\epsilon = 4 \times 10^{-3} \text{ sec}^{-1}$)

<u>Specimen No.</u>	<u>Plastic Strain Range,</u>	<u>Hold Period *(Min.)</u>
316-CG-1	.0040	
-2	.0015	
-3	.0009	
-4	.0009	
-5	.0038	
-6	.00055	
-7	Void	
-8	.0004	
-9	Not Tested	
-10	Not Tested	
-11	.00065	
-12	.00082	
-13	Void	
-14	.0015	5T
-15	.0025	--
-16	.0013	5C
-17	.0012	10T
-18	.0024	10T
-19	.0012	5T

*T denotes tensile hold, C denotes compressive hold.

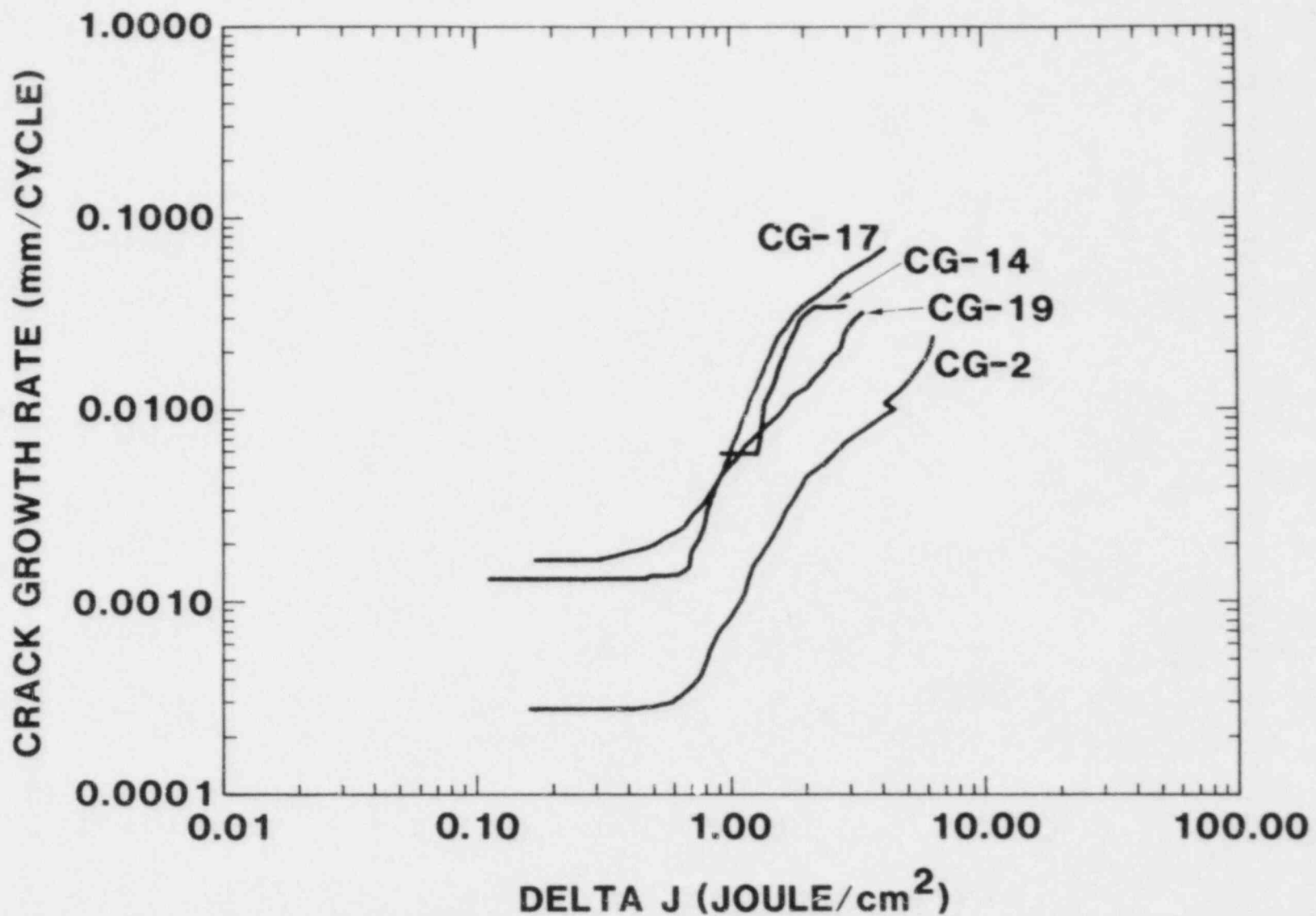


Figure 3.1-1. Crack Growth Rates for 316 Stainless Subjected to Low Cycle Fatigue (No Hold Periods) at 886K (593°C)

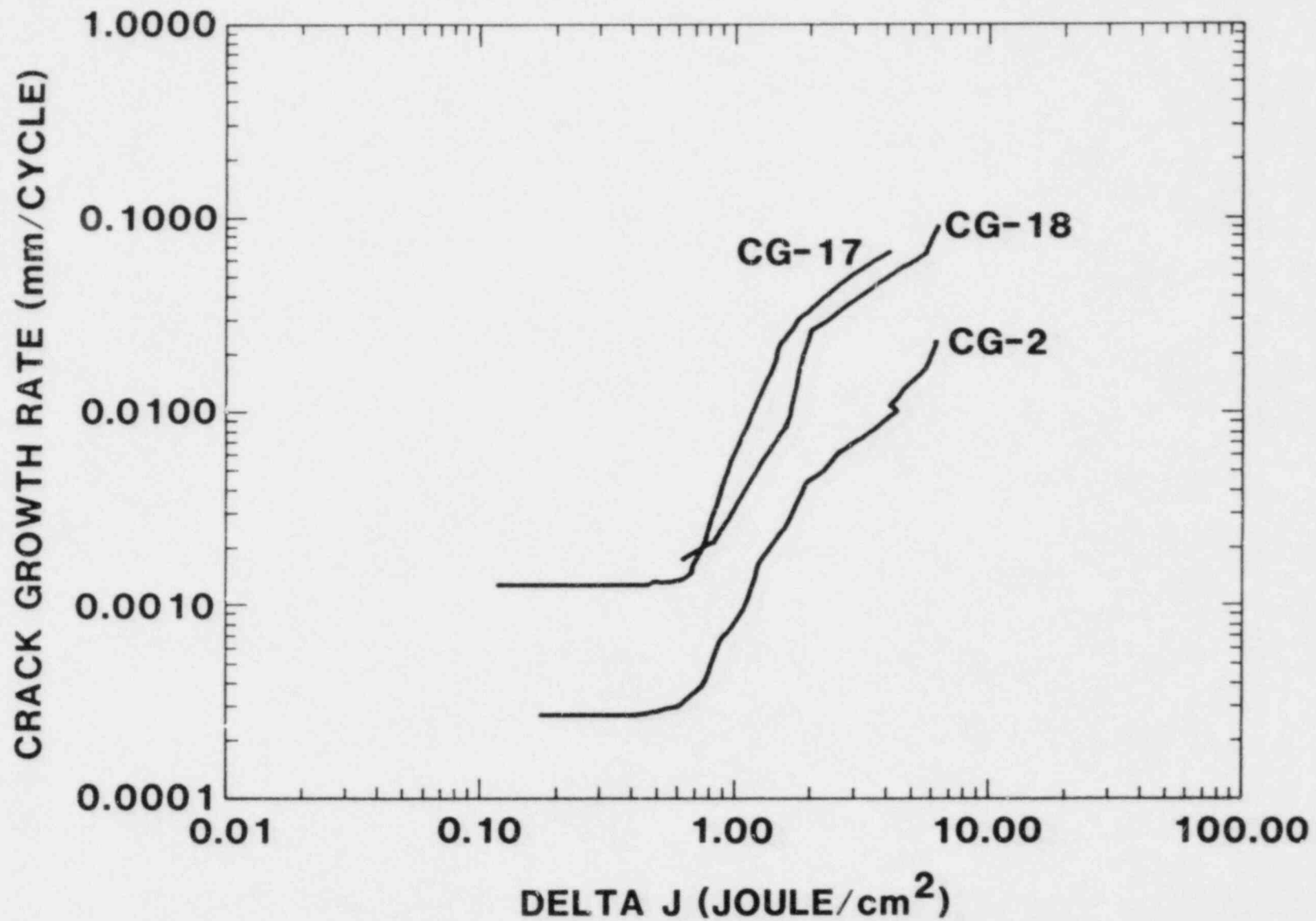


Figure 3.1-2. Crack Growth Rates for 316 Stainless Subjected to 10 min. Tensile Hold Periods at 866K (593°C)

3.2 Nondestructive Examination Studies

These studies are continuing under other funding and the results will be available to this program when progress is made.

3.3 Microstructural Analysis

The studies are continuing in cooperation with Oak Ridge National Laboratory to understand why Modified 9Cr-1Mo exhibits damaging compressive-hold-time effects even though it does not oxidize. Surface oxidation has been identified as the cause of compressive hold time effects in ferritic alloys of lower chromium content.

Microstructural studies have been performed on the starting material, isothermally aged, fatigued- and creep-fatigue-damaged specimens in order to characterize the evolution of the microstructures. Transmission electron microscopy of carbon-extraction replicas of fatigue and creep-fatigue specimens were studied. Both metal-carbide (MC) and $M_{23}C_6$ type carbides were present in the starting material. The $M_{23}C_6$ particles are primarily $(Cr, Fe)_{23}C_6$ and are several tenths of a μm in size. The MC particles are $(Nb, V)C$ and most are Nb rich and less than $0.1 \mu m$ in size. Investigators found that isothermal aging at 811 K ($538^\circ C$) for 1000 hours without mechanical deformation does not affect the carbide distribution.

Cycling with hold times (creep-fatigue) results in growth of the carbide precipitates. Hold times of 0.1 hr produce $M_{23}C_6$ particles of approximately $1 \mu m$ in size. These are also shown to pick up significant amounts of Mo, becoming $(Cr, Fe, Mo)_{23}C_6$. There was no evidence of Mo_2C type carbides as had been observed in 2 1/4 Cr-1Mo steel. The fatigued samples showed no observable change in dislocation density or carbide characteristics.

4. LMFBR ACCIDENT DELINEATION

4.1 Introduction and Overview (D. C. Williams, 4424)

The purpose of the LMFBR Accident Delineation Study⁴⁻¹ (ADS) is to investigate the applicability of the methodology developed by the Reactor Safety Study (WASH-1400) to advanced systems such as an LMFBR, and to apply this methodology insofar as is possible to systematize the existing body of LMFBR safety information. Goals include: (a) provide a demonstrated methodology for delineating LMFBR accident sequences, (b) determine dominant accident sequences with corresponding radioisotope-release categories, and (c) identify and systematize the key phenomena governing the accident sequences. Illustrative facilities used in the study include the CRBRP and, more recently, alternative designs such as the DOE's Conceptual Design Study (CDS). The delineation study is organized into three major areas designated engineered safety systems (ESS), accident phenomenology, and postaccident phenomenology.

Phase I of the ADS was completed at the end of FY80 and results were described in detail in the Phase I Final Report.⁴⁻¹ This work included comprehensive qualitative delineation of LMFBR accident sequences from the initiating subsystem failures to definition of radiological release categories. Event tree methodology was used throughout and simplified fault tree models were developed (but not quantified) for three ESS functions (detection, SCRAM, and shutdown heat removal system (SHRS) availability).

In Phase II of the ADS, now underway, ADS personnel will undertake a more detailed, more quantitative evaluation for certain selected topics identified in Phase I as being of great interest. In the ESS area, the work involves an approximate quantification of the simplified Phase I fault trees in order to estimate relative recurrence frequencies of the various accident categories and, thus, permit analyses in the Accident Phenomenology area to concentrate on the categories found to be most important. Consistent with this goal and with the level of effort involved, results obtained in the ESS analysis are to be treated as relative probability estimates, not predictions of actual recurrence frequencies or absolute probabilities.

During this quarter, work in the ESS area concentrated on analyzing the contributions to the various accident categories that arise from loss of offsite power and from earthquake initiators. Results indicate that these are potentially significant contributors to major accident categories but that these initiators may not be dominant, i.e., the estimated contributions to the various recurrence frequencies from these causes did not exceed corresponding contributions estimated for other major accident scenarios.

Application of the SAS3D code continued in order to analyze UTOP accidents resulting from uncontrolled rod withdrawal without SCRAM in the CRBRP heterogeneous core (BOC4 configuration). Withdrawal of a single rod inserts 65¢, which was found to be insufficient to lead to probable pin failure. Withdrawal of a bank of six rods at maximum possible speeds (72 in/min) can insert up to \$2.86 at rates of 20¢/s; for this scenario, pin failures are predicted to occur after sodium boiling has started in some coolant channels. Difficulties with the SAS3D code and its User's Manual have slowed this work significantly.

Work was initiated to define better the protected accident scenarios that could threaten core integrity, and also to define the time of onset of core disruption for various postulated SHRS failures. Toward this end, negotiations were initiated with the University of Arizona for obtaining assistance with installation of its BRENDA code on a VAX computer system available to the investigators. Also, five SHRS-failure scenarios were defined and sent to Brookhaven National Laboratory (BNL) for analysis with its SSC code.

In the postaccident phenomenology area, the current effort to clarify containment-research priorities has been largely completed. A draft report describing this effort and its results has been completed and is now in the Sandia review process. Though significant revisions of the draft are likely, the major results of the study are not expected to differ greatly from those cited in previous quarterly reports.

An effort was initiated to assess the response of the CRBRP containment systems to large accidents. Work during this period included planning, data collection, and familiarization with the CONTAIN code which will be the principal analysis tool. Important phenomena that CONTAIN cannot yet treat were identified. In addition, prior analyses of containment response were subjected to a brief review. This work included gathering information on the primary boundary's ability to withstand CDA energetics, and also obtaining information on the capabilities and limitations of existing analysis tools for treating this problem.

At the NRC's request, the possibility of scaling up the ADS into a risk assessment for CRBRP was addressed in some detail. This proposal, named the Clinch River Risk Assessment Study (CRRAS), would draw upon the expertise and methodologies developed in both the Interim Reliability Evaluation Program (IREP) and the ADS program. The proposed CRRAS was found to be a desirable program provided its purpose is accepted as being largely exploratory rather than concentrating principally on the development of firm numerical risk estimates for CRBRP. A formal proposal for the CRRAS was prepared and sent to NRC.

Detailed results for the three major areas of the ADS are discussed further in Sections 4.2-4.4 to follow, and Section 4.5 presents some additional information on the CRRAS proposal.

4.2 Engineered Safety Systems (ESS) (E. R. Copus, 4424)

4.2.1 Introduction

The ADS Phase I Report⁴⁻¹ developed a set of reduced initiating-accident event trees for the Clinch River Breeder Reactor Plant. These event trees describe a set of accident categories which result from initiators affecting the heat transfer capability of CRBRP. The branch points of the Engineered Safety Systems (ESS) event trees described in the Phase I report are: detection, SCRAM, pump trip, SHRS, and forced flow. Fault tree models which describe these ESS functions have been developed and independent failure probabilities with uncertainty bounds have been estimated. These values are tabulated below.⁴⁻²

<u>ESS Function</u>	<u>Failure per Challenge</u>	<u>Uncertainty Factor</u>
Detection	8×10^{-10}	10
SCRAM	7×10^{-8}	10
Pump Trip	3×10^{-4}	5
SHRS	2×10^{-8}	5
Forced Flow	5×10^{-6}	5

Quantitative analyses of the accident categories identified for CRBRP in Chapter 3 of the Phase I report involved four steps for each of the major CRBRP systems involved in the generation, control, and transfer of heat (i.e., operator, reactor, primary heat transfer, intermediate heat transfer, and steam/electrical generation) within the plant. These four steps are:

- a. Systems initiators and their recurrence frequencies were identified.
- b. ESS common cause relationships were established for each initiator.
- c. Conditional ESS branch-point-failure probabilities were estimated for each initiator.
- d. Relative accident-category recurrence frequencies were estimated using the appropriate event trees.

The methodology employed here can be used to generate absolute recurrence frequency estimates for such purposes as risk assessment. However, the objective of the present work is the more limited goal of estimating the relative probabilities of different accident categories in order to permit analyses in the accident phenomenology and containment areas to concentrate on the dominant categories. Hence, all results will be reported as relative recurrence frequencies. After the results are combined to give totals for the various accident categories, they can be normalized relative to the total estimated CDA recurrence frequency; the present results are intermediate values not normalized to any specific quantity.

This report continues this approach for accident scenarios that are initiated by a loss of offsite power or earthquake. These initiators are often categorized as external events and have the potential to affect all of the ESS functions simultaneously. Consequently, Steps 2 and 3 of the analysis for these external events are more detailed than in the previous work, resulting in a number of potentially dominant accident paths.

4.2.2 Loss of Offsite Power Initiator

Traditionally, the loss of offsite power is considered one of the potentially dominant common-cause initiators because almost all reactor and heat transfer control devices are electrically driven. While the estimated recurrence frequency and duration of this type of event varies considerably from study to study, the values used for the present analysis are assumed to lie in the range of .03 to 0.3 per year with a median value of 0.1 per year and with no chance for recovery after failure.⁴⁻³ Common cause relationships for the ESS are assumed to vary directly according to their dependence on emergency diesel or DC power sources as well as the number of components within each system which might conceivably be affected by an adverse electrical environment. These relationships range from zero for the detection and pump trip functions to moderate for the SCRAM and forced flow functions and high for the SHRS function. Numerical estimates for the conditional failure probability of the ESS functions due to a loss of offsite power are summarized in Table 4-1. Uncertainty factors quoted below, and in subsequent tables, include only contributions from initiating component or subsystem failure-frequency uncertainties. Contributions to the uncertainty from the simplified system model used and the uncertainties in the assumed common cause relationships are not included and could well dominate a comprehensive error estimate.

Table 4-I

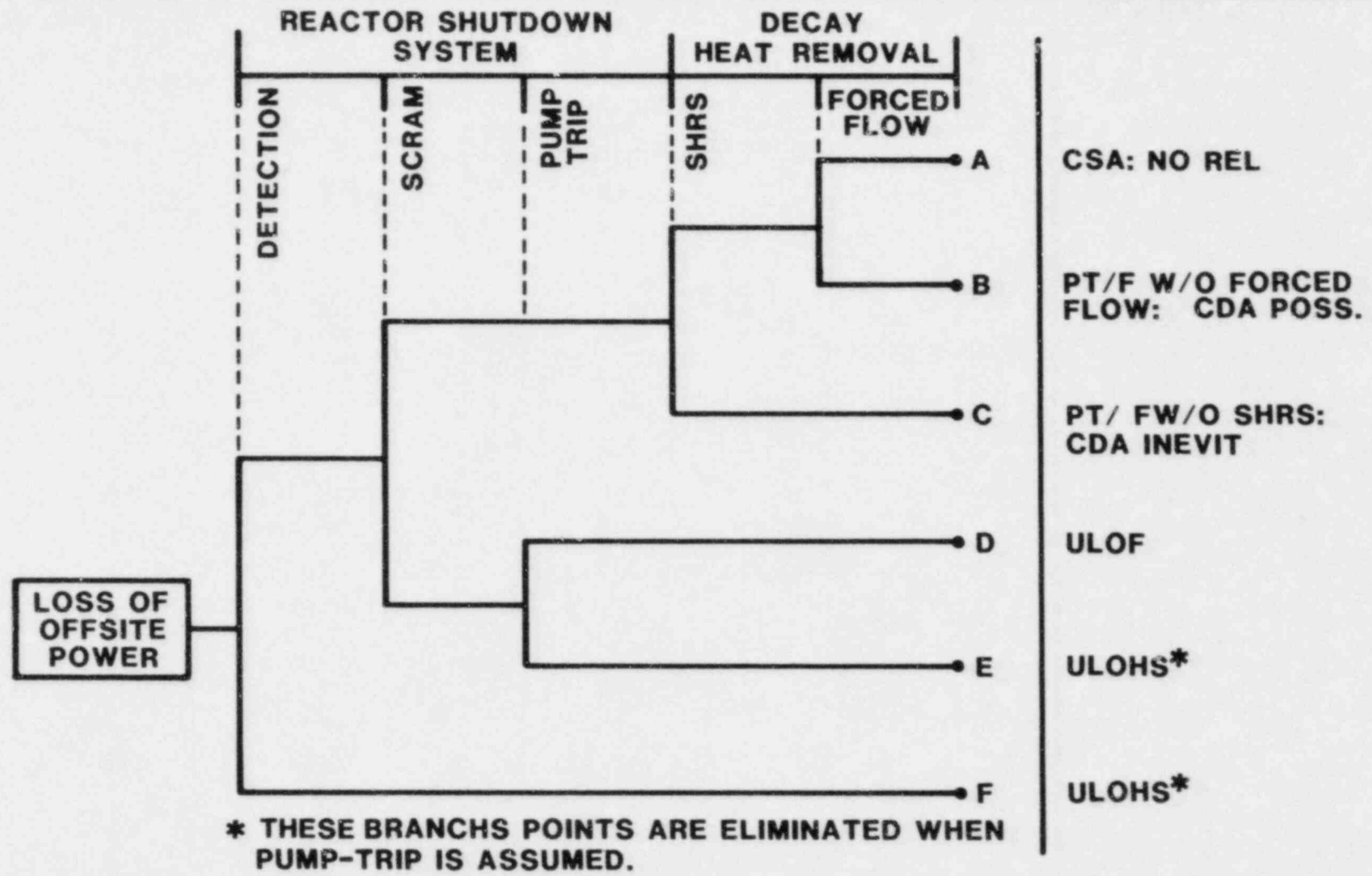
ESS Common Cause Relationships for
Loss of Offsite Power

<u>ESS Function</u>	<u>Common Cause Considerations</u>	<u>Relative Failure Probability and Uncertainty Factor</u>
Detection	Probability of failure (Pf) = 0. if pump trip assured	0.
SCRAM	Unknown; 10X increase in electrical faults per rod	2.0×10^{-7} (5)
Pump Trip	No backup power to pumps	0.
SHRS	30 critical components affected (3-100X)	1.8×10^{-4} (2)
Forced Flow	3X per pump increase	1.4×10^{-4} (5)

In Table 4-I, the detection function and the pump trip function are eliminated from further consideration since pump trip is virtually assured in the absence of any backup power supply. This means that the only credible unprotected accident scenario for the loss of offsite power initiator is a ULOF and that points E and F can be ignored in the event tree of Figure 4.2-1 which can be used to describe the remaining loss of offsite power accident scenarios.

The SHRS function has at least 30 critical components which can be affected by a loss of offsite power.⁴⁻² These components include pumps, control valves, fans, and pony motors within the normal heat train as well as similar components within the DHRS and SGAHRS. The failure probabilities for these components were initially estimated to increase by factors ranging from 3 to 100 in order to sort out the leading terms in the SHRS minimal-cut-set equation. Sensitivity studies were then performed on these leading terms in order to determine the envelope of SHRS response as a function of the common cause related increase in the failure probabilities of the critical components. The results of these studies are summarized in Table 4-II.

INITIATOR	ENGINEERED SAFETY SYSTEM (ESS) RESPONSES	SEQ. I.D.	INITIATING ACCIDENT CATEGORIES
-----------	--	-----------	--------------------------------



4-7

Figure 4.2-1. Initiating Accident Event Tree for a Loss of Offsite Power

Table 4-II

SHRS Response as a Function of
Common Cause Relationships

<u>Critical Component Pf Increase</u>	<u>SHRS Failure Probability</u>
1X	$1.08 \times 10^{-4} *$
2X	1.22×10^{-4}
5X	1.5×10^{-4}
10X	2.4×10^{-4}
20X	6.1×10^{-4}
Best Estimate (3X-100X)	1.8×10^{-4}

*Leading term due to diesel failure ($Pf \approx 10^{-4}$).

These studies reveal that while common-cause failures other than those caused by diesel failure are important, they will not dominate the conditional SHRS-failure probability unless each identified critical component is at least 20 times more likely to fail during a loss of offsite power than under normal conditions. Since this seems unlikely, the original component estimates are assumed to be best estimates and the reported failure probability for the SHRS function is 1.8×10^{-4} .

Using the conditional failure probabilities from Table 4-I in conjunction with the event tree paths identified in Figure 4.2-1, the generic accident category frequency estimates shown in Table 4-III are produced.

From Table 4-III the path with the highest potential for a Core Disruptive Accident is a Protected Fault without SHRS with an estimated frequency of 1.8×10^{-5} per year. This path is expected to contribute significantly towards the overall frequency of the PT/F w/o SHRS generic accident category.

Table 4-III

Accident Types and Frequencies for the
Loss of Offsite Power Initiators

Accident Type	Estimated Relative Frequency	Uncertainty Factor
A. CSA: No Release	.1	3
B. PT/F w/o Forced Flow	1.4×10^{-5}	7
C. PT/F w/o SHRS	1.8×10^{-5}	4
D. ULOF	2.0×10^{-8}	7

4.2.3 Earthquake Initiators

Severe earthquakes are often considered as the most serious threat to a reactor system and most reactors are designed to withstand an operating base earthquake (OBE) of at least magnitude five on the Richter Scale. Nevertheless, almost any significant earthquake will affect the conditional failure probability of all of the engineered reactor safety systems to some degree and, therefore, represents a potentially dominant common-cause accident initiator. Three different earthquake initiators were chosen in order to analyze the CRBR design: (a) The CRBR Operating Base Earthquake (OBE) with an estimated frequency of 1.4×10^{-3} per year and a ground acceleration of 0.125 g. This earthquake measures 5.5 on the Richter Scale and is described as "difficult to stand" on the Mercali damage index. (2) The CRBR Safe Shutdown Earthquake (SSE) with an estimated frequency of 1.5×10^{-4} per year and a ground acceleration of 0.25 g. This earthquake measures 6.5 on the Richter Scale and is described as "difficult to drive" on the Mercali index; (3) A greater than Safe Shutdown Earthquake (BFE) with a frequency of 3.4×10^{-5} per year and a ground acceleration of 0.4 g. This earthquake measures at least 7 on the Richter Scale and is described as "general panic" on the modified Mercali Scale.^{4-3,4-4} Each of these three earthquake initiators was then arbitrarily subdivided into five separate initiator scenarios. Each of these five scenarios is illustrated by an event tree (Figures 4.2-2 through 4.2-6). Scenario 1 is a reactivity insertion without core damage or loss of

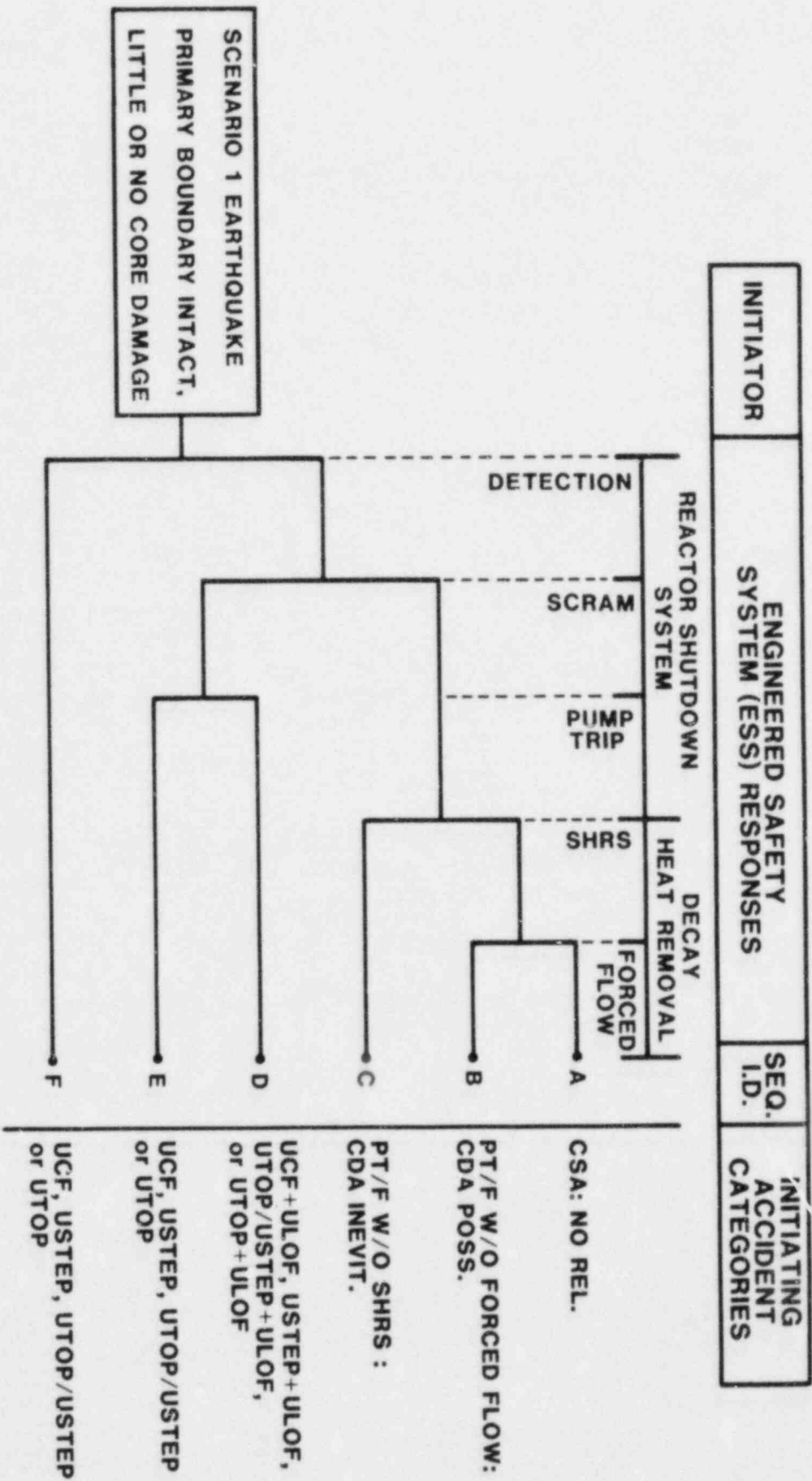


Figure 4.2-2. Initiating Accident Event Tree for Scenario 1 Earthquakes

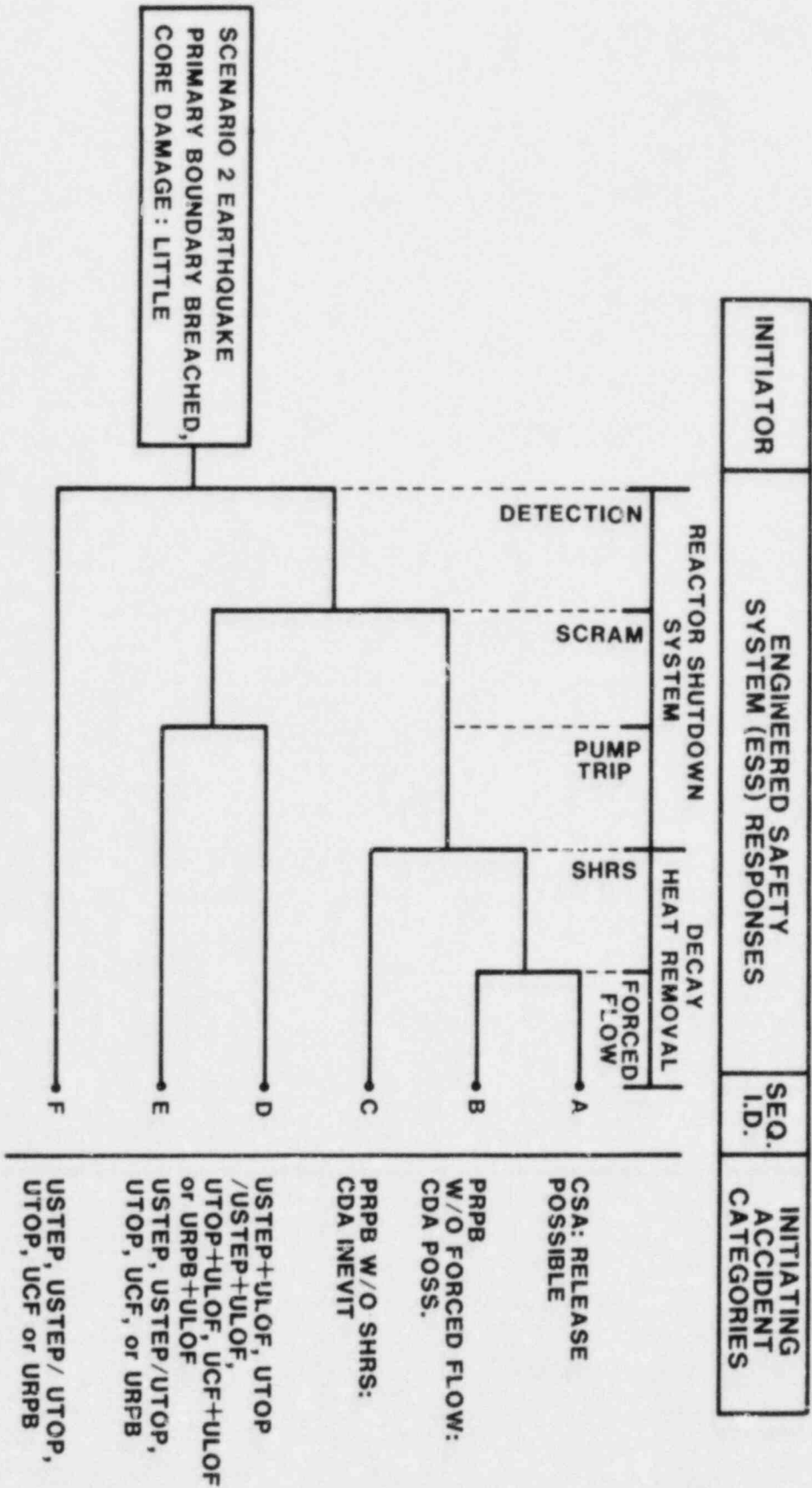


Figure 4.2-3 Initiating Accident Event Tree for Scenario 2 Earthquakes

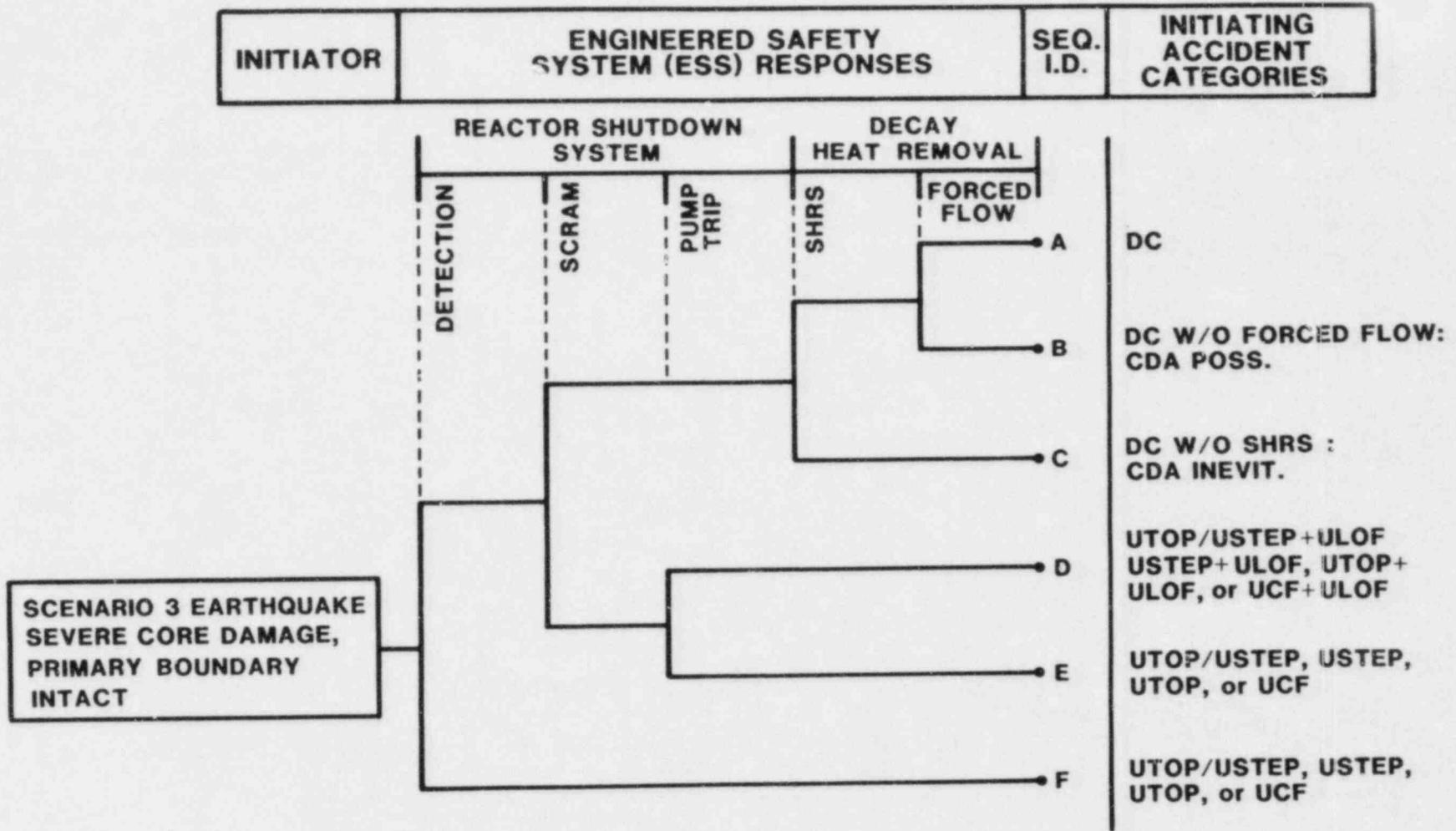


Figure 4.2-4. Initiating Accident Event Tree for Scenario 3 Earthquakes

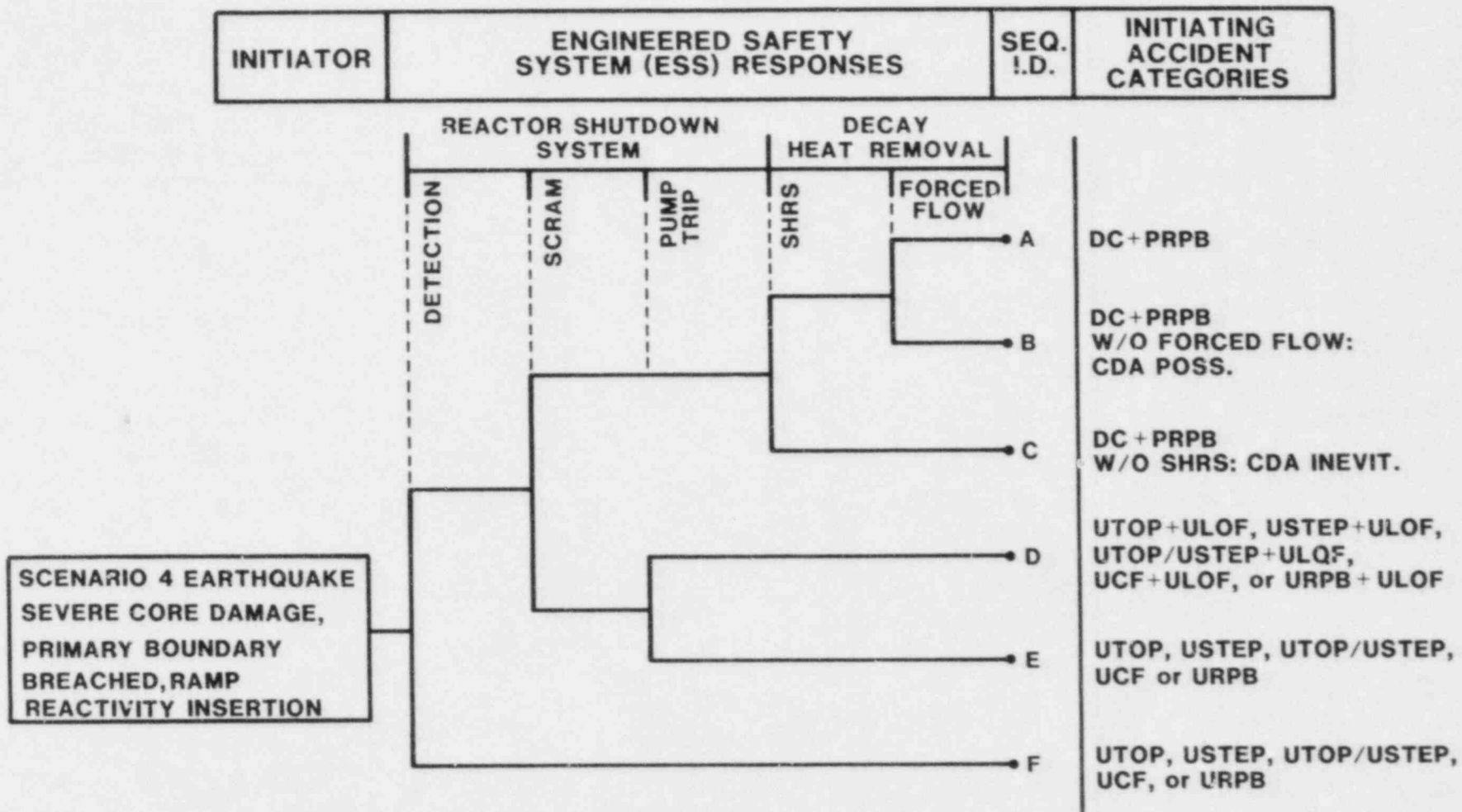


Figure 4.2-5. Initiating Accident Event Tree for Scenario 4 Earthquakes

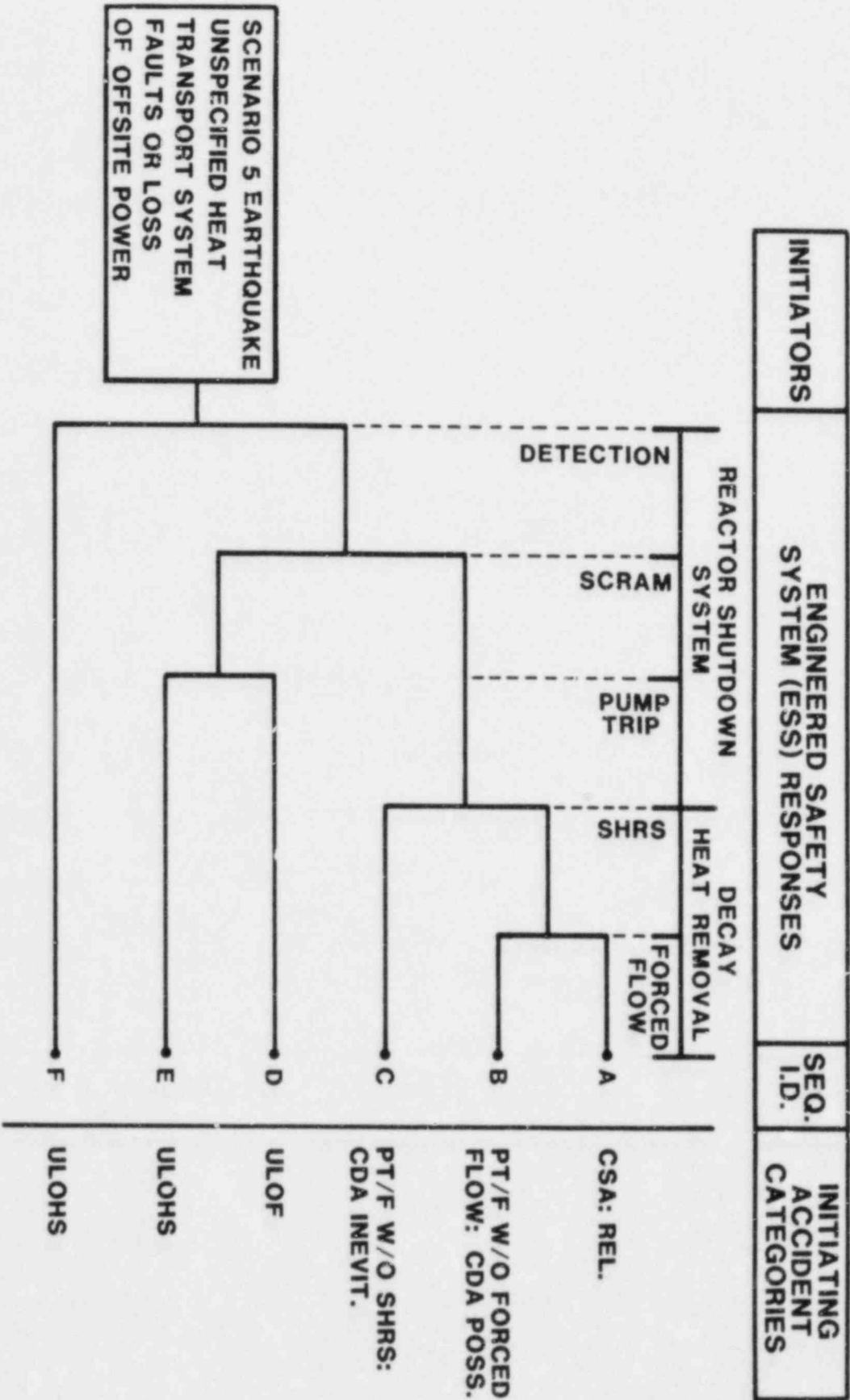


Figure 4.2-6. Initiating Accident Event Tree for Scenario 5 Earthquakes

primary boundary, whose outcomes are the end points of the event tree in Figure 4.2-2. Scenario 2 is a reactivity insertion with minor core damage and a loss of primary boundary, whose outcomes are the end points of the event tree in Figure 4.2-3. Scenario 3 is a reactivity insertion with severe core damage and with primary boundary intact, whose outcomes are the end points of the event tree shown in Figure 4.2-4. Scenario 4 is a reactivity insertion with severe core damage and the loss of the primary boundary, whose outcomes are the end points of the event tree shown in Figure 4.2-5. Scenario 5 is unspecified heat transport system failures, or loss of offsite power, whose outcomes are the end points of the event tree shown in Figure 4.2-6.

Thus, 15 individual initiating scenarios exist that can be evaluated using the event trees shown in Figures 4.2-2 through 4.2-6. By assuming that the relative incidence of primary boundary rupture and core damage increases with earthquake intensity, and by arbitrarily assigning these values, each earthquake initiator can be expressed as the sum of five scenario-related initiators. These initiators are summarized in Table 4-IV.

Table 4-IV
Earthquake Initiator Frequencies, Per Year

Total	Scenario 1	Scenario 2	Scenario 3	Scenario 4	Scenario 5
	No PB* No DC*	PB No DC	DC No PB	DC PB	HTS*
OBE (1.4×10^{-3})	5.7×10^{-4}	6.3×10^{-5}	6.3×10^{-5}	7×10^{-6}	7×10^{-4}
SSE (1.5×10^{-4})	3.6×10^{-5}	2.4×10^{-5}	9×10^{-6}	6×10^{-6}	7.5×10^{-5}
BFE (3.4×10^{-5})	2×10^{-6}	8.2×10^{-6}	1.4×10^{-6}	5.4×10^{-6}	1.7×10^{-5}

PB = Primary Boundary Failure
DC = Damaged Core
HTS = Heat Transport Systems Failure

Common-cause considerations for the engineered safety systems vary for each of the 15 earthquake initiators and are dependent on four main factors: reactivity insertion, flow disturbance, loss of power, and most importantly, ground acceleration. The failure rates for components within each of the ESS functions are assumed to vary linearly with ground acceleration while reactivity and flow disturbances each increase failure rates 10% for the OBE, 5% for the SSE, and only 1% for the BFE. Loss of offsite power is assumed to occur 90% of the time during a BFE, 50% during a SSE, and 10% during an OBE. The results of summing all of these effects for each of the ESS systems and each earthquake initiator are presented in Table 4-V.

The detection function is assumed to occur in one of two ways: detection due to reactivity transients within the core or detection due to flow and heat transfer perturbations throughout the system. For detection due to reactivity transients, the base failure probability is taken as 4×10^{-8} per challenge⁴⁻² and is increased by factors of 30, 500, and 1.5×10^4 for the OBE, SSE, and BFE, respectively. When detection is due to flow and heat transfer perturbations, the base failure probability is 8×10^{-10} and is increased by factors of 120, 8×10^3 , and 7.5×10^5 for the OBE, SSE, and BFE. The essential difference between the two means of detection lies in the number of protection functions (five for reactivity events and seven for flow/heat transfer) which will sense the anomalous condition. The failure probability for each of these protective functions is assumed to increase linearly with ground acceleration, resulting in the reported factors.

The scram-function-conditional-failure probability was assumed to increase linearly with ground acceleration on a per rod basis with four rods required to fail for system failure.⁴⁻² Reactivity and flow perturbations added 10, 5, or 1% to the increase as previously reported. Pump trip and forced flow failure rates also increased with ground acceleration and were further affected by the loss of one pump for those cases when primary boundary failure was presumed.

Table 4-V

Consolidated Conditional ESS Probabilities (and Uncertainty Factors)
for Earthquake Initiators

	Scenario 1	Scenario 2	Scenario 3	Scenario 4	Scenario 5	
<u>ORE</u>	DTECT	1.2x10 ⁻⁶ (10)	9x10 ⁻⁸ (10)	1.2x10 ⁻⁶ (10)	9x10 ⁻⁸ (10)	9x10 ⁻⁸ (10)
	SCRAM	1.6x10 ⁻⁴ (4)	2.3x10 ⁻⁴ (4)	1.6x10 ⁻⁴ (4)	2.3x10 ⁻⁴ (4)	1x10 ⁻⁴ (4)
	PTRIP	5.4x10 ⁻⁴ (5)	3.6x10 ⁻⁴ (5)	5.4x10 ⁻⁴ (5)	3.6x10 ⁻⁴ (5)	5.4x10 ⁻⁴ (5)
	SHRS	1.2x10 ⁻³ (1.3)	6x10 ⁻² (1.2)	1.2x10 ⁻³ (1.3)	6x10 ⁻² (1.2)	1.2x10 ⁻³ (1.3)
	PFLOW	2.2x10 ⁻³ (2)	1.7x10 ⁻² (2)	2.2x10 ⁻³ (2)	1.7x10 ⁻² (2)	2.2x10 ⁻³ (2)
<u>SSE</u>	DTECT	2x10 ⁻⁵ (7)	6.4x10 ⁻⁶ (7)	2x10 ⁻⁵ (7)	6.4x10 ⁻⁶ (7)	6.4x10 ⁻⁶ (7)
	SCRAM	2.1x10 ⁻³ (3)	2.6x10 ⁻³ (3)	2.1x10 ⁻³ (3)	2.6x10 ⁻³ (3)	1.7x10 ⁻³ (3)
	PTRIP	6x10 ⁻⁴ (5)	4x10 ⁻⁴ (5)	6x10 ⁻⁴ (5)	4x10 ⁻⁴ (5)	6x10 ⁻⁴ (5)
	SHRS	2.6x10 ⁻² (1.3)	2.8x10 ⁻¹ (1.2)	2.6x10 ⁻² (1.3)	2.8x10 ⁻¹ (1.2)	2.6x10 ⁻² (1.3)
	PFLOW	1.8x10 ⁻² (2)	6.8x10 ⁻² (2)	1.8x10 ⁻² (2)	6.8x10 ⁻² (2)	1.8x10 ⁻² (2)
<u>BFE</u>	DTECT	6x10 ⁻⁴ (5)	6x10 ⁻⁴ (5)	6x10 ⁻⁴ (5)	6x10 ⁻⁴ (5)	6x10 ⁻⁴ (5)
	SCRAM	1.6x10 ⁻² (2)	1.7x10 ⁻² (2)	1.6x10 ⁻² (2)	1.7x10 ⁻² (2)	1.6x10 ⁻² (2)
	PTRIP	2x10 ⁻⁴ (5)	1.3x10 ⁻⁴ (5)	2x10 ⁻⁴ (5)	1.3x10 ⁻⁴ (5)	2x10 ⁻⁴ (5)
	SHRS	4.2x10 ⁻¹ (1.3)	9x10 ⁻¹ (1.1)	4.2x10 ⁻¹ (1.3)	9x10 ⁻¹ (1.1)	4.2x10 ⁻¹ (1.3)
	PFLOW	1.4x10 ⁻¹ (2)	2.7x10 ⁻¹ (2)	1.4x10 ⁻¹ (2)	2.7x10 ⁻¹ (2)	1.4x10 ⁻¹ (2)

To determine the conditional failure probability for the SHRS function, the 90 basic components in that function were grouped into four categories: electrical, stiff mechanical, flexible mechanical, and electro-mechanical. Examples of electrical components are isolation and control valves, start signals, and batteries. Stiff mechanical components include diesel generators, relief valves, and internal service water fault mechanisms. Flexible mechanical components are pipes, heat exchangers, and pressure vessels while electro-mechanical components include fans, pumps, and protected air condensers. Failure probabilities for each of the four groups of components increase linearly with ground acceleration but to different degrees. Electrical components were assumed to be the least fragile component group and were assigned an initial OBE conditional failure-probability-increase factor of 3. Stiff mechanical components were next in line with an initial OBE-increase factor of 6, then came flexible components with an initial increase factor of 12, and finally electro-mechanical components with a factor of 15. These factors are similar to values derived from the CRBR Safety Study analysis which implies an initial OBE component increase factor of approximately 10 and assumes a linear-component-failure rate increase with increasing ground acceleration.⁴⁻³

When the RSS conditional-failure probabilities from Table 4-IV are applied with the initiator frequencies in Table 4-III to the event trees shown in Figures 4.2-2 through 4.2-6, the generic accident category relative frequency estimates in Tables 4-VI through 4-X are produced).

As Tables 4-VI through 4-X show, some 90 separate accident paths were considered in the earthquake analysis. These paths contributed to 10 of the 13 generic unprotected accident categories and all 12 generic protected accident categories identified in Chapter 3 of the Phase I ADS report. Estimated relative recurrence frequencies for the earthquake initiated accident scenarios range from 6×10^{-13} for an OBE-generated UTOP to 6.3×10^{-5} for a Damaged Core: CDA possible due to an OBE. Most (57%) of these scenarios lie in the 10^{-5} to 10^{-8} range. These scenarios are highly likely to dominate, or at least contribute significantly towards, the overall recurrence frequency for many of the identified generic accident categories, especially those dealing with either Damaged Cores or Primary Boundary Ruptures.

Table 4-VI

Accident Category Frequencies Associated
With Earthquake Scenario 1

Event Tree Sequence & Accident Category	Estimated Relative Frequency and (Uncertainty Factor)		
	OBE	SSE	BFE
A. CSA -- No Rel.	5.7×10^{-4} (3)	3.6×10^{-5} (3)	1×10^{-6} (3)
B. PT/F w/o Forced Flow	1.3×10^{-6} (4)	6.3×10^{-7} (4)	1.5×10^{-7} (4)
C. PT/F w/o SHRS*	6.6×10^{-7} (3)	9.4×10^{-7} (3)	8.5×10^{-7} (3)
D. UCF + ULOF, USTEP + ULOF, UTOP/USTEP + ULOF, or UTOP + ULOF	9×10^{-8} (6)	7.6×10^{-8} (5)	3.3×10^{-8} (4)
E. UCF, USTEP, UTOP/ USTEP, or UTOP	5×10^{-11} (10)	4.5×10^{-11} (8)	7×10^{-12} (7)
F. UCF, USTEP, UTOP/ USTEP, or UTOP	6.5×10^{-10} (10)	7.2×10^{-10} (10)	1.2×10^{-9} (7)

*PT/F = Protected Transient/Fault
 UCF = Unprotected Core Fault
 ULOF = Unprotected Loss of Flow
 USTEP = Unprotected STEP Insertion
 UTOP = Unprotected Transient Overpower

Table 4-VII

Accident Category Frequencies Associated
With Earthquake Scenario 2

Event Tree Sequence & Accident Category	Estimated Relative Frequency and (Uncertainty Factor)		
	OBE	SSE	BFE
A. CSA -- Rel. Poss.	6.3×10^{-5} (3)	2.4×10^{-5} (3)	8.2×10^{-7} (3)
B. PRPB w/o Forced Flow	1×10^{-6} (4)	1.6×10^{-6} (4)	2.2×10^{-7} (4)
C. PRPB w/o SHRS*	3.8×10^{-6} (3)	6.7×10^{-6} (3)	8.1×10^{-6} (3)
D. USTEP + ULOF, * UCF + ULOF, UTOP/USTEP + ULOF, UTOP + ULOF, or URPB + ULOF	1.5×10^{-8} (6)	6.2×10^{-8} (5)	1.4×10^{-7} (4)
E. USTEP, UTOP/USTEP, UTOP, UCF, or URPB	5×10^{-12} (10)	2.5×10^{-11} (10)	1.8×10^{-11} (7)
F. USTEP, UTOP/USTEP, UCF or URPB	5×10^{-12} (13)	1.5×10^{-10} (10)	4×10^{-9} (7)

*PRPB = Protected Rupture of the Primary Boundary

UCF = Unprotected Core Fault

ULOF = Unprotected Loss of Flow

USTEP = Unprotected STEP Insertion

UTOP = Unprotected Transient Overpower

Table 4-VIII

Accident Category Frequencies Associated
With Earthquake Scenario 3

Event Tree Sequence & Accident Category	Estimated Relative Frequency and (Uncertainty Factor)		
	OBE	SSE	BFE
A. DC	6.3×10^{-5} (3)	9×10^{-6} (3)	7.0×10^{-7} (3)
B. DC w/o Forced Flow	1.4×10^{-7} (4)	1.6×10^{-7} (4)	1×10^{-7} (4)
C. DC w/o SHRS*	7.2×10^{-8} (3)	2.3×10^{-7} (3)	5.8×10^{-7} (3)
D. UTOP/USTEP + ULOF, UCF + ULOF, UTOP + ULOF, USTEP + ULOF	1×10^{-8} (6)	1.9×10^{-8} (5)	2.3×10^{-8} (4)
E. UTOP/USTEP, USTEP, ULOF, or UCF	5.4×10^{-12} (10)	1.1×10^{-11} (8)	4.8×10^{-12} (7)
F. UTOP/USTEP, USTEP, ULOF, or UCF	7.2×10^{-11} (13)	1.8×10^{-10} (10)	1.1×10^{-9} (7)

- * DC = Damaged Core
 UCF = Unprotected Core Fault
 ULOF = Unprotected Loss of Flow
 USTEP = Unprotected STEP Insertion
 UTOP = Unprotected Transient Overpower

Table 4-IX

Accident Category Frequencies Associated
With Earthquake Scenario 4

Event Tree Sequence & Accident Category	Estimated Relative Frequency and (Uncertainty Factor)		
	OBE	SSE	BFE
A. DC + PRPB	7×10^{-6} (3)	6×10^{-6} (3)	5.4×10^{-7} (3)
B. DC + PRPB w/o Forced Flow	1.2×10^{-7} (4)	4×10^{-7} (4)	1.5×10^{-7} (4)
C. DC + PRPB w/o SHRS	4.2×10^{-7} (3)	1.7×10^{-6} (3)	5×10^{-6} (3)
D. UTOP + ULOF, USTEP + ULOF, USTEP/UTOP + ULOF, UCF + ULOF or URPB + ULOF	1.6×10^{-9} (6)	1.6×10^{-8} (5)	9×10^{-8} (4)
E. UTOP, USTEP, UTOP/ USTEP, UCF, or URPB	5.8×10^{-13} (10)	6.5×10^{-12} (8)	1.2×10^{-11} (7)
F. UTOP, USTEP, UTOP/ USTEP, UCF, or URPB	6.3×10^{-13} (13)	3.6×10^{-11} (10)	3.2×10^{-9} (7)

DC = Damaged Core
 UCF = Unprotected Core Fault
 ULOF = Unprotected Loss of Flow
 USTEP = Unprotected STEP Insertion
 UTOP = Unprotected Transient Overpower
 PRPB = Protected Rupture of the Primary Boundary

Table 4-X

Accident Category Frequencies Associated
With Earthquake Scenario 5

Event Tree Sequence & Accident Category	Estimated Relative Frequency and (Uncertainty Factor)		
	OBE	SSE	BFE
A. CSA -- No Rel.	$7 \times 10^{-4}(3)$	$7.5 \times 10^{-5}(3)$	$8.0 \times 10^{-6}(3)$
B. PT/F w/o Forced Flow	$1.5 \times 10^{-6}(4)$	$1.3 \times 10^{-6}(4)$	$1.2 \times 10^{-6}(4)$
C. PT/F w/o SHRS	$8 \times 10^{-7}(3)$	$2 \times 10^{-6}(3)$	$7 \times 10^{-6}(3)$
D. ULOF	$7 \times 10^{-8}(6)$	$1.3 \times 10^{-7}(5)$	$2.8 \times 10^{-7}(4)$
E. ULOHS	$3.8 \times 10^{-11}(10)$	$7.7 \times 10^{-11}(8)$	$5.6 \times 10^{-11}(7)$
F. ULOHS	$6.3 \times 10^{-11}(13)$	$4.8 \times 10^{-10}(10)$	$1.4 \times 10^{-8}(7)$

PT/F = Protected Transient/Fault
 ULOF = Unprotected Loss of Flow

4.2.4 Future Work

Some 356 potential CRBRP accident paths have been quantified. This work includes that previously done that addressed accident initiators dealing with the CRBR heat transport systems. These paths stem from approximately 50 individual initiators and 20 different functional event trees. The results will now be collected, combined, and analyzed in order to estimate the relative recurrence frequencies associated with each of the 25 generic accident categories identified in the Phase I ADS report as well as unprotected and protected accidents as classes. Work will then begin on a final report which focuses upon these results as well as the attendant accident path analysis.

4.3 Accident Phenomenology

(P. J. McDaniel, 4424; D. C. Williams, 4424)

4.3.1 UTOP Analysis

During this quarter, work continued on the low-ramp-rate UTOP accident sequences for CRBR, with the SAS3D code. The two most interesting cases were: (a) withdrawal of one of the power-level control rods at the maximum rate possible (72 in/min) resulting in a ramp of $\sim 4.5\%$ /s and a total reactivity insertion of 65% , and (b) withdrawal of all six power-level control rods at the maximum rate possible (72 in/min) producing a ramp of $\sim 20\%$ /s and a total reactivity insertion of $\$2.86$.

Withdrawal of one control rod produces a rise in power to approximately 1.8 times normal and a small amount of fuel melting (10-15%) in the lead subassemblies. No pin failures are predicted and sodium does not void. Based on this calculation, more than one control rod would appear to have to be withdrawn to generate severe pin failures or voided subassemblies.

Withdrawal of all six power-level control rods clearly leads to pin failures and subassembly disruptions. However after several attempts, investigators have been able to obtain a consistent prediction from the SAS3D code. Currently, SAS3D predicts that the accident will proceed to a point in the transient at which the power level has risen to about 3.4 times

nominal, a total of 97.5¢ of reactivity has been inserted with Doppler feedback compensating for 55¢ of this, and all channels remain at full flow. At this point, the SLUMPY model of SAS3D (SLUMPY predicts fuel motion for ULOF scenarios) indicates that pins should fail in Channel 9 (the fuel assemblies loaded at BOC4). Shortly after this, sodium starts voiding in Channel 1. However, no fuel pins have been predicted to fail by this time, based on the HEDL correlation or reasonable melt fraction/temperature criteria. Therefore, further investigations are warranted and will be pursued next quarter. Clearly, however, pins will fail and an FCI is very probable. The slowness of the transient appears to allow Doppler feedback to keep up with the inserted reactivity to a greater degree than for the higher-ramp ($> 50\text{¢/s}$) transients postulated in the past. This means that by the time an FCI occurs there will not be as much reactivity left to be inserted as there is for the higher ramp cases. This may or may not have implications for the meltdown sequence. Further calculations are necessary.

4.3.2 Protected Accident Analysis

A major conclusion of the ADS Phase I Report was that protected accidents (i.e., SCRAM succeeds but core disruption eventually occurs anyway due to inadequate decay heat removal) are likely to be major contributors to the total risk in CRBRP and, perhaps, in other LMFBRs as well. One important parameter in these accidents is the length of time between the system failure(s) initiating the accident and the actual onset of irreversible core damage. This time interval determines how much time is available for remedial action to prevent CDA occurrence and also affects such accident management parameters as time available for evacuation. In addition, it directly impacts the meltdown progression and behavior after CDA through its influence on decay heat levels and radionuclide inventories.

To obtain information on this parameter, and also to define better other key aspects of protected accidents, a set of five scenarios was defined and arrangements were made for their analysis using the Super Systems Code (SSC) at Brookhaven National Laboratory (BNL). All five scenarios involve SHRS failures sufficiently severe so that a CDA will be inevitable if recovery is indefinitely delayed. The scenarios were defined to span a wide range of thermohydraulic problems for the plant and, at the same time, represent reasonably plausible loss-of-SHRS scenarios.

Hence, results are expected to be useful for both the current ADS program and also the proposed CRBRP risk assessment, if the latter is approved.

These five scenarios may be summarized as follows:

a. Scenario I -- Prolonged Loss of All AC Power. Offsite power is lost and both diesels fail; no additional failures occur except those entailed by the loss of AC power. The 250-volt DC battery therefore supplies power via the Diverse Power Supply to assure heat removal through Loop 3. After two hours, the battery is exhausted and heat removal is possible only by natural circulation through the sodium loops and steam venting. After dryout of the steam generator system occurs, no heat sink exists (other than stray heat losses) and the sodium portion of the plant begins to heat up with natural circulation only available for heat transport from the core to the coolant and core disruption will occur eventually. In the CRBRP Safety Study,⁴⁻³ this scenario was estimated to contribute approximately 50 percent of the total CDA probability. In the Safety Study, however, the course of events following battery exhaustion was not analyzed; instead, a CDA was assumed to occur immediately at that time. Actually, additional delays of at least several hours are likely for this scenario.

b. Scenario II -- Loss of All Feedwater, Forced Flows, and DHRS. In this scenario, only natural circulation occurs in all three PHTS and IHTS loops once pump coast-down is complete. Heat rejection is via steam venting and whatever heat removal can occur through the PACCs with natural air circulation only until dryout occurs, whereupon heat-up of the sodium portion of the plant commences. In effect, this scenario resembles that portion of Scenario I that follows battery exhaustion, except that these conditions are imposed immediately after shutdown when sensible heat and decay heat loads are substantially higher.

c. Scenario III -- Loss of All Feedwater and DHRS. This scenario is the same as Scenario II except that pony flow and the PACC blower are assumed available on Loop 3. The importance of running this scenario depends upon the degree to which the limitations of natural circulation govern results in Scenario II; if these limitations are not important, priority for this scenario is reduced.

d. Scenario IV -- Loss of All IHTS Loops, DHRS, and Forced Flow. Common-cause failures (e.g., earthquake-induced actuation of all three IHTS rupture disks) are assumed to eliminate all heat transfer across the IHXs, pony flow is assumed lost in the PHTS, and the DHRS is assumed inoperative. Once pump coast-down occurs, only natural circulation within the primary boundary is available to transfer heat from the core to the primary coolant. This scenario is intended to represent the most severe core cooling problem that is credible with a physically intact PHTS (that is, no primary boundary rupture, massive structural failure, etc.).

e. Scenario V --- Loss of All IHTS and DHRS. This scenario is the same as Scenario IV except for the assumption that pony flow is available in at least one PHTS loop. This scenario is intended to represent the most rapid credible rate of PHTS and core heat-up of any scenario for which at least the PHTS heat capacity is available and limitations of natural circulation are not involved. If the operating pump fails (due to cavitation or other causes) when sodium temperatures become high enough, and if this process can be modeled in SSC, the transient should still be continued as far as possible after this point.

The currently-available version of SSC does not have a boiling model for natural circulation and other low-heat-flux conditions. The analyses described above can determine only the times and locations at which boiling temperatures are exceeded; the subsequent course of events cannot be followed. An important question requiring attention is whether core coolability can be maintained after the onset of in-core boiling. If so, additional delays in the onset of core disruption of up to many hours might be obtained.

Still another important question is whether CDA onset could be hastened by failure of the primary boundary and/or failure of in-vessel structure (e.g., core support structure failure) due to the severe overheating conditions that develop in these scenarios. The calculations to be performed here cannot address this question. However, they will generate time-temperature histories for key nodes of the primary system, and this information will be essential for any treatment of the problem of structural failures due to overheating.

In addition to arranging for the SSC calculations, work in the protected accident area has included negotiation of a contract with the University of Arizona to continue development of its BRENDA code. BRENDA is a simulation code that models the whole reactor plant with various levels of detail. However, it runs relatively rapidly and can provide estimates of potentially hazardous accident sequences. BRENDA can also be used to provide initial conditions for more detailed calculations with codes such as SAS3D and SIMMER. The current plan is to have the University of Arizona provide Sandia with a version of the code that is compatible with Sandia's VAX system. This version will be run by ADS personnel to supplement and expand the calculations provided by the University of Arizona.

Investigators hope that the BRENDA code will provide a useful complement to the capabilities of the SSC code. The latter provides a more detailed and sophisticated modeling of the core and the PHTS thermohydraulics, while BRENDA provides a considerably more detailed description of the balance-of-plant. Thus, BRENDA can provide more detailed treatment of the plant response to specific SHRS failures.

4.4 Postaccident Phenomenology (F. W. Sciacca, 4424)

4.4.1 Containment Research Priorities

Sandia National Laboratories has undertaken an effort to establish key areas of LMFBR containment research and to establish priorities among these areas. This is a continuing effort, and priorities must be continually reevaluated in light of progress made in the related research programs.

The current effort to establish containment research priorities has been largely completed. A report has been written which presents the approaches used in the effort, describes each of the primary and secondary containment research areas, and presents the results of the evaluation. The rationale and basis used in ranking the research areas are discussed.

This draft report on containment-research priorities is currently undergoing internal review within Sandia National Laboratories. This review process was not completed in this quarter. The report will be revised as appropriate based on the reviewer comments and suggestions. The author anticipates that this will occur in the next quarter. The study results will then be presented in the appropriate quarterly report.

4.4.2 Analysis of CRBRP Containment Response to Large Accidents

The LMFBR Accident Delineation Study will use the CRBRP design as an illustrative facility for performing an assessment of containment responses to large accidents. Both primary and secondary containment responses are to be included. This analysis effort was initiated during this quarter.

Previous containment response analyses received a brief review. Part of this review emphasized work related to primary containment response to energetic CDA events. Cognizant Sandia and program personnel evaluated suitable methods, approaches, and resources needed to carry out this kind of analysis for the CRBRP primary containment.

The secondary containment evaluations will employ the CONTAIN code as the primary analysis tool. The investigators initiated data collection for proper representation of the CRBRP system. Familiarization with the CONTAIN code was also initiated.

A preliminary plan has been generated for carrying out the secondary containment evaluations. The plan broadly outlines several specific analysis cases and defines the parameter sensitivity studies that should be performed. These parametric studies are needed to gain a better understanding of the modeling sensitivities and limitations. They will also assist in defining the relative importance of the various post-accident phenomenological challenges to the secondary containment system.

The CONTAIN code cannot yet simulate some of the phenomena expected to occur in an LMFBR core-meltdown scenario. Capabilities that will make the code more complete include simulation of liner vents, allowing

for condensation of both sodium vapor and steam, allowing for chemical reactions of sodium vapor (especially in the upper RCB), and simulation of sodium spray-fire phenomena. These and other features of the code needed for the analysis of the CRBRP system have been discussed with the CONTAIN developers. The CRBRP analysis will be carried out as the code development progresses.

A Clinch River Risk Assessment Study may be performed by Sandia and other laboratories. An abbreviated description of the containment-response analysis needed for such a study was prepared. This included preliminary definition of the resources and time needed to perform this portion of such a risk assessment.

4.5 CRBRP Risk Assessment Proposal (D. C. Williams, 4424)

The Clinch River Breeder Reactor Plant Safety Study,⁴⁻³ published by the CRBRP Project Office in 1977, provided much useful information for assessing LMFBR risks in general and the CRBRP risk in particular. Nonetheless, important limitations exist in terms of the applicability of the Safety Study to current needs. For example, important design changes have occurred since 1977, such as the change from a homogeneous to a heterogeneous core. The 1977 work gave only limited explicit information on the important question of the magnitude of the impact of phenomenological uncertainties upon the risk estimates.

Since 1977, the Interim Reliability Evaluation Program (IREP), the LMFBR Accident Delineation Study (ADS), and other NRC and DOE safety research programs have led to substantial contributions to the technical understanding and data base required for assessment of risk to the public associated with LMFBR systems. This growth in knowledge has reached the point where the capabilities and limitations of current understanding can best be ascertained by actually performing a risk assessment for a specific LMFBR plant, the CRBR. At the request of the NRC, the feasibility and expected benefits of performing such a risk assessment have been evaluated and the results used to prepare a formal proposal for a Clinch River Risk Assessment Study (CRRAS). This risk assessment will identify both the principle factors governing risk associated with the CRBR plant and also the major limitations of current risk assessment capabilities. In addition, it will fulfill the

widely-perceived need for the NRC to perform risk assessments independently of analyses sponsored by potential or actual licensees.

More specifically, the objectives of the proposed Clinch River Risk Assessment Study (CRRAS) are:

Primary Objectives

1. To apply and extend the IREP methodology to develop and quantify logic models (event trees and fault trees) of the CRBR systems whose unavailability or failure contributes to risk.
2. To identify the dominant accident sequences governing CRBR risk and identify the plant design and operational features most heavily involved in these sequences.
3. To assess the uncertainty in the risk estimates obtained in this study and to identify the dominant phenomenological uncertainties contributing to the uncertainty in the estimated risk.
4. To expand the NRC capability in the use of probabilistic risk assessment techniques to include LMFBR plants including treatment of the effect of phenomenological uncertainties.

Secondary Objectives

5. To obtain an estimate of the numerical magnitude of the CRBR risk.
6. To compare the CRBR risk estimate with estimated LWR risks.

The insights into the dominant accident sequences for CRBR and the dominant phenomenological uncertainties would provide useful input to both the NRC's licensing needs and the NRC's regulatory research programs. The uncertainty in the risk estimates may be too large to permit these estimates to be very useful in judging CRBR licensability or public acceptability issues. In this case, primary emphasis should be on the identification of the dominant factors contributing to the uncertainty in risk rather than upon the numerical risk estimates themselves.

The Accident Delineation Study has shown that risk assessment must concentrate heavily upon sequences resulting in core disruptive accidents (CDAs). Analysis of core disruptive sequences and subsequent containment response would require extensive application of large accident analysis computer codes; e.g., SAS, SIMMER, SSC, CONTAIN. These codes and their phenomenological modeling have important limitations, and assessment of the impact of these limitations would constitute a major portion of the work required to meet Objective 3 above. However, code development, phenomenological model development, etc., fall outside the scope of this proposal.

Accidents not involving core degradation (e.g., fuel-handling accidents, sodium spills) have little potential for yielding high-consequence events; their frequency can be kept sufficiently small so that their contribution to total risk will be small; and they undoubtedly will contribute little to the uncertainty in total risk. Hence, such accidents would not receive detailed treatment in this risk assessment.

In the ESS area, much of the work would employ the methodologies developed for the IREP program. Subtasks closely paralleling the IREP work include plant familiarization, development of event trees, fault tree development and quantification for front-line and support systems, component reliability data development, and accident sequence quantification (preliminary and final). Human error, common mode failure effects, impacts of uncertainties and sensitivity studies would be included using the procedures developed for IREP. In addition, fire, flood, and seismic events would be addressed to evaluate their effects upon the CRBRP risk. Success in these efforts would require the closest possible collaboration with the CRBRP Project.

A substantial proportion of the total effort would be allocated to the accident phenomenology area, i.e., the delineation and quantification of the in-core sequences of events characterizing core disruptive accidents. The need for this high level of effort follows from the ADS conclusion that accident phenomenology is a major factor governing LMFBR risk and may well be the dominant factor governing the uncertainty in LMFBR risk.

Considerable insight has been obtained from the ADS as to the problems upon which the greatest effort should be concentrated; additional refinements in the apportionment of effort will be made as improved estimates as to the relative likelihood of the various accident categories are developed in the ESS area.

The ADS concluded that the most likely paths to a CDA in CRBR involve failures in the SHRS leading to inadequate decay heat removal following successful neutronic shutdown. Plant systems codes (BRENDA, SSC) would be used to identify classes of SHRS failures that could jeopardize core integrity, and the time of onset of core disruption, if such occurs, would be determined for these accidents. The subsequent meltdown sequences would be evaluated as best possible in view of the absence of large-scale analysis codes designed for this purpose; the simpler analyses that do exist (e.g., those performed at UCLA and BNL) would be used and the possibility of applying the SAS code to meltdown under decay heat conditions would be investigated. A key question is whether criticality can result from such a meltdown; this is primarily determined by the degree of separation between control and fuel materials and the phenomenologies governing this issue would be carefully evaluated. The ADS indicates that if recriticality does occur, the best available model for subsequent events appears to be the late transition phase arising in unprotected loss-of-flow (ULOF) accidents. Hence, results of ULOF transition-phase analyses would likely be employed here after allowing as best as is possible for identified differences between these events and the ULOF transition phase.

Of the various categories of unprotected (i.e., SCRAM fails to occur) accidents identified in the ADS, the ULOF accident was found to be most important in terms of its probability and potential consequences. The initiation phase would be analyzed using the SAS3D and SAS4A codes to determine whether severe energetics can arise in the initiation phase (despite the reduction in this concern due to adoption of a heterogeneous core in CRBR) and also to establish initial conditions for transition phase analysis. The ULOF transition phase evaluation would employ SIMMER-II calculations and evaluation of available phenomenological modeling where appropriate. The ULOF transition phase would warrant substantial attention both because it is important for its own sake and also because it is expected to serve as a model for recriticality following

meltdown under decay heat conditions. Using the ADS results as a guide, lesser amounts of effort would be apportioned to the analysis of other unprotected accident categories such as combined ULOF & UTOP accidents, ULOHS, UTOP, and local fault propagation accidents.

Assessment of the uncertainty in calculated risk due to the phenomenological uncertainties involved in CDA analysis would be performed, in part, by comparing risks calculated for best-estimate or "conventional wisdom" phenomenological assumptions (i.e., not chosen to be especially conservative) with results obtained using sets of phenomenological assumptions judged to be reasonably but not excessively conservative. Another approach would involve identification of sets of phenomenological assumptions which would imply accident energetics exceeding thresholds for primary and secondary containment failures corresponding to substantial increases in consequences; these sets of assumptions would then be evaluated for plausibility and results for failures requiring implausible assumptions would be eliminated. Substantial sensitivity studies would be required for the uncertainty assessment.

Obtaining the best results from the accident analysis codes to be used in this task would require participation by the staff at the laboratories that developed the codes. In formulating this proposal, program personnel assumed that support would be available at Los Alamos, Argonne National Laboratory (ANL) and BNL for studies involving the SIMMER, SAS and SSC codes, respectively.

Work in the postaccident phenomenology area would include evaluation of the response of primary and secondary containment systems to CDA and post-CDA conditions. It would include definition of radioactivity release categories for the consequence analysis. The following specific subtasks would be involved:

a. Preparatory Work. This subtask would include familiarization with the available analysis tools and gathering pertinent CRBR plant-specific information. Using the ADS results as a guide, key issues requiring the greatest attention would be identified.

b. Limits and Threshold Analysis. In this subtask, thresholds would be defined for primary and secondary containment failures which would correspond to significant increases in potential consequences. For the primary containment, failure thresholds (including missile generation)

would be defined as a function of CDA energetics and post-CDA debris-coolability characteristics as key parameters. For the definition of secondary containment-failure thresholds, parameters requiring consideration include missile generation, thermal and pressure loadings, gas and vapor generation rates due to core-sodium-cavity interactions, loadings from hydrogen burns or explosions, etc. Since the ADS indicates that vessel meltthrough is a likely event given that a CDA has occurred, primary vessel failures due to CDA energetics would be judged important only if they significantly augment the reactor containment building (RCB) challenge and radiological consequences to be expected due to vessel meltthrough.

c. Best Estimate Analysis. Using the CONTAIN code and other applicable analysis codes, response of the containment systems would be analyzed for best estimate input assumptions. The latter include both assumptions for post-CDA containment phenomenologies and also the results of the best-estimate CDA analyses.

d. Uncertainties and Sensitivity Analysis. Impact of uncertainties would be assessed by comparing results for both best-estimate and conservative input assumptions in a manner similar to that employed for CDA analysis uncertainties in the accident phenomenology area. Special attention would be devoted to identifying input assumptions that would lead to exceeding failure thresholds identified in (b) above and assessing the phenomenological plausibility of these assumptions. Substantial sensitivity analysis would be required.

e. Definition of Release Categories. Release categories would be defined from the results of CONTAIN calculations combined with containment systems functionality states identified in the ESS area. Probabilities would be assigned using results of the containment analysis together with sequence probability information developed in the ESS and in-core sequence analyses. Results would be modified as necessary to allow for any sequences involving conditions exceeding containment failure thresholds identified in (b) above. When required, separate release categories and probability estimates would be defined for the best-estimate and conservative cases to be used for uncertainty assessment.

Unlike some other portions of the CRRAS, consequence analysis does not involve large numbers of major uncertainties that are unique to LMFBRs. A partial exception may be presented by any sequences where consequences are dominated by release of plutonium and/or other transuranics. Such sequences would be given special attention when necessary to define the associated uncertainties. Otherwise, the radiological consequence evaluations would be performed using the CRAC2 code in essentially the same manner as has been done for LWR risk assessments. Separate evaluations would be made for the best-estimate and the conservative cases when required for the uncertainty assessment.

References for Section 4

- 4-1. D. C. Williams et al., LMFBR Accident Delineation Study, Phase I Final Report, SAND80-1267, NUREG/CR-1507 (Albuquerque, NM: Sandia National Laboratories, November 1980).
- 4-2. E. R. Copus, Quantified Fault Tree Models for the Clinch River Breeder Reactor Engineered Safety Systems, SAND81-0260, NUREG/CR-1923 (Albuquerque, NM: Sandia National Laboratories, May 1981).
- 4-3. CRBRP Safety Study -- An Assessment of Accident Risks in the CRBRP (CRBRP-1), (Oak Ridge, TN: Project Management Corporation, March 1977).
- 4-4. E. E. Lewis, Nuclear Power Reactor Safety (New York, NY: Wiley and Sons, 1977).

5. ADVANCED REACTOR CORE PHENOMENOLOGY

The Advanced Reactor Core Phenomenology Program is directed toward developing a data base for the understanding of the key in-core events in a core disruptive accident which determine the progression and severity of a reactor accident. For the advanced reactor, understanding in-core events is particularly important since significant energy release from the core is possible. The magnitude of this energy release, and therefore the ultimate threat to the containment, is determined by the competing positive and negative reactivity effects caused by the motion and temperature of fuel, cladding and coolant.

This program involves experimental and analytical efforts to determine the magnitude and characteristics of these reactivity effects in the three phases of an advanced reactor core disruptive accident. These phases are:

- a. Initiation Phase -- Fuel Dynamics
- b. Disassembly Phase -- Energetics
- c. Transition Phase -- Fuel Freezing and Streaming.

5.1 Initiation Phase -- Fuel Dynamics (S. A. Wright, 4423; P. K. Mast, 4425; F. Briscoe, 4425)

5.1.1 Fuel Disruption Experiment Program

5.1.1.1 Introduction

The major efforts this quarter focused on defining the FD2/4 test matrix, reviewing the PIE work for the FD1 series of fuel disruption experiments, and drafting a topical report for the HRR series of experiments. A brief summary of the work performed for each of these tasks is given below.

5.1.1.2 FD2/4 Test Series Definition

The goal of the FD2/4 test series is to investigate the initial fuel disruption process for LOF accident transients in LMFBRs. This series of experiments will be performed under an international exchange agreement

between the West German nuclear research center, KfK, and Sandia National Laboratories. High speed photography along with other instrumentation will be used to study the disruption phenomena. Posttest analysis of the data will determine the timing of the disruption, the state of the fuel at the time of disruption, the general mode of the disruption (e.g., swelling, solid state break up, slumping, etc. ...), and the roles played by molten fuel expansion, fission products, and fuel vapor pressure.

A range of LOF accident transients and fuel types will be used in the FD2/4 test series. Two types of heating transients are proposed. The first transient simulates LOF heating conditions for homogeneous core reactors such as SNR-300 or CRBR. The second transient simulates LOF heating conditions for heterogeneous core reactors, such as the new CRBR. Burnup will also be a parameter. Burnups between 0 and 9 atmosphere-percent will be used.

An initial test matrix and a preliminary schedule for these experiments are shown in Tables 5-I and 5-II. Ten experiments are planned. Four of the experiments use fresh fuel and 10 use irradiated fuel. In some experiments the fuel will be completely disrupted while in others the heating will be stopped just before total disruption. The non-disrupted fuel will then be examined for fission gas content and fuel microstructure changes. The postirradiation examination (PIE) work will be done mainly at KfK though some will be done at Sandia.

Seven experiments will use the first transient type. This transient simulates the heating conditions of an LOF accident representative of the German SNR-300 LMFBR. (Note that this transient is equally valid for the CRBR homogeneous core reactor.) The accident analysis code SAS-3D was used to determine the time-dependent temperature profiles in a 10-channel model of SNR-300.⁵⁻¹ Figure 5-1 shows the SNR reactor power for the LOF accident. Investigators proposed that this transient be simulated in the Sandia ACRR reactor by a steady state power of 11.5 MW lasting for 6 seconds. This is followed by a power excursion having a period of 100 ms. When the power reaches 200 MW it is then reduced at a 1-second period. This power transient is also shown in Figure 5.1-1.

Table 5-I. Preliminary Test Matrix for the FD2/4 Experiments

Fuel	LHR (w/cm)	BU %	High Power Transient (homo. core)		Low Power Transient (hetero. core)	
			Failure Yes	Failure No	Failure Yes	Failure No
PNL 10-74	251	5.5	4.2	4.3	2.8	2.9
PNL 11-57	318	9-11	4.4	4.5	2.11	2.11
PNL 11-18	362	4.7	4.1		2.13	
Fresh UO ₂	-	-	2.5	2.6	2.7	2.10

Table 5-II. Time Schedule for the FD2/4 Experiment Series

Experiments	Date of Completion
2.5, 4.1	October 1981
2.6, 4.2, 4.3	December 1981
2.7, 2.8, 2.9	March 1982
2.10, 4.4	January 1982
4.5	September 1982

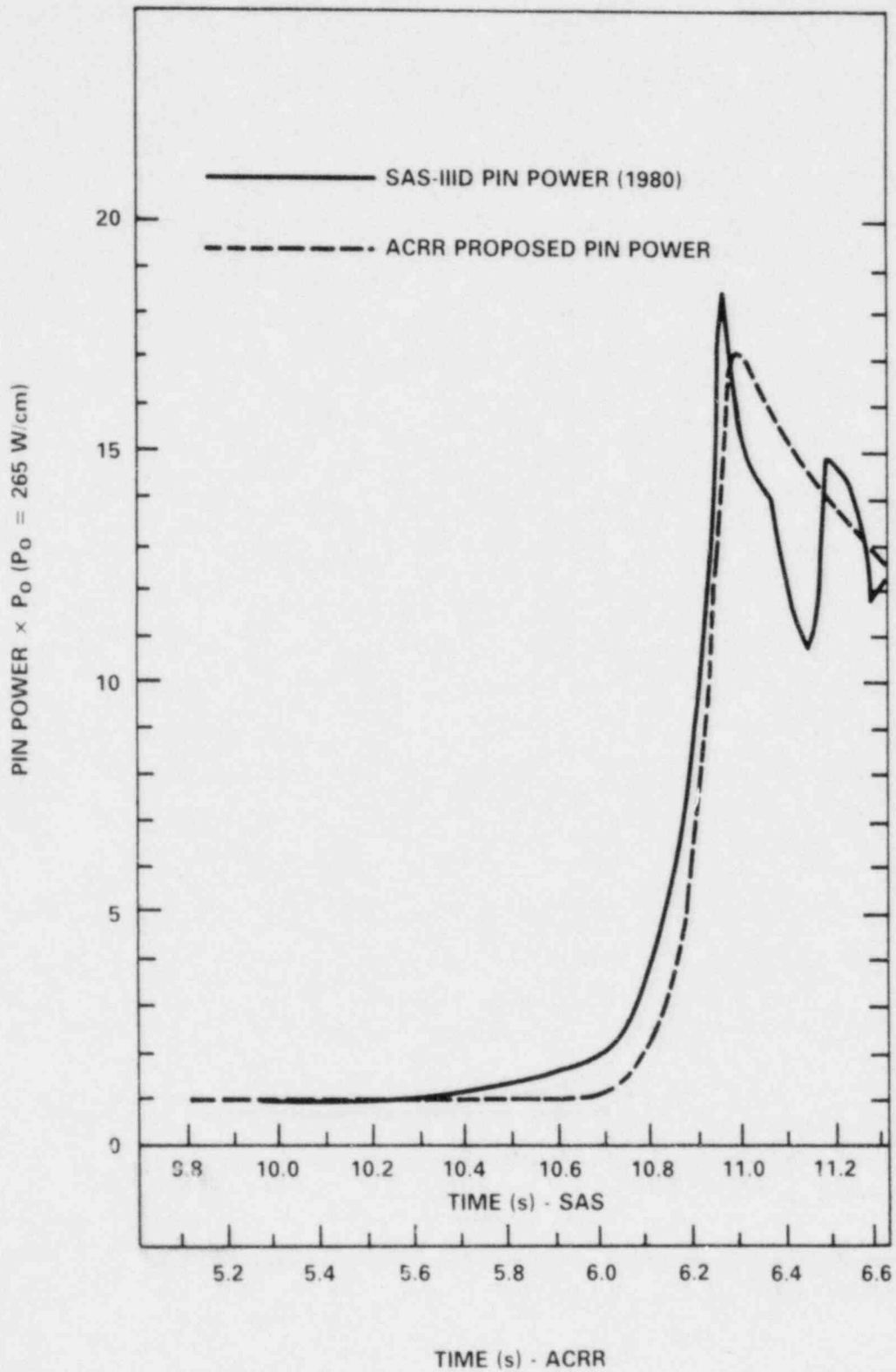


Figure 5.1-1. Pin Power Profiles for the SAS-IIID LOF and the Proposed ACRR Power Transient

The fuel pin temperature histories produced by the ACRR transient and predicted by SAS are shown in Figures 5.1-2 and 5.1-3. Near the time of fuel melting the heating rates are approximately 3-5 K/ms. The fuel temperatures from the ACRR transient were calculated with the fuel pin behavior code SANDPIN that is currently being developed at Sandia. A coupling factor of 11.76 J/g/MJ and a peak-to-minimum radial energy density of 1.64 were used. These constants assume a fuel pin enrichment of 68% and a 5 μm gadolinium filter.

The second series of experiments will investigate LOF accident conditions for heterogeneous core reactors. Seven experiments of this type will be performed. The power transient for this series of experiments is expected to be longer and of lower power (1-3 times nominal power for many seconds) than the transient for the homogeneous core experiments. Little published data is currently available to determine the power transient in detail. However, a report⁵⁻² should be published soon which will be used as a guideline in defining the transients. Also, the SACO code⁵⁻³ (a fast running code which simulates SAS) will be used to determine the general features of the power transient.

5.1.3 KfK Postirradiation Examination of the FDI Fuel

In 1979, 4 samples of irradiated fuel were sent to KfK for PIE studies. The fuel consisted of one PNL10-12 sibling fuel pellet and 1 fuel pellet each from tests FDI.4, FDI.7, and FDI.8; these latter 3 pellets had not failed. Only the sibling fuel pellet and the FDI.7 fuel pellet have been examined. The examinations included microphotographs, porosity measurements, scanning electron microscopy, and electron microprobe analysis for Xe and Cs radial distributions. Retained-fission-gas analysis for Xe and Kr will also be performed once all the nondestructive analysis is complete.

The fundamental observations presented by KfK covered the posttest melt front, the regions of swelling, and the Xe and Cs distributions. Each of these topics is discussed.

A direct measure of the melt front radius determined from the photomicrographs is difficult. In the FDI.7 experiment, the radius of total melt (temperatures at or above the liquids) extended from the center to a fractional

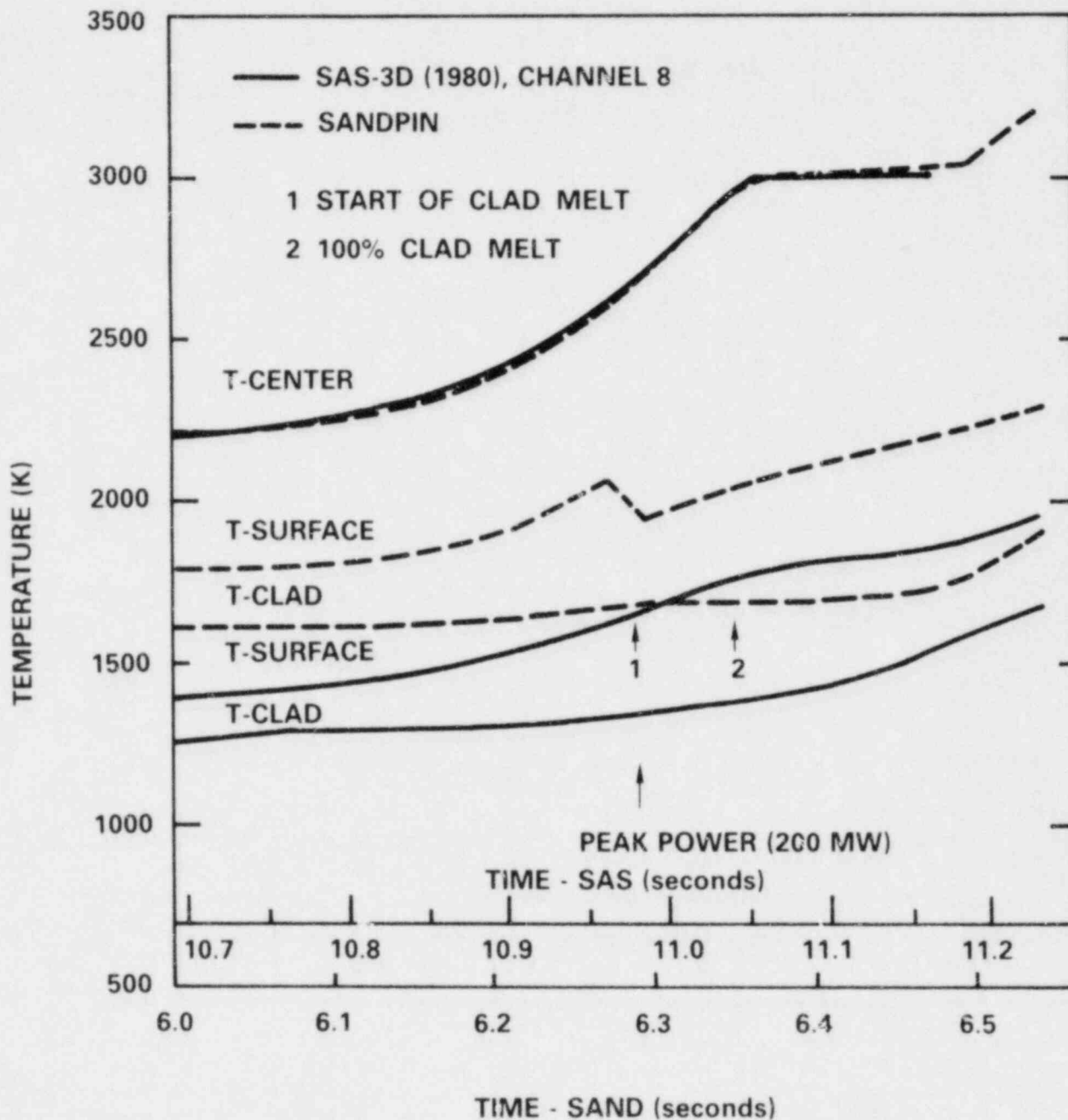


Figure 5.1-2. Temperatures Calculated by SANDPIN at Different Radii (Preheat = 11.5 MW for 6 seconds, transient = exponential with a period of 0.1 seconds rising to 200 MW followed by a decaying exponential with a 1 second period.)

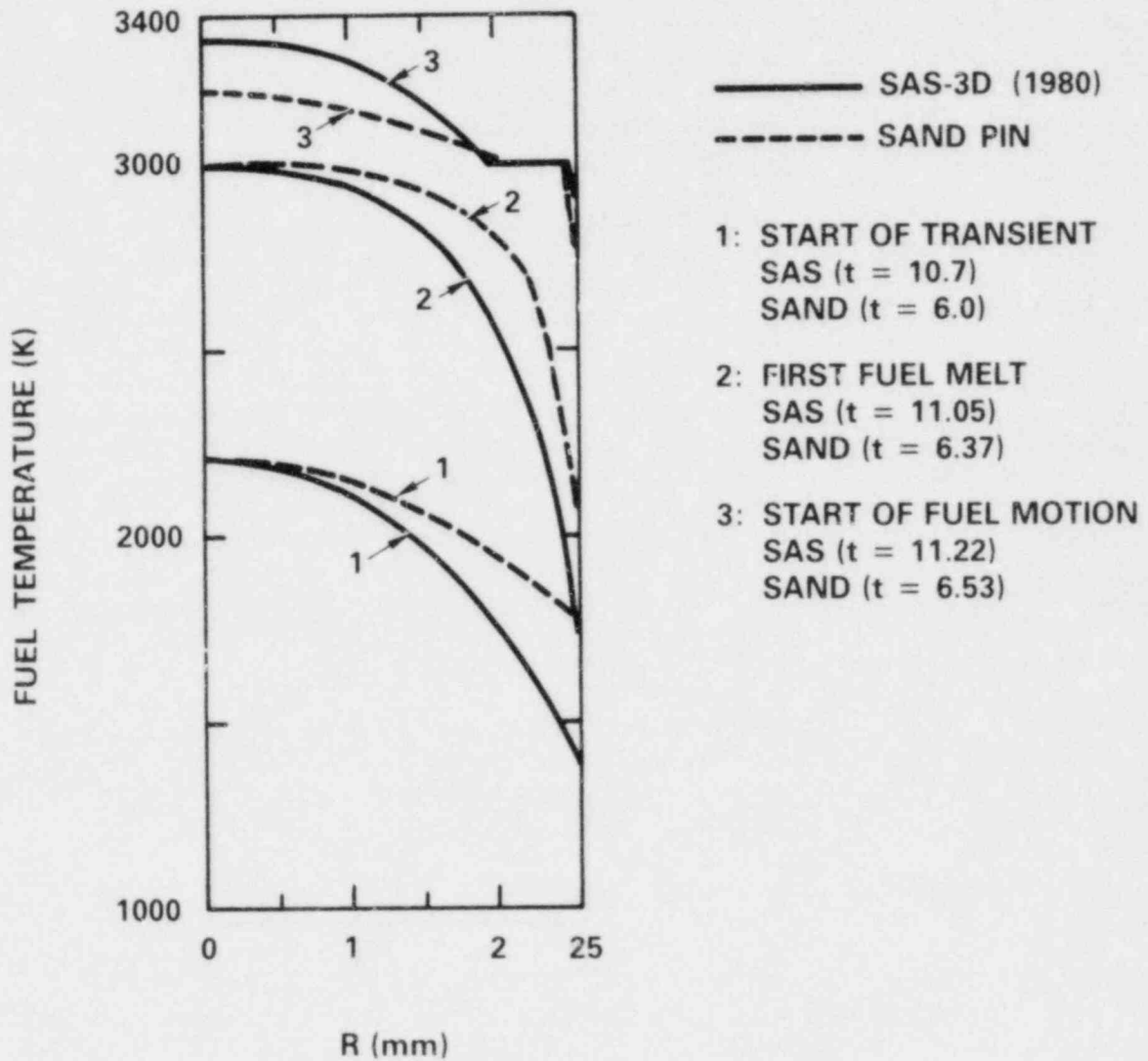


Figure 5.1-3. Radial Temperature Distributions for SNR-300 Calculated by SAS-3D (1980) and SANDPIN (SANDPIN power profile: 11.5 MW for 6 seconds, transient = exponential with a period of 0.1 second rising to 200 MW followed by a decaying exponential with a 1 second period.)

radius of approximately 0.3. In addition, a region of partial melting extended from $r/R=0.3$ to 0.75. These results appear to be consistent with the early calculation published by Cano, Ostensen, and Young.⁵⁻⁴

Significant fuel swelling was observed in these experiments. To determine the radial distribution of the swelling, KfK made densitometer measurements of the photomicrographs. This analysis showed that for the FD1.7 experiment, the swelling occurred mainly in the unrestructured and equiax zones. Furthermore, the swelling in the unrestructured zone appeared to be caused by extensive intragranular fractures.⁵⁻⁵ Some swelling of smaller magnitude also occurred near the pin center.

This swelling pattern conflicts with Sandia's previous interpretation of the swelling and cracking. The earlier interpretation was based on the expectation of significant swelling in the columnar and equiaxed zones and little or none in the unrestructured zone. Since the KfK data is the first quantitative measurement of the radial distribution of the swelling, more analysis must be performed to resolve the differences in interpretation of the results.

Electron microprobe techniques were used to measure the Xe and Cs distributions in the sibling (PNL10-12) fuel pellet. Figures 5.1-4 and 5.1-5 show these distributions.

The Xe radial concentration shown in Figure 5.1-4 refers to the intragranular gas concentration. It shows that approximately 33% of all the gas is located in the outer 5% of the fuel radius. This distribution is inconsistent with the generally accepted distributions given by Randklev.⁵⁻⁶ No explanation for the inconsistency is available at present, but more attention will be placed in confirming these results by further measurements and analysis.

5.1.4 Topical Report for the HRR Experiments

During 1980 the High Ramp Rate (HRR) series of experiments was completed. The goal of these experiments was to investigate the timing and mode of fuel disruption under prompt burst heating conditions. This type of information is important because the timing of the disruption and its dispersive or nondispersive nature can

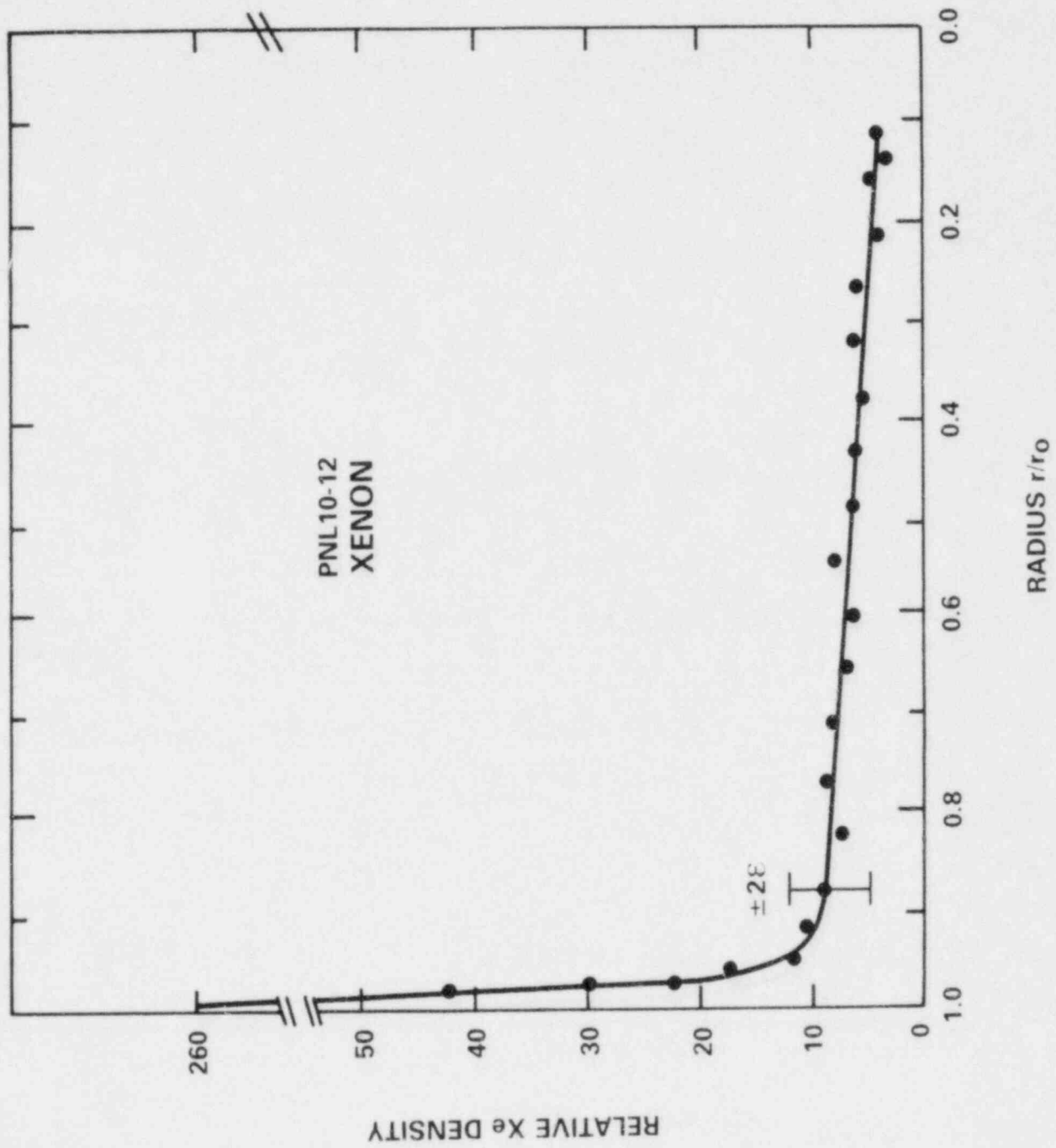


Figure 5.1-4. Radial Distribution of Xenon for the Sibling Fuel Pellet PNL 10-12

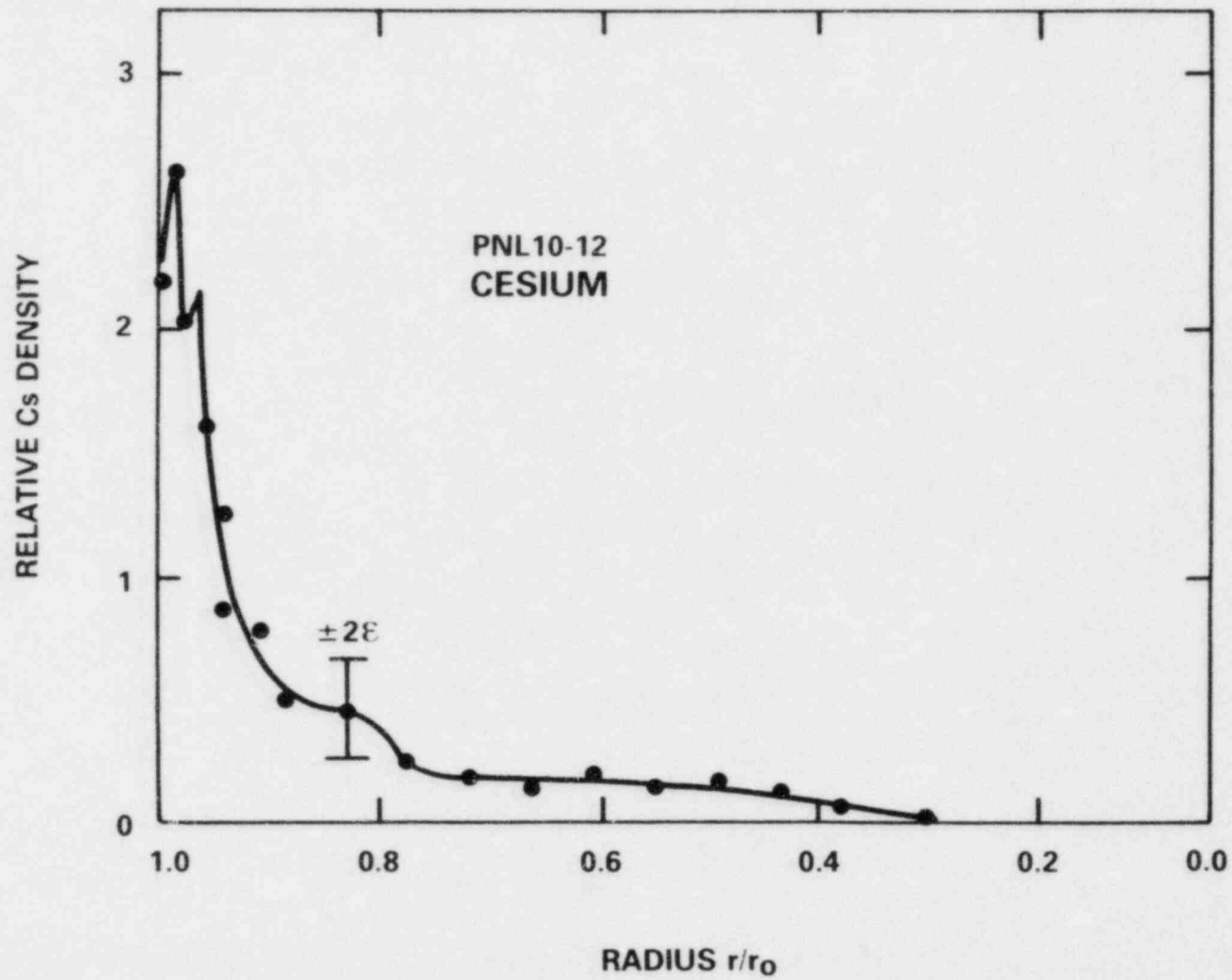


Figure 5.1-5. Radial Distribution of Cesium for the Sibling Fuel Pellet PNL 10-12

significantly affect the work energy release of a prompt burst disassembly. A topical report for these experiments was written this quarter.⁵⁻⁷ The report describes the experimental details of experiments HRR-2, 3, 5, and 6. It also describes the preliminary analysis. In this report the experimental details are described sufficiently well so that personnel from other laboratories can use their own fuel behavior codes to analyze these experiments. The analysis was performed with the SANDPIN code, which is a fuel behavior code based on LAFM.⁵⁻⁸ The major conclusions of these experiments are:

- a. Fuel disruption occurs well before fuel vapor pressure generation for both fresh and irradiated fuel.
- b. Irradiated fuel disrupts earlier than fresh fuel and is more energetic. The melt fractions at the time of disruption are near 60 percent for irradiated fuel and 100 percent for fresh fuel.
- c. The disruption appears as a rapid expansion of very small particles (<1 mm) which are near the fuel melt temperature. The particle velocities are approximately 5 m/s, consequently under prompt burst time scales (a few ms) not enough fuel motion can occur to cause significant reactivity feedback. Thus, the fuel-particle interactions with sodium vapor and other structural materials must be examined to study extended fuel motion and its reactivity effects.

5.2 Disassembly Phase -- Energetics (K. O. Reil, 4423; M. F. Young, 4425; W. M. Breitung, 4425)

Studies are being performed to examine the energetic response of reactor fuel-clad-coolant systems to super-prompt critical conditions. In particular, the objective is to identify and characterize the phenomena resulting in pressure generation and in the conversion of thermal energy to work. Attention is focused on the pressure source associated with fuel vapor pressure, inherent impurities in the fuel, fission products and the coolant vapor pressure as well as the determination of coolant voiding rates.

On prompt burst timescales the pressure source from fuel vapor, inherent impurity gases, and fission gases as well as the accelerations produced by these pressure sources are of central importance. Thus the program in this area centers on determination of the Effective Equation of State (EEOS) of fresh and irradiated fuels, the dynamics of pressurization (rate effects) and the ability of this pressure to disperse fuel. The experiment consists of a closed volume instrumented with a pressure transducer and an associated calorimeter. From the pressure history, reactor power history, and total energy deposition (from calorimeter) obtained during an ACRR transient, the EEOS can be deduced.

Efficient heat transfer from fuel to coolant can give rise to significant work energy driven by expansion of coolant vapor. The fundamental question here is whether the oxide-fuel-sodium-coolant system is capable of supporting large-scale efficient thermal interactions. The program in this area is directed at determining if significant fuel coolant interactions (FCIs) can occur in the oxide-sodium system and to determine the dominant controlling parameters and corresponding sensitivities. The mixture will be formed by dispersing coarse UO_2 particulate in sodium in a one-dimensional shock-tube geometry and then melting the particulate during an ACRR transient. An integral part of this program is the development of a hydrodynamic FCI analysis code which provides a necessary structure to evaluate phenomenological models against the results of experiments.

These separate effects experiments (EEOS and FCI) are coupled with the integral Prompt Burst Energetics (PBE) experiments. These experiments examine energy conversion obtained from disassembly of intact pin geometries. The main functions of the integral experiments are to provide qualitative information about the importance of various pressure sources to energy conversion, to identify mitigating effects which influence energy conversion, and to estimate total work potential. In tests performed to date, single fuel pins surrounded by coolant have been subjected to power transients in the Annular Core Research Reactor (ACRR) resulting in fuel vaporization and pin failure. The pin and associated coolant channel were contained in a rigid pressure vessel instrumented with thermocouples and pressure transducers and filled

with a movable piston at its upper end. Estimates of the conversion of thermal energy to work result from comparisons of the kinetic energy of the piston to the fission energy input to the fuel. This work has led to the development of the EXPAND pin failure model. Due to resource constraints, the Disassembly Phase area will be limited to performing the KfK-NRC collaborative EEOS experiments and performing preliminary planning and analysis for future sodium-UO₂ FCI experiments.

5.2.1 Introduction

During this quarter, a critical review of reactor fuel vapor-pressure data was completed. This study, summarized in this quarterly report, shows that the requisite precision for these data has not yet been attained. Preparations for the joint KfK-NRC EEOS experiments are continuing.

The development of a 1-dimensional FCI analysis code, Thermal Explosion Analysis System (TEXAS), is continuing along with the development of the experiment technologies for the coarse dispersed mixture (CDM) FCI experiments.

5.2.2 Vapor Pressure of Liquid Oxide Fuels: A Review

5.2.2.1 Introduction

As part of the on-going EOS research effort at Sandia, the numerous theoretical and experimental results published for the vapor pressures of unirradiated UO₂ and (U,Pu) O₂ over the past 15 years, were summarized and critically reviewed. To allow a clear presentation of this extensive task, the available data base was divided into three sub-areas:

- a. Theoretical $p_{sat} - T$ results
- b. Experimental $p_{sat} - T$ results, and
- c. Theoretical and experimental $p_{sat} - U$ results.

5.2.2.2 Definition of Research Goals

As a first step in the assessment, the precision was quantified; this is required in the fuel saturation vapor pressure data for the purpose of HCDA calculations. Such a precision estimate will serve as the goal against which the accomplishments of the various theoretical and experimental methods can be compared. Because only intuitive feelings have been expressed so far about the required vapor pressure precision - often a factor of two - the derivation of a quantitative estimate was attempted in the following way:

The quantity of primary interest in core disassembly calculations is the excursion yield, Y. Uncertainties in the calculated yield arise from the uncertainty in the vapor pressure as well as from other accident variables like reactivity ramp rate, $\dot{\xi}$, Doppler coefficient, D, etc. The total yield uncertainty Y can be written as:

$$Y = \frac{\partial Y}{\partial P_{\text{sat}}} \cdot \delta P_{\text{sat}} + \frac{Y}{\dot{\xi}} \delta \dot{\xi} + \frac{\partial Y}{\partial D} \cdot \delta D + \text{terms for other variables} \quad (5.1)$$

Obviously, the term from vapor pressure uncertainties should be some fraction "a" of this dominant term:

$$\frac{\partial Y}{\partial P_{\text{sat}}} \cdot \delta P_{\text{sat}} = a \cdot \frac{\partial Y}{\partial \dot{\xi}} \cdot \delta \dot{\xi} \quad (5.2)$$

A value of $a = 0.5$ appears as a reasonably balanced value. The two derivatives in Equation (5.2) were evaluated from sensitivity studies which investigated the dependence of the calculated excursion yield Y on the fuel saturation vapor pressure p_{sat} and the ramp rate at prompt critical, $\dot{\xi}$. Integration yields the following relation:

$$P_{\text{sat}} = \left(\frac{\dot{\xi}}{\dot{\xi}_0} \right)^{ab/s} \quad (5.3)$$

where the quantities b and s result from the sensitivity studies.⁵⁻⁹ Equation (5.3) defines the factor $(p_{\text{sat}}/P_{\text{sat},0})$ by which the saturation vapor pressure may vary if the ramp rate of the accident is uncertain by the factor ξ/ξ_0 . Equation (5.3) leads to the conclusion that the fuel saturation pressure should be known within a factor of 2 to 4, depending on how well the ramp rate of the considered accident is known.

Owing to the exponential relationship between pressure and energy variable (T or U), these acceptable pressure uncertainties $(P_{\text{sat}}/P_{\text{sat},0})$ translate into very small acceptable uncertainties in temperature T or internal energy U . Table 5-III summarizes the research goals against which the accomplishments of the various methods for determining fuel saturation pressures were compared.

Table 5-III. Research Goals

Precision Level	Uncertainty Range in ξ/ξ_0	Acceptable Pressure Uncertainty $P_{\text{sat}}/P_{\text{sat},0}$	or Acceptable temperature uncertainty $\delta T/T$	or Acceptable internal energy uncertainty $\delta U/U$
I	.66 to 1.5	4.0	$\pm .05$	$\pm .057$
II	.83 to 1.2	2.0	$\pm .025$	$\pm .029$

5.2.2.3 Assessment of Vapor Pressure Results for Liquid UO_2

5.2.2.3.1 Theoretical $P_{\text{sat}} - T$ Results

Figure 5.2-1 summarizes the theoretical results for the saturation vapor pressure of liquid UO_2 . Four theoretical methods were used to derive these $P_{\text{sat}} - T$ data.

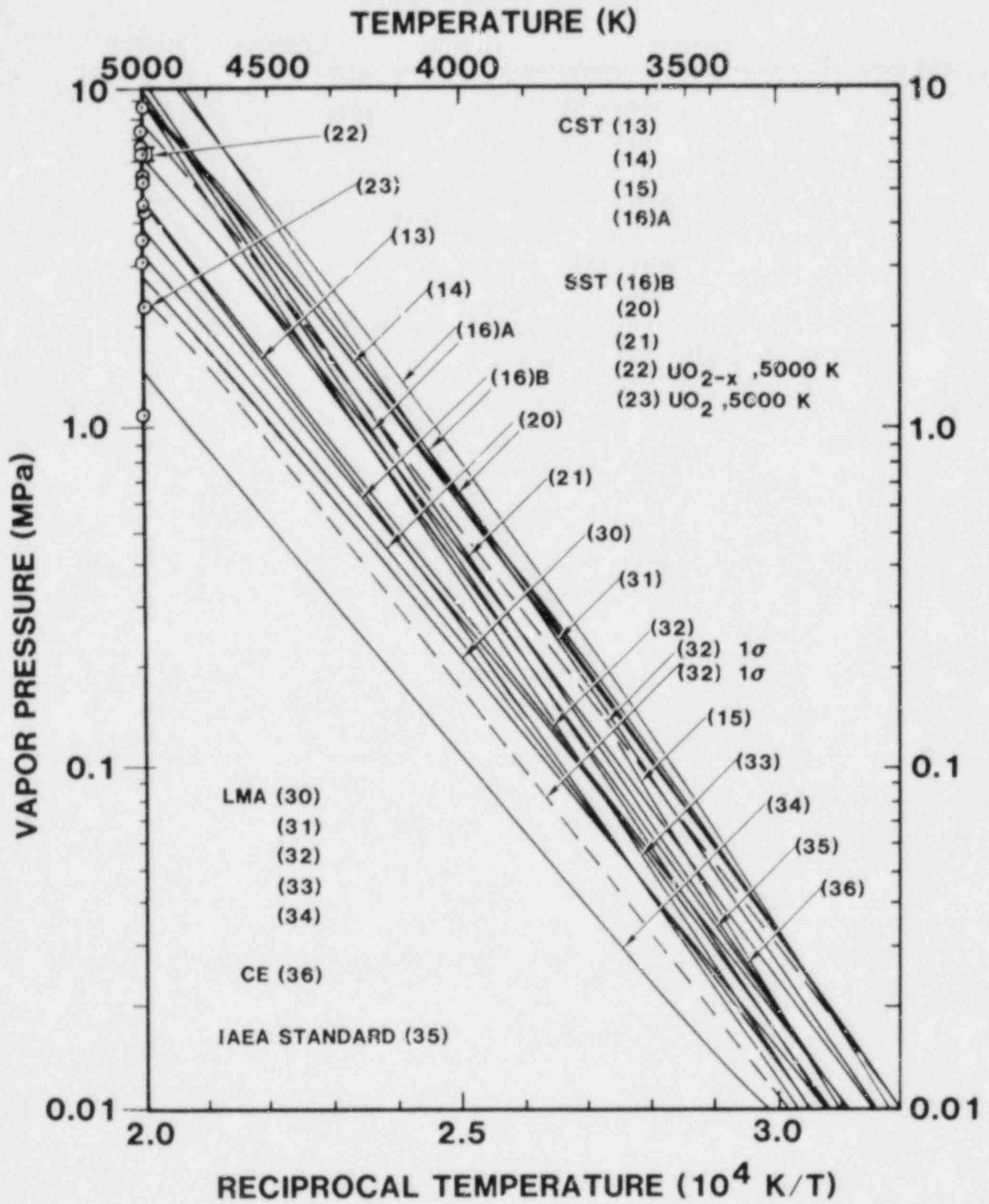


Figure 5.2-1. Calculated Saturation Vapor Pressures of Liquid UO_2 as Function of Reciprocal Temperature⁵⁻¹⁰

a. Corresponding States Theory (CST) -- The published saturation vapor pressures from CST differ by a factor of 3. These differences originate mainly from the different sets of critical UO_2 data, used in generalized CST. At present, no experimental or theoretical basis exists for favoring one particular set of critical data over any other proposed set.

An additional more fundamental source of uncertainty lies in the empirical nature of generalized CST. Little molecular similarity is likely to exist between the reference liquids and liquid UO_2 , so that the empirical CST-data basis for predicting UO_2 properties may not be applicable. The errors associated with applying the CST data to liquid UO_2 are not amenable to a quantitative estimate. So aside from the above mentioned factor of 3, an additional uncertainty of unknown size exists. Consequently, to state that the true UO_2 vapor pressure is within a factor of 4 around any CST pressure curve is not possible. Thus, general CST results do not appear to meet the Level I precision defined above (factor of 4 in pressure).

b. Significant Structure Theory (SST) -- SST results for UO_2 vapor pressure depend strongly on the particular set of input data. In sensitivity studies the calculated vapor pressure changed by a factor of 6 at 5000 K when the solid input data were adjusted to the most recent recommendations. A not unreasonable variation in the electron densities caused vapor pressure differences of a factor of 8 at 5000 K.

Furthermore, SST is a semi-empirical approach for picturing the behavior of a liquid. Although the basic assumption and the intuitively modified partition function of the solid-like molecules allowed a successful description of properties for quite a number of substances, SST is by no means a universally proven approach. Systematic errors cannot be excluded when SST is applied to an exotic liquid like UO_2 , aside from the above mentioned input data uncertainties. The SST vapor pressures published so far, do not appear to allow location of the true UO_2 vapor pressure within a factor of 4.

c. Law of Mass Action (LMA) -- The LMA method is based on a proven physical law, contains no free parameters and fully describes the chemical reactions associated with equilibrium vaporization of UO_2 . If the

uncertainties in the input data are known, the uncertainty in the calculated saturation vapor pressure can be estimated also. The first attempt at narrowing down the probable vapor pressure region gave a factor of 3 for the 1- σ band (curves 32 in Figure 5.2-1). Since the 1- σ band corresponds to only 70-% confidence, there is still a 1:3 chance to find the actual vapor pressure outside this band. The 2- σ band, which corresponds to 95-% confidence, extends in these calculations from essentially 0 to 10 MPa at 5000 K, a rather inconclusive result. So the standard deviations of the input data need further reductions before the 2- σ band (which would be a really conclusive band) can meet the requirements defined in Section 5.2.2.2.

d. Clapeyron-Equation (CE) -- The CE approach, as used so far, is a simplified LMA method which only considers gaseous UO_2 and which neglects important vapor species like UO_3 and O.

The results obtained with this method merely demonstrate that measured vapor-pressure data can be fitted by postulating a very high electronic contribution to the enthalpy of gaseous UO_2 . The CE calculations did not yield new independent results for the partial pressure of gaseous UO_2 and clearly not for the complete saturation vapor pressure of liquid UO_2 which is of interest for the HCDA analysis.

e. Summary -- Despite substantial theoretical efforts, none of the methods discussed above is presently capable of locating the factor-of-4 vapor pressure band (Level I precision) which undoubtedly contains the true UO_2 vapor pressure. In this situation, the IAEA standard (curve 35 in Figure 5.2-1) appears to be a reasonable recommendation because this line is close to the average of all published results.

Of the different theoretical methods, the Law-of-Mass-Action seems to offer the most direct way to achieving this goal because uncertainties in LMA results come from input data uncertainties only. Results obtained with generalized CST or SST underlie additional unresolved uncertainties, based on the theoretical models themselves. Further research needs for the theoretical methods are discussed in Section 6.1 of Reference 5-1.

5.2.2.3.2 Experimental p_{sat} - T Results

Figure 5.2-2 summarizes the vapor pressure measurements on liquid UO_2 . In this section, the accomplishments of the 5 different measurement techniques used are compared to the above defined research goal.

a. Transpiration Technique -- Although the transpiration results extend only a few hundred degrees into the liquid range, they appear to be very valuable data points for the following reasons:

- o The results for solid UO_2 agree well with those of other techniques, suggesting that the important requirements of the transpiration method, e.g., carrier gas saturation, were also met in the measurements on liquid UO_2 .
- o The evaporation conditions are very similar to those expected in HCDA situations, in the sense that the liquid-vapor mass transfer is driven solely by equilibrium-energy transfer from phonons to surface atoms.
- o Combination of pressure uncertainties ($\pm 10\%$) and temperature uncertainties ($\pm 1\%$) lead to a pressure band which is within the factor-of-2 goal.

Consequently, the transpiration data deserve a high weight in the overall picture of Figure 5.2-2.

b. KfK-INR Technique -- The pressure evaluation model addresses the main gas-dynamic features of the free vapor expansion encountered in laser-induced UO_2 vaporization. One subsequent conclusion (5-9) was that the combined pressure uncertainty from random and systematic errors could be somewhat larger than a factor of 3. The temperature uncertainty in the first measurement was relatively large ($\pm 6\%$) mainly due to uncertainties in the number of relaxing degrees of freedom in the off-streaming vapor. The later measurements used optical pyrometry based on UO_2 emissivities which were measured by the same group with the same pyrometry technique. The resulting temperature uncertainty was estimated to less than $\pm 1\%$.

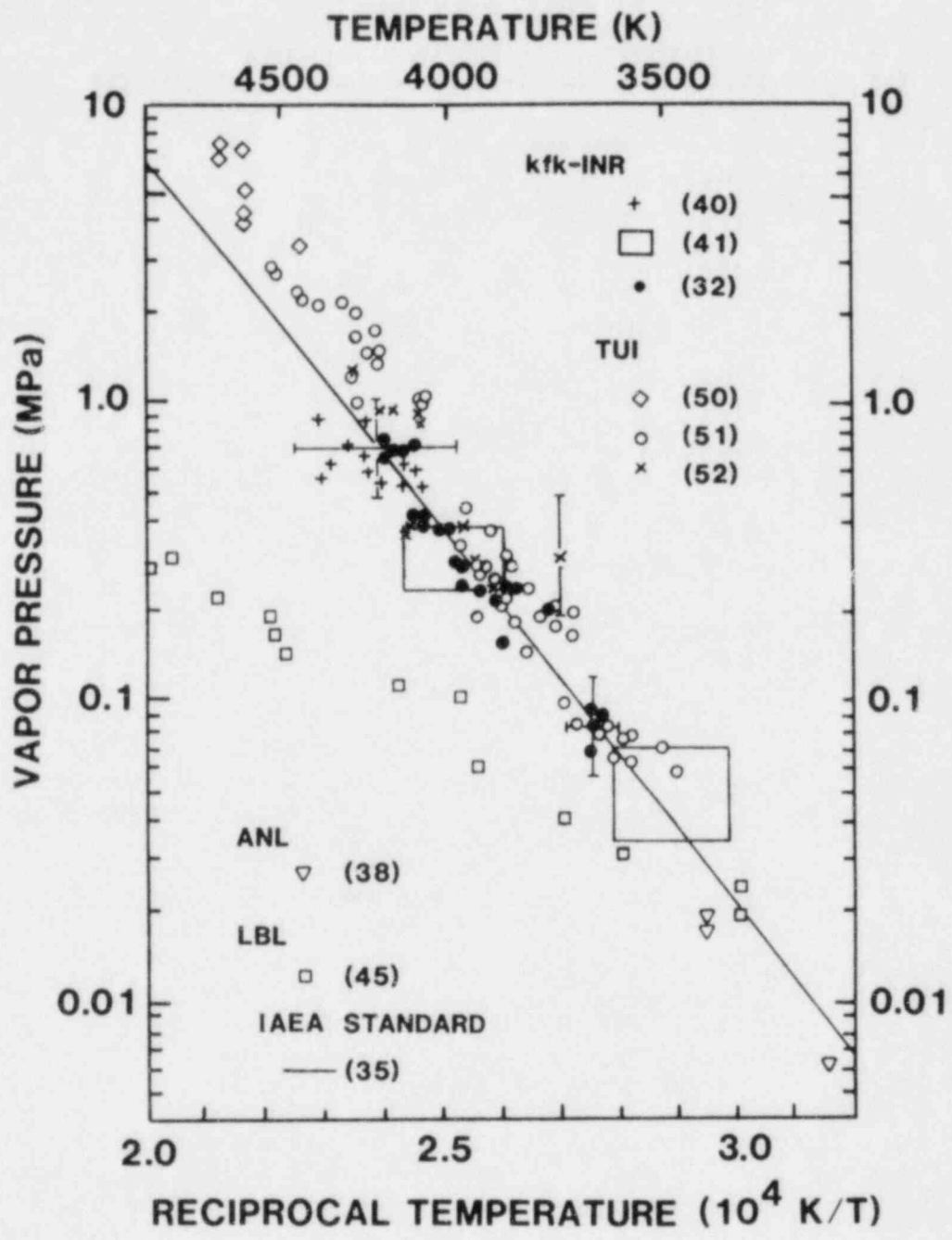


Figure 5.2-2. Measured Vapor Pressures of Liquid UO_2 as Function of Reciprocal Temperature⁵⁻¹⁰

So, apart from the below discussed problem of optical absorption in laser evaporation, the KfK- $\bar{I}NR$ technique appears to be a valid approach for measuring the laser-induced vapor pressure of UO_{2-x} . The achieved degree of uncertainty corresponds roughly to the factor-of-4 goal, defined in section 5.2.2.2.

c. LBL-NASA Technique -- The first Mach Disk results for UO_2 must be considered preliminary until the phenomena involved are fully understood. Most importantly, a more appropriate and convincing redefinition of the effective orifice diameter, d , is needed for the case of laser-induced evaporation. The present work at LBL addresses this point and other important aspects of the Mach Disk method. These efforts will probably allow an improved reinterpretation of the first measurement series and will contribute to the further development of the Mach Disk method.

d. ITU Vacuum Evaporation -- The pressure evaluation in this technique is based on a relation which appears to have little or no physical relevance for the conditions encountered in laser-induced evaporation. Its formal application to laser evaporation may result in significant errors, but a reliable estimate is not possible at the present time.

With respect to the pyrometric temperature measurement, a systematic correction of the temperatures seems necessary since a constant UO_2 emissivity of $\epsilon_{.65} = 0.84$ was used in the evaluation. The emissivity data, which became available meanwhile, indicate that the temperatures plotted in Figure 5.2-2 should be about 2% lower at 4200 K and probably 3% lower at 4700 K.

Significant unresolved uncertainty margins are thought to be associated with the ITU pressure evaluation, making it unfeasible to assign an overall uncertainty estimate to these p-T data.

e. ITU Mach Disk Method -- The ITU group redefined reservoir pressure p_0 and sonic orifice diameter, d , of the original Mach Disk approach on the basis of a gas dynamic analogy. Since the resulting modifying constant for the derived vapor pressure is large, a factor of 9 to 11, the error margins in the ITU Mach Disk method are governed by the accuracy with which the modifying constant ($1/(A \cdot \delta^2)$)

is known. Although the gas dynamic calculations done so far largely extended the theoretical basis for this technique, apparently important characteristics of UO_2 vapor, such as internal degrees of freedom were neglected. Further work must show if the constructed gas dynamic analogy between reservoir expansion and laser-induced vaporization is compatible with the properties of multi-component UO_2 vapor and if so, what their influence on the calculated values for A and δ is. The published pressure uncertainty of a factor 2.5 (see Figure 5.2-2) may or may not cover the effects from ignored UO_2 vapor properties.

f. Open Questions in Laser Evaporation -- Aside from the above discussed uncertainties in the individual laser results, three open questions exist with all laser techniques. Answers to these questions will be needed before a final assessment of the laser results and their significance for HCDA conditions can be made.

(1) Optical Absorption in UO_2 Vapor -- A common problem of the pyrometric temperature measurement is that light emanating from the laser crater could be absorbed in the UO_2 vapor plume. However, optical absorption was neglected in all pyrometric temperature measurements.

The theoretical investigations done so far do not fully address the conditions of interest because optical absorption is not determined by the translational temperature of the vapor molecules, as was assumed, but rather by their electronic temperature. Factors that are important for the actual absorption are, therefore:

- The electronic temperature of the laser-generated vapor molecules as they leave the liquid-vapor interface, and
- The relaxation of this electronic temperature during vapor expansion.

The optical absorption in laser-induced UO_2 vapor can probably only be quantified with the necessary precision by performing transmission experiments on UO_2 vapor clouds.

(2) Composition Changes in the Evaporating Surface -- Because UO_2 generally evaporates incongruently, composition changes in the evaporating surface are to be expected (UO_2 changing into UO_{2-x}). This effect, which

may imply vapor pressure changes, must be understood for the complete interpretation of laser results.

Calculated equilibrium vapor pressures of substoichiometric oxides depend only weakly on the O/U ratio, and in the first approximation, surface changes can be neglected up to 4500 K.

However, if thermodynamic equilibrium should not be present at the liquid-vapor interface, the extent of surface changes and their consequences on vapor pressures is again an open question. Experimental investigations for UO_2 appear necessary before the effect of surface changes on laser vapor pressures can be established without doubt.

(3) Laser-Induced Evaporation -- The third point needing clarification concerns the evaporation mechanism that is active in laser-induced evaporation. This important question was only recently addressed by the ITU group which investigated the energy transfer under laser heating conditions. As indicated below, the incoming laser photons are absorbed by electrons and their energy is then passed on through the various statistical subsystems:

photons \rightleftharpoons electrons \rightleftharpoons phonons \rightleftharpoons surface atoms \rightleftharpoons vapor

The microscopic, multistep evaporation process acting in laser vaporization must be understood before the significance of laser-induced vapor pressures for HCDA calculations (which require equilibrium vapor pressures) can be evaluated.

g. Summary -- The quite precise transpiration data, which have a pressure uncertainty factor below 2, indicate a saturation vapor pressure slightly below the IAEA standard (Figure 5.2-2). Unfortunately, these data extend only to 3400 K. At higher temperatures only laser results are available. From the assessment of the pressure and temperature evaluation in the various laser techniques, the overall pressure uncertainty factor, p/p_0 , appears to be either greater than, or close to 4 (KfK-INR technique), mainly due to uncertainties in the pressure evaluation. Little uncertainties result in principle from the pyrometric temperature measurement, provided correct UO_2 emissivities are used. However, in addition to these

experiment-related uncertainties, open questions remain which must be answered before a final assessment of the laser results can be made. At present, with these questions unanswered, the measured laser vapor pressure data above 3400 K remain very uncertain and their significance for HCDA calculations, which require equilibrium later, is unclear.

5.2.2.3.3 Theoretical and Experimental p_{sat} -U Results

Figure 5.2-3 summarizing the calculated and measured p-U data of liquid UO_2 .

a. Theoretical Work -- Pressure-energy relations for UO_2 were calculated using CST or SST. In both theoretical approaches, appreciable uncertainty margins enter from the input data and from the model itself. No basis exists to support the expectation that any of the CST or SST results is within the goal defined in section 5.2.2.2. In addition, because no clear reason exists for preferring one of the curves, a wide band of possible p-U relations exists. Only careful measurements can narrow these uncertainties down to the desired level. The dotted curve in Figure 5.2-3 is obtained if the IAEA p-T standard from Figure 5.2-2 is converted with $c_p = 0.5 \text{ J/gK}$. This curve should only serve as a temporary reference line between Figures 5.2-2 and 5.2-3 because the heat capacity of liquid UO_2 is still very uncertain above 1800 J/g.

b. Experimental Work

(1) Sandia Technique -- The measured pressures are likely to be higher than that of pure $\text{UO}_{2.00}$ for two reasons:

- The fuel sample was hyperstoichiometric (O/U = 2.08) and
- Extrinsic contamination could have been introduced during test preparation.

With respect to the energy evaluation, an important open question is that of fuel geometry after melting. If a compacted geometry was attained in the liquid state, the peak energy curves in Figure 5.2-3 would have to be shifted to higher energies, into the vicinity of the IAEA reference line.

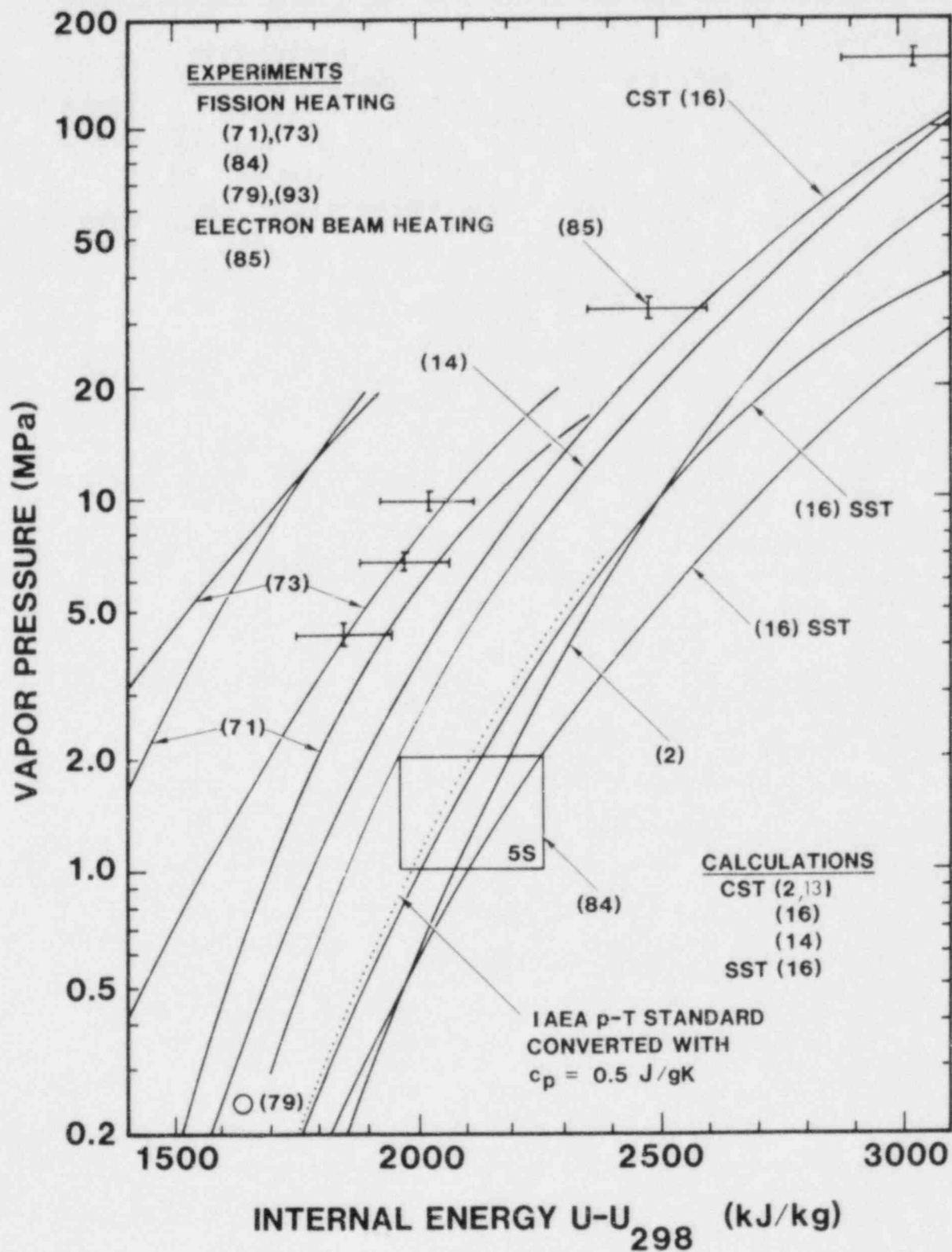


Figure 5.2-3. Measured and Calculated Saturation Vapor Pressures of Liquid UO_2 as Function of Internal Energy⁵⁻¹⁰

(2) CEA Technique -- The measured pressure can be considered HCDA typical because extrinsic impurities from the test preparation were avoided. With an apparent uncertainty of $\pm 20\%$ the pressure evaluation is very good. However, the energy evaluation of the boiling fuel zone is much less precise, mainly because energy deposition gradients in the fuel sample and the time dependence of the coupling factor were neglected. A rough estimate for these effects⁽⁵⁻¹⁰⁾ resulted in $16 \pm 3\%$ more energy deposition. Evaluation of the fuel energy with the required precision (± 3 to $\pm 6\%$) remains the main task for the improvement of this promising technique.

(3) Sandia Experiment PBE-5S -- Note that the p-U region shown in Figure 5.2-3 does not result from a direct measurement, but from a SIMMER sensitivity study of this integral pin experiment. The uncertainties in the pressure might be quite large. Nevertheless, the analysis seems to indicate a UO_2 vapor pressure in the vicinity of the IAEA reference line.

(4) REBA Experiments -- The energy state of the liquid sample prior to expansion seems to be defined quite well ($\pm 6\%$). Conclusions with respect to the measured pressures were:

- Non-prototypical pressure contributions from absorbed water vapor, gases or other extrinsic impurities can be expected.
- The hyperstoichiometric sample composition ($\text{O/U} = 2.08$) should result in high pressures compared to $\text{UO}_{2.00}$.
- The isobaric expansion observed in REBA experiments is not compatible with fuel vapor alone, an additional pressure source is needed to explain the isobaric expansion.

Consequently the REBA pressures should be considered upper bounds for the saturation vapor pressure of hyperstoichiometric uranium oxide ($\text{O/U} \approx 2.08$). The saturation vapor pressure of $\text{UO}_{2.00}$ is thought likely to be substantially lower than the REBA data.

The assessment of the REBA results indicated that several poorly understood effects exist in this technique. Unfortunately, this interesting method remained in an experimental stage where the concern that unresolved physical mechanisms influenced the measured data cannot be excluded.

c. Summary -- The above assessment of the existing p-U work resulted in a noticeable amount of evidence that the saturation vapor pressure of UO_2 is located in the vicinity of the IAEA reference line. However, this conclusion needs further experimental confirmation.

Comparing the different experimental and theoretical methods, in-pile EOS experiments appear to provide the most promising approach to determining p-U relations of nuclear fuels. The reasons are twofold:

- o Heating method and heating time are HCDA-typical. Unknown or not well understood pressure phenomena will thus be included empirically in the measurements.
- o The technique can be extended in a relatively easy way to irradiated (U,Pu) mixed oxide, which is the fuel of ultimate interest for HCDA analyses.

The in-pile EOS experiments now underway at Sandia will provide new high precision data and contribute to an improved p-U data base for liquid UO_2 .

5.2.2.4 Assessment of Vapor Pressure Results for Liquid (U,Pu) O_2

Although (U,Pu) mixed oxide is the actual fast breeder fuel, only a limited work has been carried out on vapor pressures of (U,Pu) oxides compared to UO_2 . Theoretical treatments are impeded by the significantly increased complexity of the U-Pu-O system and by the more limited data base on which a model could be founded. Experimental work is hampered mainly by the excessive technical requirements, associated with handling plutonium bearing fuel. As a result, vapor pressure data for (U,Pu) mixed oxides are scarce and subject to even larger uncertainties than those of UO_2 .

Figure 5.2-4 summarizes the few published results for unirradiated (U,Pu) mixed oxide.

5.2.2.4.1 Calculations

The LMA calculations for (U,Pu) mixed oxide rely on the additional assumption, compared to UO_2 , of ideal solution behavior between uranium and plutonium oxides. Moreover, the plutonium related LMA input data are less well known than those of UO_2 .

5.2.2.4.2 Measurements

The measured data in Figure 5.2-4 were obtained with the laser technique discussed in 5.2.2.3.2(d). Aside from the already mentioned problems of this method with UO_2 , the measurements on (U,Pu) mixed oxide suffer from 2 additional difficulties:

- o The emissivity of liquid (U,Pu) mixed oxide is not known for the measuring temperatures.
- o The surface composition of the sample is even more uncertain because not only the oxygen/metal ratio but also the $U/(U + Pu)$ ratio in the evaporating crater is likely to change during the measurements, possibly implying vapor pressure changes.

5.2.2.4.3 Summary

The pressure uncertainty factor for mixed (U,Pu) oxides is currently greater than 4, the research goal defined in Section 5.2.2.2. Apparently, the existing theoretical and experimental methods for vapor pressure determinations first need to be improved and tested for the case of UO_2 before meaningful data for (U,Pu) O_2 can be obtained. However, theoretical calculations and laser experiments are restricted to fresh UO_2 and (U,Pu) O_2 . For irradiated mixed oxide, the fuel of ultimate interest, vapor pressures relevant to HCDAs seem obtainable only from in-pile fission-heating experiments.

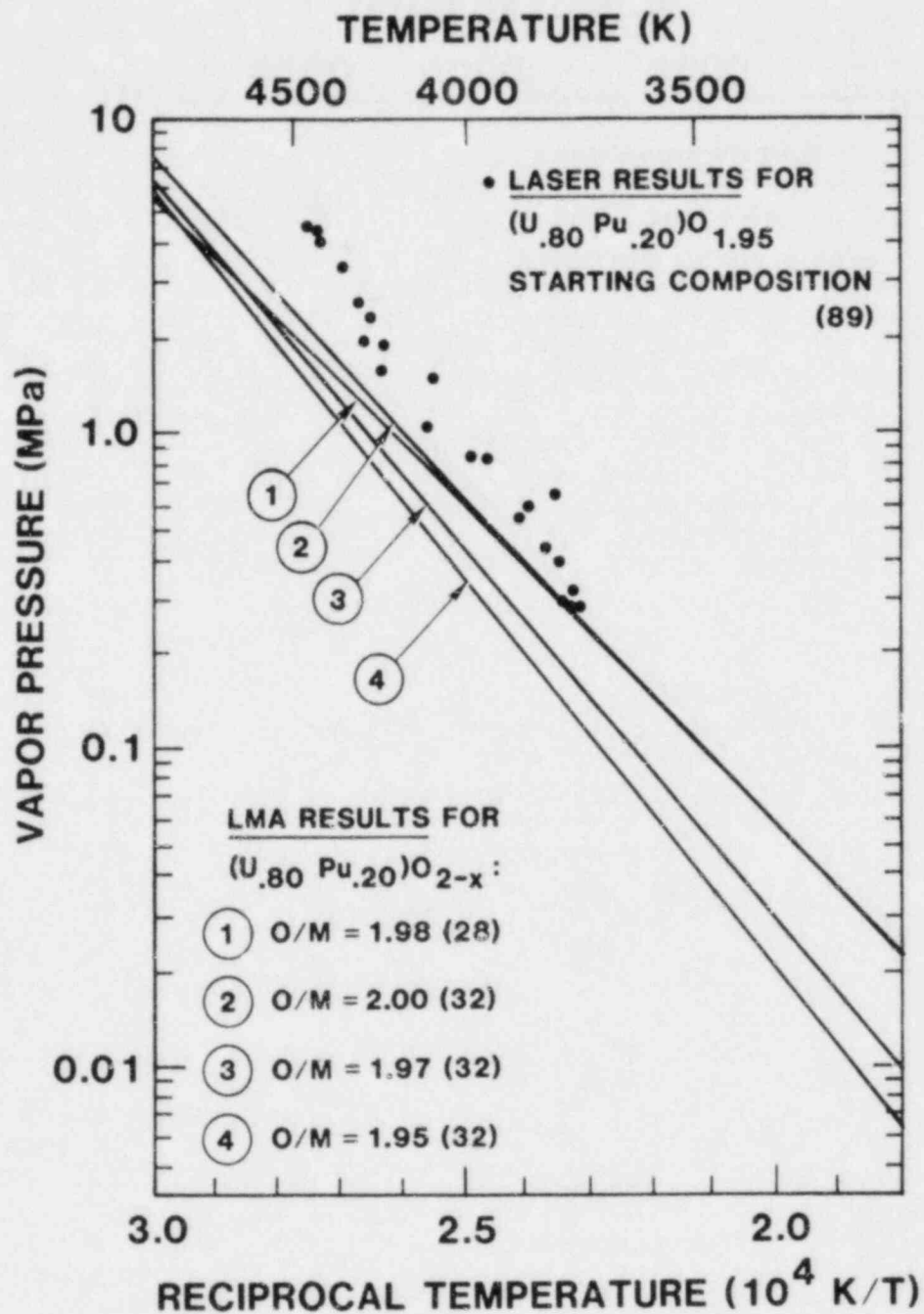


Figure 5.2-4. Measured and Calculated Saturation Vapor Pressures of Liquid (U,Pu) Mixed Oxide as Function of Reciprocal Temperature⁵⁻¹⁰

5.2.3 EEOS Experiment Status

Preparations for the upcoming EEOS experiments are continuing. The primary activities currently include fabrication of the in-pile experiment hardware, completion of the safety analysis and review, and construction of the clean glove box-ultra high vacuum (UHV) facility used for experiment assembly.

The fabrication of the radiological containment and filter structures is nearly complete. Proof tests of the design of the prototype pressure cells and calorimeter pressure vessels showed the closure flanges to be inadequate. Minor changes were made in the designs of those components and the production of the balance of the calorimeters and pressure cells was initiated. Apparently the assembly of the clean glovebox UHV facility within the glove box laboratory will require the most time of all the EEOS preparations. The glovebox and the main vacuum system have been connected and the atmosphere control system has been installed. The installation of all the related external plumbing and support systems, however, is just now starting. The computer interface for the mass spectrometer has been designed and is being fabricated. Investigators expect that this facility will be completed in September or October.

5.2.4 Thermal Explosion Analysis System (TEXAS)

To facilitate design of the CDM experiments and eventually to permit comparison of experiment results with models, a one-dimensional FCI-analysis code is being developed. The code is currently called the thermal explosion analysis system (TEXAS). The basic framework of the code consists of Lagrangian fuel particles moving through an Eulerian vapor-liquid field. Slip and energy exchange are allowed between all components, and mass exchange exists between vapor and liquid. The Lagrangian treatment of the fuel eliminates most of the numerical mixing that has been a problem in Eulerian codes. Current activity is involved with evaluation of the routines dealing with two phase fluid interactions.

5.2.5 CDM Experiment Development

Four major aspects of the CDM experiments are under development. These are:

- a. Fabrication of UO_2 spheres
- b. Piston motion diagnostic
- c. Formation of a uniform fuel-sodium mixture
- d. Introduction of known pressure transients into the mixture.

The fabrication of 1-3-mm-OD UO_2 spheres by "Sol Gel" processes is under evaluation at Oak Ridge National Laboratory (ORNL). This activity primarily involves extension of ORNL's existing technology to large (3 mm) diameters.

A means of following piston motion over a 2-m travel is required for these experiments. Current designs will use an array of discrete magnetic sensors to note the passage of the magnetic alloy piston. The outer surface of the piston will consist of a series of rings of different widths to increase the spatial resolution of the detector array.

The fuel-sodium mixture will be formed by dispersing solid UO_2 spheres into a column of liquid sodium and then melting the fuel during an ACRR transient. A prototype device for releasing the fuel spheres has been fabricated and tested. It consists of a number of channels in the wall of a tube that can be opened at the bottom end to permit the spheres to run out into the coolant.

The mixtures formed with the prototype were not as uniform as desired. (Variations of $\pm 50\%$ were noted from photographs of lead shot released into water.) Some of these variations were attributed to coarse surface finishes in the channels of the plexiglass prototype. A new stainless steel prototype is being designed including the high temperature solenoid for opening the channels.

Development of the trigger mechanism has not yet been initiated.

5.3 Transition Phase (D. A. McArthur, 4423; N. K. Hayden, 4425)

The key issues in the Transition Phase are the formation of fuel blockages leading to a confined or "bottled" core configuration, and the behavior and reactivity implications of this pool of fuel-steel in the core region if the fuel blockages do lead to this state. The Transition Phase program addresses the question of fuel penetration into the upper core structure. If deep penetrations occur, nonenergetic shutdown is probable while short penetration will lead to a transition phase and the possibility of further energetics.

Unique experiments are being performed to address this question using prototypic reactor materials under carefully controlled conditions. The ACRR is used to create high temperature fuel-steel melts which are driven under controlled pressure into a heated channel to determine melt penetration behavior. The experiments provide a data base for the evaluation and further development of fuel freezing and streaming models for use in accident analysis.

5.3.1 Preliminary Results of the TRAN-2 Experiment

The second TRAN Series I experiment, TRAN-2, was performed at a steel temperature $T_s = 873$ K (600°C), a fuel temperature $T_f \sim 3773$ K (3500°C), and a driving pressure $P_D = 10$ bar He. Compared to TRAN-1, the driving pressure was applied earlier, at about the time of fuel melt, to protect the nearest pressure transducer from molten fuel, and to minimize downward movement of fuel. The pressure transducer in the dump tank was also protected from streaming fuel by a shadow shield. Self-powered gamma ray detectors were installed at both ends of the fuel melting chamber, and at the entrance and exit of the fuel freezing channel, to investigate whether transient fuel-motion data could be obtained. Good data were obtained from all three pressure transducers. All transducers indicated no detectable gas flow through the channel until ~ 0.5 s after the reactor pulse peak. Thus the channel appears to have been blocked successively by the molten and frozen fuel, until the freezing process was essentially complete. This is in contrast to TRAN-1, in which the channel appeared to open up while the fuel was possibly still molten, with a somewhat porous blockage forming later.

The final fuel distribution in TRAN-2 has been studied with X-radiography and axial gamma-ray scans of the ^{140}La 1596 keV line.⁵⁻¹⁰ Both the radiographs and the gamma scan indicate a distribution which is qualitatively similar to TRAN-1 (a frozen layer of UO_2 in the lower 50 cm of the channel, a blocked region of channel, a channel section without any frozen fuel, and clearly observable amounts of fuel debris beyond the freezing channel). However, in TRAN-2 there were two dense and very well-defined blockages 9 mm apart and 6 mm long, filling the channel 8 cm beyond the frozen layer. Some indirect evidence of fuel slumping was also observed in the freezing-channel radiographs.

The self-powered detectors produced noise-free data during the reactor pulse but after the pulse, the signals decreased sufficiently in magnitude that they were obscured by environmental and digitizing noise. Even during the reactor pulse, small signal variations (unique to each detector location, perhaps) have thus far prevented unambiguous determination of fuel motion. However, with adequate support, computer analysis of these data might reveal fuel motion. Self-powered detectors will therefore be employed on TRAN-3.

Examination of TRAN-2 in the hot cell facility will continue as soon as manpower and scheduling permits.

5.3.2 Postirradiation Examination (PIE) of TRAN-1

The shapes of some of the fuel debris in the TRAN-1 experiment have been examined, because these shapes might reveal whether the debris initially froze on a given surface, or whether it froze elsewhere and was deposited on the surface as a dust of solid particles.⁵⁻¹⁰

A few grams of material were removed from the bottom surface of the dump tank cover plate at the very top of the TRAN-1 apparatus. This material consisted of large flakes and fine fibers of an organic sealant material, perhaps 1 gram of fuel particles, and a small amount of steel which appeared to be filings resulting from machining. The sealant was deposited on the walls of the dump tank during efforts to seal a vacuum leak. When this material was removed from the cover plate, a dark gray mark < 1 cm in diameter was uncovered, approximately at the center of the cover plate. The fuel particles were examined

with optical- and scanning-electron microscopes. The particle sizes ranged from $\lesssim 5 \mu\text{m}$ to $\sim 2 \text{ mm}$. About 67% of the particles had fractured edges, indicating that the fuel had frozen elsewhere, broken away, and been deposited later on the cover plate. The remaining 33% had globular shapes indicative of freezing in flight. No well-defined solid fuel layers or large frozen droplets of fuel were observed anywhere in the dump tank. The amount ($\lesssim 1 \text{ g}$) of fuel observed on the cover plate is much less than would have been expected, based on the axial gamma ray scans.⁵⁻¹¹

5.3.3 Preparation of TRAN-3

The TRAN-3 experiment package has been completely assembled, and used in a preliminary experiment to calibrate the energy deposition in the TRAN test fuel. In this experiment, direct transient measurements have been made of the fuel temperature rise at the center of the fuel load caused by a low-level ACRR pulse. These measurements are being analyzed with a heat transfer code to unfold the energy deposition coupling factor. TRAN-3 will be performed as soon as this coupling factor is determined (assuming no problems are encountered in reaching the 1073 K (800°C) initial steel temperature). The results of TRAN-1, -2, and -3 will be summarized in a topical report.⁵⁻¹²

5.3.4 TRAN Series II Design

A preliminary design has been drawn for the second series of TRAN experiments. In this series a thin-wall, insulated, cylindrical freezing channel will be used. The freezing-channel diameter and wall thickness have been chosen to simulate the hydraulic diameter and cladding heat capacity associated with a single subchannel of the LMFBR blanket structure.

5.3.5 Analysis of TRAN Experiments

The transition phase analysis is proceeding on two levels: a) data analysis for the TRAN Series experiments, and b) modeling of freezing/plugging phenomena. The current data analysis consists of interpretation of the pressure transducer data and calculations of the energy coupling factor* from the fuel temperatures measured in the calorimetry tests mentioned earlier in this report. The results of both the data analysis and modeling efforts are summarized below.

Calibration experiments were performed in October 1980, to measure the He flow rates in the evacuated TRAN Series I experiment package as functions of fill pressures. This data provided the rates of pressure drop in the He reservoir and corresponding rates of pressure rise in the dump tank, as functions of fill pressure, when there is no fuel in either the melt chamber or freezing channel. The rates of pressure rise (and drop) turned out to be linear functions of the fill pressure in the evacuated channel.

To analyze the data from the pressure transducers in TRAN-1 and TRAN-2, rates of pressure rise and pressure drop in the dump tank and He reservoir, respectively, were plotted against the corresponding average pressure difference in effect over discrete periods of time. (This difference decreases in time as He enters the dump tank.) The rates of pressure change were then compared to the rates for an evacuated channel. Blockages are indicated in both experiments, although the TRAN-1 blockage was apparently much more porous than the blockage in TRAN-2. This is evidenced by the relative flow rates. The pressure-transducer data thus confirm the radiograph data, i.e., fuel blockage formation. The detailed results for TRAN-1 and TRAN-2 are included in the topical report.

To verify experimentally the coupling factor in TRAN Series I, calorimetry tests were performed in which fuel temperatures were measured during 3 separate ACRR low

*The energy coupling factor is a parameter that must be experimentally verified for in-pile experiments. It relates the amount of energy deposited in the experiment fuel to the reactor energy.

level pulses. Numerical heat transfer calculations are being performed to emulate the fuel temperatures. In these calculations, the coupling factor is varied until the calculated temperatures match those that were measured. The calculations are necessary for data interpretation because heat losses by conduction are not negligible over the timescale of the thermocouple response time.

The results of TRAN-1 and TRAN-2, i.e., simultaneous crust and blockage formation have been used in the development of an analytic freezing/plugging model which can be used to predict fuel penetration distances. This model combines aspects of both the conduction and bulk-freezing models, which have been formulated by previous workers. The model solves for the distance traveled by the UO₂ when all the initial superheat and latent heat has been lost. At this point the formation of a frozen blockage is assumed. The final equation for this "penetration distance," Z_p, is:

$$Z_p = Z_c + \left(K_{S/L} \left[\frac{h_{S/L}/C_p}{T_{mp} - T_w} \right] \right)^{1/1.1} \quad (5.4)$$

$$\text{where } Z_c = K_L \ln \left(\left[\frac{.883(T_{f,0} - T_{mp}) + h_{S/L}/C_p}{h_{S/L}/C_p} \right] \right)^{1/1.1} \quad (5.5)$$

$$\text{and } K = 12.218 \frac{\rho^{.9} C_p^{1.3} \gamma^{.8}}{k Pr^{.6}} \left[\frac{p}{f_{app}} \right]^{0.1} \quad (5.6)$$

In Equation (5.5), Z_c is the distance traveled by the fuel when the superheat has been lost. The subscripts L and S/L indicate whether liquid UO₂ properties or averaged solid/liquid properties are to be used in evaluating the coefficient K. In evaluating K, ΔP corresponds to the driving pressure, and f_{app}, the apparent friction factor, is taken to be f_{app} = .007.

The distances predicted by Equation (5.4) for both TRAN-1 and TRAN-2 are shown below:

	<u>TRAN-1</u>	<u>TRAN-2</u>
<u>Observed Crust Length</u>	50 cm	55 cm
Z_p , Equation (5.4)	49.6 cm	57.3

The parameters and subscripts in Equations (5.4)-(5.6) are described in more detail in the paper, "An Analytic Model of Freezing Liquid Penetration in Tube Flow," which will be presented at the ANS winter meeting in San Francisco. Included in the paper are details of the analytic model and equation derivation.

The analytic model, while yielding good agreement with the TRAN results, as well as the thermite experiments of Spencer, is not firmly related to mechanistic phenomena. Efforts will continue to establish specific mechanisms for the heat transfer and, particularly, the development of a simultaneous slurry flow (which must be present for bulk-freezing and blockage formation) and stable crust formation.

References

- 5-1. P. Royl, M. Cramer et al, "Analysis of Hypothetical Loss of Flow Accidents Without Scram in the SNR-300 End of Life Mark 1A Core Using the SAS3D Code System," Proceedings of the Int. Mtg. on Fast Reactor Safety Technology, Seattle, WA, Aug 19-23, 1979, pg. 624.
- 5-2. To be published, GEFR-00523.
- 5-3. C. J. Mueller, J. E. Cahalan, J. K. Vaurio, SACO-1: A Test-running LMFBR Accident Analysis Code, ANL-80-6.
- 5-4. G. L. Cano, R. W. Ostensen, M. F. Young, Visual Investigation of Reactor Fuels Response to Simulated LOF Heating Conditions, First Series, NUREG/CR-0914, SAND79-0940 (Albuquerque, NM: Sandia National Laboratories, 1979).
- 5-5. G. Karsten, "Restructuring in Nuclear Ceramics, Transformations of Thermal into Kinetic, Surface and Plastification Energy," Proceedings of Reactor Safety Aspects of Fuel Behavior, Aug 2-6, 1981.
- 5-6. E. H. Randklev, "Radial Distribution of Retained Fission Gas in Irradiate Mixed-Oxide Fuel," Trans. Am. Nucl. Soc., 28 234 (1978).
- 5-7. S. A. Wright, et al, Fuel Disruption Experiments Under High Ramp Rate Heating Conditions, SAND81-0413 (Albuquerque, NM: Sandia National Laboratories, to be published.)
- 5-8. P. K. Mast, The Los Alamos Failure Model (LAFM): A Code for the Prediction of LMFBR Fuel Pin Failure, LA-T161-MS (Los Alamos, NM: Los Alamos Scientific Laboratory, March 1978.)
- 5-9. W. Breitung, Vapor Pressures of Oxide Reactor Fuels above 3000 K: Review and Perspective, SAND81-1383, NUREG/CR-2261 (Albuquerque, NM: Sandia National Laboratories, July 1981).
- 5-10. D. A. McArthur, S. F. Duliere, and D. J. Sasmor, "Posttest Analysis of TRAN-1 and TRAN-2 Final Fuel Distributions," submitted to the Winter ANS Meeting (San Francisco, CA).

- 5-11. D. A. McArthur, R. W. Ostensen and N. Hayden,
Trans. Am. Nucl. Soc. 38, 393, 1981.
- 5-12. D. A. McArthur et al, In-Core Experiments on Fuel
Freezing in Thick Wall Tubular Channels:
Preliminary Report on TRAN Series I Experiments,
SAND81-1726 (Albuquerque, NM: Sandia National
Laboratories, to be published).

6. LIGHT WATER REACTOR (LWR) DAMAGED
FUEL PHENOMENOLOGY
(A. C. Marshall, 4423; P. K. Mast, 4425;
E. D. Bergeron, 4425; J. B. Rivard, 4421;
P. S. Pickard, 4423)

6.1 Introduction

This program is directed toward examining the key phenomena that determine the fuel-damage configuration during the progression of a core melt sequence in an LWR loss-of-coolant accident. This program uses the information and perspectives gained in current LWR safety programs such as SASA and the MARCH Code Assessment Project and focuses on the design of experiments that can contribute to the resolution of important severe-damage issues.

The two major areas of interest regarding in-vessel core retention are:

- a. The behavior of fuel and cladding during the stages of major core deformation from a pin-lattice geometry to a mass of rubble, and
- b. The response of the severely damaged core to reintroduction of (ECCS) coolant especially the questions of redistribution of quenched material, increased steam generation, and oxidation reaction kinetics.

Resolution of the first item is required to predict the course and duration of core disruption and associated effects in containment; resolution of the second provides the essential information to guide action that would terminate the accident and/or mitigate its consequences, and to preclude action that could exacerbate the accident. Obviously, resolution of issues in (b) above depends strongly upon knowledge of the phenomena implied in (a). Initial research priorities and the program proposed here should therefore focus on the behavior of fuel and cladding during major deformation sequences without introduction of additional liquid coolant.

Early work under this subtask focuses on the in-pile experiments because neutronic heating allows prototypic heat generation under severely damaged conditions.

Primary activities for this reporting period focused on the feasibility studies of visual diagnostics for severe core damage experiments. In the previous quarterly report,⁶⁻¹ an assessment of LWR severe-core-damage research needs was discussed. The overall conclusion of the assessment was that the apparent emphasis of most of the current programs is on early phase phenomenological issues such as cladding ballooning and rupture, solid cladding oxidation, etc. The safety issues related to the middle phase of the accidents (transition from pin geometry to debris bed), especially phenomenological data concerning the transient core coolability, are not being extensively investigated.

Note that there are several proposed programs directed at investigating this middle phase of the accident. These programs, such as the PBF experiments, for example, should provide valuable data concerning the time-dependent hydrogen evolution (zircaloy oxidation) and fission-product release during the accident, as well as the effect of quench upon the degraded core geometry. Thus, they contribute much to the resolution of the phenomenological uncertainties. However, these experiments do not intend to provide information concerning the time-dependent reconfiguration of the core geometry resulting from liquefaction and/or reduction to rubble. In terms of the geometry configuration, they primarily provide end-state data through postirradiation examination (PIE).

Without this time-dependent-geometry configuration data, the core configuration at the time of reflood, for example, is not known. Thus, mechanistic interpretation of the obtained data on core coolability and quench consequences is very difficult. Without such a mechanistic understanding, application of the experimental data to the large number of scenarios possible during an actual reactor accident is impractical.

Thus, a very obvious need for additional experimental data involves the characterization of the core geometry during the transition from intact-pin geometry to some damaged configuration. This phenomenological need forms the basis for the Debris Formation and Relocation (DFR) Program. This program is intended to provide real-time data characterizing the core geometry during a

severe accident sequence, as well as data on additional core reconfiguration resulting from quench. This data should have sufficient detail to be useful for the development and verification of models that characterize the phenomena. The models can then be used both to aid in the interpretation of large scale tests such as PBF and to extrapolate from the results of the experiments to the results that would be expected in a severe accident.

6.2 Steam Loop Design

The DFR experiments using the ACRR are planned to involve a small bundle (4-16 pins) of pins about 2 ft in length. Time-varying prototypic steam-flow conditions will be provided by an externally controlled boiler. Fission heating will be used to simulate the decay heating during an accident. Because of the phenomenology to be investigated (loss of pin geometry), fission heating appears to be the most reasonable simulant of the decay heat.

The ACRR experiments are intended to be phenomenological in nature, and as such are fairly small scale. Two very preliminary conceptual designs for these experiments are illustrated in Figures 6.2-1 and 6.2-2. Figure 6.2-1 shows a completely in-pile system including steam supply (boiler, test section, and condenser). Such an in-pile system has the advantage that primary and secondary containment of the experiment apparatus is readily achieved by enclosing the entire system in a dual-walled capsule. Figure 6.2-2 shows an in-pile test section with the principal steam-system components located out-of-pile. Because larger boilers and condensers could be used for such a hybrid system, much larger pin-bundles can be used in the experiments.

A third conceptual design has also been proposed. This design may incorporate some of the advantages of both of the previous design concepts. In this design, the boiler is isolated from possible contamination by a series of check valves; also, the containment wall serves as the heat exchange surface for the condenser. An external coolant system would cool the outer containment wall and contaminated steam is condensed inside the containment boundary. The PAHR-type helium coolant loop or a water coolant may be used to supply the coolant for the

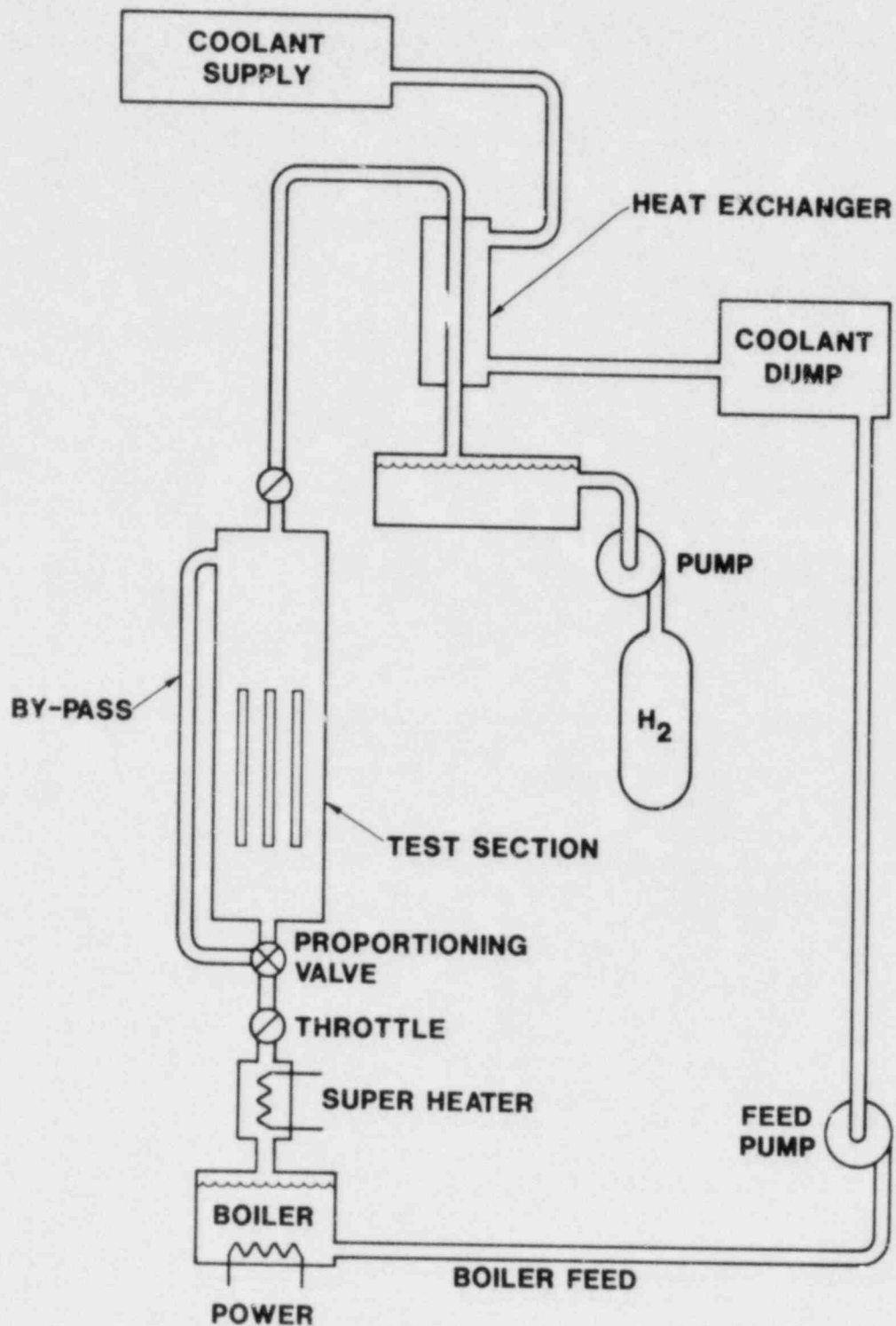


Figure 6.2-1. In-Pile Steam System Conceptual Design

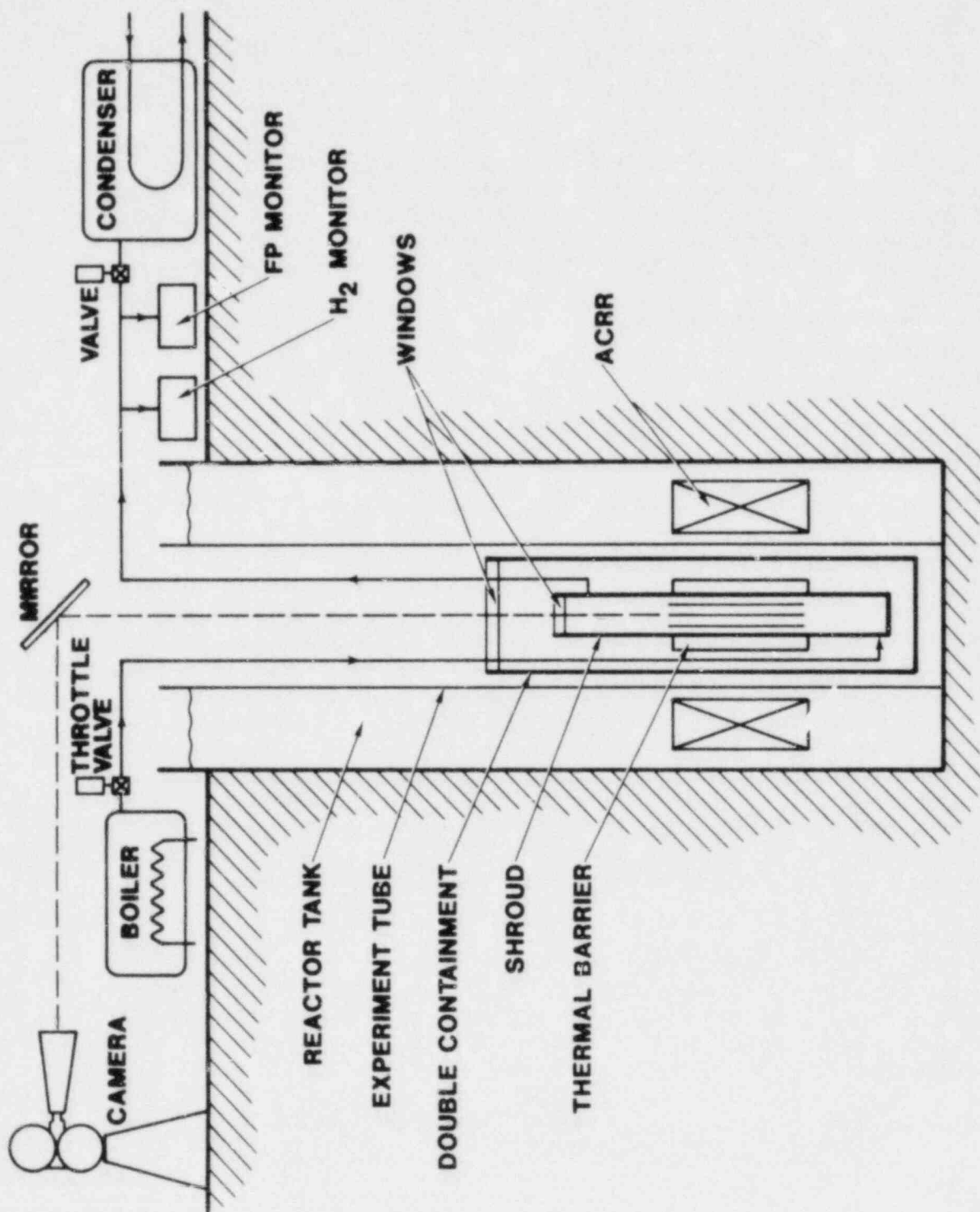


Figure 6.2-2. Schematic of DFR Experiment

containment wall. In this manner, the external systems are isolated from contamination and a relatively small test package is possible.

The test capsule itself consists of the test pin bundle, flow shroud, and thermal shield. The primary function of the shroud is to retain the high-temperature steam/hydrogen in a well-defined flow boundary. Program personnel are currently analyzing several designs for the shroud including a Y_2O_3 stabilized ZrO_2 tube, and a tungsten canister supporting several ZrO_2 sections. The thermal shield is used to prevent excessive heat loss from the test section and may be simply a layer of insulation outside the shroud, or it may consist of a series of thermal radiation shields. Several heated-wall concepts have also been proposed.

Note that the test section shown in Figures 6.2-1 and 6.2-2 suggest a bypass steam system. The bypass steam serves to cool the upper end of the test section shroud.

One of the primary justifications for additional experiments that complement the more integral experiments is "improved" diagnostics to obtain real-time data concerning the core reconfiguration. The ACRR program has been structured around the use of visual observation as the principal diagnostic tool to delineate and quantify the time-dependent damage progression. This allows actual observation of the changing test-section geometry not possible with other less direct diagnostic techniques. The choice of visual diagnostics stems in part from the successful application of this approach in ACRR LMFBR safety experiments. Visual diagnostics have, for example, provided unique data on the mode of fuel disruption under heating conditions representative of loss-of-flow and prompt-burst-accident scenarios leading to a much improved knowledge of fast reactor fuel damage phenomena. Several visual diagnostic approaches are being explored. One design concept includes a sapphire window at the top section of the shroud. A series of mirrors then reflects the pin-bundle image, as viewed through the sapphire window, to a recording camera.

Aside from visual diagnostics, investigators also intend to use more conventional instrumentation including PIE to characterize the end-state conditions (debris particle size distribution, for example). Hydrogen detection systems would also be used to determine the time-dependent hydrogen evolution. The possibility also exists that the

ACRR Coded Aperture Imaging System could be used to augment the visual fuel-relocation data and as a primary diagnostic tool for those phenomena where direct observation is not practical.

As discussed earlier, the ACRR, DFR and DFQ experiments are phenomenological in nature and may have less severe prototypicality requirements. This is especially important relative to the size of the pin bundle that must be used. For the sake of discussion, three bundle sizes have been defined. These are: single pin, few-pin bundles (≤ 9), and multi-pin bundles (> 32). With the emphasis on visual diagnostics, minimizing the bundle size would be desirable because visual observation in the interior of a large-size bundle is not practical. If visual observation is only possible near the exterior of a multi-pin bundle, then little advantage results from going to bundles having more than a "few pins" for those issues that can be addressed in this mode.

Most of the phenomenological issues to be addressed involve possible reconfiguration of the pin geometry and, hence, pin-to-pin interaction. These considerations effectively eliminate single-pin experiments for all but very early issues such as the mode of initial cladding disruption and the timing at initial liquid flow. An assessment of the phenomenological issues to be addressed in the program does, however, indicate that for many of the issues, useful phenomenological data can be obtained in a small-bundle (≤ 9 pins) experiment. Thus, apparently many issues can be addressed by reasonably small-scale low-cost experiments; their size makes them suitable for the use of visual diagnostics.

A test matrix for the DFR program would need to include a sufficient number of experiments to investigate the effects of system pressure, heat-up rates, and different quench times. Because these experiments would typically involve a small pin bundle, a few experiments would be wise to investigate specifically the effect of bundle size on the results. Somewhat nonprototypic results in the small-bundle experiments are only acceptable if the basic phenomenological understanding obtained leads to the development of models that can predict the results of both small-bundle as well as large-bundle experiments. Based on these considerations, a preliminary test matrix for the program is being developed.

References

- 6-1. Advanced Reactor Safety Research Quarterly Report, January-March, 1981, SAND81-1529 (1 of 4), NUREG/CR-2238 (1 of 4) (Albuquerque, NM: Sandia National Laboratories, to be published).

7. TEST AND FACILITY TECHNOLOGY

7.1 ACRR Fuel Motion Detection System (K. T. Stalker, 4426; J. G. Kelly, 4426)

7.1.1 Introduction

The ACRR fuel motion detection system is designed to monitor the motion of nuclear fuel in simulated reactor accidents by imaging (through a slot in the core) gamma rays emitted by the test fuel. Currently the imaging is accomplished by modulating the collimated gamma-ray beam with a coded aperture and allowing the modulated beam to strike a thin scintillator. The visible-light image is then amplified and recorded with an optical image intensifier and framing camera, respectively. Both of these are protected from background radiation by a massive shield.

In the preceding quarterly report the arguments were presented in favor of changing the geometries of the collimators and apertures. During this quarter, the changes required to test two configurations (different from the Fresnel zone code) were drafted and procedures for fabrication of parts were initiated. Both configurations are designed to reduce the influence of spatial noise in the images of test fuel. The first aperture will be a uniformly redundant array (URA) and the second will be the crossed slit aperture (CSA).

Sandia Laboratories, Los Alamos, and the University of Arizona are continuing to investigate coded aperture responses in the presence of spatial noise. These studies use both idealized and experimentally generated data.

An experiment plan has been devised to test the new configurations during November of 1981.

7.1.2 The URA Configuration

Although images of test fuel taken with the Fresnel Coded Aperture have been excellent when the coded image is recorded at the detector plane with X-ray film, the images recorded with the active detector system suffer from graininess and low contrast because of additional

noise introduced in the recording train. Investigators believe that the noise can be reduced significantly if the scale of the image can be expanded with respect to the fluctuations in film-grain density and if the Fresnel coded aperture is replaced by the URA.

The scale of the image on the film will be changed by incorporating 35 mm instead of 16 mm framing cameras. In addition, a change in the image coupling optics between the optical image intensifiers and the cameras will permit the image to be expanded to fill the frame.

Calculations and experiments have shown that the URA will perform better than the currently used Fresnel zone plates for the following reasons.

a. The modulation of the Fresnel plate is not very good because the thicknesses of the zone vanes were made for the theoretical value that would give optimum attenuation of 1 MeV photons. However, the result is that the vanes effectively over-attenuate because the average photon energy, as has been found, is less than the expected 1 MeV. Thus, optimum beam transmission through each zone cannot occur. The vanes and narrow zones of the URA, constructed of tungsten, were made to the correct width, however, and will exhibit better average modulation. Figure 7.1-1 compares these two geometries. The Fresnel code exhibits narrow spikes in the open zones, which are narrower than theoretical (see above), and thus they do not carry as much signal power as had been expected.

b. In the URA the zones of different widths are spread fairly uniformly over the whole plate, while in the Fresnel plate the fine zones which define the resolution are all near the edges of the field of view where the distortions in the active system are highest and where the signal is weakest.

c. The URA is theoretically more tolerant of spatial noise. Simulation studies carried out at Los Alamos have demonstrated that in the same simulated noise environment the reconstructed images are much clearer and have higher contrast than those obtained with the Fresnel code. This may be a result of the flat side lobe structure of the URA.

d. If the URA were designed with fewer zones and placed closer to the object it could maintain the same photon collection solid angle and the same spatial resolution as the present URA has. The advantage would be

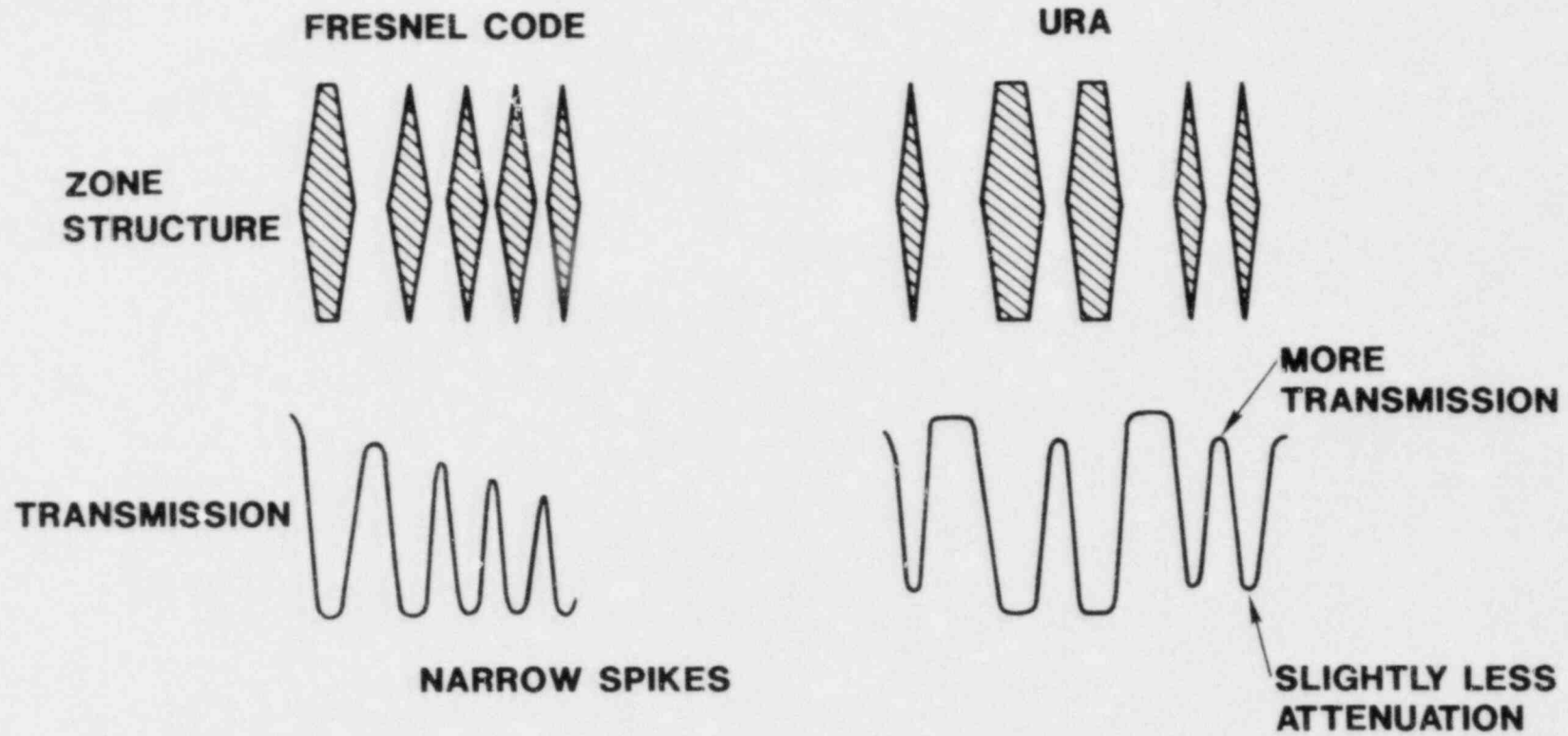


Figure 7.1-1. Comparison of Modulations Provided by the Current Fresnel Code Plate and the URA

a greatly expanded scale of the structure that has to be recorded on the film. This would permit averaging over grain noise without loss of signal. However, discussions with Mike Cannon at Los Alamos, where the pioneering work on URAs has been carried out, confirmed that with few zones the signal-to-noise-ratio advantage of a coded aperture over a pinhole is quickly lost, especially if noise is present. The URA plates with 127 zones already built to operate at the same position as the Fresnel plates might be outperformed by a 63-bit code somewhat closer to the object. However the cost of fabricating and testing the latter would be much higher than testing the current URA. Thus the current URA will be tested first.

Because URA's of even fewer zones can be outperformed by a single forward slit that will cost much less to prepare, the extreme forward aperture configuration can be evaluated properly as part of the crossed slit aperture to be discussed in the next section.

7.1.3 The CSA Configuration

As the introduction mentioned, the reasons for testing the crossed slit aperture geometry, illustrated in Figure 7.1-2, were discussed in detail in the previous quarterly. The principal points were (a) that the image structure at the detector plane will be expanded by about 7.5 times that which has been used thus far, hence, noise can be averaged over more effectively, and (b) that some of the photon collection solid angle will be preserved by moving the slit far forward. Only the portion of the collimator structure that goes into the slot in the core will need to be altered to make it compatible with the slit next to the central test section. This geometry is illustrated in Figure 7.1-3.

The fission gamma rays from the ^{252}Cf source have been used to investigate the imaging capabilities of the CSA geometry. The arrangement is shown in Figure 7.1-4. A narrow slit collimator formed by two lead blocks (with edges curved with a 36 cm radius) was placed 18 cm from the source. X-ray film was mounted in a cassette housed in a lead and borated-polyethylene-walled "dog house" 138 cm from the source. Two separate exposures were made on the same film. The second exposure was made after moving the source 3 mm away from its position for the first exposure; this movement was along a line perpendicular to the line of sight.

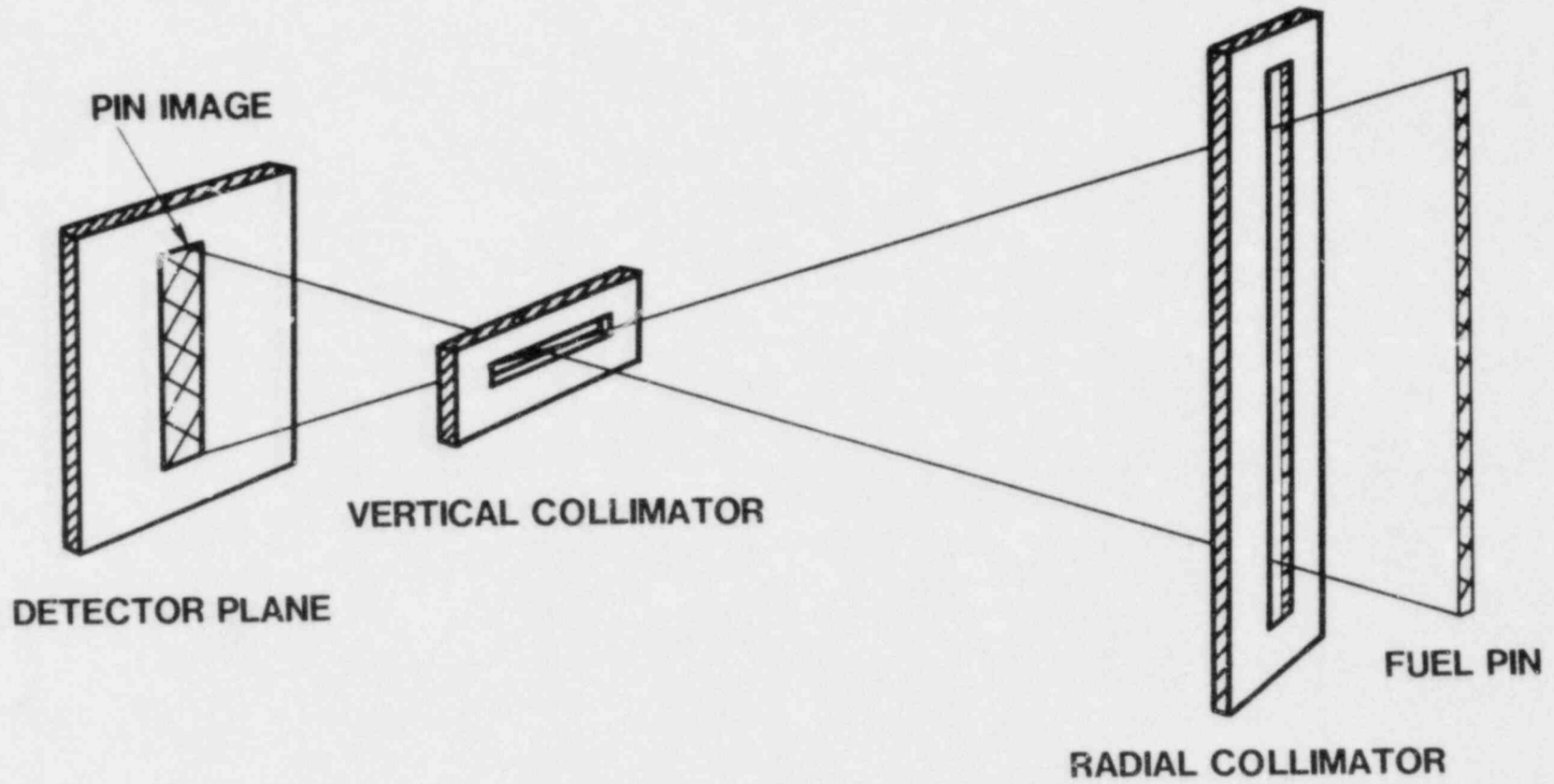


Figure 7.1-2. Crossed Slit Aperture Geometry

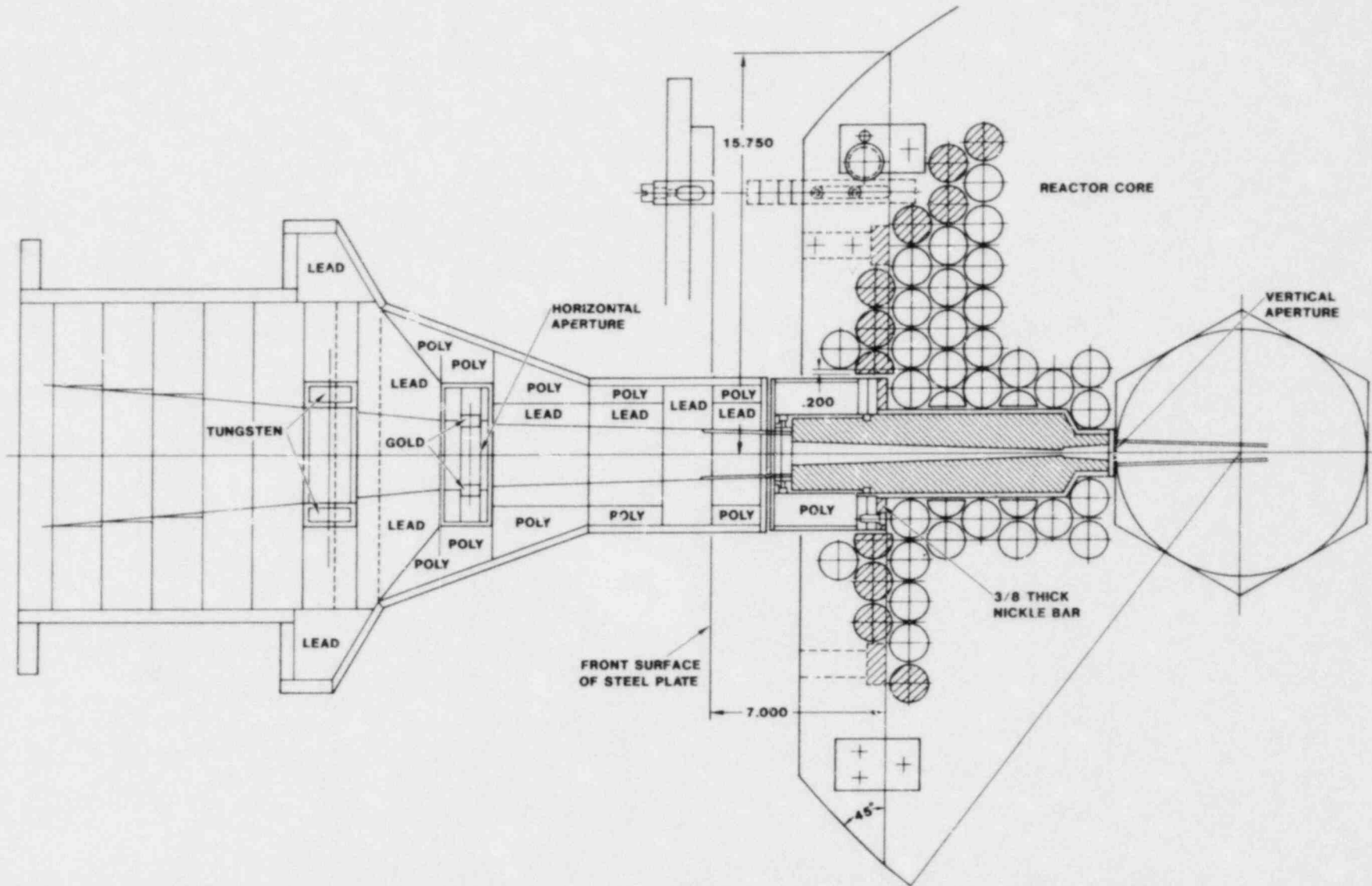


Figure 7.1-3. Crossed Slit Aperture Collimator Design for the Core Slot

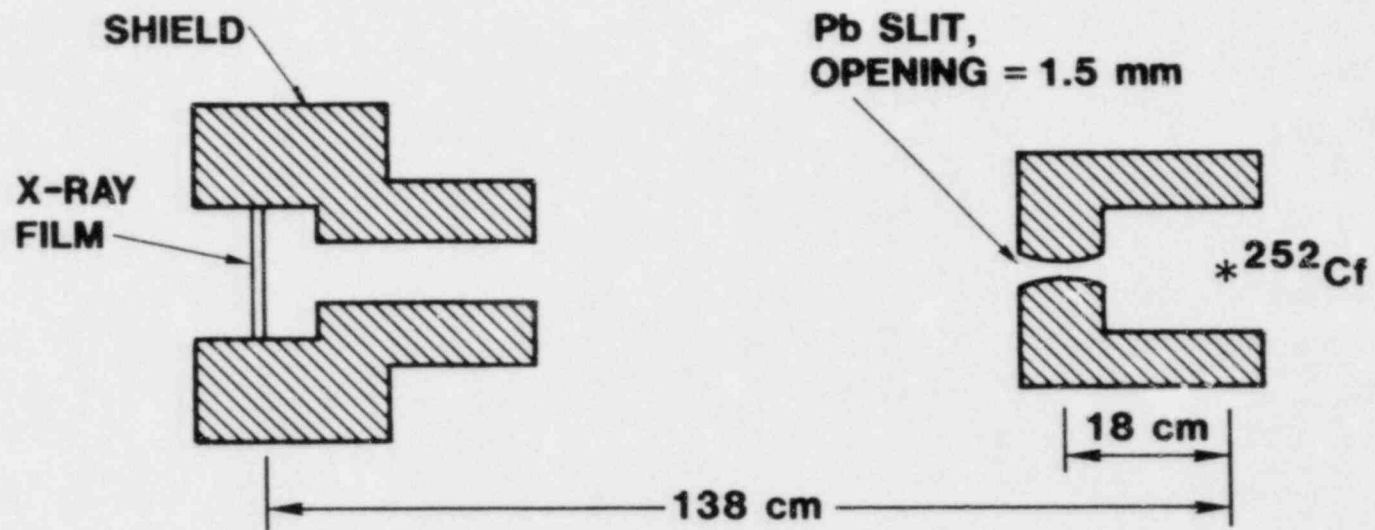


Figure 7.1-4. Geometry for Response Function Measurement of Forward Slit Aperture

Although the ^{252}Cf source size is approximately 1 mm across there are also decreasing side lobes in the source profile. Therefore it is far from an ideal point source for determining the transmission properties of the aperture. However, Figure 7.1-5 shows that the two exposures are well separated in space and indicates a radial resolution in the 1 mm range. The 3 mm spacing at the object plane has been amplified to 1.9 cm at the detector plane. This example indicates that the expanded detector-plane geometry will preserve or improve the radial resolution while permitting the better averaging over noise.

7.1.4 Reduction in Scene Background

Despite the reduction in background radiation that has resulted from shielding improvements, 70% of the exposure at the detector plane in the current configuration is caused by radiation passing through the collimators but not coming from the fuel pin. This radiation has been called "scene" background. Fortunately, as noted in earlier reports, little of this radiation seems to come from the collimator walls; most of it originates within the canister. Therefore, efforts to reduce this background are being concentrated in the test chamber. Although the lead wall behind the pin is of great benefit in reducing the radiation that comes from the core opposite the slot, it is still a source of radiation generated by inelastic scattering neutron capture and subsequent gamma emission.

Additional computer analysis has shown that close to 70% of the "scene" background comes from this lead, indicating that this is the place to make improvements by modification of geometry and materials. Although lead has a thermal-neutron cross section 10 to 100 times smaller than most other high-Z elements, right next to it in the periodic table is bismuth which has a thermal-neutron cross section 5 times lower. In addition, when bismuth captures a neutron the energy released in the form of gamma rays is less on the average than that for lead.

Therefore the fuel-pin-canister geometry shown in Figure 7.1-6 will be tested in the ACRR along with the two aperture geometries. Although bismuth melts at a temperature 60°C lower than lead, it is protected from X-ray heating by the lead around it and will not be in danger of melting.

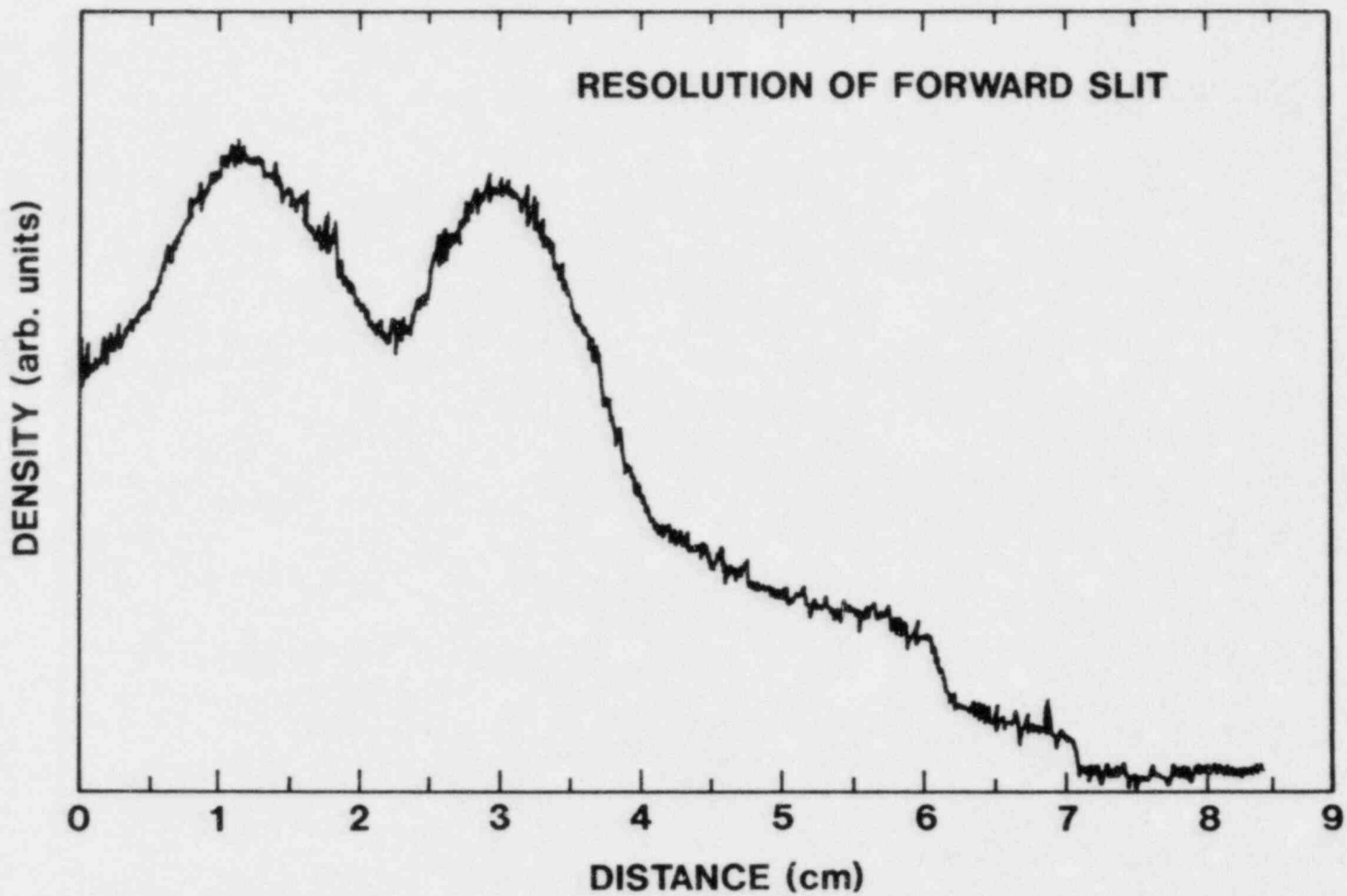


Figure 7.1-5. Slit Image of ^{252}Cf Source Exposures Separated by 3 mm

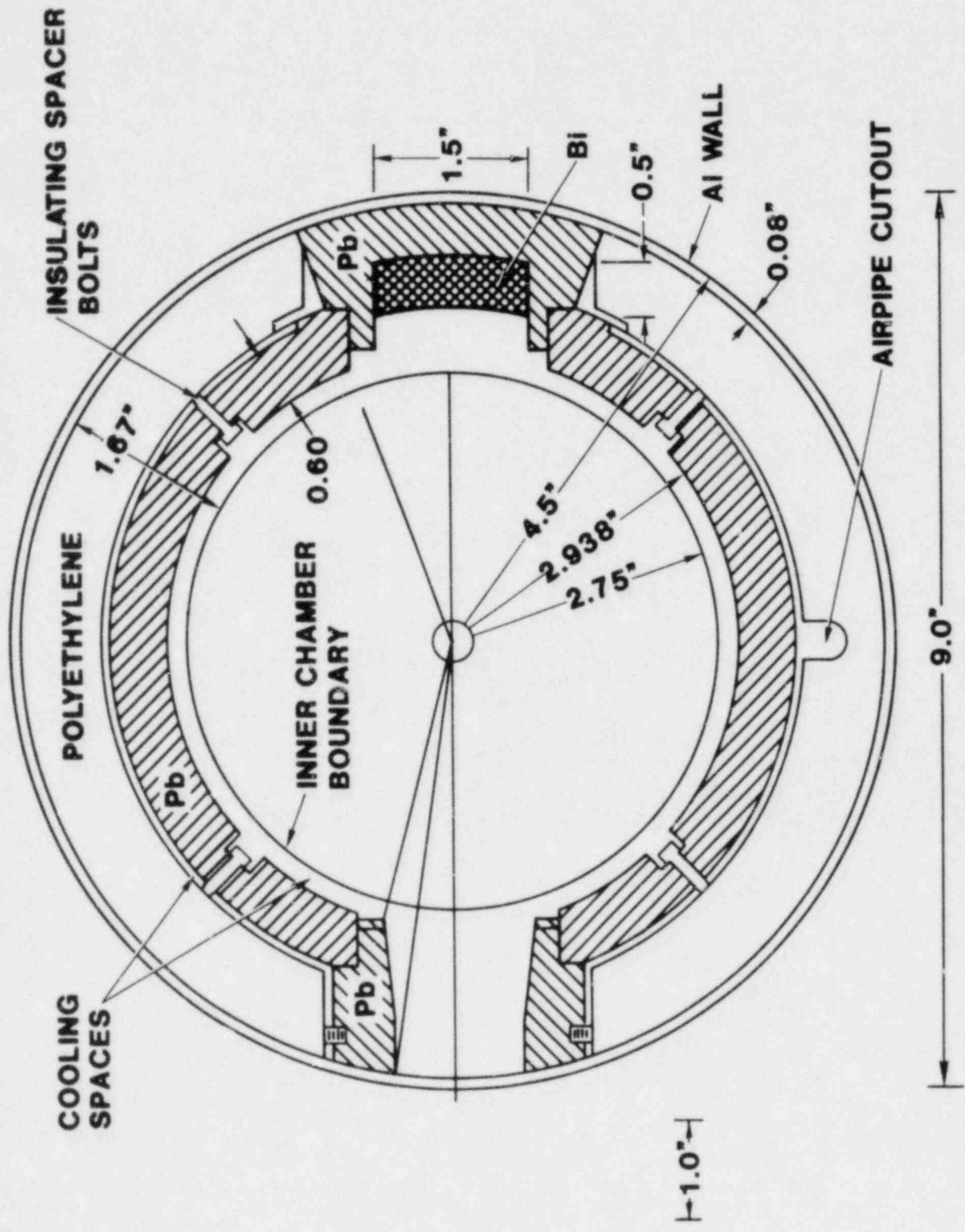


Figure 7.1-6. Canister Geometry with Bismuth Cup Background

Program personnel are not yet certain how much this change in material will change the rear wall emission because the calculations to predict the relative contributions from scattering and from capture have not yet been completed.

7.1.5 Scintillator Design

A fourth area of the CAIS system will be tested in the November experiments. The potential for improvement in the scintillator is a direct result of the enlargement of the image scale at the detector plane. The thin scintillators presently required extract only about 2% of the incident beam energy, but if the resolution requirement is reduced by a factor of 8, the scintillator in principle could be 8 times thicker. The increased light signal would more than make up for the reduction of signal strength of 5 which results from the conversion to the crossed slit geometry.

Commercially available scintillator structures suitable for imaging in the CAIS are not available. Also, resources are not available at the present time to develop in-house the mosaic scintillator described in a quarterly report over 4 years ago (January-March 1977, SAND77-0611). Investigators estimate that a scintillator plate 5 mm thick could be assembled with small bars of ZnS:Ag with dimensions of 2x2x5 mm separated by thin layers of MgO to keep light from traversing to adjacent blocks. There would be about 4 blocks per resolution distance in the image. Investigations are going on to estimate the feasibility of this design.

A simpler configuration using ZnS:Ag powder will be tested in the November experiment. Powder scintillators about 0.75 mm thick were used in the March 1980 proof tests with considerable success. It is possible that 2 mm layers will produce more light; however, saturation is expected to become noticeable because of the excessive light scattering among the many micron size scintillator crystals. Presumably the thickness saturation limit will be determined in these tests. If crystals approximately 0.5 mm on a side could be used, the scattering losses are estimated as small.

7.2 ACFR Status

This section contains comments on the general status of overall ACRR operation and remarks concerning experimental activities involving the ACRR.

The ACRR is operating normally in support of weapons program research and advanced reactors safety experiments.

DISTRIBUTION:

US NRC Distribution Contractor (CDSI)
(275 copies for R7)
7300 Pearl Street
Bethesda, MD 20014

U.S. Nuclear Regulatory Commission (4)
Division of Accident Evaluation
Office of Nuclear Regulatory Research
Washington, DC 20555
Attn: C. N. Kelber, Assistant Director,
Advanced Reactor Safety Research
R. T. Curtis, Chief
Analytical Advanced Reactor Safety Research, ARSR
M. Silberberg, Chief
Experimental Fast Reactor Safety
R. W. Wright
Experimental Fast Reactor Safety

U.S. Department of Energy
Office of Nuclear Safety Coordination
Washington, DC 20545
Attn: R. W. Barber

U.S. Department of Energy (2)
Albuquerque Operations Office
P.O. Box 5400
Albuquerque, NM 87185
Attn: J. R. Roeder, Director
Operational Safety Division
D. L. Krenz, Director
Energy Research & Technology Division
For: C. B. Quinn
R. L. Clark

T. Ginsberg
Department of Nuclear Energy
Bldg. 820
Brookhaven National Laboratory
Upton, NY 11973

University of Michigan
Nuclear Engineering Department
Ann Arbor, MI 48104

DISTRIBUTION (Cont'd)

General Electric Corporation (7)

310 De Guigne Drive
Sunnyvale, CA 94086

Attn: S. M. Davies, Mgr., Conceptual Design Study
M. I. Temme, Mgr., Safety Criteria & Assessments
K. H. Chen, M/C S-54

W. E. Nyer
P.O. Box 1845
Idaho Falls, ID 83401

W. Tarbell
K Tech Corp
901 Pennsylvania NE
Albuquerque, NM 87110

Projekt Schneller Brueter (4)
Kernforschungszentrum Karlsruhe GMBH
Postfach 3640
D75 Karlsruhe
West Germany
Attn: Dr. Kessler (2)
Dr. Heusener (2)

M. S. Hayns
E. V. Gilby
R. S. Peckover
UKAEA
Safety and Reliability Directorate
Wigshaw Lane
Culcheth
Warrington, WA3 4NE
Cheshire
England

J. Gittus, AETB
J. Collier, AETB
J. R. Matthews, Theoretical Physics Division
AERE Harwell
Oxfordshire, OX11 0RA
England

DISTRIBUTION (Cont'd)

B. Cowkins
D. Hicks
UKAEA
Risley
Warrington WA3 6AT
Cheshire
England

F. Briscoe
Culham Laboratory
Culham
Abingdon
Oxfordshire OX14 3DB
England

R. Potter
J. G. Tyror, RDD
UKAEA - Atomic Energy Establishment
Winfrith, Dorchester
Dorset DT2 8DH
England

Joint Research Centre (2)
Ispra Establishment
21020 Ispra (Varese)
Italy
Attn: R. Klersy
H. Holtbecker

Power Reactor & Nuclear Fuel (3)
Development Corporation (PNC)
Fast Breeder Reactor Development Project (FBR)
9-13, 1-Chome, Akasaka
Minato-Ku, Tokyo
Japan
Attn: Dr. Watanabe

DISTRIBUTION (Cont'd)

2150 C. B. McCampbell
 3431 B. N. Yates
 4230 J. E. Powell
 4231 T. P. Wright
 5500 O. E. Jones (Actg.)
 5510 D. B. Hayes
 5520 T. B. Layne
 5530 W. Herrmann
 5534 D. A. Benson
 5541 W. Luth
 5800 R. S. Claassen (Actg.)
 5830 M. J. Davis
 5835 C. H. Karnes
 5840 N. J. Magnani
 5846 R. A. Sallach
 5846 R. K. Quinn
 7100 C. D. Broyles
 Attn: J. D. Plimpton, 7110
 T. L. Pace, 7120
 G. L. Ogle, 7125

 7530 W. E. Caldes
 7537 N. R. Keltner
 7537 R. U. Acton
 7550 F. W. Neilson
 Attn: O. J. Burchett, 7552
 J. H. Gieske, 7552

 7737 T. Y. Chu
 9000 G. A. Fowler
 9400 A. W. Snyder
 9410 D. J. McCloskey
 9412 J. W. Hickman
 9415 D. C. Aldrich
 9420 J. V. Walker (5)
 9421 T. R. Schmidt
 9421 J. E. Gronager
 9421 J. T. Hitchcock
 9421 G. W. Mitchell
 9421 C. Ottinger
 9421 J. B. Rivard
 9422 D. A. Powers
 9422 J. E. Brockmann
 9422 E. R. Copus
 9422 R. M. Elrick
 9422 E. Randich
 9422 A. R. Taig
 9423 P. S. Pickard
 9423 A. C. Marshall
 9423 D. A. McArthur
 9423 K. O. Reil
 9424 M. J. Clauser

DISTRIBUTION (Cont'd)

9424 J. P. Odom
9424 F. W. Sciacca
9424 M. E. Senglaub
9424 D. C. Williams
9425 W. J. Camp
9425 E. Bergeron
9425 W. M. Breitung
9425 R. J. Lipinski
9425 K. K. Murata
9425 P. Herter
9425 M. Pilch
9425 A. Suo-Anttila
9425 A. Wickett
9425 M. F. Young
9426 G. L. Cano
9426 J. G. Kelly
9426 K. T. Stalker
9426 W. H. Sullivan
9426 S. A. Wright
9440 D. A. Dahlgren
9441 M. Berman
9442 W. A. von Riesmann
9450 J. A. Reuscher
9451 T. Luera
9452 M. Aker
9453 W. A. Whitfield
9530 R. W. Lynch
9550 R. M. Jefferson
9723 D. O. Lee
8214 M. A. Pound
3141 L. J. Erickson (5)
3151 W. L. Garner (3)
For: DOE/TIC (Unlimited Release)
3154-3 C. H. Dalin (25)
For: NRC Distribution to NTIS

